Dissertation

submitted to the

Combined Faculty of Natural Sciences and Mathematics

of the Ruprecht-Karls-Universität of Heidelberg, Germany

for the degree of

Doctor of Natural Sciences

Put forward by

Jae Yeon Kim

born in Pohang, South Korea

Oral examination: 17.04.2023

Quantifying the environmental dependence of the molecular cloud lifecycle in 54 main sequence galaxies

Referees: Dr. Mélanie Chevance
                 Prof. Dr. Simon C. O. Glover

Zusammenfassung

Riesenmolekülwolken (GMCs) bilden Sterne unter den von ihrer Wirtsgalaxie vorgegebenen Anfangsbedingungen, die Energie und Materie in ihre Umgebung zurückführen und so zur Galaxienentwicklung beitragen. Die detaillierten Eigenschaften dieser Prozesse zwischen molekularem Gas und jungen Sternen sind jedoch nach wie vor schwer fassbar, vor allem aufgrund fehlender Beobachtungsdaten. Unter Ausnutzung der CO- und Hα-Beobachtungen von PHANGS haben wir systematisch die Zeitachse der Entwicklung von GMCs zu exponierten Hɪɪ-Regionen in 54 Galaxien gemessen, der bisher größten und statistisch vollständigsten Stichprobe. Es wurden starke Korrelationen zwischen den Zeitskalen der GMC-Evolution und den Eigenschaften der Wirtsgalaxie festgestellt, die den Zusammenhang zwischen der Dynamik im galaktischen Maßstab und dem kleinräumigen Lebenszyklus der GMCs aufzeigen. Darüber hinaus haben wir in den 5 nächstgelegenen Galaxien meiner Stichprobe ($D < 3,5\,\mathrm{Mpc}$) festgestellt, dass die erste Hälfte der eingebetteten Sternentstehung, die in *Spitzer* $24\,\mu\mathrm{m}$ nachgewiesen wurde, in Hα unsichtbar ist. Schließlich haben wir anhand neuartiger JWST-Beobachtungen von NGC628 mit einer im Vergleich zu *Spitzer* 10-fach besseren Auflösung gezeigt, dass die eingebettete Phase der Sternentstehung in einer größeren Entfernung (D=9,8Mpc) charakterisiert werden kann. Damit haben wir den Weg für die systematische Bestimmung der frühen Phasen der Sternentstehung in der gesamten nahen Galaxienpopulation (bis zu 20Mpc) mit PHANGS-JWST bereitet.

Abstract

Giant molecular clouds (GMCs) form stars with initial conditions set by their local host galaxy environment, which feedback energy and matter into their surroundings, contributing to galaxy evolution. However, the detailed characteristics of these processes between molecular gas and young stars remain elusive, primarily due to a lack of observational constraints. By capitalizing on CO and Hα observations from PHANGS, we have systematically measured the evolutionary timeline from GMCs to exposed Hɪɪ regions, across 54 galaxies, the largest and most statistically complete sample to-date. Strong correlations between GMC evolutionary time-scales and the host galaxy properties have been identified, revealing the connection between galactic-scale dynamics and the small-scale GMC lifecycle. Furthermore, in the 5 nearest galaxies of my sample ($D < 3.5\,\mathrm{Mpc}$), we have established that the initial half of the embedded star formation detected in *Spitzer* $24\,\mu\mathrm{m}$ is invisible in Hα. Finally, using novel JWST observations of NGC628 with 10 times better resolution compared to *Spitzer*, we have further demonstrated that the embedded phase of star formation can be characterized at a greater distance (D=9.8Mpc), pioneering the way for the systematic determination of the early phases of star formation across the nearby galaxy population (up to 20Mpc) with PHANGS-JWST.

Contents

Acknowledgements   85

Bibliography   87

Chapter 1

Introduction and background

Galaxies are shaped by the complex interplay between star formation and feedback. Gas flows into galaxies and becomes molecular gas, which later collapses and produces stars. These newly formed stars, in the form of feedback, inject energy, metals, and matter into their surroundings, creating H II regions and ultimately revealing the young stars from their parental clouds. Together, these processes are the engine that turns gas into stars and shapes galaxies. One of the major unresolved questions in the field is the detailed characterisation of the physical processes regulating the cycle of matter between molecular gas and young stars and how they differ in various environments.

There are several physical mechanisms that are related to GMC evolution, such as galactic shear and spiral arm passage on a galactic-scale or internal GMC collapse time-scale and stellar feedback on a smaller scale, which all act on different time-scales ranging from $\lesssim 1 \, \mathrm{Myr}$ to $\sim 100 \, \mathrm{Myr}$ (Jeffreson and Kruijssen, 2018; Chevance et al., 2020a, 2022a; Sun et al., 2022). Therefore, one way of answering the aforementioned question is determining the characteristic timescales of the successive phases of star-forming processes, which requires a multi-wavelength, high-resolution, and systematic approach. The work presented in the following chapters aims to achieve this by capitalising the PHANGS[1] survey data (Leroy et al., 2021). With this, we quantify the environmental dependence of the evolutionary timeline of giant molecular clouds (GMCs), which are large complexes ($\sim 100 \, \mathrm{pc}$) of cold gas ($T_{\mathrm{gas}} \approx 10-50 \, \mathrm{K}$) that are massive ($10^4-10^7 \, M_{\odot}$) and dense ($n(\mathrm{H_2}) \approx 10^2-10^5 \, \mathrm{cm^{-3}}$), providing sites for ongoing star formation (Solomon et al., 1987; Blitz, 1993; McKee and Ostriker, 2007; Bigiel et al., 2008; Leroy et al., 2008; Kennicutt and Evans, 2012; Rosolowsky et al., 2021).

This introduction is organised as follows. Section 1.1 is devoted to an overview of the observed relation between star formation and molecular gas from a galactic-scale to GMC-scale. Section 1.2 focuses on the observed properties of GMCs. Finally, the current understanding of the life and times of GMCs is introduced in Section 1.3.

---

[1]The Physics at High Angular resolution in Nearby GalaxieS project: http://phangs.org

1.1   Star formation and gas in galaxies

In extragalactic astronomy, one of the most used scaling relations is the correlation between gas (including both atomic and molecular) and star formation rate (SFR) surface densities (Σ_{gas} and Σ_{SFR}, respectively). This association is tight when observed on a scale of a galaxy and often referred to as the *"star formation relation"*. Schmidt (1959) has first proposed the theoretical model of star formation, demonstrating a connection between the amount of newly formed stars and the mass of interstellar gas. Using observations of various galaxies, including normal spiral galaxies (Kennicutt, 1989, 1998; Wong and Blitz, 2002; Heyer et al., 2004; Kennicutt et al., 2007; Schuster et al., 2007; Bigiel et al., 2008; Kennicutt and Evans, 2012), low surface brightness galaxies (Wyder et al., 2009), dwarf galaxies (Leroy et al., 2005; Verley et al., 2010), starbursting high-redshift galaxies (Bouché et al., 2007; Daddi et al., 2010; Genzel et al., 2010), this correlation has been observed to obey the form

$$\Sigma_{\mathrm{SFR}} \propto \Sigma_{\mathrm{gas}}^n. \tag{1.1.1}$$

The index $n \approx 1.4-3.0$ when the total gas (both atomic and molecular) density is used for estimating Σ_{gas}, whereas $n \approx 1.0-1.4$ when only the molecular gas component is considered.

At first glance, the star formation relation seems to be easily interpreted reflecting the fact that gas is the most critical factor for driving star formation. However, the link between this empirical relation on a global scale to that on a scale of fundamental units of star formation, such as molecular clouds and young stellar populations, remains obscure. For example, the time it takes for galaxies to deplete their gas into stars while forming stars at the current rate (depletion time-scale, $t_{\mathrm{dep}} = \Sigma_{\mathrm{gas}}/\Sigma_{\mathrm{SFR}}$) is $2-10\,\mathrm{Gyr}$ for total gas (Kennicutt, 1989, 1998; Bigiel et al., 2008) and $1-3\,\mathrm{Gyr}$ for denser molecular gas (Kennicutt, 1989, 1998; Wong and Blitz, 2002; Bigiel et al., 2008; Leroy et al., 2008, 2013; Utomo et al., 2017; Muraoka et al., 2019; Ellison et al., 2021). These observed gas depletion time-scales are one or two orders of magnitude longer than any processes that are relevant for star formation activity (Jeffreson and Kruijssen, 2018; Sun et al., 2022), such as internal physical processes (GMC free-fall and turbulence crossing time; $5-20\,\mathrm{Myr}$) and dynamical processes (orbital, shearing and, cloud-cloud collision times; $\sim 100\,\mathrm{Myr}$).

Following a theoretical description by Krumholz and McKee (2005), star formation law may also be expressed as

$$\Sigma_{\mathrm{SFR}} = \frac{\epsilon_{\mathrm{SF}}}{t_{\mathrm{GMC}}}\Sigma_{\mathrm{gas}}, \tag{1.1.2}$$

where ϵ_{SF} is the mass fraction of gas converted into stars (star formation efficiency) and t_{GMC} represents the timescale of this transition, i.e. the lifetime of GMCs. This Equation Equation (1.1.2) can be rearranged to express t_{dep} as $t_{\mathrm{GMC}}/\epsilon_{\mathrm{SF}}$, indicating that ϵ_{SF} and t_{GMC} are degenerate quantities when obtaining t_{dep}. Therefore, the large values for t_{dep} in galaxies as discussed above, exceeding the GMC dynamical time-scale by several orders of magnitude, can either be explained 1) if star formation proceeds slowly and efficiently within GMCs, converting most of the gas into stars over many dynamical time-scales, resulting in long t_{GMC} and high ϵ_{SF} or 2) if star formation is fast and inefficient, converting

only a small fraction of gas into stars before GMCs are dispersed within a dynamical time-scale, resulting in short t_{GMC} and low ϵ_{SF} (Kruijssen and Longmore, 2014; Kruijssen et al., 2019). In the first case, one should expect to see significant spatial overlap between molecular clouds and young stellar populations, whereas in the second case, they should show spatially distinct distributions.

During recent decades, various high-resolution observations resolving galaxies into independent units of star-forming regions have reported that the tight correlation observed between gas and young stars on a global scale breaks down on a cloud scale (Engargiola et al., 2003; Blitz et al., 2007; Bigiel et al., 2008; Kawamura et al., 2009; Onodera et al., 2010; Schruba et al., 2010; Miura et al., 2012; Meidt et al., 2015; Corbelli et al., 2017; Kruijssen et al., 2019; Schinnerer et al., 2019; Chevance et al., 2020a,b; Pan et al., 2022). The breakdown of the relationship illustrates that gas and young stars are spatially separated, most likely due to stellar feedback rapidly reshaping the interstellar medium via kinetic dislocation of parental clouds from the newly formed stars or photodissociation molecular gas (or its tracer molecule; Schruba et al., 2010; Kruijssen et al., 2019). This points toward a view where GMCs are short-lived, contradicting the traditional view where GMCs are considered to represent a quasi-equilibrium structure that survives over many dynamical time-scales ($\sim 100\,\mathrm{Myr}$; Scoville and Hersh, 1979; Koda et al., 2009). With an aim to understand why the time-scale for depleting molecular gas via star formation in galaxies is much longer compared to the internal dynamical time-scales (e.g. free-fall) of GMCs, this thesis performs systematic measurements of the GMC lifetime and star formation efficiency in the local universe.

1.2 Giant molecular clouds

1.2.1 Observations of giant molecular clouds

Star formation occurs dominantly in GMCs, which are reservoirs of cold, dense, interstellar medium in a molecular gas phase (H_2). Molecular gas forms on the surfaces of dust grains and are destroyed by resonant absorption of Lyman- and Werner-band photons in far ultraviolet (van Dishoeck and Black, 1986; Black and van Dishoeck, 1987; Sternberg, 1988; Krumholz et al., 2008, 2009; Wolfire et al., 2010; Dobbs et al., 2014). The reason why stars form in molecular gas is related to the fact that the molecular gas fraction drastically increase in high densities, typically at surface densities of $1-100\,M_\odot \mathrm{pc}^{-2}$, as molecular gas becomes shielded from ultraviolet radiation allowing the gas to cool ($\sim 10-50\,\mathrm{K}$), condense and eventually form stars.

One might assume that the most precise way of observing molecular gas and GMCs would be to directly use emission lines from H_2. Unfortunately, the cold H_2 at temperatures of a few 10s of K is invisible in emission not only because of its diatomic molecule lacking in dipole moment (thus no corresponding dipolar rotational transition) but also because of its low mass (Kennicutt and Evans, 2012; Bolatto et al., 2013). For H_2, rotational excitation states require the lowest energies. However, even the temperature required to excite molecular gas to this lowest energy is too high ($T \gtrsim 100\,\mathrm{K}$) that almost no molecules

in the cold and dense interstellar medium will be able to occupy it. Even if these lines can be used, the emission originates from surfaces of clouds probing only 1 to 30% of the gas (Roussel et al., 2007).

Since using emission lines of Hydrogen molecules is not a viable option, indirect tracers of molecular gas, such as black body radiation from dust grains and emission lines from other heavier molecules, have been widely used. The most popular indirect tracer is CO, which is a combination of the two most abundant elements in the universe after Hydrogen and Helium. The formation of CO is prevalent in conditions where molecular gas is dominant. CO also has low excitation energy, making it to be readily excited even in cold molecular clouds. Furthermore, the emission is strong and lies at a wavelength ($2.6\,\mathrm{mm}$ for $J = 1 \to 0$) that can easily pass through the atmosphere of Earth. However, CO also has its own shortcomings. In particular, at a low-metallicity regime, there is less dust and therefore a higher column density is required to shield CO from photodissociating. On the other hand, H_2 is harder to destroy compared to CO and therefore the change in the column density required to protect H_2 is much smaller than that of CO (Wolfire et al., 2010; Madden et al., 2020; Wolfire et al., 2022). Thus, in such low-metallicity environments, CO emission traces only the densest core region of molecular clouds while H_2 is still located at the envelope of CO emitting region. This H_2 not being traced with CO is referred to as CO-dark molecular gas (Bolatto et al., 2013).

In the Milky Way, Wilson et al. (1970) have reported the first detection of intense CO emission in the interstellar medium by looking at the Orion nebula with 36-foot NRAO antenna at Kitt Peak. Mapping of CO emission in nearby star-forming regions along the Galactic Plane has discovered that this emission arises from giant molecular complexes extending of about $\sim 100\,\mathrm{pc}$ (Lada, 1976; Kutner et al., 1977; Blitz and Thaddeus, 1980) and constitute quite a significant mass fraction in the interstellar medium, especially in the inner Galaxy where molecular gas mass is found to dominate over atomic gas mass (Burton et al., 1975; Scoville and Solomon, 1975; Stecker et al., 1975; Gordon and Burton, 1976; Burton and Gordon, 1978; Sanders et al., 1984). Molecular gas was found to be prevalent in the inner region with clumpy distributions, showing more similarities with HII regions in terms of morphological features compared to relatively diffuse atomic gas (Solomon et al., 1972; Wilson et al., 1974; Scoville and Solomon, 1975).

In the extragalactic observations, the first CO emission was detected in several galaxies, which was found to be especially strong in the central regions of galaxies with nuclear activity (e.g., M82 and NGC 253; Rickard et al., 1975; Solomon and de Zafra, 1975). During the last 40 years, the number of galaxies with CO observations has drastically increased thanks to the development of facilities providing improved sensitivity. These observations either have surveyed integrated CO emission in galaxies (e.g., the FCRAO Extragalactic CO Survey, Young et al., 1995; AMIGA, Lisenfeld et al., 2011; COLD GASS, Saintonge et al., 2011; ALLSMOG, Bothwell et al., 2014; xCOLD GASS, Saintonge et al., 2017; and JINGLE, Saintonge et al., 2018) or resolved CO emission down to structures of a kpc-scale, which is not sufficient to distinguish individual regions within galaxies (e.g., BIMA SONG, Helfer et al., 2003; the Nobeyama CO Atlas, Kuno et al., 2007; HERACLES, Leroy et al., 2009; the JCMT NGLS, Wilson et al., 2012; CARMA STING, Rahman et al.,

2012; ATLAS-3D CO, Alatalo et al., 2013; CARMA EDGE, Bolatto et al., 2017; NRO COMING, Sorai et al., 2019; and ALMAQUEST, Lin et al., 2019). It was only after the commissioning of powerful interferometric facilities such as the Atacama Large Millimeter Array (ALMA) that we were able to obtain high-resolution CO images of galaxies located outside the Local Group, resolving GMCs (e.g., NUGA, Combes et al., 2009; PHANGS, Leroy et al., 2021; WISDOM, Davis et al., 2022; and many individual programs, e.g., Faesi et al., 2018; Imara and Faesi, 2019; Miura et al., 2021).

These high-resolution CO observations at scales of $\sim 100\,\mathrm{pc}$ have established demographic studies of GMCs, providing a wealth of insights on physical processes that regulate the cycle of matter from gas to stars and build galaxies. For example, molecular clouds exhibit masses ranging from $\sim 10^4$ to $10^7\,M_\odot$ (e.g, Rosolowsky et al., 2021), where their mass distribution, above a certain cutoff mass ($\sim 10^5 - 10^6\,M_\odot$), follows a power-law $dN/dM = M^{-\gamma}$, indicating that there are few very massive ones and many low mass clouds. In the Milky Way observations, γ is measured to be between 1.5 to 1.8 (Solomon et al., 1987; Kramer et al., 1998; Heyer et al., 2001; Roman-Duval et al., 2010). Extragalactic measurements suggest a steeper value ($\gamma \approx 1.6 - 3.4$) compared to the Milky Way observations, possibly due to a lack of completeness, missing out on small and faint clouds (Rosolowsky, 2005; Fukui et al., 2008; Wong et al., 2011; Gratier et al., 2012; Rosolowsky et al., 2021). Solomon et al. (1987) and Roman-Duval et al. (2010) have found that the average molecular gas surface density of GMCs in the Milky Way is $\Sigma_{\mathrm{GMC}} \approx 150^{+95}_{-70}\,M_\odot\mathrm{pc}^{-2}$, where the errors indicate 1σ interval. Measured averages of Σ_{GMC} in extragalactic observations vary significantly ranging from $50\,M_\odot\mathrm{pc}^{-2}$ for GMCs in the Magellanic Clouds (Fukui et al., 2008; Hughes et al., 2010; Schruba et al., 2019) and up to $\sim 100 - 200\,M_\odot\mathrm{pc}^{-2}$ in nearby molecular gas-rich spiral galaxies (Colombo et al., 2014b; Sun et al., 2020b; Rosolowsky et al., 2021; Sun et al., 2022). Starbursting galaxies often show even higher Σ_{GMC} of $\sim 1000\,M_\odot\mathrm{pc}^{-2}$ (Leroy et al., 2015; Pereira-Santaella et al., 2016; Miura et al., 2018).

CO observations also provide information on the velocity dispersion of molecular clouds along the line of sight (σ_v). This σ_v, along with sizes (R_{GMC}) and masses (M_{GMC}) of GMCs are often used to gauge the balance between the kinetic energy (E_k) and gravitational binding energy (U_g), so called the virial parameter (α_{vir}; Bertoldi and McKee, 1992). Simplistically, the virial parameter is expressed as

$$\alpha_{\mathrm{vir}} = 2E_k/U_g = 5\sigma_v^2 R_{\mathrm{GMC}}/GM_{\mathrm{GMC}}. \qquad (1.2.1)$$

A cloud is defined to be bound if $\alpha_{\mathrm{vir}} < 2$ and unbound if $\alpha_{\mathrm{vir}} > 2$. Using an archival CO survey data, Evans et al. (2021) have shown that the virial parameter decreases with increasing mass of the structures, finding that, in terms of mass fractions, 19% of structures in the Milky Way are bound and 35% for other galaxies (see also a compilation by Chevance et al., 2020b). However, we caution in the interpretation of the GMC boundness due to the oversimplifications in obtaining α_{vir}. Other factors such as surface pressure from the surrounding medium, magnetic fields, tidal effects, and external gravitational potential are likely to play a major role (e.g., Dib et al., 2007; Mao et al., 2020; Kim et al., 2021b). How the GMC properties described above vary in different environments is discussed in more detail in Section 1.2.3.

1.2.2   Observations of star formation in giant molecular clouds

To estimate how quickly GMCs are converting their gas into stars, the star formation efficiency per free-fall time, ϵ_{ff}, is widely used (Krumholz and McKee, 2005). This is defined as

$$\epsilon_{\mathrm{ff}} = \Sigma_{\mathrm{SFR}}/(\Sigma_{\mathrm{gas}}/t_{\mathrm{ff}}), \qquad (1.2.2)$$

where t_{ff} is the free-fall time and corresponds to the time it takes for an object experiencing no significant force other than gravity to collapse to a singularity. Cloud-scale observations of star formation activities can be performed using various direct and indirect indicators, such as the number of young stellar objects, Hα, ultraviolet, and mid-infrared emission (e.g., Kennicutt and Evans, 2012). The most direct way to measure SFR is to count the number of young stellar objects. This method has been used to estimate star formation efficiencies in individual, spatially resolved GMCs at a resolution of $< 10\,\mathrm{pc}$ (residing in the Milky Way system), which is found to be on average of $\epsilon_{\mathrm{ff}} \approx 0.01-0.03$ (Evans et al., 2009; Heiderman et al., 2010; Evans et al., 2014; Lee et al., 2016; Vutisalchavakul et al., 2016; Ochsendorf et al., 2017; Pokhrel et al., 2021).

The star counting method, however, is not applicable for molecular clouds located further than the Magellanic clouds. Therefore, studies of nearby galaxies have relied on other tracers (e.g., ultraviolet, Hα, and mid-infrared emission). The ultraviolet emission, revolutionised by the launch of the Galaxy Evolution Explorer mission (GALEX; Martin et al., 2005), has been widely utilised as a tracer for SFR. It directly captures the photospheric emission from O- through late-type B-stars with masses above $\sim 3\,M_\odot$ and thus is sensitive to stars formed over the past of $10-100\,\mathrm{Myr}$ (Hao et al., 2011). Hα emission arises from the recombination of Hydrogen in H<small>II</small> regions, which have been ionised by ionising photons ejected from relatively massive stars with their mass spectrum ranging from O- through early-type B-stars (masses above $\sim 20\,M_\odot$). This emission, therefore, traces the most current star formation activity within a few million years (Kennicutt and Evans, 2012; Haydon et al., 2020). Dust is also an important component in estimating SFR as it absorbs a significant fraction of stellar light and re-emits in mid-infrared (Calzetti et al., 2007; Kennicutt and Evans, 2012). Especially in the early star-forming phases where young massive stars are still deeply embedded in the densest, dust-enshrouded cores of molecular clouds, Hα and UV emission is attenuated from the extinction provided by surrounding gas and dust. This attenuated stellar light can be accounted for using mid-infrared (e.g. *Spitzer* at $24\,\mu\mathrm{m}$ and JWST at $21\,\mu\mathrm{m}$), capturing the on-going star formation.

These SFR indicators have been extensively utilised to estimate star formation activities in various galaxies. Leroy et al. (2019) have presented an atlas of ultraviolet and infrared images of local galaxies at a $\sim$kpc resolution with distances less than $50\,\mathrm{Mpc}$ using GALEX and Wide-field Infrared Survey Explorer (WISE; Wright et al., 2010). At infrared wavelength, the seminal work by (Kennicutt et al., 2003) have provided infrared observations of nearby galaxies using *Spitzer* (The SIRTF Nearby Galaxy Survey), as well as in Hα emission from ground-based telescopes. JWST is transforming this view in the infrared making huge improvements on the sensitivity and resolution (e.g., PHANGS-JWST, Lee et al., 2022b), enabling the detection of embedded young stellar populations across the

disks of galaxies at $< 100\,\mathrm{pc}$ scales. Optical integral field spectroscopy from the Multi Unit Spectroscopic Explorer (MUSE) aboard the Very Large Telescope (VLT) has obtained spectral maps, including Hα emission, of ~ 30 galaxies, breaking galaxies into individual H$\textsc{ii}$ regions and capturing physical properties of the ionised gas (e.g., MAGNUM, Mingozzi et al., 2019; MUSE Atlas of Disks, den Brok et al., 2020; PHANGS-MUSE, Emsellem et al., 2022). The Hubble Space Telescope (HST) has also greatly expanded the number of galaxies with measurements of Hα emission in broadband and narrowband photometry, allowing the identification and characterisation of individual star clusters and associations (e.g., LEGUS, Calzetti et al., 2015; PHANGS-HST, Lee et al., 2022a). Using combinations of SFR tracers, commonly ultraviolet together with mid-infrared or optical Hα together with mid-infrared, studies in nearby galaxies at scales of $100\,\mathrm{pc}$ find ϵ_{ff} to range from 0.003 to 0.03, with an average of ~ 0.01 (Leroy et al., 2017; Utomo et al., 2018; Schruba et al., 2019; Sun et al., submitted). These values show a good agreement with those measured in Milky Way clouds discussed above.

1.2.3 Influence of large-scale environment on the properties of giant molecular clouds

The formation and evolution of GMCs are closely linked with their host galaxies through multiple interrelated physical processes, including the gas distribution, gravitational potential, radiation field, and feedback-driven flows within the host galaxy (Dobbs et al., 2014; Chevance et al., 2022b). In turn, the internal structure and dynamics of molecular clouds establish the initial conditions for star formation, which have an impact on the matter and radiation distribution within the galaxy via stellar feedback processes (McKee and Ostriker, 2007; Klessen and Glover, 2016). We thus expect strong correlations to exist between molecular clouds and host galaxy properties due to these complex interactions. Understanding these correlations can provide key insights into the physics of cloud evolution, star formation and ultimately galaxy evolution.

Observations of molecular clouds in our Galaxy and nearby galaxies have revealed several trends supporting the connection between the properties of GMCs and their large-scale environment. Sun et al. (2020a) have analysed CO emission in $\sim 100{,}000$ GMC-sized regions across 70 PHANGS-ALMA galaxies, revealing a broad spectrum of molecular gas properties. Molecular gas surface densities span a range of $3.4\,\mathrm{dex}$, velocity dispersions of $1.7\,\mathrm{dex}$, and turbulent pressures of $6.5\,\mathrm{dex}$. The observed variations in the GMC internal turbulent pressure correlate strongly with the pressure required to hold up the disk (dynamical equilibrium pressure), implying a link between cloud-scale cold gas and overall disk structure (Sun et al., 2020b). Molecular clouds near the centre of a galaxy appear to be denser, more massive, and more turbulent, compared to those farther away (e.g., Oka et al., 2001; Colombo et al., 2014b; Freeman et al., 2017; Hirota et al., 2018; Miura et al., 2018; Brunetti et al., 2021). Furthermore, using a statistically representative sample, Sun et al. (2022) have shown that GMC properties correlate widely with their local kpc-scale measures of disk structures (e.g., stellar density, SFR surface density, molecular gas surface density, and galaxy rotation), again supporting the previous findings that cold interstellar medium at $\sim 100\,\mathrm{pc}$ scales reflects the disks it lives in.

Galaxy-to-galaxy variations have also been identified, where clouds in more massive and actively star-forming galaxies exhibit increased sizes, masses, surface densities, and velocity dispersions (Hughes et al., 2013; Leroy et al., 2015, 2016; Schruba et al., 2019; Sun et al., 2020a). Galaxy morphology also matters and the location of the clouds within the galaxy as molecular gas in the centres of barred galaxies shows significantly higher molecular gas surface densities ($\gtrsim 100\,M_\odot \mathrm{pc}^{-2}$) and velocity dispersions ($\gtrsim 10\,\mathrm{km\,s}^{-1}$), compared to those in galaxy discs and in the centres of unbarred galaxies (Colombo et al., 2014a; Egusa et al., 2018; Sun et al., 2020a). Davis et al. (2022) have shown that spiral galaxies show a clumpier distribution of CO emission compared to a smoother CO morphology observed in early-type galaxies.

1.3   Time-scales for the evolution of giant molecular clouds

Measuring the evolutionary timeline of GMCs in various galactic surroundings enables us to understand how star formation is controlled in different physical circumstances. In this section, we discuss characteristic time-scales of molecular cloud evolution from a theory perspective and those estimated using cloud-scale observations.

1.3.1   GMC lifetime estimates from theory

For a self-gravitating cloud, the free-fall time (t_{ff}; see also Section Section 1.2.2) serves as the natural benchmark for time, which equals to

$$t_{\mathrm{ff}} = \sqrt{\frac{3\pi}{32G\rho}} = \sqrt{\frac{\pi^2 R_{\mathrm{GMC}}^3}{8GM_{\mathrm{GMC}}}}, \qquad (1.3.1)$$

where G is the gravitational constant, ρ the density of the gas. Using a statistically representative sample of CO observations from PHANGS-ALMA, Sun et al. (2022) have found t_{ff} to be on average of $\sim 7\,\mathrm{Myr}$, when weighted by the molecular gas mass (see also Schruba et al., 2019; Rosolowsky et al., 2021).

This free-fall time should be considered as the lower limit on the GMC lifetime as it only considers the influence of gravity while ignoring other important factors. These include an asymmetric geometry of the clouds (e.g., Toalá et al., 2012), magnetic fields (e.g., Heitsch et al., 2001; Federrath and Klessen, 2012; Kim et al., 2021b), turbulence (e.g., Krumholz and McKee, 2005; Padoan and Nordlund, 2011), and accretion of low-density material (e.g., Rieder et al., 2022; Jeffreson et al., 2023), which can provide supports against the collapse thus making the free-fall time longer.

Furthermore, measurements of virial parameters of GMCs suggest that they are mostly gravitationally unbound or only marginally bound (see Section 1.2.1; also Evans et al., 2021). This indicates that GMCs evolution takes place on turbulence crossing time rather than on free-fall time. Turbulence crossing time (t_{cr}) represents the time for a turbulent flow to cross molecular clouds and is expressed as

$$t_{\mathrm{cr}} = R_{\mathrm{GMC}}/\sigma_v. \qquad (1.3.2)$$

By this definition, the crossing time is linked to the free-fall time and the virial parameter through the equation $t_{\mathrm{ff}}/t_{\mathrm{cr}} = 0.5\alpha_{\mathrm{vir}}^{0.5}$. As a result, the crossing time of a virialized molecular cloud ($\alpha_{\mathrm{vir}} \approx 1$) is approximately twice the free-fall time. In nearby galaxies, t_{cr} is measured to be on average of $\sim 13\,\mathrm{Myr}$ when weighted by GMC masses (Schruba et al., 2019; Rosolowsky et al., 2021; Sun et al., 2022).

Various theoretical studies have shown that the influence of large-scale dynamical processes on the GMC evolution cannot be ignored (Dobbs et al., 2014; Jeffreson and Kruijssen, 2018; Meidt et al., 2018, 2020). These galactic dynamical processes include orbital motion around the galactic centre, shear induced by galactic differential rotation, and cloud-cloud collisions. Chevance et al. (2020a) suggests that these large-scale dynamics matter in environments with high molecular gas surface densities ($\Sigma_{\mathrm{H}_2} > 8\,M_{\odot}\mathrm{pc}^{-2}$), whereas at lower density environment GMCs appear to be governed by internal processes (gravitational free-fall collapse and turbulence). Sun et al. (2022) measures the characteristic time-scales for these dynamical processes to be an order of magnitude longer than t_{ff} and t_{cr}, implying that the impact of galactic-scale dynamics on individual molecular clouds is probably minor.

Numerical radiation hydrodynamic and magnetohydrodynamic simulations of GMCs are providing insights into their evolutionary sequences and associated time-scales. Various simulations including realistic treatments for stellar feedback (e.g., photoionisation, radiation pressure, stellar winds, and supernovae) have shown that cloud dispersal takes about one free-fall time ($\sim 2-10\,\mathrm{Myr}$), after the onset of star formation (e.g., Rahner et al., 2017; Kim et al., 2018; Grudić et al., 2019; Li et al., 2019; Kim et al., 2021b; Lancaster et al., 2021).

Several interstellar medium simulations on a galactic scale have been conducted, including cosmological zoom, isolated galaxy, and kpc-scale disk patch, which incorporate star formation and various feedback models. These simulations have explored the lifetimes of clouds and the impacts of feedback on cloud destruction. Using cloud tracking analysis to the Milky-Way-like isolated galaxy simulations, Jeffreson et al. (2020) find cloud lifetime of $\sim 10-20\,\mathrm{Myr}$. Using similar simulations, (Jeffreson et al., 2021) reports that the inclusion of early stellar feedback decreases lifetimes of the smallest clouds, but lifetimes of larger clouds with masses above $10^6\,M_{\odot}$ remain unchanged. Supernovae feedback is also crucial in preventing clouds from becoming excessively massive and dense compared to observed clouds (Grisdale et al., 2018; Smith et al., 2020). Benincasa et al. (2020) have also tracked GMCs in simulations of Milky-Way-like galaxies and measured GMC lifetimes of $5-7\,\mathrm{Myr}$, corresponding to $1-2$ free-fall times. An environmental dependence was also identified, where GMC lifetimes becomes shorter with increasing virial parameter.

1.3.2   GMC lifetime estimates from observations

From observations, we only see snapshots of molecular clouds undergoing evolution from gas to stars. Therefore, measuring lifetimes of GMCs requires indirect methods. Over the past several decades, various techniques have been developed, often based on tracking the evolution of GMCs along their trajectory or making use of the spatial distributions of molecular clouds relative to H II regions. Below, we list and describe previous applications

of these methods to nearby galaxies.

Scoville and Hersh (1979) have first attempted to measure the GMC lifetime by tracking evolutionary sequences of GMCs in the Milky Way, assuming that the formation of clouds primarily takes place in spiral arms and then GMCs migrate into the inter-arm regions due to differences in orbital angular velocities between the spiral arms and the galactic disk. Based on the fact that these clouds are found in the inter-arm regions, it is claimed that they can survive for inter-arm crossing time of $\sim 100\,\mathrm{Myr}$. This longevity of clouds was further strengthened in Scoville et al. (2023), by using the concept of conservation of mass flux between molecular gas and atomic hydrogen from one arm to the next spiral arm within an annulus around the centre of the galaxy (H$\textsc{ii}$ is neglected as it constitutes a small mass fraction). In this case, the time-scale of molecular gas is $t_{\mathrm{H_2}} = t_{\mathrm{H\textsc{i}}} \times M_{\mathrm{H_2}}/M_{\mathrm{H\textsc{i}}}$, where $t_{\mathrm{H\textsc{i}}}$ is the spiral arm passage time for atomic hydrogen, $M_{\mathrm{H_2}}$ and $M_{\mathrm{H\textsc{i}}}$ are the masses of molecular and atomic gas within the region. When typical values of $t_{\mathrm{H\textsc{i}}} \approx 100\,\mathrm{Myr}$ and $M_{\mathrm{H_2}}/M_{\mathrm{H\textsc{i}}} \approx 10$ are assumed, the lifetime of molecular gas ($t_{\mathrm{H_2}}$) becomes $\sim 1000\,\mathrm{Myr}$. A similar technique was also applied to the GMCs in spiral arm and inter-arm regions of M51, again supporting the existence of long-lived clouds that survives much longer than GMC free-fall or crossing time (Koda et al., 2009).

Also using properties of clouds observed in the inter-arm regions, Meidt et al. (2015) followed the evolution of GMCs in M51 by observing the changes in cloud number densities along the passage of clouds, departing from the downstream of one spiral arm and moving on to the upstream of the next arm. The estimated GMC lifetime was short ($20-30\,\mathrm{Myr}$) and appeared to be controlled by galactic shear and stellar feedback. It might seem like this method is similar to that of Scoville and Hersh (1979), however, the reason why Meidt et al. (2015) reach a completely different conclusion is because Scoville and Hersh (1979) characterised the time-scale of hydrogen molecules that go through a series of shorter phases of GMC evolution from diffuse to bound objects, and ultimately star-forming.

Kinematics can be used to constrain GMC evolutionary sequence. Engargiola et al. (2003) have used observed velocity differences between GMCs and H$\textsc{i}$ filaments in M33 and suggested that GMCs can not live longer than $10-20\,\mathrm{Myr}$ based on the remarkable spatial correspondence observed between GMC and the distribution of atomic hydrogen. Otherwise, molecular clouds would have drifted off the filaments after their formation, disagreeing with the observed correlation.

By using age spreads of stars in nearby star-forming regions and young stellar associations in the Milky Way and the Large Magellanic Clouds, Efremov and Elmegreen (1998), Elmegreen (2000), and Hartmann (2001) have constrained the duration of star formation in GMCs. This duration of star formation represents the time it takes for GMCs to be dispersed by stellar feedback after the onset of star formation as star formation can only continue as long as there is gas. These studies suggest a rapid dispersion of clouds within an internal GMC dynamical time ($\lesssim 10\,\mathrm{Myr}$).

For extragalactic applications of the age measurement method, one has to adopt a spectral energy distribution fitting technique as it is hard to resolve young stellar populations. This method has been used to measure ages of young stellar populations still deeply embedded in their natal cloud (inferred from the excess in infrared emission and/or visual

inspection of the star-forming region). This duration represents the duration of the heavily obscured phase of star formation ($\sim 1\,$Myr; Whitmore et al., 2014; Calzetti et al., 2015; Hollyhead et al., 2015; Messa et al., 2020).

Such age measurements of young stellar populations, but for fully exposed young stellar populations, also act as a clock when obtaining time-scales associated with different phases of GMC evolution from inert to star-forming and feedback, and finally to fully exposed H_II regions. In the Large Magellanic Cloud, Kawamura et al. (2009) classified GMCs into different types based on their (in)existence of massive star formation: Type I is inert, showing no signs of massive star formation; Type II is ones overlapping with relatively small H_II regions; and Type III is GMCs observed with fully developed H_II regions, as well as young stellar associations or clusters. The number ratio of different types of GMCs can be assumed approximately scale with the time GMCs spend in each phase of their evolution. Thus, by measuring the ages of young stellar clusters as a reference time-scale, an absolute GMC lifetime can be obtained. Kawamura et al. (2009) finds that GMCs survive for $20-30\,$Myr, where $\sim 60\%$ of this time is spent overlapping with young stellar regions. The measured GMC lifetime is two to three times longer than that recently estimated by Ward et al. (2022), using a statistical method (Kruijssen and Longmore, 2014; Kruijssen et al., 2018) described below. This difference is mainly attributed to the reference time used to anchor the absolute timeline. Kawamura et al. (2009) adopts $6.6\,$Myr as a reference time-scale for Type III GMCs based on their observations where 66% of stellar clusters and associations with ages $< 10\,$Myr show associations with molecular gas. Ward et al. (2022) claims that this is not accurate as young stellar clusters and associations must also go through H_II region phase, defined as Type II GMC in Kawamura et al. (2009). Ward et al. (2022) suggest that a consistent GMC lifetime can be obtained when, a more appropriate reference time-scale of $10\,$Myr is used that accounts for the phases of Type II and III GMCs, as well as stellar clusters and associations isolated from their parental clouds.

In recent decades, cloud-scale observations illustrating a spatial decorrelation between molecular clouds and young stellar regions have been increasing fast. Such decorrelations are inevitable if the gas and young stellar phases (often traced using CO and Hα) represent different stages in the lifespan of GMCs, providing further support to the view that GMCs are transient objects that survives for a GMC free-fall or turbulence crossing time ($10-40\,$Myr) and are quickly dispersed by violent feedback from young massive stars (Onodera et al., 2010; Schruba et al., 2010; Miura et al., 2012; Whitmore et al., 2014; Meidt et al., 2015; Corbelli et al., 2017; Schinnerer et al., 2019; Barnes et al., 2020; Pan et al., 2022). Ages of stellar associations or clusters when they stop showing associations with their parental GMCs can also be used to constrain the time it takes for the stellar feedback to disperse the gas. Using this method, the feedback time-scale is estimated to be $2-7\,$Myr in ~ 10 nearby galaxies (Grasha et al., 2018, 2019).

Most of these studies appear to show a coherent picture, where clouds are rapidly evolving with a survival time of $\sim 10-40\,$Myr followed by a fast dispersal of gas via violent stellar feedback. However, these methods have limitations. For example, for methods relying on cloud identification or classification, the definition of cloud categories is subjective, making it hard to compare results from one study to those of others. Furthermore, most of

the techniques described above require resolving cloud structures and stellar populations (at scales of $\lesssim 10\,\mathrm{pc}$), indicating that the application is limited to very nearby galaxies.

In an effort to alleviate these shortcomings, Kruijssen and Longmore (2014) and Kruijssen et al. (2018) have developed a statistically rigorous method that translates the observed spatial decorrelation between cold molecular gas and young stellar regions into their underlying timescales, ranging from an inactive gaseous phase followed by star formation and cloud dispersal, and finally to fully revealed HII regions. This method quantifies the spatial decorrelation by measuring deviations of gas-to-SFR tracer flux ratios on small-scale ($\sim 100\,\mathrm{pc}$) compared to those measured globally. To these observed flux ratios, an analytical function is fitted, which is described by the relative durations of successive phases in the timeline of cloud evolution, as well as the typical distance between independent regions. Assuming a certain reference times-scale, often Hα emitting time-scale of $\sim 5\,\mathrm{Myr}$ (Haydon et al., 2020), the analytical function is described by three independent quantities: cloud lifetime, feedback time-scale (the duration over which gas and SFR tracers are found coincident), and the region separation length.

This method has advantages in that it only requires the emission maps to resolve down to $\sim 100\,\mathrm{pc}$ and is insensitive to the identification and definition of GMCs and young stellar regions. By applying this method to CO and Hα observations, evolutionary timelines between quiescent molecular gas to exposed young stellar regions have been characterised in a dozen galaxies (Kruijssen et al., 2019; Chevance et al., 2020a; Zabel et al., 2020; Lu et al., 2022; Ward et al., 2022). This has revealed that lifetimes of GMCs is $10-30\,\mathrm{Myr}$, showing a good agreement with previous analysis using different methods. The time period during which CO and Hα emission coincide is short, lasting only 1 to 5 Myr. This short duration suggests that pre-supernova feedback, such as photoionization and stellar winds, plays a crucial role in the dispersal of molecular clouds. Ward et al. (2020) have extended this timeline by including HI and found that the lifetime of atomic gas clouds in the Large Magellanic Clouds is approximately 50 Myr.

1.4   This thesis

The first applications of the statistical method (Kruijssen and Longmore, 2014; Kruijssen et al., 2018) to ~10 nearby galaxies have measured that GMCs survive for a GMC dynamical time-scale of 10 to 30 Myr and quickly dispersed by violent feedback from young massive stars within a few Myr (Kruijssen et al., 2019; Chevance et al., 2020a, 2022a). So far, such measurements of time-scales have been limited to a small number of galaxies due to the lack of CO imaging at cloud-scale resolution. Therefore, these previous studies did not allow us to identify key environmental factors and cloud properties that are responsible for setting these time-scales. Now, this can be solved by using data sets provided by the PHANGS survey, which has assembled a multi-wavelength database at a GMC-scale resolution ($\sim 100\,\mathrm{pc}$), encompassing the majority of nearby ($\leq 25\,\mathrm{Mpc}$), main sequence star-forming galaxies (with stellar masses $M_* = 10^{9.5}-10^{11.5} M_\odot$) that are accessible via ALMA (Leroy et al., 2021). In this thesis, we have capitalised these observations to (1) systematically measure an evolutionary sequence of GMCs from gas to stars and quantitatively examine the

connection between small-scale GMC evolution and galactic-scale environmental properties, and (2) further refine the obtained evolutionary timeline by specifically characterising the heavily obscured phase of star formation for a subset of nearest galaxies using infrared emission.

In Chapter 2, we apply the statistical method to CO and Hα observations of 54 galaxies from the PHANGS survey and obtain systematical measurements of the cloud lifetime and feedback time-scale for 54 PHANGS galaxies. To determine the impact of the galactic environment on the evolution of GMCs, we search for statistically strong correlations between our measurements and the average properties of the GMCs, as well as their large-scale surroundings.

In Chapter 3, for six nearby galaxies, we proceed further in the characterisation of the GMC lifecycle by utilizing CO, $24\,\mu$m, and Hα emission as indicators of molecular gas, embedded star formation, and fully revealed H II regions free of cold molecular gas, respectively. The use of mid-infrared emission at $24\,\mu$m from *Spitzer*, enables us to study the initial phase of star formation, where the stars are heavily obscured. We determine how long it takes for young star-forming regions to emerge from their birth clouds, becoming visible in Hα emission as H II regions by ionising radiation that they produce.

Before JWST, such measurements including the heavily obscured phase could only be done for a handful of the nearest galaxies with distances less than $3.5\,$Mpc, due to the limited angular resolution and sensitivity of *Spitzer*. Thanks to the innovative abilities of JWST, it has become possible to investigate the matter cycle during the early stages of star formation in relation to galactic environments. In Chapter 4, using the initial data of NGC628 from JWST, we perform an application of the same method to a more distant galaxy for the first time to demonstrate the feasibility of PHANGS-JWST (Lee et al., 2022b) in characterising the early star-forming phase across the nearby galaxy population.

Finally, we conclude in Chapter 5 by summarising what we have learned from these studies and discussing how the constrained time-scales can be improved to provide a complete picture of star formation processes, incorporating their multi-phase nature, from atomic gas to H II regions in the era of JWST.

Chapter 2

Environmental dependence of the molecular cloud lifecycle in 54 main sequence galaxies

Authors:

Jaeyeon Kim, Mélanie Chevance, J. M. Diederik Kruijssen,
Adam K. Leroy, Andreas Schruba et al.

Jaeyeon Kim is the principal author of this article. The method was developed by Dr. Kruijssen. The original idea was suggested by Dr. Kruijssen and Dr. Chevance. Jaeyeon Kim developed it and performed the application of the method to observations. Jaeyeon Kim carried out the calculations, produced all the figures and tables, and wrote the manuscript. All authors collaborated with corrections and suggestions to the manuscript, and Jaeyeon Kim performed the last improvements during the review process.

Environmental dependence of the molecular cloud lifecycle in 54 main-sequence galaxies

Jaeyeon Kim [ORCID],[1]★ Mélanie Chevance [ORCID],[1,2] J. M. Diederik Kruijssen [ORCID],[1] Adam K. Leroy,[3] Andreas Schruba,[4] Ashley T. Barnes [ORCID],[5] Frank Bigiel,[5] Guillermo A. Blanc,[6,7] Yixian Cao,[4] Enrico Congiu [ORCID],[7] Daniel A. Dale [ORCID],[8] Christopher M. Faesi [ORCID],[9] Simon C. O. Glover [ORCID],[2] Kathryn Grasha [ORCID],[10,11] Brent Groves [ORCID],[12] Annie Hughes [ORCID],[13,14] Ralf S. Klessen [ORCID],[2,15] Kathryn Kreckel [ORCID],[1] Rebecca McElroy,[16] Hsi-An Pan [ORCID],[17] Jérôme Pety [ORCID],[18,19] Miguel Querejeta [ORCID],[20] Alessandro Razza [ORCID],[7] Erik Rosolowsky [ORCID],[21] Toshiki Saito [ORCID],[22] Eva Schinnerer [ORCID],[23] Jiayi Sun [ORCID],[24,25] Neven Tomičić,[26,27] Antonio Usero[28] and Thomas G. Williams [ORCID][23]

Affiliations are listed at the end of the paper

ABSTRACT

The processes of star formation and feedback, regulating the cycle of matter between gas and stars on the scales of giant molecular clouds (GMCs; $\sim 100\,\mathrm{pc}$), play a major role in governing galaxy evolution. Measuring the time-scales of GMC evolution is important to identify and characterize the specific physical mechanisms that drive this transition. By applying a robust statistical method to high-resolution CO and narrow-band H α imaging from the PHANGS survey, we systematically measure the evolutionary timeline from molecular clouds to exposed young stellar regions on GMC scales, across the discs of an unprecedented sample of 54 star-forming main-sequence galaxies (excluding their unresolved centres). We find that clouds live for about $1-3$ GMC turbulence crossing times ($5-30$ Myr) and are efficiently dispersed by stellar feedback within $1-5$ Myr once the star-forming region becomes partially exposed, resulting in integrated star formation efficiencies of $1-8$ per cent. These ranges reflect physical galaxy-to-galaxy variation. In order to evaluate whether galactic environment influences GMC evolution, we correlate our measurements with average properties of the GMCs and their local galactic environment. We find several strong correlations that can be physically understood, revealing a quantitative link between galactic-scale environmental properties and the small-scale GMC evolution. Notably, the measured CO-visible cloud lifetimes become shorter with decreasing galaxy mass, mostly due to the increasing presence of CO-dark molecular gas in such environment. Our results represent a first step towards a comprehensive picture of cloud assembly and dispersal, which requires further extension and refinement with tracers of the atomic gas, dust, and deeply embedded stars.

Key words: stars: formation – ISM: clouds – ISM: structure – galaxies: ISM – galaxies: star formation.

1 INTRODUCTION

Giant molecular clouds (GMCs) are the most important sites for star formation. The properties of the clouds are set by the large-scale environment of their host galaxies, directly linking the initial conditions of star formation to galactic-scale properties (Hughes et al. 2013; Colombo et al. 2014; Schruba, Kruijssen & Leroy 2019; Sun et al. 2018, 2020a, b). In turn, the energy, momentum, and metals deposited by stellar feedback drive the continuous evolution of the interstellar medium (ISM) in general (e.g. Krumholz 2014). The characterization of the evolutionary time-scales from molecular cloud assembly to star formation, and to young stellar regions devoid of cold gas provides important insights into which physical mechanisms regulate this multi-scale cycle, and is therefore crucial to understanding the evolution of galaxies.

Theoretical studies of GMCs indicate that their evolution is influenced by various environmentally dependent dynamical properties such as gravitational collapse of the ISM, collisions between clouds, epicyclic motions, galactic shear, and large-scale gas streaming motions (Dobbs & Pringle 2013; Dobbs, Pringle & Duarte-Cabral 2015; Meidt et al. 2013, 2018, 2020; Jefferson & Kruijssen 2018; Jefferson et al. 2020, 2021; Tress et al. 2020, 2021). During recent decades, growing cloud-scale observational evidence, revealing a spatial decorrelation between molecular gas and young stellar regions, points towards a view of GMCs as transient objects that are dispersed within a free-fall or dynamical time-scale ($10-30\,\mathrm{Myr}$) by violent feedback from young massive stars (Elmegreen 2000; Engargiola et al. 2003; Blitz et al. 2007; Kawamura et al. 2009; Onodera et al. 2010; Schruba et al. 2010; Miura et al. 2012; Meidt et al. 2015; Corbelli et al. 2017; Kruijssen et al. 2019b; Schinnerer et al. 2019; Chevance et al. 2020a, b; Barnes et al. 2020; Kim et al. 2021a; Pan et al. 2022). This contradicts a conventional view where GMCs are considered to represent quasi-equilibrium structures that survive over a large fraction of a galactic rotation period (Scoville & Hersh 1979).

★ E-mail: kim@uni-heidelberg.de

Despite these previous efforts, it has been challenging to understand what determines the evolutionary time-scales of cloud assembly, star formation, and cloud dispersal due to the limited range of galactic properties and ISM conditions probed so far. Now, the dynamic range of environments that can be investigated at required cloud-scale resolution has been significantly widened thanks to PHANGS,[1] which has mapped ^{12}CO($J = 2-1$) emission with the Atacama Large Millimeter/submillimeter Array (ALMA) at cloud-scale resolution across 90 star-forming main-sequence galaxies (Leroy et al. 2021b). In addition, subsets of these galaxies have been targeted by observations at various other wavelengths including radio (PHANGS–VLA; Sardone et al. in preparation), mid-/near-infrared (Leroy et al. 2019), optical (PHANGS–*HST*; Lee et al. 2022, PHANGS–MUSE; Emsellem et al. 2022, PHANGS–H α; Razza et al. in preparation), and near-/far-ultraviolet (Leroy et al. 2019). These observations reveal that the GMC populations of nearby galaxies, with molecular gas surface densities spanning 3.4 dex (Sun et al. 2020b), reside in diverse galactic environments covering a substantial range of local galaxy properties such as gas and stellar mass surface densities, orbital velocities, and shear parameters (Sun et al. 2022).

Onodera et al. (2010) and Schruba et al. (2010) first quantified the spatial decorrelation of gas and young stellar regions observed at small scales in the Local Group galaxy M33. Kruijssen & Longmore (2014) and Kruijssen et al. (2018) developed a statistical method that translates the observed scale dependence of this spatial decorrelation between gas and young stellar regions into their underlying evolutionary timeline, ranging from cloud assembly to subsequent star formation and cloud dispersal, and finally to young stellar regions free of molecular gas. This method has utilized CO and H α observations of nearby galaxies to characterize the evolutionary timeline between quiescent molecular gas to exposed young stellar regions for 15 galaxies (Kruijssen et al. 2019b; Chevance et al. 2020b; Zabel et al. 2020; Kim et al. 2021a; Ward et al. 2022). So far, these measurements of time-scales, have been limited to a small number of galaxies due to the lack of CO imaging of star-forming discs at cloud-scale resolution and the fact that our method requires us to resolve at least the separation length between independent star-forming regions (100−300 pc). These previous studies did not allow us to identify the key environmental factors and cloud properties (e.g. total, gas, molecular gas surface densities, and masses) responsible for setting these time-scales.

The first application of this method to a subset of nine PHANGS galaxies by Chevance et al. (2020b) revealed that the time-scale for GMC survival is 10−30 Myr, agreeing well with the Local Group measurements by Fukui et al. (2008), Kawamura et al. (2009), and Corbelli et al. (2017), using a different methodology. Chevance et al. (2020b) also found that at high molecular gas surface density (with kpc-scale molecular gas surface density $\Sigma_{H_2} > 8 \, M_\odot \, pc^{-2}$), the measured cloud lifetime is consistent with being set by large-scale dynamical processes, such as large-scale gravitational collapse and galactic shear. In the low surface density regime ($\Sigma_{H_2} \leq 8 \, M_\odot \, pc^{-2}$), time-scales associated with internal dynamical processes, such as the free-fall and crossing times, govern the cloud lifetime. The duration over which CO and H α emission overlap is found to be short (1−5 Myr), indicating that pre-supernova feedback, such as photoionization and stellar winds, plays a key role for molecular cloud disruption. This method also has been applied to other

wavelengths. Ward et al. (2020) used HI data to infer a duration of ∼50 Myr for the atomic gas cloud lifetime in the LMC. For six nearby galaxies, Kim et al. (2021a) incorporated *Spitzer* 24 µm observations to measure the time-scale of the heavily obscured star formation, which is missed when using H α only, due to attenuation provided by surrounding gas and dust. The measured duration for the heavily obscured star formation is 1−4 Myr, constituting 10−25 per cent of the cloud lifetime.

In this paper, we greatly increase the number of main-sequence galaxies analysed by this statistical method from nine considered by Chevance et al. (2020b) to 54 galaxies here. We capitalize on our CO observations from PHANGS–ALMA (Leroy et al. 2021b) and a new, large narrow-band H α survey by Razza et al. (in preparation; PHANGS–H α). By applying our analysis to these galaxies, we systematically obtain the evolutionary sequence of GMCs from a quiescent molecular cloud phase to feedback dispersal phase, and finally to gas-free H II region phase. This statistically representative PHANGS sample covers a large range of galactic properties (∼2 dex in stellar mass) and morphologies. It enables us to quantitatively study the connection between the small-scale evolutionary cycle of molecular clouds and galactic-scale environmental properties.

The structure of the paper is as follows. In Section 2, we summarize the observational data used in our analysis. In Section 3, we describe the statistical method used here and the associated main input parameters. In Section 4, we present the inferred cloud lifetime, the duration for which CO and H α emission coincide, the mean separation length between star-forming regions undergoing independent evolution, as well as several other quantities derived from our measurements. In Section 5, we explore how these time-scales vary with galactic and average GMC properties. We also compare them with theoretical values. Lastly, we present our conclusions in Section 6.

2 OBSERVATIONAL DATA

2.1 Descriptions of CO and H α emission maps

PHANGS has constructed a multiwavelength data base at GMC-scale resolution (∼100 pc), covering most of the nearby (≤20 Mpc), ALMA accessible, star-forming galaxies ($M_* = 10^{9.5}-10^{11.5} \, M_\odot$) lying around the main sequence (see Leroy et al. 2021b). In this paper, we focus on the galaxies where both ^{12}CO($J = 2-1$), denoted as CO(2–1) in the following, and ground-based continuum-subtracted H α observations are available. This results in a sample of 64 galaxies. For a robust application of our statistical method, we need a minimum of 35 identified emission peaks in each map (Kruijssen et al. 2018). This requirement made us remove 10 galaxies (IC 5332, NGC 1317, NGC 2566, NGC 2775, NGC 3626, NGC 4207, NGC 4293, NGC 4424, NGC 4457, NGC 4694), as they do not have enough peaks identified in either the CO or H α map.[2] In the end, our final sample consists of 54 galaxies and their physical and observational properties are listed in Table 1. In the next paragraphs, we briefly summarize the main features of the PHANGS–ALMA (CO(2–1)) and PHANGS–H α data sets.

In order to trace the molecular gas, we use the PHANGS–ALMA survey, which has mapped the CO(2–1) emission in the star-forming part of the disc across 90 galaxies. Full descriptions of the sample

---

[1]The Physics at High Angular resolution in Nearby GalaxieS project: http://phangs.org.

[2]Most of these galaxies have centrally concentrated star formation making it hard to distinguish emission peaks. Excluding these galaxies does not bias our galaxy sample in terms of stellar mass, as they seem to be distributed evenly across the observed range (see Fig. 6).

3008   *J. Kim et al.*

Table 1. Physical and observational properties of our galaxy sample.

Galaxy	(a) $M_{*, \text{global}}$ ($\log_{10} M_\odot$)	(b) SFR_{global} ($\log_{10} M_\odot \text{yr}^{-1}$)	(c) $M_{\text{HI, global}}$ ($\log_{10} M_\odot$)	(d) $M_{\text{H}_2, \text{global}}$ ($\log_{10} M_\odot$)	(e) ΔMS	(f) Dist. (Mpc)	(g) Incl. (deg)	(h) PA (deg)	(i) Hubble Type
IC1954	9.7	− 0.4	8.8	8.7	− 0.04	12.8	57.1	63.4	3.3
IC5273	9.7	− 0.3	9.0	8.6	0.09	14.18	52.0	234.1	5.6
NGC 0628	10.3	0.2	9.7	9.4	0.18	9.84	8.9	20.7	5.2
NGC 0685	10.1	− 0.4	9.6	8.8	− 0.25	19.94	23.0	100.9	5.4
NGC 1087	9.9	0.1	9.1	9.2	0.33	15.85	42.9	359.1	5.2
NGC 1097	10.8	0.7	9.6	9.7	0.33	13.58	48.6	122.4	3.3
NGC 1300	10.6	0.1	9.4	9.4	− 0.18	18.99	31.8	278.0	4.0
NGC 1365	11.0	1.2	9.9	10.3	0.72	19.57	55.4	201.1	3.2
NGC 1385	10.0	0.3	9.2	9.2	0.50	17.22	44.0	181.3	5.9
NGC 1433	10.9	0.1	9.4	9.3	-0.36	18.63	28.6	199.7	1.5
NGC 1511	9.9	0.4	9.6	9.2	0.59	15.28	72.7	297.0	2.0
NGC 1512	10.7	0.1	9.9	9.1	− 0.21	18.83	42.5	261.9	1.2
NGC 1546	10.4	− 0.1	8.7	9.3	− 0.15	17.69	70.3	147.8	-0.4
NGC 1559	10.4	0.6	9.5	9.6	0.50	19.44	65.4	244.5	5.9
NGC 1566	10.8	0.7	9.8	9.7	0.29	17.69	29.5	214.7	4.0
NGC 1672	10.7	0.9	10.2	9.9	0.56	19.4	42.6	134.3	3.3
NGC 1792	10.6	0.6	9.2	9.8	0.32	16.2	65.1	318.9	4.0
NGC 1809	9.8	0.8	9.6	9.0	1.08	19.95	57.6	138.2	5.0
NGC 2090	10.0	-0.4	9.4	8.7	− 0.25	11.75	64.5	192.46	4.5
NGC 2283	9.9	-0.3	9.7	8.6	− 0.04	13.68	43.7	− 4.1	5.9
NGC 2835	10.0	0.1	9.5	8.8	0.26	12.22	41.3	1.0	5.0
NGC 2997	10.7	0.6	9.9	9.8	0.31	14.06	33.0	108.1	5.1
NGC 3059	10.4	0.4	9.7	9.4	0.29	20.23	29.4	− 14.8	4.0
NGC 3351	10.4	0.1	8.9	9.1	0.05	9.96	45.1	193.2	3.1
NGC 3507	10.4	− 0.0	9.3	9.3	− 0.10	23.55	21.7	55.8	3.1
NGC 3511	10.0	− 0.1	9.4	9.0	0.06	13.94	75.1	256.8	5.1
NGC 3596	9.7	− 0.5	8.9	8.7	− 0.12	11.3	25.1	78.4	5.2
NGC 3627	10.8	0.6	9.1	9.8	0.19	11.32	57.3	173.1	3.1
NGC 4254	10.4	0.5	9.5	9.9	0.37	13.1	34.4	68.1	5.2
NGC 4298	10.0	− 0.3	8.9	9.2	− 0.18	14.92	59.2	313.9	5.1
NGC 4303	10.5	0.7	9.7	9.9	0.54	16.99	23.5	312.4	4.0
NGC 4321	10.7	0.6	9.4	9.9	0.21	15.21	38.5	156.2	4.0
NGC 4496A	9.5	-0.2	9.2	8.6	0.28	14.86	53.8	51.1	7.4
NGC 4535	10.5	0.3	9.6	9.6	0.14	15.77	44.7	179.7	5.0
NGC 4540	9.8	− 0.8	8.4	8.6	− 0.46	15.76	28.7	12.8	6.2
NGC 4548	10.7	− 0.3	8.8	9.2	− 0.58	16.22	38.3	138.0	3.1
NGC 4569	10.8	0.1	8.8	9.7	− 0.26	15.76	70.0	18.0	2.4
NGC 4571	10.1	− 0.5	8.7	8.9	− 0.43	14.9	32.7	217.5	6.4
NGC 4654	10.6	0.6	9.8	9.7	0.36	21.98	55.6	123.2	5.9
NGC 4689	10.2	− 0.4	8.5	9.1	− 0.37	15.0	38.7	164.1	4.7
NGC 4731	9.5	− 0.2	9.4	8.6	0.30	13.28	64.0	255.4	5.9
NGC 4781	9.6	− 0.3	8.9	8.8	0.09	11.31	59.0	290.0	7.0
NGC 4941	10.2	− 0.4	8.5	8.7	− 0.30	15.0	53.4	202.2	2.1
NGC 4951	9.8	− 0.5	9.2	8.6	− 0.14	15.0	70.2	91.2	6.0
NGC 5042	9.9	− 0.2	9.3	8.8	0.01	16.78	49.4	190.6	5.0
NGC 5068	9.4	− 0.6	8.8	8.4	0.02	5.2	35.7	342.4	6.0
NGC 5134	10.4	− 0.3	8.9	8.8	− 0.45	19.92	22.7	311.6	2.9
NGC 5248	10.4	0.4	9.5	9.7	0.25	14.87	47.4	109.2	4.0
NGC 5530	10.1	− 0.5	9.1	8.9	− 0.37	12.27	61.9	305.4	4.2
NGC 5643	10.3	0.4	9.1	9.4	0.36	12.68	29.9	318.7	5.0
NGC 6300	10.5	0.3	9.1	9.3	0.13	11.58	49.6	105.4	3.1
NGC 6744	10.7	0.4	10.3	9.5	0.06	9.39	52.7	14.0	4.0
NGC 7456	9.6	− 0.4	9.3	9.3	− 0.02	15.7	67.3	16.0	6.0
NGC 7496	10.0	0.4	9.1	9.3	0.53	18.72	35.9	193.7	3.2

Note. (a) and (b) Stellar mass and global SFR (Leroy et al. 2021b). (c) Atomic gas mass from Lyon-Meudon Extragalactic Database (LEDA). (d) Aperture corrected total molecular gas mass from PHANGS–ALMA observations (Leroy et al. 2021a). (e) Offset from the star-forming main sequence (Leroy et al. 2021b). (f) Distance (Anand et al. 2021). (g) and (h) Inclination and Position angle (Lang et al. 2020). (i) Hubble type from LEDA.

and the survey design are presented in Leroy et al. (2021b). Detailed information about the image production process can be found in Leroy et al. (2021a). The observations were carried out using 12 m, 7 m, and total power antennas of the ALMA. The resulting maps have a resolution of ∼1 arcsec, which translates into a physical scale of ∼25–200 pc for the galaxies considered here. We use the first public release version of moment-0 maps generated with an inclusive signal masking scheme to ensure a high detection completeness (the 'broad' masking scheme; see Leroy et al. 2021a) at native resolution. The typical 1σ surface density sensitivity of these broad maps is $\Sigma_{H_2} \approx 5.8\,M_\odot\,pc^{-2}$ (assuming the Galactic CO(1–0)-to-H$_2$ conversion factor of $4.35\,M_\odot\,pc^{-2}(K\,km\,s^{-1})^{-1}$ and a CO(2–1)-to-CO(1–0) ratio of 0.65; Leroy et al. 2013; Den Brok et al. 2021; Leroy et al. 2022).

To trace the star formation rate (SFR), we use the continuum-subtracted narrow-band Hα imaging from PHANGS–Hα (Preliminary version; Razza et al. in preparation). We assume that all the Hα emission originates from the gas ionized by young, massive stars, ignoring the contributions from other sources such as supernova remnants and planetary nebulae. For the 19 galaxies in PHANGS–Hα that were also surveyed by PHANGS–MUSE (Emsellem et al. 2022), we can use measurements of other diagnostic lines (e.g. [N II], [O III]) to quantify the fraction of Hα emission originating from H II regions as a function of galactocentric radius. Using the nebula catalogue introduced in Santoro et al. (2022) and described in more detail in Groves et al. (in preparation), we find that more than 80 per cent of the Hα emission from discrete sources comes from H II regions, except for in a few galactic centres, which are not included in our analysis. This calculation does not account for Hα emission from the diffuse ionized gas (DIG), but Belfiore et al. (2022) demonstrate that the majority of this emission also originates from young stars, and in any case this diffuse emission is largely filtered out of our maps by the Fourier filtering described in Section 3. The PHANGS–Hα sample consists of 65 galaxies, of which 36 galaxies were observed by the du Pont 2.5-m telescope at the Las Campanas Observatory, and 32 galaxies by the Wide Field Imager (WFI) instrument at the MPG-ESO 2.2-m telescope at the La Silla Observatory, including three galaxies that overlap with the du Pont 2.5-m telescope targets. For the overlapping galaxies, we use the observations with the best angular resolution. NGC 1097 is not included in PHANGS–Hα and therefore we use the Hα map from SINGS (Kennicutt et al. 2003). This observation was carried out using the CTIO 1.5m telescope with the CFCCD imager. For all the galaxies, a correction for the Milky Way dust extinction is applied following Schlafly & Finkbeiner (2011) and an extinction curve with $R_V = 3.1$ (Fitzpatrick 1999). We note that we do not correct for internal extinction caused by gas and dust surrounding the young stars in these Hα maps. In Haydon et al. (2020a), we have addressed the potential impact of internal extinction on our time-scale measurements, finding that it is negligible for kpc-scale molecular gas surface densities below $20\,M_\odot\,pc^{-2}$. Most of the galaxies fall below this threshold (see Fig. 6). However, for those with higher molecular gas surface densities, extinction may decrease the measured molecular cloud lifetimes and feedback time-scales. We remove the contamination due to the [N II] lines by assuming an intensity ratio $I(N\,II)/I(H\alpha) = 0.3$ (Kreckel et al. 2016, 2019; Santoro et al. 2022). This correction factor for [N II] contamination is known to vary with galaxy mass, as well as within a galaxy with a large-scale metallicity gradient. We note that galaxy-to-galaxy variations do not affect our time-scale measurements, because we use the ratio between the flux on GMC scales and the galactic average when constraining the time-scales and this correction factor cancels out. By contrast, variations within a galaxy can potentially affect the

measured deviations of flux ratios and thus the inferred time-scales. However, we expect this effect to be small as long as a random distribution of peaks in terms of radial distances can be assumed, such that any variations in [N II] correction average out. The typical resolution of the Hα maps is ∼1 arcsec. Razza et al. (in preparation) have measured the size of the point spread function (PSF) for each image and find that it is close enough to be approximated as Gaussian. For more detailed information about the image reduction process, we refer readers to the survey paper by Razza et al. (in preparation) and our previous papers using a subset of the same data set (Schinnerer et al. 2019; Chevance et al. 2020b; Pan et al. 2022).

2.2 Homogenization of maps to common pixel grid and masking

In our analysis, we require gas and SFR tracer maps of a given galaxy to have the same pixel grid. Therefore, for each galaxy, we reproject both gas and SFR tracer images to share a common astrometric grid, choosing to work with the astrometry of whichever image has the coarser pixel size. When the map that is being transformed has a finer resolution than the reference map, we first convolve the map with a Gaussian kernel to the resolution of the reference map to avoid introducing artifacts. If the map being reprojected already has a coarser resolution, no additional step is performed at this stage and both maps will be convolved to similar resolutions at a later stage during the analysis. This working resolution for each galaxy is listed as $l_{ap,\,min}$ in Table 2. This implies that we do not homogenize the resolution across the survey but work at the best available resolution.

Due to the limited field of view of the CO maps, we restrict our analysis to regions where CO observations have been made. For most galaxies, we mask the galaxy centre because these regions are crowded and we cannot separate distinct regions at our working resolution. The radius of the galactic centre mask is listed in Table 2. Following the prescription by Kim et al. (2021a), we also mask some of very bright molecular gas or SFR tracer peaks identified within a galaxy. This is necessary because our method utilizes small-scale variation of the gas-to-SFR flux ratios to constrain the evolutionary timeline and implicitly assumes that this timeline is well-sampled by the ensemble of gas and SFR peaks identified. Therefore, by construction, bright peaks constituting a significant fraction of the total flux might bias our results (also see Kruijssen et al. 2018). In our previous work (Chevance et al. 2020b; Kim et al. 2021a), these regions were found to correspond to super-luminous regions like 30 Doradus in the LMC, or regions located at the intersection of a spiral arm and the co-rotation radius (e.g. the headlight cloud in NGC 0628, Herrera et al. 2020). In order to find these potential overly bright regions, we first sort the peaks that are identified within our method using CLUMPFIND (see Section 3), by descending intensity. Then, we look for any gaps, which we define to exist when the nth peak is more than twice as bright as the $(n + 1)^{th}$ peak. Whenever such a gap is found, we mask all the peaks that are brighter than the $(n + 1)^{th}$ brightest peak. This typically results in a maximum of three masked peaks in any particular galaxy.

3 METHOD

In this section, we provide a brief description of our analysis method (formalized in the HEISENBERG[3] code) and explain the main input parameters used. A detailed explanation of the concept can be found

---

[3]https://github.com/mustang-project/Heisenberg

Table 2. Main input parameters used in our analysis of each galaxy. Other parameters not listed here are set to the default value from Kruijssen et al. (2018).

Galaxy	r_{min} (kpc)	$l_{ap, min}$ (pc)	$l_{ap, max}$ (pc)	N_{ap}	$N_{pix,min}$	$\Delta\log_{10}\mathcal{F}_{CO}$	$\delta\log_{10}\mathcal{F}_{CO}$	$\Delta\log_{10}\mathcal{F}_{H\alpha}$	$\delta\log_{10}\mathcal{F}_{H\alpha}$	t_{ref} (Myr)	$t_{ref, errmin}$ (Myr)	$t_{ref, errmax}$ (Myr)	SFR ($M_\odot yr^{-1}$)	σ(SFR) ($M_\odot yr^{-1}$)	$\log_{10}\alpha_{CO}$	$\sigma_{rel}(\alpha_{CO})$	n_λ
IC1954	0.3	132	3000	15	7	2.0	0.05	2.5	0.05	4.32	0.23	0.09	0.29	0.06	0.83	0.5	14
IC5273	0.8	154	3000	15	6	2.0	0.05	2.5	0.05	4.32	0.23	0.09	0.37	0.07	0.83	0.5	12
NGC 0628	0.7	54	3000	15	20	1.4	0.10	2.8	0.10	4.28	0.22	0.08	0.76	0.15	0.76	0.5	13
NGC 0685	0.0	170	3000	15	10	2.0	0.05	3.0	0.05	4.32	0.23	0.09	0.42	0.08	0.82	0.5	13
NGC 1087	0.5	144	3000	15	20	1.5	0.10	3.0	0.05	4.31	0.23	0.09	1.02	0.20	0.80	0.5	13
NGC 1097	1.9	137	3000	15	7	2.1	0.05	2.1	0.05	4.24	0.22	0.07	1.03	0.21	0.67	0.5	14
NGC 1300	2.7	123	3000	15	8	1.5	0.05	1.8	0.05	4.22	0.21	0.06	0.67	0.13	0.64	0.5	11
NGC 1365	5.4	174	3000	15	9	2.7	0.05	2.5	0.05	4.25	0.22	0.07	1.17	0.23	0.69	0.5	13
NGC 1385	0.0	125	3000	15	5	1.7	0.05	3.0	0.05	4.29	0.23	0.08	1.82	0.36	0.77	0.5	14
NGC 1433	3.4	110	3000	15	10	1.9	0.05	1.8	0.05	4.23	0.22	0.06	0.45	0.09	0.65	0.5	12
NGC 1511	0.3	196	6000	15	15	1.8	0.05	3.0	0.05	4.33	0.23	0.09	1.52	0.30	0.84	0.5	12
NGC 1512	4.0	110	3000	15	8	1.2	0.05	2.0	0.05	4.24	0.22	0.07	0.32	0.06	0.68	0.5	11
NGC 1546	0.4	217	3000	15	3	2.2	0.05	3.0	0.05	4.29	0.22	0.08	0.61	0.12	0.76	0.5	15
NGC 1559	0.0	201	6000	15	8	2.8	0.05	2.3	0.15	4.29	0.23	0.08	4.12	0.82	0.78	0.5	13
NGC 1566	0.5	115	3000	15	5	1.8	0.05	2.6	0.05	4.25	0.22	0.07	3.02	0.60	0.69	0.5	12
NGC 1672	2.7	212	3000	15	10	1.9	0.03	3.0	0.10	4.26	0.22	0.07	2.09	0.42	0.72	0.5	14
NGC 1792	1.5	233	3000	15	7	1.8	0.05	2.5	0.05	4.27	0.22	0.08	2.90	0.58	0.73	0.5	14
NGC 1809	0.0	186	6000	15	6	2.0	0.05	3.0	0.05	4.33	0.23	0.09	0.18	0.04	0.84	0.5	13
NGC 2090	0.7	112	3000	15	10	2.0	0.05	2.5	0.05	4.32	0.23	0.09	0.15	0.03	0.83	0.5	12
NGC 2283	0.0	102	3000	15	17	1.4	0.05	3.0	0.05	4.35	0.22	0.09	0.49	0.10	0.88	0.5	13
NGC 2835	0.0	74	3000	15	15	1.2	0.05	3.0	0.05	4.32	0.23	0.09	0.39	0.08	0.83	0.5	12
NGC 2997	2.0	132	3000	15	30	1.8	0.05	2.8	0.05	4.25	0.22	0.07	2.61	0.52	0.68	0.5	12
NGC 3059	0.8	150	5000	15	20	2.0	0.05	3.5	0.05	4.28	0.22	0.08	1.33	0.27	0.75	0.5	10
NGC 3351	2.0	84	3000	15	12	1.8	0.05	2.8	0.05	4.25	0.22	0.07	0.20	0.04	0.69	0.5	12
NGC 3507	2.0	176	7000	15	7	1.8	0.05	3.0	0.10	4.25	0.22	0.07	0.60	0.12	0.70	0.5	12
NGC 3511	0.8	240	6000	15	6	2.0	0.05	2.5	0.05	4.33	0.23	0.09	0.66	0.13	0.84	0.5	13
NGC 3596	0.3	75	3000	15	10	2.0	0.05	3.5	0.10	4.38	0.22	0.08	0.23	0.05	0.93	0.5	14
NGC 3627	1.1	121	3000	15	12	3.2	0.10	3.1	0.10	4.25	0.22	0.07	2.71	0.54	0.70	0.5	13
NGC 4254	0.2	125	3000	15	12	2.0	0.05	3.5	0.05	4.27	0.22	0.08	2.62	0.52	0.74	0.5	13
NGC 4298	0.6	160	3000	15	7	2.5	0.05	3.5	0.05	4.29	0.23	0.08	0.38	0.08	0.77	0.5	14
NGC 4303	1.2	156	3000	15	5	1.6	0.10	2.5	0.05	4.24	0.22	0.07	3.61	0.72	0.68	0.5	13
NGC 4321	1.0	139	3000	15	10	1.6	0.15	1.6	0.25	4.24	0.22	0.07	2.20	0.44	0.68	0.5	12
NGC 4496A	0.0	118	3000	15	10	2.5	0.05	3.0	0.05	4.36	0.22	0.09	0.18	0.04	0.90	0.5	12
NGC 4535	3.0	141	7200	15	10	2.5	0.05	2.7	0.10	4.24	0.22	0.07	0.76	0.15	0.67	0.5	12
NGC 4540	0.0	112	3000	15	3	3.0	0.05	3.0	0.05	4.33	0.23	0.09	0.14	0.03	0.85	0.5	14
NGC 4548	1.4	150	3000	15	8	1.8	0.05	2.5	0.05	4.24	0.22	0.07	0.22	0.04	0.67	0.5	14
NGC 4569	1.6	220	5000	15	3	1.4	0.03	2.0	0.03	4.23	0.21	0.06	0.68	0.14	0.65	0.5	13
NGC 4571	0.4	128	3000	15	7	2.0	0.05	3.0	0.40	4.30	0.23	0.08	0.17	0.03	0.78	0.5	12
NGC 4654	2.1	243	5000	15	15	2.0	0.05	3.2	0.05	4.28	0.06	0.32	2.31	0.46	0.74	0.5	12
NGC 4689	1.7	111	3000	15	15	1.4	0.05	3.0	0.05	4.27	0.22	0.08	0.41	0.08	0.74	0.5	13
NGC 4731	0.0	149	3000	15	5	2.5	0.16	2.5	0.05	4.36	0.22	0.09	0.19	0.04	0.90	0.5	13
NGC 4781	0.0	100	3000	15	15	1.8	0.05	1.6	0.05	4.32	0.23	0.09	0.40	0.08	0.83	0.5	12
NGC 4941	1.4	149	3000	15	10	1.6	0.05	2.5	0.05	4.28	0.22	0.08	0.13	0.03	0.75	0.5	12
NGC 4951	0.5	167	5000	15	10	2.0	0.05	2.4	0.05	4.34	0.23	0.09	0.17	0.03	0.86	0.5	12
NGC 5042	0.7	134	3000	15	10	2.5	0.10	2.5	0.05	4.36	0.22	0.09	0.22	0.04	0.89	0.5	12
NGC 5068	0.0	32	3000	15	40	1.6	0.30	3.4	0.10	4.43	0.21	0.08	0.18	0.04	1.03	0.5	10
NGC 5134	1.2	124	3000	15	10	1.3	0.05	3.4	0.05	4.28	0.22	0.08	0.30	0.06	0.75	0.5	12
NGC 5248	1.2	113	3000	15	10	2.0	0.10	2.4	0.03	4.27	0.22	0.08	1.35	0.27	0.74	0.5	13
NGC 5530	0.0	105	3000	15	15	1.6	0.05	2.0	0.05	4.30	0.23	0.08	0.33	0.07	0.79	0.5	10
NGC 5643	1.1	86	3000	15	15	1.4	0.10	2.5	0.10	4.26	0.22	0.07	1.11	0.22	0.72	0.5	11
NGC 6300	1.7	85	3000	15	15	1.2	0.15	2.2	0.05	4.25	0.22	0.07	0.63	0.13	0.69	0.5	13
NGC 6744	3.0	78	3000	15	10	1.4	0.05	2.6	0.30	4.28	0.22	0.08	0.49	0.10	0.75	0.5	12
NGC 7456	0.0	206	5000	15	3	4.0	0.05	3.5	0.05	4.48	0.20	0.07	0.10	0.02	1.12	0.5	11
NGC 7496	1.3	169	5000	15	5	3.0	0.05	3.2	0.05	4.27	0.22	0.08	0.53	0.11	0.73	0.5	13

in Kruijssen & Longmore (2014), the presentation and validation of the code and a full description of its input parameters in Kruijssen et al. (2018), and applications of the method to observed galaxies in Kruijssen et al. (2019b), Chevance et al. (2020b, 2022), Haydon et al. (2020a), Ward et al. (2020), Zabel et al. (2020), and Kim et al. (2021a).

Our method makes use of the observational fact that galaxies are composed of numerous GMCs and star-forming regions, which are spatially decorrelated at small scale while being tightly correlated on galactic scale, defining the well-known 'star formation relation' (e.g. Kennicutt 1998). This decorrelation was first pointed out by Schruba et al. (2010), and is inevitable if the CO and H α-emitting phases represent temporally distinct stages of the GMC lifecycle (Kruijssen & Longmore 2014): the GMCs and star-forming regions represent instantaneous manifestations of individual regions undergoing independent evolution, during which molecular clouds assemble, form stars, and get disrupted by stellar feedback, only leaving young stellar regions to be detected without molecular gas.

In order to translate this observed decorrelation between gas and young stars into their evolutionary lifecycle, we first identify emission peaks in gas and SFR tracer maps using CLUMPFIND (Williams, de Geus & Blitz 1994). This algorithm finds peaks by contouring the data for a set of flux levels, which are spaced by an

interval of $\delta\log_{10}\mathcal{F}$ and are spread over a flux range ($\Delta\log_{10}\mathcal{F}$) below the maximum flux level. We then reject peaks that contain less than $N_{pix, min}$ pixels. Around each identified peak, we then place apertures of various sizes ranging from cloud scales ($l_{ap, min}$) to galactic scales ($l_{ap, max}$) and measure the relative changes of the gas-to-SFR tracer flux ratio, compared to the galactic average, at each given aperture size. We set the number of aperture sizes to be $N_{ap} = 15$.

We then fit an analytical function (see section 3.2.11 of Kruijssen et al. 2018) to the measured flux ratios, which assumes that the measured flux ratios reflect the superposition of independently evolving regions and depend on the relative durations of the successive phases of the cloud and star formation timeline, as well as on the typical separation length between independent regions (λ). The absolute durations of the successive phases are obtained by scaling the resulting constraints on time-scale ratios by a reference time-scale (t_{ref}). Here, we use the duration of the isolated H α emitting phase as t_{ref} (≈ 4.3 Myr). This value is appropriate for a delta-function star formation history and thus does not correspond to the full duration of the H α emitting phase if the age spread is non-zero (which is accounted for, see below). This t_{ref} is dependent on metallicity and listed for each galaxy in Table 2, and was calibrated by Haydon et al. (2020a,b) using the stellar population synthesis model SLUG2 (Da Silva, Fumagalli & Krumholz 2012, 2014; Krumholz

et al. 2015). Therefore, our fitted model is described by three independent non-degenerate parameters: the cloud lifetime (t_{CO}), the phase during which both molecular gas and SFR tracers overlap (t_{fb}), and the characteristic separation length between independent regions (λ). The overlapping time-scale represents the duration from when massive star-forming regions start emerging to when the surrounding molecular gas has been completely removed or dissociated by feedback, and is therefore often referred to as the feedback time-scale. The SFR tracer-emitting time-scale ($t_{H\alpha}$) then simply follows as $t_{fb} + t_{ref}$, where the addition of t_{fb} allows for the presence of an age spread in individual regions.

To focus our analysis specifically on the peaks of emission, we follow Kruijssen et al. (2019b), Chevance et al. (2020b), and Kim et al. (2021a) and apply a Fourier filter to remove the large-scale structure from both maps, using the method presented in Hygate et al. (2019). In the Hα maps, this will suppress diffuse ionized gas emission, which often forms a large halo around H II regions (see e.g. Haffner et al. 2009; Rahman et al. 2011; Belfiore et al. 2022) and add a large-scale reservoir of emission that does not originate from peaks within the aperture. In the CO maps, the operation isolates clumps of emission, likely to be the individual massive clouds or complexes, most directly associated with the massive H II regions that we identify. In practice, we filter out emission on spatial scales larger than n_λ times the typical separation length between independent star-forming regions (λ; constrained in our method), using a Gaussian high-pass filter in Fourier space. We choose the smallest possible value of n_λ (see Table 2), while ensuring that flux loss from the compact regions is less than 10 per cent, following the prescription by Hygate et al. (2019), Kruijssen et al. (2019b), Chevance et al. (2020b), and Kim et al. (2021a). Because the width of the filter depends on the region separation length, which is a quantity constrained by the analysis, this procedure must be carried out iteratively until a convergence condition is reached. This condition is defined as a change of the measured λ by less than 5 per cent for three consecutive iterations.

Using this method, we also derive other physical properties, such as the compact molecular gas surface density ($\Sigma_{H_2}^{compact}$), SFR surface density of the analysed region (Σ_{SFR}), depletion time of the compact molecular gas ($t_{dep}^{compact}$), which assumes that all of the SFR results from the compact molecular gas component,[4] and integrated star formation efficiency achieved by the average star-forming region (ϵ_{sf}). To derive these properties, we adopt a CO(2–1)-to-H_2 conversion factor (α_{CO}) and use the global SFR, which includes a contribution from diffused ionized gas and a correction for the internal extinction. We adopt a metallicity-dependent α_{CO} following Sun et al. (2020b), expressed as

$$\alpha_{CO} = 4.35 \, Z'^{-1.6}/R_{21} \, M_\odot \, \left(K \, km \, s^{-1} \, pc^2 \right)^{-1} , \qquad (1)$$

where R_{21} is the CO(2–1)-to-CO(1–0) line ratio (0.65; Leroy et al. 2013; Den Brok et al. 2021; Leroy et al. 2022) and Z' is the CO luminosity-weighted metallicity in units of the solar value. To calculate this, we adopt the metallicity from the global stellar mass–metallicity relation (Sánchez et al. 2019) at the effective radius (R_{eff}) and assume a fixed radial metallicity gradient within the galaxy (-0.1dex/R_{eff}; Sánchez et al. 2014). The global SFR, accounting for extinction, is adopted from Leroy et al. (2019) and is measured by combining maps from the *Galaxy Evolution Explorer* (*GALEX*) far-ultraviolet band (155 nm) and the *Wide-field Infrared Survey Explorer* (*WISE*) W4 band (22 μm), convolved to 15 arcsec angular resolution.

---

[4]We also derive molecular gas surface density (including the diffuse component; Σ_{H_2}) and depletion time for all the molecular gas t_{dep}.

Here, we only consider star formation within the analysed region, excluding galactic centres and bright regions that are masked in our analysis. We assume a conservative uncertainty for α_{CO} of 50 per cent and a typical SFR uncertainty of 20 per cent, denoted as $\sigma_{rel}(\alpha_{CO})$ and $\sigma(SFR)$, respectively, in Table 2.

The main input parameters explained above are listed in Table 2 for each galaxy. We use the distance, inclination angle, and position angle listed in Table 1. For other parameters not mentioned here, we use the default values as listed in Kruijssen et al. (2018), which are related to the fitting process and error propagation.

4 EVOLUTIONARY TIMELINE FROM MOLECULAR GAS TO EXPOSED YOUNG STELLAR REGIONS

In this section, we present our results obtained from the application of our statistical method to CO and Hα observations as tracers of molecular gas and SFR for the 54 PHANGS galaxies described in Section 2. We note that our results include the re-analysis of 8 galaxies from Chevance et al. (2020b, excluding M51, which is not in our galaxy sample). Here, we use an updated Hα map for NGC 3627, which is reduced with a better continuum subtraction (Razza et al. in preparation), as well as improved CO data products for all of the re-analysed galaxies. In addition, we introduced an additional step where, for each CO–Hα pair of maps, we convolve one map to match the resolution of the other map, *before* reprojecting it to the coarsest pixel grid (as explained in Section 2.2). Despite these changes, our results agree to within the 1σ uncertainties with those from Chevance et al. (2020b).

Fig. 1 shows the variations of the gas-to-SFR tracer flux ratios measured within apertures centred on CO and Hα peaks relative to the galactic average, as a function of the aperture size, together with our best-fitting model for each galaxy. For all the galaxies in our sample, the measured flux ratios increasingly diverge from the galactic average as the size of the aperture decreases (from ∼1 kpc to ∼50 pc), both for apertures focused on gas and SFR tracer peaks. This demonstrates a universal spatial decorrelation between molecular gas and young stellar regions on the cloud scale at the sensitivity limits of our data. In Table 3, we present the best-fitting free parameters constrained by the model fit to each galaxy, as well as additional quantities that can be derived from our measurements: the feedback outflow velocity (v_{fb}; see Section 4.4), the integrated cloud-scale star formation efficiency (ϵ_{sf}; see Section 4.5), and the fractions of diffuse molecular and ionized gas ($f_{diffuse}^{CO}$ and $f_{diffuse}^{H\alpha}$; see Section 4.6), which are determined during our diffuse emission filtering process described in Section 3. Fig. 2 shows an illustration of the resulting evolutionary lifecycles of GMCs in our galaxy sample, from the assembly of molecular gas to the feedback phase powered by massive star formation, and finally to exposed young stellar regions. Star formation regions emit in only CO in the beginning, then also in Hα after the massive star-forming region has become partially exposed, and finally only in Hα after cloud disruption. In Fig. 3, we show the distributions of our main measurements across the galaxy sample.

4.1 Cloud lifetime (t_{CO})

Across all the galaxies in our sample, the range of measured cloud lifetimes (i.e. the duration over which CO is visible) is $5-30$ Myr, with an average of 16 Myr and a $16-84$ per cent range of $11-22$ Myr. The range of our measurements of t_{CO} corresponds to $1-3$ times the average crossing time-scale of massive GMCs in PHANGS–ALMA (see also Sun et al. 2022; and Section 5.2), which suggests that
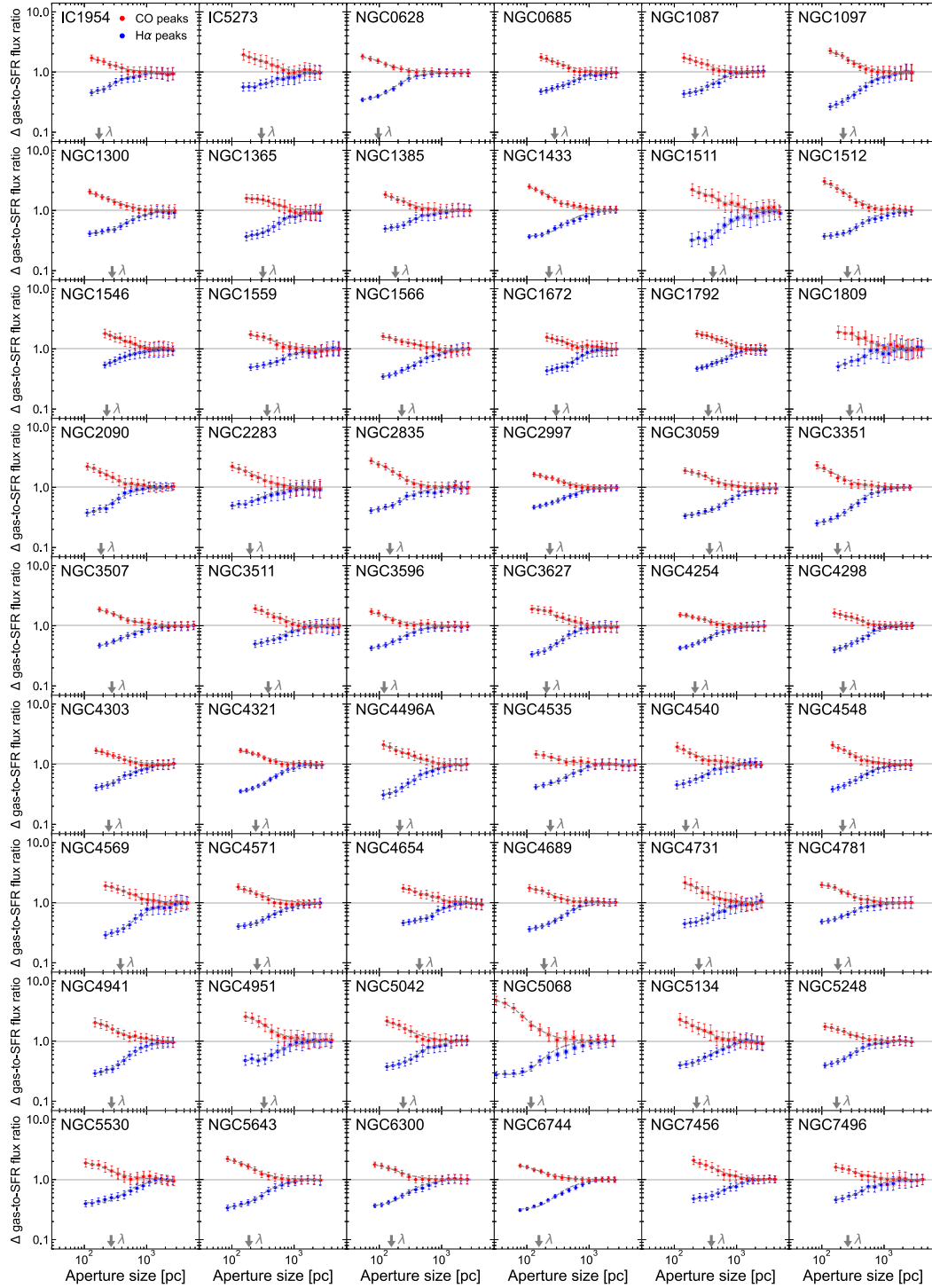
Figure 1. Measured variation of the gas-to-SFR tracer flux ratio (CO-to-H α) relative to the galactic average as a function of the size of apertures placed on CO (red) and H α (blue) emission peaks. The error bars indicate a 1σ uncertainty on each individual measurement whereas the shaded area around each error bar represents the effective 1σ uncertainty used in the fitting process, which takes into account the covariance between measurements. The galactic average is shown as the solid horizontal line and the dashed line indicates our best-fitting model. The best-fitting region separation length (λ) is indicated in each panel with an arrow and other constrained parameters are listed in Table 3.

Table 3. Physical quantities constrained by applying the method presented in Section 3, describing the evolution of molecular clouds to exposed young stellar regions. The columns list the cloud lifetime (t_{CO}), the feedback time-scale (t_{fb}), the H α-emitting time-scale ($t_{H\alpha} = t_{fb} + t_{ref}$), the characteristic region separation length (λ), the feedback velocity (v_{fb}), the integrated star formation efficiency (ϵ_{sf}), the diffuse emission fraction in the molecular gas and SFR tracer maps ($f_{diffuse}^{CO}$ and $f_{diffuse}^{H\alpha}$, respectively), and the depletion time-scale of the compact molecular gas ($t_{dep}^{compact}$), as well as the depletion time-scale for total molecular gas (t_{dep}), which includes the diffuse component. For some galaxies, only a 1σ upper limit can be obtained on t_{fb}, $t_{H\alpha}$, and λ, because the independent star-forming regions are not sufficiently resolved (see the Appendix).

Galaxy	t_{CO} (Myr)	t_{fb} (Myr)	$t_{H\alpha}$ (Myr)	λ (pc)	v_{fb} (km s^{-1})	ϵ_{sf} (per cent)	$f_{diffuse}^{CO}$	$f_{diffuse}^{H\alpha}$	$t_{dep}^{compact}$ (Gyr)	t_{dep} (Gyr)
IC1954	$13.6^{+3.5}_{-2.5}$	< 4.3	< 8.6	< 225	$18.6^{+10.0}_{-5.2}$	$1.9^{+1.6}_{-0.8}$	$0.37^{+0.06}_{-0.05}$	$0.72^{+0.02}_{-0.02}$	$0.7^{+0.5}_{-0.3}$	$2.2^{+1.6}_{-0.9}$
IC5273	$14.9^{+5.8}_{-3.4}$	$4.7^{+2.6}_{-1.6}$	$9.1^{+2.6}_{-1.6}$	299^{+166}_{-68}	$14.2^{+5.8}_{-4.2}$	$4.9^{+4.9}_{-2.1}$	$0.47^{+0.04}_{-0.03}$	$0.65^{+0.05}_{-0.03}$	$0.3^{+0.2}_{-0.1}$	$0.9^{+0.6}_{-0.4}$
NGC 0628	$24.0^{+2.4}_{-2.4}$	$3.2^{+0.5}_{-0.6}$	$7.4^{+0.6}_{-0.6}$	96^{+13}_{-10}	$8.0^{+1.4}_{-1.0}$	$5.5^{+4.0}_{-2.3}$	$0.52^{+0.03}_{-0.03}$	$0.38^{+0.03}_{-0.03}$	$0.4^{+0.3}_{-0.2}$	$1.6^{+1.2}_{-0.7}$
NGC 0685	$16.1^{+3.8}_{-3.2}$	$4.2^{+1.3}_{-1.3}$	$8.5^{+1.3}_{-1.4}$	280^{+44}_{-45}	$18.1^{+7.1}_{-4.0}$	$3.6^{+2.9}_{-1.6}$	$0.13^{+0.05}_{-0.05}$	$0.59^{+0.02}_{-0.03}$	$0.4^{+0.3}_{-0.2}$	$1.0^{+0.7}_{-0.4}$
NGC 1087	$19.7^{+6.3}_{-3.7}$	< 6.1	< 10.5	< 290	$15.7^{+6.4}_{-4.9}$	$5.3^{+4.6}_{-2.3}$	$0.45^{+0.03}_{-0.03}$	$0.53^{+0.04}_{-0.04}$	$0.4^{+0.3}_{-0.2}$	$1.2^{+0.8}_{-0.5}$
NGC 1097	$15.9^{+3.7}_{-2.7}$	< 1.9	< 6.2	220^{+39}_{-25}	$52.7^{+47.4}_{-18.8}$	$2.4^{+2.0}_{-1.0}$	$0.35^{+0.04}_{-0.03}$	$0.70^{+0.02}_{-0.02}$	$0.7^{+0.5}_{-0.3}$	$1.8^{+1.3}_{-0.8}$
NGC 1300	$16.6^{+1.9}_{-2.5}$	$3.6^{+0.7}_{-0.8}$	$7.8^{+0.7}_{-0.9}$	280^{+46}_{-35}	$16.9^{+4.6}_{-2.2}$	$2.9^{+2.1}_{-1.3}$	$0.43^{+0.02}_{-0.02}$	$0.43^{+0.03}_{-0.03}$	$0.6^{+0.4}_{-0.2}$	$1.5^{+1.0}_{-0.6}$
NGC 1365	$21.3^{+4.7}_{-3.5}$	$3.9^{+1.1}_{-1.1}$	$8.1^{+1.2}_{-1.1}$	315^{+126}_{-65}	$22.0^{+5.0}_{-3.9}$	$2.4^{+1.9}_{-1.0}$	$0.34^{+0.05}_{-0.05}$	$0.51^{+0.06}_{-0.05}$	$0.9^{+0.6}_{-0.4}$	$2.5^{+1.8}_{-1.0}$
NGC 1385	$13.5^{+5.0}_{-2.6}$	< 4.1	< 8.5	< 238	$20.0^{+7.5}_{-6.3}$	$4.7^{+4.3}_{-2.0}$	$0.50^{+0.04}_{-0.03}$	$0.62^{+0.04}_{-0.03}$	$0.3^{+0.2}_{-0.1}$	$0.9^{+0.7}_{-0.4}$
NGC 1433	$14.6^{+1.6}_{-1.7}$	$2.1^{+0.4}_{-0.4}$	$6.3^{+0.5}_{-0.5}$	227^{+27}_{-21}	$22.6^{+5.4}_{-3.6}$	$3.6^{+2.7}_{-1.5}$	$0.48^{+0.02}_{-0.01}$	$0.36^{+0.05}_{-0.04}$	$0.4^{+0.3}_{-0.2}$	$1.2^{+0.8}_{-0.5}$
NGC 1511	$15.2^{+5.9}_{-3.4}$	$2.0^{+1.4}_{-0.8}$	$6.3^{+1.4}_{-0.8}$	417^{+182}_{-96}	$49.7^{+28.6}_{-18.8}$	$4.4^{+4.1}_{-1.9}$	$0.55^{+0.07}_{-0.05}$	$0.83^{+0.04}_{-0.02}$	$0.3^{+0.2}_{-0.1}$	$1.5^{+1.0}_{-0.6}$
NGC 1512	$11.9^{+1.0}_{-1.6}$	$1.8^{+0.2}_{-0.4}$	$6.0^{+0.3}_{-0.3}$	258^{+37}_{-30}	$27.9^{+8.3}_{-2.5}$	$2.2^{+1.5}_{-0.9}$	$0.53^{+0.02}_{-0.02}$	$0.33^{+0.02}_{-0.02}$	$0.5^{+0.4}_{-0.2}$	$1.7^{+1.2}_{-0.7}$
NGC 1546	$8.5^{+5.4}_{-2.4}$	< 3.8	< 8.1	< 348	$44.2^{+32.0}_{-19.2}$	$0.7^{+0.8}_{-0.3}$	$0.69^{+0.10}_{-0.04}$	$0.31^{+1.07}_{-0.37}$	$1.2^{+0.9}_{-0.5}$	$7.6^{+5.4}_{-3.1}$
NGC 1559	$16.2^{+11.9}_{-4.0}$	$4.7^{+4.2}_{-1.5}$	$9.0^{+4.2}_{-1.5}$	369^{+140}_{-63}	$21.1^{+7.9}_{-9.1}$	$3.3^{+4.2}_{-1.4}$	$0.43^{+0.04}_{-0.03}$	$0.28^{+0.23}_{-0.14}$	$0.5^{+0.3}_{-0.2}$	$1.4^{+1.0}_{-0.6}$
NGC 1566	$23.8^{+3.5}_{-3.2}$	$4.7^{+1.2}_{-1.0}$	$9.0^{+1.2}_{-1.1}$	229^{+50}_{-35}	$12.6^{+2.8}_{-2.2}$	$4.1^{+3.1}_{-1.8}$	$0.36^{+0.02}_{-0.02}$	$0.46^{+0.04}_{-0.03}$	$0.6^{+0.4}_{-0.2}$	$1.3^{+1.0}_{-0.6}$
NGC 1672	$23.4^{+4.2}_{-4.8}$	< 5.9	< 10.2	< 442	$20.1^{+7.3}_{-3.4}$	$4.7^{+3.4}_{-2.1}$	$0.28^{+0.07}_{-0.07}$	$0.43^{+0.05}_{-0.05}$	$0.5^{+0.4}_{-0.2}$	$1.3^{+0.9}_{-0.5}$
NGC 1792	$11.4^{+1.7}_{-1.5}$	$2.4^{+0.7}_{-0.7}$	$6.6^{+0.8}_{-0.8}$	352^{+96}_{-58}	$43.8^{+13.8}_{-7.2}$	$1.3^{+0.9}_{-0.5}$	$0.49^{+0.04}_{-0.03}$	$0.67^{+0.03}_{-0.03}$	$0.9^{+0.6}_{-0.4}$	$3.2^{+2.3}_{-1.3}$
NGC 1809	$4.9^{+4.0}_{-1.0}$	$1.6^{+2.4}_{-0.8}$	$6.0^{+2.5}_{-0.8}$	280^{+602}_{-83}	$50.8^{+30.2}_{-23.6}$	$0.8^{+1.2}_{-0.4}$	$0.34^{+0.25}_{-0.09}$	$0.62^{+0.21}_{-0.06}$	$0.6^{+0.4}_{-0.2}$	$1.6^{+1.1}_{-0.6}$
NGC 2090	$10.3^{+2.5}_{-1.9}$	< 2.4	< 6.7	185^{+43}_{-28}	$31.3^{+23.3}_{-10.1}$	$0.8^{+0.7}_{-0.4}$	$0.46^{+0.04}_{-0.03}$	$0.81^{+0.01}_{-0.01}$	$1.2^{+0.9}_{-0.5}$	$4.5^{+3.2}_{-1.9}$
NGC 2283	$9.2^{+2.7}_{-1.9}$	$2.8^{+1.4}_{-1.1}$	$7.2^{+1.4}_{-1.1}$	195^{+93}_{-40}	$17.3^{+8.9}_{-4.8}$	$2.6^{+2.2}_{-1.1}$	$0.23^{+0.10}_{-0.07}$	$0.56^{+0.04}_{-0.03}$	$0.4^{+0.3}_{-0.1}$	$0.9^{+0.6}_{-0.4}$
NGC 2835	$8.4^{+1.5}_{-1.3}$	$1.3^{+0.5}_{-0.4}$	$5.6^{+0.6}_{-0.5}$	148^{+31}_{-19}	$26.5^{+11.7}_{-6.9}$	$2.1^{+1.6}_{-0.9}$	$0.34^{+0.04}_{-0.03}$	$0.18^{+0.10}_{-0.08}$	$0.4^{+0.3}_{-0.2}$	$1.0^{+0.7}_{-0.4}$
NGC 2997	$15.5^{+2.2}_{-1.8}$	$3.8^{+0.9}_{-0.7}$	$8.1^{+1.0}_{-0.8}$	234^{+46}_{-30}	$16.4^{+2.9}_{-2.6}$	$3.0^{+2.2}_{-1.3}$	$0.35^{+0.04}_{-0.03}$	$0.33^{+0.04}_{-0.04}$	$0.5^{+0.4}_{-0.2}$	$1.5^{+1.1}_{-0.6}$
NGC 3059	$29.0^{+7.7}_{-4.6}$	$5.4^{+1.6}_{-1.2}$	$9.7^{+1.7}_{-1.2}$	369^{+50}_{-40}	$13.7^{+3.5}_{-3.0}$	$7.5^{+6.3}_{-3.2}$	$0.36^{+0.04}_{-0.03}$	$0.52^{+0.12}_{-0.08}$	$0.4^{+0.3}_{-0.2}$	$1.2^{+0.8}_{-0.5}$
NGC 3351	$22.7^{+5.0}_{-2.7}$	$2.5^{+0.9}_{-0.6}$	$6.8^{+1.0}_{-0.7}$	179^{+24}_{-20}	$14.4^{+4.2}_{-3.7}$	$3.4^{+2.8}_{-1.4}$	$0.49^{+0.01}_{-0.01}$	$0.23^{+0.02}_{-0.02}$	$0.7^{+0.5}_{-0.3}$	$2.0^{+1.5}_{-0.8}$
NGC 3507	$11.0^{+2.5}_{-1.3}$	$2.3^{+1.0}_{-0.6}$	$6.6^{+1.0}_{-0.6}$	277^{+91}_{-38}	$32.9^{+8.1}_{-8.0}$	$2.4^{+1.9}_{-1.0}$	$0.46^{+0.03}_{-0.03}$	$0.64^{+0.05}_{-0.04}$	$0.5^{+0.3}_{-0.2}$	$1.4^{+1.0}_{-0.6}$
NGC 3511	$8.3^{+2.2}_{-1.4}$	$2.8^{+1.4}_{-1.1}$	$7.1^{+1.4}_{-1.1}$	383^{+146}_{-91}	$37.6^{+17.8}_{-10.3}$	$0.6^{+0.5}_{-0.2}$	$0.53^{+0.03}_{-0.03}$	$0.61^{+0.03}_{-0.03}$	$1.4^{+1.0}_{-0.6}$	$4.8^{+3.4}_{-2.0}$
NGC 3596	$19.2^{+4.2}_{-2.5}$	$3.3^{+1.4}_{-0.8}$	$7.7^{+1.4}_{-0.8}$	119^{+34}_{-18}	$9.8^{+2.2}_{-2.5}$	$2.7^{+2.2}_{-1.1}$	$0.49^{+0.04}_{-0.03}$	$0.15^{+0.07}_{-0.07}$	$0.7^{+0.5}_{-0.3}$	$2.3^{+1.6}_{-0.9}$
NGC 3627	$14.1^{+3.1}_{-2.0}$	< 2.7	< 7.0	207^{+47}_{-31}	$31.6^{+14.0}_{-8.4}$	$1.8^{+1.5}_{-0.8}$	$0.39^{+0.05}_{-0.04}$	$0.60^{+0.03}_{-0.03}$	$0.8^{+0.6}_{-0.3}$	$2.4^{+1.7}_{-1.0}$
NGC 4254	$17.7^{+3.0}_{-1.9}$	$4.7^{+1.3}_{-1.0}$	$9.0^{+1.3}_{-1.0}$	215^{+48}_{-34}	$12.3^{+2.2}_{-1.9}$	$2.8^{+2.2}_{-1.2}$	$0.34^{+0.05}_{-0.05}$	$0.39^{+0.04}_{-0.04}$	$0.6^{+0.5}_{-0.3}$	$2.0^{+1.4}_{-0.8}$
NGC 4298	$22.6^{+7.5}_{-4.4}$	< 5.8	< 10.2	< 263	$16.7^{+7.4}_{-5.2}$	$1.8^{+1.6}_{-0.8}$	$0.51^{+0.03}_{-0.03}$	$0.48^{+0.03}_{-0.03}$	$1.3^{+0.9}_{-0.5}$	$4.9^{+3.5}_{-2.1}$
NGC 4303	$20.7^{+4.7}_{-3.2}$	$4.0^{+1.7}_{-1.2}$	$8.3^{+1.8}_{-1.2}$	247^{+77}_{-40}	$17.1^{+5.5}_{-4.1}$	$5.5^{+4.5}_{-2.3}$	$0.48^{+0.02}_{-0.02}$	$0.49^{+0.03}_{-0.03}$	$0.4^{+0.3}_{-0.2}$	$1.2^{+0.8}_{-0.5}$
NGC 4321	$20.0^{+2.8}_{-2.3}$	$3.1^{+0.7}_{-0.6}$	$7.4^{+0.7}_{-0.7}$	242^{+23}_{-21}	$20.5^{+4.3}_{-3.4}$	$3.0^{+2.3}_{-1.3}$	$0.47^{+0.01}_{-0.01}$	$0.45^{+0.02}_{-0.02}$	$0.7^{+0.5}_{-0.3}$	$2.1^{+1.5}_{-0.9}$
NGC 4496A	$14.6^{+2.7}_{-2.5}$	$1.9^{+0.8}_{-0.8}$	$6.3^{+0.8}_{-0.9}$	213^{+52}_{-37}	$27.2^{+17.9}_{-6.9}$	$2.4^{+1.8}_{-1.0}$	$0.38^{+0.03}_{-0.03}$	$0.55^{+0.03}_{-0.03}$	$0.6^{+0.4}_{-0.3}$	$1.7^{+1.2}_{-0.7}$
NGC 4535	$24.5^{+8.5}_{-3.6}$	$4.6^{+2.2}_{-1.0}$	$8.9^{+2.3}_{-1.1}$	239^{+60}_{-40}	$13.5^{+3.0}_{-3.8}$	$3.0^{+3.1}_{-1.3}$	$0.43^{+0.03}_{-0.03}$	$0.41^{+0.04}_{-0.04}$	$0.8^{+0.6}_{-0.3}$	$2.3^{+1.7}_{-1.0}$
NGC 4540	$14.0^{+2.7}_{-2.9}$	< 2.6	< 7.0	< 215	$22.4^{+12.6}_{-3.8}$	$2.0^{+1.5}_{-0.9}$	$0.55^{+0.04}_{-0.03}$	$0.66^{+0.03}_{-0.03}$	$0.7^{+0.5}_{-0.3}$	$2.4^{+1.7}_{-1.0}$
NGC 4548	$13.9^{+4.4}_{-2.6}$	< 2.7	< 6.9	< 250	$39.3^{+17.1}_{-15.2}$	$1.6^{+1.4}_{-0.7}$	$0.47^{+0.03}_{-0.02}$	$0.74^{+0.01}_{-0.01}$	$0.9^{+0.6}_{-0.4}$	$2.5^{+1.8}_{-1.0}$
NGC 4569	$16.1^{+3.9}_{-2.5}$	< 2.2	< 6.5	380^{+83}_{-61}	$72.3^{+33.9}_{-22.4}$	$1.1^{+0.9}_{-0.5}$	$0.61^{+0.04}_{-0.03}$	$0.27^{+0.04}_{-0.04}$	$1.4^{+1.0}_{-0.6}$	$6.5^{+4.7}_{-2.7}$
NGC 4571	$19.3^{+5.7}_{-2.8}$	$4.5^{+1.7}_{-1.0}$	$8.8^{+1.8}_{-1.1}$	255^{+50}_{-36}	$13.1^{+3.2}_{-3.4}$	$3.3^{+2.8}_{-1.4}$	$0.64^{+0.02}_{-0.02}$	$0.29^{+0.07}_{-0.06}$	$0.6^{+0.4}_{-0.2}$	$2.8^{+2.0}_{-1.2}$
NGC 4654	$19.8^{+4.3}_{-3.7}$	$4.9^{+1.8}_{-1.5}$	$9.1^{+1.8}_{-1.5}$	441^{+145}_{-79}	$23.4^{+8.0}_{-4.9}$	$2.8^{+2.2}_{-1.2}$	$0.34^{+0.04}_{-0.04}$	$0.45^{+0.04}_{-0.04}$	$0.7^{+0.5}_{-0.3}$	$2.0^{+1.5}_{-0.9}$
NGC 4689	$23.6^{+4.1}_{-3.7}$	$3.8^{+1.0}_{-1.0}$	$8.1^{+1.0}_{-1.0}$	189^{+25}_{-22}	$13.0^{+4.0}_{-2.4}$	$4.6^{+3.5}_{-2.0}$	$0.53^{+0.02}_{-0.02}$	$0.61^{+0.03}_{-0.03}$	$0.5^{+0.4}_{-0.2}$	$1.7^{+1.2}_{-0.7}$
NGC 4731	$13.1^{+3.1}_{-2.8}$	$2.6^{+1.1}_{-1.0}$	$7.0^{+1.2}_{-1.1}$	248^{+93}_{-49}	$24.8^{+14.1}_{-6.5}$	$1.8^{+1.4}_{-0.8}$	$0.36^{+0.06}_{-0.05}$	$0.44^{+0.09}_{-0.07}$	$0.7^{+0.5}_{-0.3}$	$1.6^{+1.1}_{-0.6}$
NGC 4781	$8.3^{+1.5}_{-1.1}$	$2.1^{+0.8}_{-0.6}$	$6.4^{+0.9}_{-0.6}$	182^{+53}_{-32}	$22.7^{+6.4}_{-5.2}$	$1.4^{+1.1}_{-0.6}$	$0.46^{+0.04}_{-0.03}$	$0.72^{+0.02}_{-0.02}$	$0.6^{+0.4}_{-0.2}$	$1.9^{+1.4}_{-0.8}$
NGC 4941	$21.1^{+4.2}_{-3.6}$	$2.7^{+1.0}_{-0.9}$	$7.0^{+1.0}_{-1.0}$	273^{+56}_{-36}	$23.1^{+11.0}_{-5.8}$	$2.5^{+1.9}_{-1.1}$	$0.57^{+0.02}_{-0.02}$	$0.87^{+0.01}_{-0.01}$	$0.8^{+0.6}_{-0.4}$	$3.2^{+2.3}_{-1.3}$
NGC 4951	$7.9^{+4.4}_{-2.1}$	$1.9^{+1.6}_{-0.8}$	$6.2^{+1.7}_{-0.9}$	329^{+130}_{-66}	$38.3^{+27.2}_{-16.8}$	$1.1^{+1.2}_{-0.5}$	$0.67^{+0.02}_{-0.02}$	$0.73^{+0.05}_{-0.03}$	$0.7^{+0.5}_{-0.3}$	$3.2^{+2.3}_{-1.3}$
NGC 5042	$14.7^{+3.7}_{-2.8}$	$2.5^{+1.1}_{-1.0}$	$6.8^{+1.2}_{-1.0}$	242^{+68}_{-45}	$23.2^{+12.8}_{-6.8}$	$2.0^{+1.6}_{-0.9}$	$0.48^{+0.02}_{-0.02}$	$0.65^{+0.04}_{-0.03}$	$0.7^{+0.5}_{-0.3}$	$2.0^{+1.4}_{-0.8}$

Table 3 – *continued*

Galaxy	$t_{\rm CO}$ (Myr)	$t_{\rm fb}$ (Myr)	$t_{\rm H\alpha}$ (Myr)	λ (pc)	$v_{\rm fb}$ (km s^{-1})	$\epsilon_{\rm sf}$ (per cent)	$f_{\rm diffuse}^{\rm CO}$	$f_{\rm diffuse}^{\rm H\alpha}$	$t_{\rm dep}^{\rm compact}$ (Gyr)	$t_{\rm dep}$ (Gyr)
NGC 5068	$11.4^{+2.3}_{-1.9}$	$1.1^{+0.3}_{-0.3}$	$5.5^{+0.4}_{-0.3}$	117^{+18}_{-12}	$16.1^{+5.3}_{-3.6}$	$2.7^{+2.1}_{-1.2}$	$0.54^{+0.01}_{-0.01}$	$0.11^{+0.14}_{-0.10}$	$0.4^{+0.3}_{-0.2}$	$1.1^{+0.8}_{-0.5}$
NGC 5134	$15.0^{+3.3}_{-2.9}$	$2.5^{+0.7}_{-0.9}$	$6.8^{+0.7}_{-0.9}$	229^{+49}_{-37}	$21.2^{+9.8}_{-4.1}$	$3.8^{+3.0}_{-1.6}$	$0.49^{+0.01}_{-0.02}$	$0.67^{+0.04}_{-0.03}$	$0.4^{+0.3}_{-0.2}$	$1.2^{+0.8}_{-0.5}$
NGC 5248	$15.0^{+3.3}_{-2.6}$	$2.5^{+0.7}_{-0.9}$	$6.7^{+1.2}_{-0.9}$	173^{+40}_{-27}	$20.8^{+8.8}_{-5.6}$	$2.6^{+2.1}_{-1.1}$	$0.56^{+0.03}_{-0.03}$	$0.73^{+0.02}_{-0.02}$	$0.6^{+0.4}_{-0.2}$	$2.1^{+1.5}_{-0.9}$
NGC 5530	$20.4^{+5.0}_{-2.8}$	$4.3^{+1.2}_{-0.7}$	$8.6^{+1.3}_{-0.8}$	269^{+49}_{-33}	$11.6^{+2.1}_{-2.4}$	$2.3^{+1.9}_{-0.9}$	$0.51^{+0.02}_{-0.02}$	$0.70^{+0.02}_{-0.02}$	$0.9^{+0.6}_{-0.4}$	$2.7^{+2.0}_{-1.1}$
NGC 5643	$17.7^{+2.7}_{-2.7}$	$3.0^{+0.7}_{-0.8}$	$7.3^{+0.8}_{-0.8}$	188^{+33}_{-21}	$13.8^{+4.4}_{-2.3}$	$4.6^{+3.5}_{-2.0}$	$0.40^{+0.02}_{-0.02}$	$0.70^{+0.01}_{-0.01}$	$0.4^{+0.3}_{-0.3}$	$1.1^{+0.8}_{-0.5}$
NGC 6300	$21.5^{+3.6}_{-2.9}$	$3.6^{+1.0}_{-0.8}$	$7.8^{+1.1}_{-0.8}$	156^{+23}_{-23}	$11.0^{+2.7}_{-2.3}$	$3.2^{+2.4}_{-1.4}$	$0.49^{+0.02}_{-0.02}$	$0.67^{+0.02}_{-0.02}$	$0.7^{+0.5}_{-0.3}$	$2.0^{+1.4}_{-0.8}$
NGC 6744	$31.8^{+3.7}_{-3.0}$	$3.9^{+0.7}_{-0.5}$	$8.2^{+0.8}_{-0.6}$	156^{+13}_{-9}	$9.4^{+1.3}_{-1.3}$	$2.6^{+1.9}_{-1.1}$	$0.38^{+0.01}_{-0.01}$	$0.17^{+0.03}_{-0.02}$	$1.2^{+0.9}_{-0.5}$	$3.0^{+2.1}_{-1.1}$
NGC 7456	$11.0^{+4.6}_{-2.3}$	$2.6^{+1.5}_{-0.9}$	$7.1^{+1.6}_{-1.0}$	393^{+101}_{-80}	$34.7^{+15.9}_{-12.3}$	$0.8^{+0.7}_{-0.3}$	$0.36^{+0.06}_{-0.05}$	$0.81^{+0.02}_{-0.02}$	$1.4^{+1.0}_{-0.6}$	$3.5^{+2.5}_{-1.5}$
NGC 7496	$18.4^{+10.5}_{-3.0}$	$4.1^{+3.7}_{-1.2}$	$8.4^{+3.7}_{-1.3}$	262^{+161}_{-58}	$17.4^{+5.5}_{-7.3}$	$5.2^{+6.3}_{-2.1}$	$0.54^{+0.01}_{-0.02}$	$0.69^{+0.04}_{-0.03}$	$0.4^{+0.3}_{-0.1}$	$1.1^{+0.8}_{-0.5}$

clouds are transient objects that disperse within a small multiple of the dynamical time-scale.

The overall measured range of molecular cloud lifetimes is consistent with that found in previous studies, those using cloud classification methods (Engargiola et al. 2003; Blitz et al. 2007; Fukui et al. 2008; Kawamura et al. 2009; Miura et al. 2012; Meidt et al. 2015; Corbelli et al. 2017), statistics of sight line fractions with only CO or only H α or both types of emission (Schinnerer et al. 2019; Pan et al. 2022), and those using the same statistical method as described in Section 3 (Kruijssen et al. 2019b; Chevance et al. 2020b; Hygate 2020; Kim et al. 2021a; Ward et al. 2022). Similar cloud survival times have been predicted by theory and simulations (e.g. Elmegreen 2000; Hartmann 2001; Dobbs & Pringle 2013; Kim, Kim & Ostriker 2018; Benincasa et al. 2020; Jeffreson et al. 2021; Lancaster et al. 2021; Semenov, Kravtsov & Gnedin 2021). In Fig. 4, we show how the measured cloud lifetime is correlated with the position of galaxies in the $M_{*,\rm global} - {\rm SFR}_{\rm global}$ plane. The figure shows that $t_{\rm CO}$ increases with ${\rm SFR}_{\rm global}$ and $M_{*,\rm global}$ (see also top left-hand panel of Fig. 6). There seems to be no relation between $t_{\rm CO}$ and the host galaxy's offset from the main sequence (ΔMS). Pan et al. (2022) have found similar trends for the PHANGS galaxies, in which the fraction of sightlines per galaxy that is associated only with CO emission increases with $M_{*,\rm global}$, while showing no correlation with ΔMS. Although not directly comparable, other time-scales such as the average free-fall time-scale measured on cloud scales and the global depletion time-scale have also been reported to correlate strongly with galaxy mass across the PHANGS sample (Utomo et al. 2018). The galaxy mass trend of $t_{\rm CO}$ is discussed in more detail in Section 5.1.

4.2 Feedback time-scale ($t_{\rm fb}$)

The duration over which CO and H α emission is found coincident is measured to be less than 6.1 Myr in our sample of galaxies. For 12 galaxies, we do not sufficiently resolve the separation between independent regions and therefore we are only able to obtain upper limits on $t_{\rm fb}$ (see the Appendix). Without these galaxies, the range of feedback time-scale becomes 1.3 and 5.4 Myr, constituting $10-30$ per cent of the cloud lifetime, with an average and a standard deviation of 3.2 ± 1.1 Myr. This time-scale represents the time it takes for emerging massive stars (visible in H α) to disperse the surrounding molecular gas (either by kinetic dispersal or by the photodissociation of CO molecules). The range of feedback time-scales measured across our galaxy sample is comparable to that from our previous studies using the same statistical method (Kruijssen

et al. 2019b; Chevance et al. 2022; Hygate 2020; Kim et al. 2021a; Ward et al. 2022).

Our measurements of the feedback time-scales are also similar to the time it takes for optically identified stellar clusters and associations to stop being associated with their natal GMCs (1−5 Myr; Whitmore et al. 2014; Hollyhead et al. 2015; Corbelli et al. 2017; Turner et al. in preparation). Grasha et al. (2018, 2019) have measured similar ages of star clusters and associations when they become spatially decorrelated from GMCs in NGC 7793 and M51 (2 and 6 Myr, respectively). Hydrodynamical simulations of GMCs (Kim et al. 2018; Kim, Ostriker & Filippova 2021b; Grudić et al. 2021; Lancaster et al. 2021) find somewhat longer feedback time-scales ($\lesssim$ 10 Myr), constituting $\sim$ 50 per cent of the cloud lifetime. We suspect this difference could be due to different approaches for tracing star formation in simulations and observations. Indeed, simulations trace star formation by employing sink particles, which are created when a certain density threshold is reached assuming a fully populated initial mass function and include a phase of deeply embedded star formation. On the other hand, we focus on H α, which is sensitive to the most massive stars; in the case where the star formation accelerates over time (e.g. Hartmann, Ballesteros-Paredes & Heitsch 2012; Murray & Chang 2015), our measurements may be the most sensitive to the final, intense phase of star formation. Moreover, H α is attenuated during the earliest phase of star formation due to the dense gas surrounding the young stars. Including 24 μm as a tracer for the obscured star formation increases the overlapping time-scale between CO and SFR tracer by $1-4$ Myr (Kim et al. 2021a).

4.3 Region separation length (λ)

Fig. 1 reveals that there is a universal spatial decorrelation between molecular gas and young stellar regions on small spatial scales, while these quantities are correlated with each other on galactic scales. This result demonstrates that galaxies are composed of small regions undergoing independent evolution from GMCs to cold gas-free young stellar regions. Our method constrains the characteristic separation length (λ) between the small-scale independent regions, which is linked to the scale at which molecular gas-to-SFR tracer flux ratio starts to deviate from the galactic average (see Fig. 1). Excluding 8 galaxies for which we do not sufficiently resolve these independent regions (see Appendix A), we find that λ ranges from 100 to 400 pc, with an average and standard deviation of 254 ± 79 pc. This is similar to the total cold gas disc thickness (100–300 pc; Scoville et al. 1993; Yim et al. 2014; Heyer & Dame 2015; Patra 2020; Yim et al. 2020), as well as the range of values found in previous application of the same
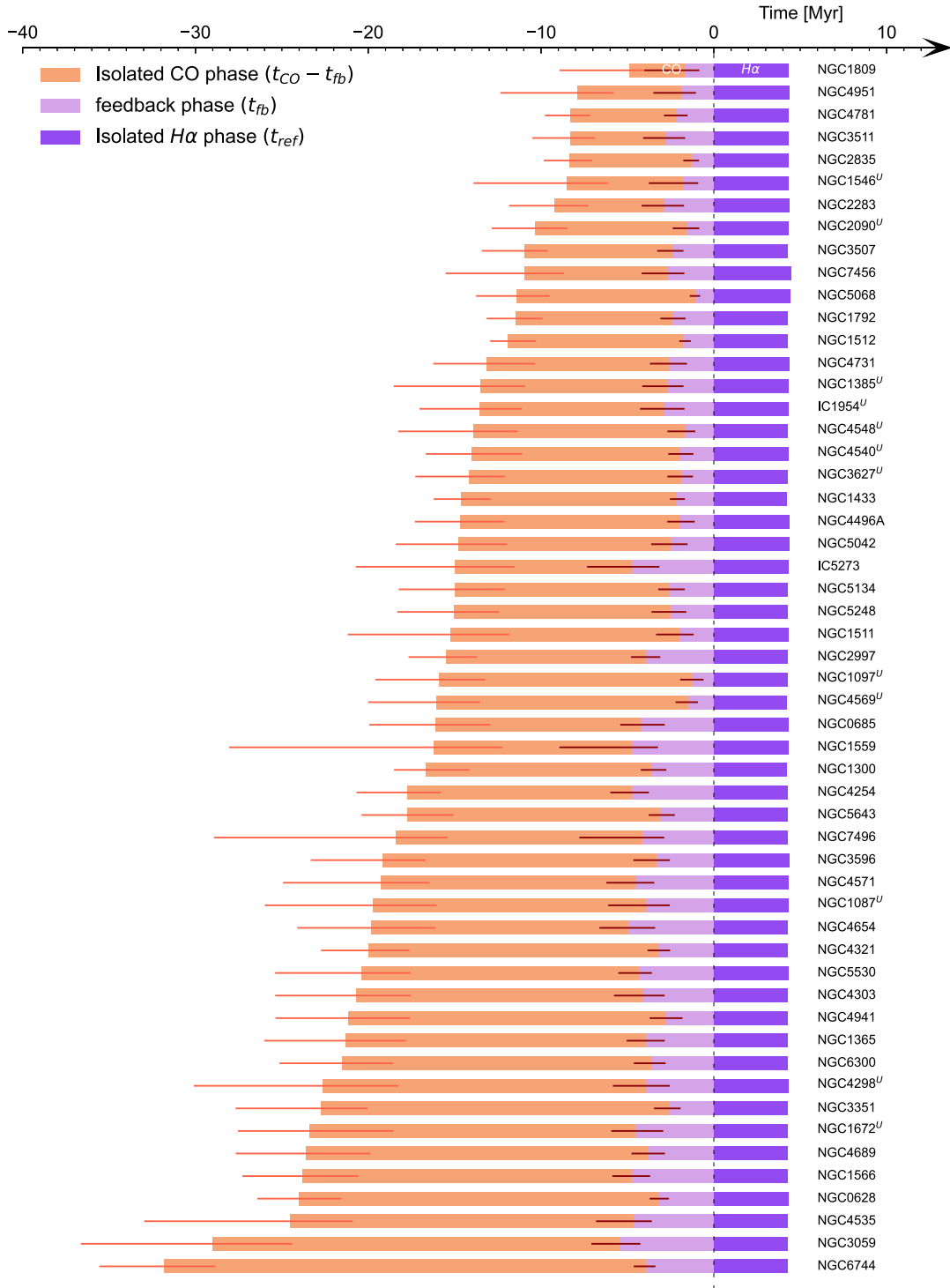
Figure 2. Evolutionary timeline of GMCs from molecular gas assembly to feedback-driven dispersal, and H II regions free of molecular gas, ordered by increasing cloud lifetime from top to bottom. Going from left to right, GMCs are initially only visible in CO (orange, for a duration of $t_{CO} - t_{fb}$). Towards the end of this phase, massive star formation has taken place, generating spatially coincident Hα emission (light purple, for a duration of t_{fb}). Finally, violent feedback from young stars has completely cleared the surrounding molecular gas, only leaving Hα emission to be detected, without any associated CO emission (dark purple, with a duration of $t_{ref} \approx 4.3$ Myr; see Section 3). The error bars on the left and in the middle indicate the uncertainties on t_{CO} and t_{fb}, respectively. U indicates galaxies with only upper limit constraints on t_{fb}.
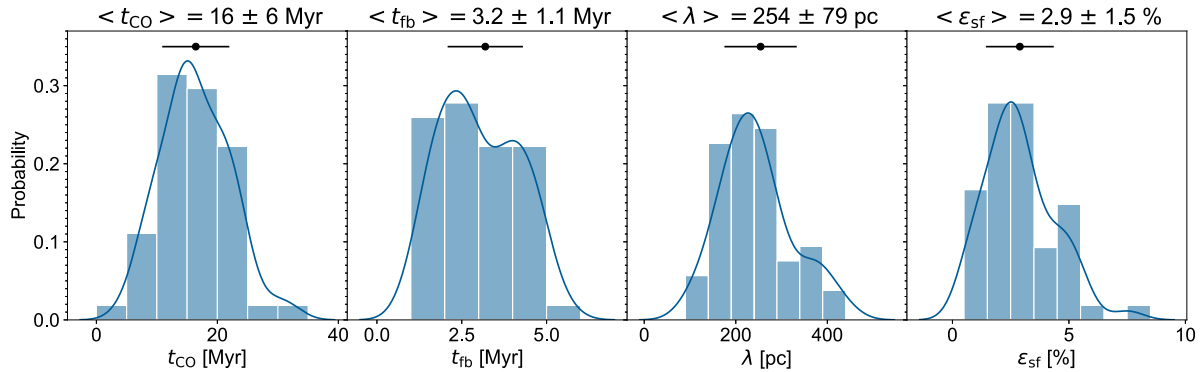
Figure 3. Distributions of the main physical quantities constrained across 54 PHANGS galaxies. From left to right, we show a Gaussian kernel density estimate of the cloud lifetime (t_{CO}), the feedback time-scale (t_{fb}), the average separation length between independent star-forming regions (λ), and the integrated star formation efficiency (ϵ_{sf}). For each histogram, the mean (black dot) and 16-84 per cent range (error bar) of the data, are indicated at the top of the panel (excluding t_{fb} and λ measurements where only upper limits are constrained; see Table 3).
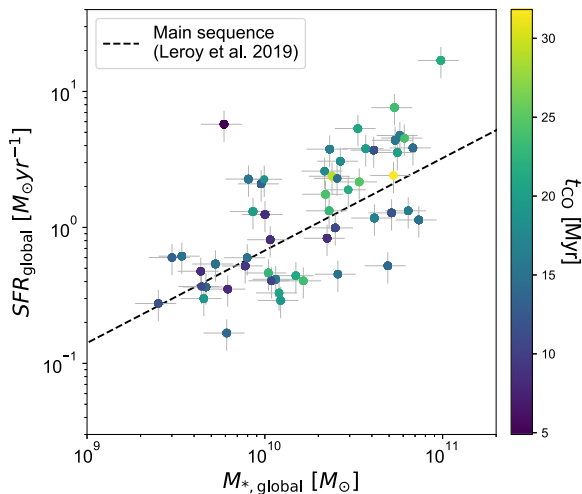
Figure 4. Galaxy-wide SFR (SFR_{global}) as a function of stellar mass ($M_{*,global}$) for our full galaxy sample, colour-coded by our measurement of the cloud lifetime (t_{CO}) for each galaxy. The dashed line is the local star-forming main sequence from Leroy et al. (2019).

method to relatively nearby and well-resolved galaxies ($100-250$ pc, Kruijssen et al. 2019b; Chevance et al. 2020b; Kim et al. 2021a). From the similarity of λ to the gas disc scale height, Kruijssen et al. (2019b) have suggested that the break-out of feedback-driven bubbles from the galactic disc, pushing the ISM by a similar distance, might be setting this characteristic length scale.

While our methodology constrains the mean separation length between regions undergoing independent lifecycles, other methods focus on characterizing the separation between detectable emission peaks. In a parallel paper on the PHANGS galaxies, Machado et al. (in preparation) investigate the spacing between emission peaks in the PHANGS CO maps. Contrary to our study, which uses the highest available resolution for each galaxy, they adopt GMC catalogue (Hughes et al. in preparation; see also Rosolowsky et al. 2021) that are generated using CO maps with matched resolution of 150 pc and sensitivity across the full sample. For a sub-set of 44 galaxies in our sample, Machado et al. (in preparation) obtain mean

distances to the first nearest neighbour from 250 to 600 pc. We have compared these distances to the nearest neighbour distance expected from the mean separation length between GMCs, obtained by $\langle r_n \rangle = 0.443\lambda_{GMC} = 0.443\lambda\sqrt{\tau/t_{CO}}$ (see the discussion of Kruijssen et al. 2019b, equation 9), where τ is the total duration of the entire evolutionary cycle ($\tau = t_{CO} + t_{H\alpha} - t_{fb}$). The $\langle r_n \rangle$ ranges from 50 to 200 pc. While the two quantities show a mild correlation (with Spearman correlation coefficient of 0.5), the mean distance to the first nearest neighbour from Machado et al. (in preparation) is larger than that expected from the mean separation length. We suspect this difference is due to the limitation in resolution (by 60 per cent coarser on average) of CO maps in Machado et al. (in preparation) compared to the maps analysed here, which results in a smaller number of identified GMCs compared to when high-resolution maps are used.

4.4 Feedback velocity (v_{fb})

After the onset of star formation, the CO emission quickly becomes undetectable due to energetic feedback from young massive stars. We use the Gaussian 1σ dispersion needed to reproduce the density contrast between the CO peaks and the local background (r_{CO}) and the time-scale over which molecular clouds are disrupted (t_{fb}) to define the feedback velocity $v_{fb} = r_{CO}/t_{fb}$ (see also Kruijssen et al. 2018). The measured v_{fb} represents the speed with which the region must be swept free of CO molecules. The measurement does not specify a physical mechanism, but the most likely candidates are kinetic removal of gas from the region, e.g. by gas pressure-driven expansion, radiation pressure, winds, or supernovae, or the photodissociation of CO molecules by massive stars (e.g. Barnes et al. 2021, 2022).

Excluding galaxies with resolution worse than 200 pc (as r_{CO} depends on the beam size; see below), the size of the clouds is between 20 and 100 pc and v_{fb} ranges between 10 and 50 km s^{-1}, with an average and standard deviation of 22 ± 11 km s^{-1}. These measured cloud sizes are comparable to the luminosity-weighted averages of those derived from GMC catalogues for each galaxy (Rosolowsky et al. 2021; Hughes et al. in preparation), with Spearman correlation coefficient of 0.7. The range of velocities is consistent with that obtained from our previous analysis (Kruijssen et al. 2019b; Chevance et al. 2020b; Kim et al. 2021a) and is comparable to the expansion velocities measured for nearby H II regions in NGC 300 (McLeod et al. 2020), the LMC (Nazé et al. 2001; Ward et al. 2016; McLeod et al. 2019), and the Milky Way (Murray & Rahman 2010; Barnes

et al. 2020). A similar range of expansion velocities is also found in numerical simulations by Rahner et al. (2017) and Kim et al. (2018).

We note that the measured r_{CO} depends on the beam size of the CO maps. If the CO emission peaks are dispersed kinetically, then the measured feedback velocity should be considered as accurate, because the measured r_{CO} is the same size scale over which the material must travel to achieve the spatial displacement necessary to cease the spatial overlap between CO and H α emission. However, if the CO emission peaks are dispersed by photodissociation, then this spatial overlap may cease before the feedback front reaches r_{CO}. In that case, v_{fb} may be subject to beam dilution and should be considered as an upper limit to the velocity of the dissociation front. For a sub-set of 19 galaxies with PHANGS–MUSE (Emsellem et al. 2022) observations, Kreckel et al. (2020) and Williams et al. (2022) have measured the metallicity distribution, as well as the scale at which the mixing in the ISM is effective, using a two-point correlation function. Kreckel et al. (2020) have found a strong correlation between the mixing scale and v_{fb} (Pearson's correlation coefficient of 0.7), indicating that dispersal of molecular gas is predominantly kinetic.

4.5 Integrated star formation efficiency (ϵ_{sf})

We define the integrated star formation efficiency per cloud lifecycle (ϵ_{sf}) as

$$\epsilon_{sf} = \frac{t_{CO}\,\Sigma_{SFR}}{\Sigma_{H_2}^{compact}} , \qquad (2)$$

where Σ_{SFR} and $\Sigma_{H_2}^{compact}$ are the surface densities of SFR and compact molecular gas of the analysed region, respectively. This allows us to directly compare the rate of SFR (Σ_{SFR}) and the rate at which molecular gas participating in the star formation enters and leaves molecular clouds, which can be expressed as $\Sigma_{H_2}^{compact}/t_{CO}$. Equation (2) can also simply be rewritten as $\epsilon_{sf} = t_{CO}/t_{dep}^{compact}$, where $t_{dep}^{compact} = \Sigma_{H_2}^{compact}/\Sigma_{SFR}$ is the depletion time-scale of non-diffuse molecular gas structures (clouds), assuming that all star formation takes place in such structures. When measuring $\Sigma_{H_2}^{compact}$, we take the sum of the compact CO emission and divide by the analysed area after filtering out diffuse emission. This is to selectively include CO emission that participates in massive star formation, while excluding CO emission from diffuse gas and faint clouds. However, to calculate Σ_{SFR}, we include all the emission, assuming that all the diffuse emission in the SFR tracer map (*WISE* W4 band in combination with *GALEX* ultraviolet band; see Section 3) is related to recent massive star formation (e.g. leakage of ionizing photons from H II regions). This assumption might not hold especially in the central region of galaxies where contributions from hot low-mass evolved stars in diffuse ionized gas is found to be non-negligible (Belfiore et al. 2022). However, galactic centres are mostly not included in our analysis.

Our measurements of $t_{dep}^{compact}$ are listed in Table 3 and range from 0.3 to 1.4 Gyr. Since we only take the compact gas emission into account, $t_{dep}^{compact}$ is shorter than that measured including all the CO emission (t_{dep}), which ranges from 0.9 to 7.6 Gyr for the fields of view considered here. The depletion time-scales of the PHANGS–ALMA galaxies across the full ALMA footprints (including galactic centres) can be found in Utomo et al. (2018), Leroy et al. (2021b), Querejeta et al. (2021), and Sun et al. (in preparation). In Fig. 5, we show the molecular cloud lifetime t_{CO} as a function of the gas depletion time of the compact molecular gas $t_{dep}^{compact}$, as measured
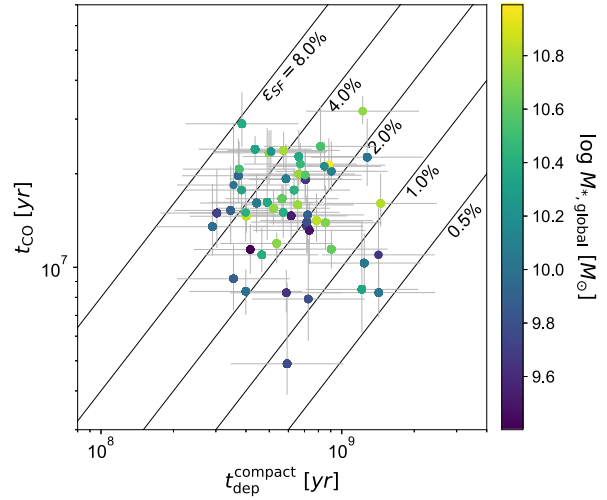
Figure 5. Our measurements of cloud lifetime (t_{CO}) against the depletion time for compact molecular gas ($t_{dep}^{compact}$). The data points are colour-coded by stellar mass ($M_{*,\,global}$). Lines of constant ϵ_{sf} are shown using equation (2).

in our analysis. Following the above procedure, we measure ϵ_{sf} to be 0.7–7.5 per cent across our galaxy sample, illustrating that star formation is inefficient in these clouds. Our previous measurements of ϵ_{sf} (Kruijssen et al. 2019b; Chevance et al. 2020b; Kim et al. 2021a) also fall within this range of values.

We have also compared our measurements of ϵ_{sf} with the star formation efficiency per free-fall time, defined as $\epsilon_{ff} = t_{ff}\,\Sigma_{SFR}/\Sigma_{H_2}$. Using a subset of PHANGS-ALMA observations, Utomo et al. (2018) have measured ϵ_{ff} (0.3–2.6 per cent) that are similar to ϵ_{sf} within a factor of few, where the difference is mostly because t_{CO} is on average three times longer than t_{ff} (see Section 5.2).

4.6 Diffuse emission fraction in CO and H α maps ($f_{diffuse}^{CO}$ and $f_{diffuse}^{H\alpha}$)

As described in Section 3, in order to robustly perform our measurements, we filter out the large-scale diffuse emission with a Gaussian high-pass filter in Fourier space. With this procedure, we can also constrain the fraction of emission coming from the diffuse component in both CO and H α maps ($f_{diffuse}^{CO}$ and $f_{diffuse}^{H\alpha}$, respectively). As shown in Table 3, we measure a fraction of diffuse CO emission ranging from 13 to 69 per cent, with an average of 45 per cent. We obtain diffuse ionized gas fractions ranging from 11 to 87 per cent, with an average of 0.53 per cent. We note that these values are determined directly from the morphological structure of the integrated emission maps. They do not contain any information regarding the dynamical state of the gas, nor do they account for galaxy-to-galaxy variations in resolution, sensitivity, or inclination. As a result, these diffuse emission fractions represent important functional quantities, but their physical interpretation may be non-trivial. Pety et al. (2013) have suggested a similar value of diffuse CO emission fraction in M51, finding that 50 per cent of the CO emission arises from spatial scale larger than 1.3 kpc. Roman-Duval et al. (2016) have measured 25 per cent of the CO emission in the Milky Way to be diffuse. As for the diffuse H α emission fraction, our range of values matches well with what is found in dedicated diffuse ionized gas studies based on H II region morphologies, where Belfiore et al. (2022) have found the diffuse emission fraction to range from $20 - 55$ per cent, with

Table 4. Spearman correlation coefficients and logarithm of p-values (in parentheses) between our measurements and galaxy (or average GMC) related properties. Our measurements are the cloud lifetime (t_{CO}), the feedback time-scale (t_{fb}), the characteristic region separation length (λ), the integrated star formation efficiency (ϵ_{sf}), the feedback velocity (v_{fb}), the diffuse emission fraction in the molecular gas and SFR tracer maps ($f_{diffuse}^{CO}$ and $f_{diffuse}^{H\alpha}$), and the depletion time-scale of the compact molecular gas ($t_{dep}^{compact}$). Statistically significant correlations are in bold.

	t_{CO}	t_{fb}	λ	ϵ_{sf}	v_{fb}	$f_{diffuse}^{CO}$	$f_{diffuse}^{H\alpha}$	$t_{dep}^{compact}$
Galaxy related properties								
Stellar mass, $M_{*,\,global}$	**0.47 (−3.33)**	0.34 (−1.58)	0.13 (−0.43)	0.04 (−0.10)	−0.02 (−0.04)	−0.13 (−0.42)	−0.17 (−0.61)	0.31 (−1.60)
Galaxy-wide SFR, SFR_{global}	0.40 (−2.48)	0.34 (−1.62)	0.20 (−0.76)	0.18 (−0.71)	−0.05 (−0.12)	−0.41 (−2.41)	−0.16 (−0.57)	0.01 (−0.02)
Atomic gas mass, $M_{HI,\,global}$	0.12 (−0.42)	0.08 (−0.21)	0.12 (−0.37)	0.00 (−0.01)	0.14 (−0.42)	**−0.52 (−3.83)**	−0.28 (−1.36)	0.02 (−0.05)
Molecular gas mass, $M_{H_2,\,global}$	**0.59 (−5.33)**	**0.49 (−3.01)**	0.14 (−0.44)	0.22 (−0.91)	−0.14 (−0.43)	−0.21 (−0.82)	−0.19 (−0.75)	0.15 (−0.54)
Offset from the main sequence, ΔMS	0.16 (−0.59)	0.09 (−0.25)	0.02 (−0.05)	0.23 (−0.99)	0.08 (−0.21)	−0.40 (−2.37)	−0.08 (−0.23)	−0.18 (−0.66)
Hubble type	−0.23 (−0.98)	−0.03 (−0.07)	−0.25 (−1.02)	−0.03 (−0.09)	−0.22 (−0.79)	−0.13 (−0.43)	−0.19 (−0.72)	−0.15 (−0.54)
Total gas mass, $M_{gas,\,global}$	0.33 (−1.78)	0.27 (−1.08)	0.09 (−0.26)	0.09 (−0.27)	0.00 (−0.00)	**−0.49 (−3.50)**	−0.29 (−1.40)	0.08 (−0.26)
Total baryonic mass, $M_{tot,\,global}$	**0.46 (−3.16)**	0.33 (−1.53)	0.11 (−0.34)	0.04 (−0.10)	−0.03 (−0.06)	−0.21 (−0.84)	−0.18 (−0.69)	0.30 (−1.48)
Molecular gas fraction, $f_{H_2,\,global}$	**0.50 (−3.72)**	**0.50 (−3.23)**	0.16 (−0.53)	0.15 (−0.52)	−0.16 (−0.50)	0.22 (−0.92)	0.07 (−0.22)	0.19 (−0.75)
Gas fraction, $f_{gas,\,global}$	−0.23 (−0.98)	−0.17 (−0.56)	−0.15 (−0.48)	0.07 (−0.20)	−0.01 (−0.03)	−0.40 (−2.32)	−0.19 (−0.73)	−0.30 (−1.48)
Specific SFR, sSFR	0.07 (−0.22)	0.08 (−0.20)	0.05 (−0.14)	−0.23 (−0.98)	−0.08 (−0.22)	0.33 (−1.71)	0.02 (−0.06)	0.36 (−2.09)
Metallicity, $12 + \log(O/H)$	0.54 (−2.43)	0.32 (−0.85)	0.17 (−0.38)	−0.27 (−0.77)	0.07 (−0.12)	−0.22 (−0.51)	0.06 (−0.11)	**0.66 (−3.77)**
Mixing scale, L_{mix}	−0.36 (−0.75)	0.07 (−0.08)	**0.78 (−3.05)**	−0.02 (−0.03)	0.66 (−1.85)	0.10 (−0.14)	0.52 (−1.40)	−0.30 (−0.60)
Average GMC related properties								
Velocity dispersion, $\sigma_{v,\,GMC}$	0.19 (−0.76)	0.22 (−0.82)	0.32 (−1.49)	0.02 (−0.06)	0.22 (−0.79)	−0.06 (−0.17)	0.25 (−1.11)	0.11 (−0.35)
Virial parameter, $\alpha_{vir,\,GMC}$	−0.32 (−1.67)	−0.23 (−0.86)	−0.21 (−0.77)	−0.13 (−0.46)	−0.07 (−0.19)	−0.03 (−0.09)	**0.47 (−3.26)**	0.06 (−0.16)
Molecular gas mass, M_{GMC}	0.37 (−2.12)	0.38 (−1.94)	0.40 (−2.26)	0.22 (−0.93)	0.15 (−0.46)	−0.03 (−0.08)	0.05 (−0.14)	−0.04 (−0.09)
Internal pressure, P_{int}	0.14 (−0.47)	0.12 (−0.36)	0.21 (−0.80)	0.07 (−0.21)	0.19 (−0.63)	−0.02 (−0.05)	0.00 (−0.01)	−0.04 (−0.10)
Molecular gas surface density, $\Sigma_{H_2,\,GMC}$	0.20 (−0.81)	0.11 (−0.33)	0.16 (−0.55)	0.13 (−0.43)	0.15 (−0.48)	0.03 (−0.08)	−0.17 (−0.62)	−0.08 (−0.25)
Galactic dynamics related properties								
Angular speed, Ω	−0.06 (−0.14)	0.04 (−0.08)	−0.41 (−1.86)	−0.13 (−0.39)	-0.34 (-1.27)	0.17 (−0.53)	0.27 (−1.03)	0.21 (−0.73)
Toomre stability parameter, Q	−0.37 (−1.74)	−0.24 (−0.74)	0.20 (−0.62)	−0.06 (−0.16)	0.38 (-1.48)	−0.07 (−0.17)	0.24 (−0.88)	−0.18 (−0.60)
Velocity dispersion, σ	0.11 (−0.34)	0.35 (−1.45)	0.23 (−0.77)	0.10 (−0.29)	-0.02 (-0.05)	−0.24 (−0.92)	0.30 (−1.37)	−0.04 (−0.09)
Other derived quantities within our method								
Surface density								
... molecular gas, Σ_{H_2}	**0.44 (−3.02)**	0.41 (−2.21)	−0.07 (−0.19)	0.05 (−0.14)	-0.23 (-0.83)	−0.02 (−0.06)	0.00 (−0.01)	0.24 (−1.03)
... compact molecular gas, $\Sigma_{H_2}^{compact}$	**0.43 (−2.81)**	0.40 (−2.13)	−0.11 (−0.32)	0.07 (−0.20)	-0.25 (-0.96)	−0.16 (−0.58)	−0.04 (−0.09)	0.21 (−0.90)
Total mass								
... molecular gas, M_{H_2}	**0.54 (−4.37)**	**0.55 (−3.85)**	0.15 (−0.49)	0.15 (−0.54)	-0.19 (-0.66)	−0.13 (−0.43)	−0.04 (−0.12)	0.18 (−0.69)
... compact molecular gas, $M_{H_2}^{compact}$	**0.53 (−4.25)**	**0.55 (−3.90)**	0.11 (−0.34)	0.16 (−0.58)	-0.19 (-0.68)	−0.28 (−1.27)	−0.07 (−0.21)	0.17 (−0.62)
SFR surface density, Σ_{SFR}	0.28 (−1.36)	0.34 (−1.59)	−0.12 (−0.39)	**0.43 (−2.85)**	-0.27 (-1.13)	−0.19 (−0.72)	−0.03 (−0.08)	−0.30 (−1.54)
SFR	**0.47 (−3.29)**	**0.53 (−3.66)**	0.14 (−0.45)	0.39 (−2.35)	-0.17 (-0.56)	−0.30 (−1.41)	−0.15 (−0.53)	−0.16 (−0.60)
CO emission density contrast, $\mathcal{E}_{CO}$	−0.35 (−1.95)	**−0.59 (−4.58)**	−0.43 (−2.55)	−0.04 (−0.10)	-0.00 (-0.01)	0.11 (−0.35)	−0.16 (−0.61)	−0.19 (−0.74)
Hα emission density contrast, $\mathcal{E}_{H\alpha}$	0.10 (−0.30)	−0.36 (−1.78)	−0.36 (−1.84)	0.18 (−0.71)	-0.22 (-0.80)	0.08 (−0.25)	−0.22 (−0.89)	−0.11 (−0.38)
Observational systematic parameters								
Inclination, i	−0.26 (−1.17)	−0.26 (−1.01)	0.20 (−0.73)	**−0.57 (−4.90)**	0.40 (-2.14)	0.07 (−0.20)	0.35 (−1.93)	0.40 (−2.54)
Resolution, $l_{ap,\,min}$	0.04 (−0.11)	0.30 (−1.32)	**0.90 (−16.72)**	−0.06 (−0.19)	**0.54 (−3.67)**	−0.07 (−0.18)	0.28 (−1.37)	0.01 (−0.03)
Noise	0.13 (−0.42)	−0.16 (−0.48)	−0.32 (−1.35)	−0.03 (−0.08)	-0.16 (-0.48)	0.19 (−0.69)	**−0.48 (−3.07)**	0.13 (−0.44)
Completeness	0.36 (−1.87)	0.41 (−1.94)	0.10 (−0.27)	0.20 (−0.75)	-0.15 (-0.42)	−0.03 (−0.07)	0.21 (-0.80)	0.06 (−0.16)

a median of 37 per cent, for the galaxies in the PHANGS–MUSE sample. Using an un-sharp masking technique, Pan et al. (2022) have estimated 40−90 per cent for the H α diffuse emission fraction for the galaxies in our sample. Tomičić et al. (2021) also finds a similar range of values for the diffuse ionized gas fraction in 70 local cluster galaxies.

5 DISCUSSION

5.1 Relations with global galaxy and average cloud properties

We have correlated our measurements shown in Table 3 with global properties of galaxies and luminosity-weighted average properties of the cloud population in each galaxy. The properties considered are listed in Table 4. We use the galaxy properties listed in Table 1, as well as combinations of these quantities. We derive the total baryonic mass of the galaxy ($M_{tot,global} = M_{*,global} + M_{HI,global} + M_{H_2,global}$),

total gas mass ($M_{gas,global} = M_{HI,global} + M_{H_2,global}$), molecular gas fraction ($f_{H_2,global} = M_{H_2,global}/M_{gas,global}$), gas fraction ($f_{gas,global} = M_{gas,global}/M_{tot,global}$), and specific SFR (sSFR = $SFR_{global}/M_{*,global}$). We also look for correlations with gas phase metallicity [$12 + \log(O/H)$] for the subset of 23 galaxies for which direct measurements are available. These measurements are taken from Kreckel et al. (2019) for the 18 galaxies in our sample with MUSE observations and from Pilyugin et al. (2014) for five galaxies that do not overlap with the MUSE sample. We also include the 50 per cent correlation scale (L_{mix}) of the two-dimensional metallicity distribution maps (after metallicity gradient subtraction) of the PHANGS–MUSE sample from Kreckel et al. (2020) and Williams et al. (2022). This scale indicates the length over which the mixing in the ISM is effective, and ranges from 200 to 600 pc.

The luminosity-weighted averages of the cloud properties are determined from the GMC catalogues that have been established for the full PHANGS–ALMA sample using the CPROPS algorithm (Rosolowsky et al. 2021; Hughes et al. in preparation). Here,

we use measurements of the cloud velocity dispersion ($\sigma_{v, GMC}$), virial parameter $\alpha_{vir, GMC}$, mass (M_{GMC}), internal pressure (P_{int}), and molecular gas surface density ($\Sigma_{H_2, GMC}$).

Metrics related to galactic dynamics are included using measurements of the rotation curve (v_c) as a function of radius (r) from Lang et al. (2020). These metrics are the angular speed ($\Omega = v_c(r)/r$) and the Toomre stability parameter of the mid-plane molecular gas ($Q = \kappa \sigma_{H_2}/\pi G \Sigma_{H_2}$), where σ_{H_2} is the velocity dispersion measured from CO moment 2 maps, at native resolution, and $\kappa = \Omega\sqrt{2(1 + \beta)}$ with $\beta = \mathrm{d} \ln v_c(R)/\mathrm{d} \ln R$, numerically calculated. Since these values vary with galactocentric radius, we first divide the galaxy into five different radial bins and calculate Ω, Q, and σ_{H_2} for each bin. We then calculate the CO luminosity-weighted average of these values.

We explored possible correlations with galaxy global properties constrained within our method. These are different from the values listed in the Table 1 in that they are calculated within the analysed region, i.e. excluding galactic bulge and bar in most galaxies, and restricted to regions where CO observations have been made. Moreover, we provide two individual measurements for the molecular gas mass surface density and total molecular gas mass, where one takes only the compact emission into account (denoted as $\Sigma_{H_2}^{compact}$ and $M_{H_2}^{compact}$, which our measurements of the time-scales are based on) and the other includes all the emission (denoted as Σ_{H_2} and M_{H_2}). The quantities $\mathcal{E}_{CO}$ and $\mathcal{E}_{H\alpha}$ are the surface density contrast between the average emission of CO (respectively H α) peaks and the galactic average value, measured on the filtered map.

In order to explore possible systematic biases, we also include our minimum aperture size ($l_{ap, min}$ in Table 2, which matches our working resolution), inclination (i; column (g) in Table 1), completeness of CO observations, and noise of the CO data cube (in mK units) from Leroy et al. (2021b) as metrics. Finally, we note that none of the properties listed here are corrected for galaxy inclination.

5.1.1 Statistically (in)significant correlations

In Table 4, for all correlations, we list the Spearman rank correlation coefficients and the associated *p*-values, which represents the probability of a correlation appearing by chance. When evaluating the correlations, we exclude eight galaxies where the resolution at which the analysis can be run is larger than 200 pc, as we are likely to not sufficiently spatially separate star-forming regions in these galaxies (NGC 1546, NGC 1559, NGC 1672, NGC 1792, NGC 3511, NGC 4569, NGC 4654, NGC 7456). Whenever a measurement of individual galaxies is considered as an upper limit, we also exclude the galaxy from our correlation analysis of a given measurement (see Appendix A). There are 12 galaxies (IC1954, NGC 1087, NGC 1097, NGC 1385, NGC 1546, NGC 1672, NGC 2090, NGC 3627, NGC 4298, NGC 4540, NGC 4548, NGC 4569) with only upper limits of t_{fb} constrained. For eight of these (IC1954, NGC 1087, NGC 1385, NGC 1546, NGC 1672, NGC 4298, NGC 4540, NGC 4548) λ is also an upper limit. Finally, we include six nearby galaxies (IC342, the LMC, M31, M33, M51, NGC 300; previously analysed by Kruijssen et al. (2019b), Chevance et al. (2020b), and Kim et al. (2021a), which extend the range of environmental properties.

We define a correlation to be statistically significant when the measured *p*-value is lower than p_{eff}, where p_{eff} is derived using the Holm–Bonferroni method (for an explanation and for an astrophysical application also see Kruijssen et al. 2019a; Holm 1979). This method is used to account for the fact that spurious significant correlations may appear when comparisons between a large number of parameters are made. Specifically, we proceed by asking whether

each of our measurement (columns in Table 4) correlates with any of the galaxy and average cloud properties (rows in Table 4). We then rank the correlations by increasing *p*-value. For each correlation with a rank (i) of $i \geq 1$, we calculate the effective maximum *p*-value (p_{eff}) below which the correlation is deemed significant (i.e. with $p < p_{eff}$). We use the definition $p_{eff} = p_{ref}/(N_{corr} + 1 - i)$, with $p_{ref} = 0.05$ the desired confidence level and N_{corr} the number of independent variables being evaluated. In order to determine N_{corr}, we subtract variables among the galaxy and average cloud properties that are trivially correlated. We find that numerous properties ($M_{*, global}$, $M_{H I, global}$, $M_{H_2, global}$, SFR$_{global}$, $\triangle$ MS, $M_{tot, global}$, $M_{gas, global}$, M_{GMC}, P_{int}, $\Sigma_{H_2, GMC}$, M_{H_2}, $M_{H_2}^{compact}$, and SFR) are correlated significantly, with correlation coefficient higher than 0.7. We treat these parameters as one metric and this results in $N_{corr} \approx 20$. Table 4 shows statistically meaningful strong correlations in red, identified according to our definition. We note that even assuming that all the variables are independent does not significantly change our result as the *p*-values of strong correlations are all very small, with $\log(p)$ ranging from -16.7 to -2.8.

As shown in Table 4, we identify biases of our measured quantities caused by the spatial resolution of maps ($l_{ap, min}$) and inclination. Specifically, we find that (1) $l_{ap, min}$ shows a strong correlation with λ and v_{fb}; (2) the inclination shows a strong correlation with ϵ_{sf}; (3) the noise of the CO data cube correlates with $f_{diffuse}^{H\alpha}$; and (4) the metallicity correlates with $t_{dep}^{compact}$. The covariance between resolution and $v_{fb} = r_{CO}/t_{fb}$ is due to the increased measured cloud size (r_{CO}) as the resolution gets worse. The dependence of λ on $l_{ap, min}$ implies that the measured region separation length (λ) would be biased upward when using maps that have poor resolution. However, despite the dependencies on resolution of these quantities, we are confident that the measured time-scales are less sensitive to the spatial resolution of the maps, because we require star-forming regions to be sufficiently resolved for our time-scale measurements to be considered as robust ($\lambda > 1.5 l_{ap, min}$; see Section A and Kruijssen et al. 2018). Unlike λ, the measured time-scales indeed do not show strong correlations with $l_{ap, min}$. The dependence of $\epsilon_{sf} = t_{CO}/t_{dep}^{compact}$ on inclination is driven by a highly significant correlation between inclination and $t_{dep}^{compact}$ ($\log(p) = -2.5$; see Table 4). We suspect that this latter correlation arises, because the filtering of the diffuse CO emission is less effective for highly inclined galaxies, and because the extinction correction applied to SFR maps may depend on inclination, as suggested by Pellegrini et al. (2020). The dependence between the noise of the CO data cube and $f_{diffuse}^{H\alpha}$ seems to arise by a random chance, despite applying a strict threshold of *p*-values for correlations to be considered significant. Indeed, there is no logical link why these two quantities should show correlation and when the three galaxies with high noise level are excluded from the analysis, the strong correlation disappears. Finally, for the correlation between metallicity and $t_{dep}^{compact}$, we conjecture it could be related to the fact that the low-mass (low-metallicity) galaxies tend to have more diffuse emission due to their low surface brightness (Leroy et al. 2021b). The surface brightness sensitivity of the CO maps is not good enough to isolate the small clouds in low-mass (and low-metallicity) galaxies, which may therefore lead to more diffuse emission and low completeness for such galaxies (Leroy et al. 2021b). However, we note that completeness of the CO maps does not show a strong trend with $t_{dep}^{compact}$ (see Table 4). The adopted metallicity-dependent α_{CO} might also contribute to this observed trend between metallicity and $t_{dep}^{compact}$. While we partially correct for the presence of molecular gas that is not traced by CO emission (CO-dark gas) with this conversion factor, the observed strong correlation seems to indicate that the correction is insufficient. In closing, we again emphasize

Table 5. Summary of the 20 statistically significant and physically meaningful correlations identified in Table 4 between our measurements listed in Table 3 and galaxy and average cloud properties. For each correlation, the table lists the Spearman correlation coefficient (r), the associated p-value, the slope of the best-fitting linear regression dy/dx, the intercept of the best-fitting y_0, and the scatter around the best-fitting relation.

Quantity (y)	Units	Correlates with(x)	Units	Spearman r	log Spearman p	dy/dx	y_0	Scatter
$\log t_{\rm CO}$	Myr	$\log M_{\rm H_2, global}$	$M_\odot$	0.59	-5.33	0.16	-0.24	0.14
$\log t_{\rm CO}$	Myr	$\log M_{\rm H_2}$	$M_\odot$	0.54	-4.37	0.16	-0.22	0.14
$\log t_{\rm CO}$	Myr	$\log M_{\rm H_2}^{\rm compact}$	$M_\odot$	0.53	-4.25	0.17	-0.22	0.14
$\log t_{\rm CO}$	Myr	$\log f_{\rm H_2, global}$	–	0.50	-3.72	0.23	1.30	0.14
$\log t_{\rm CO}$	Myr	$\log M_{*, global}$	$M_\odot$	0.47	-3.33	0.16	-0.40	0.14
$\log t_{\rm CO}$	Myr	$\log$ SFR	$M_\odot$ yr^{-1}	0.47	-3.29	0.14	1.24	0.14
$\log t_{\rm CO}$	Myr	$\log M_{\rm tot, global}$	$M_\odot$	0.46	-3.16	0.17	-0.50	0.14
$\log t_{\rm CO}$	Myr	$\log \Sigma_{\rm H_2}$	$M_\odot$ pc^{-2}	0.44	-3.02	0.17	1.02	0.15
$\log t_{\rm CO}$	Myr	$\log \Sigma_{\rm H_2}^{\rm compact}$	$M_\odot$ pc^{-2}	0.43	-2.81	0.19	1.10	0.15
$\log t_{\rm fb}$	Myr	$\log \mathcal{E}_{\rm CO}$	–	-0.59	-4.58	-0.61	1.02	0.13
$\log t_{\rm fb}$	Myr	$\log M_{\rm H_2}^{\rm compact}$	$M_\odot$	0.55	-3.90	0.24	-1.56	0.15
$\log t_{\rm fb}$	Myr	$\log M_{\rm H_2}$	$M_\odot$	0.55	-3.85	0.23	-1.64	0.15
$\log t_{\rm fb}$	Myr	$\log$ SFR	$M_\odot$ yr^{-1}	0.53	-3.66	0.24	0.53	0.15
$\log t_{\rm fb}$	Myr	$\log f_{\rm H_2, global}$	–	0.50	-3.23	0.31	0.60	0.16
$\log t_{\rm fb}$	Myr	$\log M_{\rm H_2, global}$	$M_\odot$	0.49	-3.01	0.20	-1.33	0.16
$\log \lambda$	pc	$\log L_{\rm mix}$	pc	0.78	-3.05	0.84	0.18	0.08
$\log \epsilon_{\rm sf}$	–	$\log \Sigma_{\rm SFR}$	$M_\odot$ yr^{-1} pc^{-2}	0.43	-2.85	0.31	-1.79	0.19
$f_{\rm diffuse}^{\rm CO}$	–	$\log M_{\rm H\,I, global}$	$M_\odot$	-0.52	-3.83	-0.13	1.63	0.11
$f_{\rm diffuse}^{\rm CO}$	–	$\log M_{\rm tot, global}$	$M_\odot$	-0.49	-3.50	-0.13	1.67	0.11
$f_{\rm diffuse}^{\rm H\alpha}$	–	$\log \alpha_{\rm vir, GMC}$	–	0.47	-3.26	0.30	0.48	0.17

that our main measurements ($t_{\rm CO}$, $t_{\rm fb}$, and λ) are not affected by our prescription of $\alpha_{\rm CO}$, as they are based on relative changes of flux ratios (i.e. the global H α/CO ratio does not affect the time-scale estimate).

5.1.2 Physical interpretation of significant correlations

In Table 5, we list the best-fitting relations using linear regressions, as well as their Spearman correlation coefficients and p-values, for statistically significant correlations in red in Table 4, while correlations illustrating biases in our analysis (described in Section 5.1.1), are excluded. Fig. 6 shows examples of six main strong correlations between our measurements and global galaxy properties. In this figure, we do not show all of the statistically meaningful correlations listed in Table 5, as they seem to be redundant and driven by correlations within galaxy properties (especially mass related quantities), and also within time-scales ($t_{\rm CO}$ and $t_{\rm fb}$). For example, as described above, $M_{*, global}$ strongly correlate with $M_{\rm H_2, global}$, $M_{\rm H_2}$, $M_{\rm H_2}^{\rm compact}$, $M_{\rm tot, global}$, SFR, and $M_{\rm HI, global}$. By construction, $f_{\rm H_2, global}$ and $M_{\rm H_2, global}$ are not independent. Also, $\Sigma_{\rm H_2}$ and $\Sigma_{\rm H_2}^{\rm compact}$ correlate with each other. The correlation within time-scales is most likely due to the fact that our time-scale measurements are constrained by scaling the time-scale ratios with a reference time (see Section 3).

Here, we offer explanations for how the relations in Table 5 can be understood physically. However, we do not attempt to investigate which galaxy (or average GMC) properties are the main driver for these trends, because numerous properties also correlate with each other, making it hard to assess.

First of all, the cloud lifetime ($t_{\rm CO}$) is measured to be longer with increasing stellar mass ($M_{*, global}$), which traces galaxy mass. The cloud lifetime also shows positive correlations with the total molecular gas mass, both measured globally ($M_{\rm H_2, global}$) or only considering the analysed region, with and without diffuse emission ($M_{\rm H_2}$ and $M_{\rm H_2}^{\rm compact}$, respectively). Given that galaxy mass and metallicity are correlated (see Fig. 6; upper left), we suspect this can be due

to the fact that a higher gas density threshold is required to make CO visible in low-mass galaxies compared to high mass galaxies. As shown in Table 4, when only the galaxies with direct metallicity measurements are considered, a suggestive positive trend between $t_{\rm CO}$ and metallicity is revealed (Spearman correlation coefficient of 0.54), but this tentative trend is not strong enough to be characterized as statistically meaningful. CO molecules in low-metallicity environments with low dust-to-gas ratio are photodissociated deeper into the clouds (Bolatto, Wolfire & Leroy 2013). As clouds assemble from diffuse gas and become denser, clouds in a low-mass and low-metallicity environment spend a longer time in a CO-dark molecular gas phase (see also Clark et al. 2012). This is not included in the cloud lifetime we measure, because it is based on the visibility of CO emission, leading to an underestimation of the cloud lifetime. This is supported by the fact that, when H I emission is used to trace the gas, H I overdensities exist for a much longer duration prior to the formation of CO peaks (Ward et al. 2020). High-mass galaxies also have a higher mid-plane pressure, which shapes clouds within the galaxy to have a higher internal pressure (Sun et al. 2020a), resulting in higher (surface) densities and thus making them easier to detect throughout their lifecycles (Wolfire, Hollenbach & McKee 2010).

Observational biases may also contribute to the relation between cloud lifetime and galaxy mass, where the CO emission in low-mass galaxies is typically lower than the noise level of the PHANGS–ALMA data. In low-mass galaxies, we might simply lack sensitivity to the CO emission to pick up emission from low mass GMCs at any point of their lifetime, while they are detected in high mass galaxies. Schinnerer et al. (2019) and Pan et al. (2022) also find a higher fraction of CO-emitting sightlines in high-mass galaxies compared to low-mass galaxies and discuss that this trend is due to intrinsically low visibility of CO emission in low-mass galaxies. However, we expect this effect of sensitivity to be minor in our analysis, as our measurements are based on flux measurements and thus biased towards bright regions.
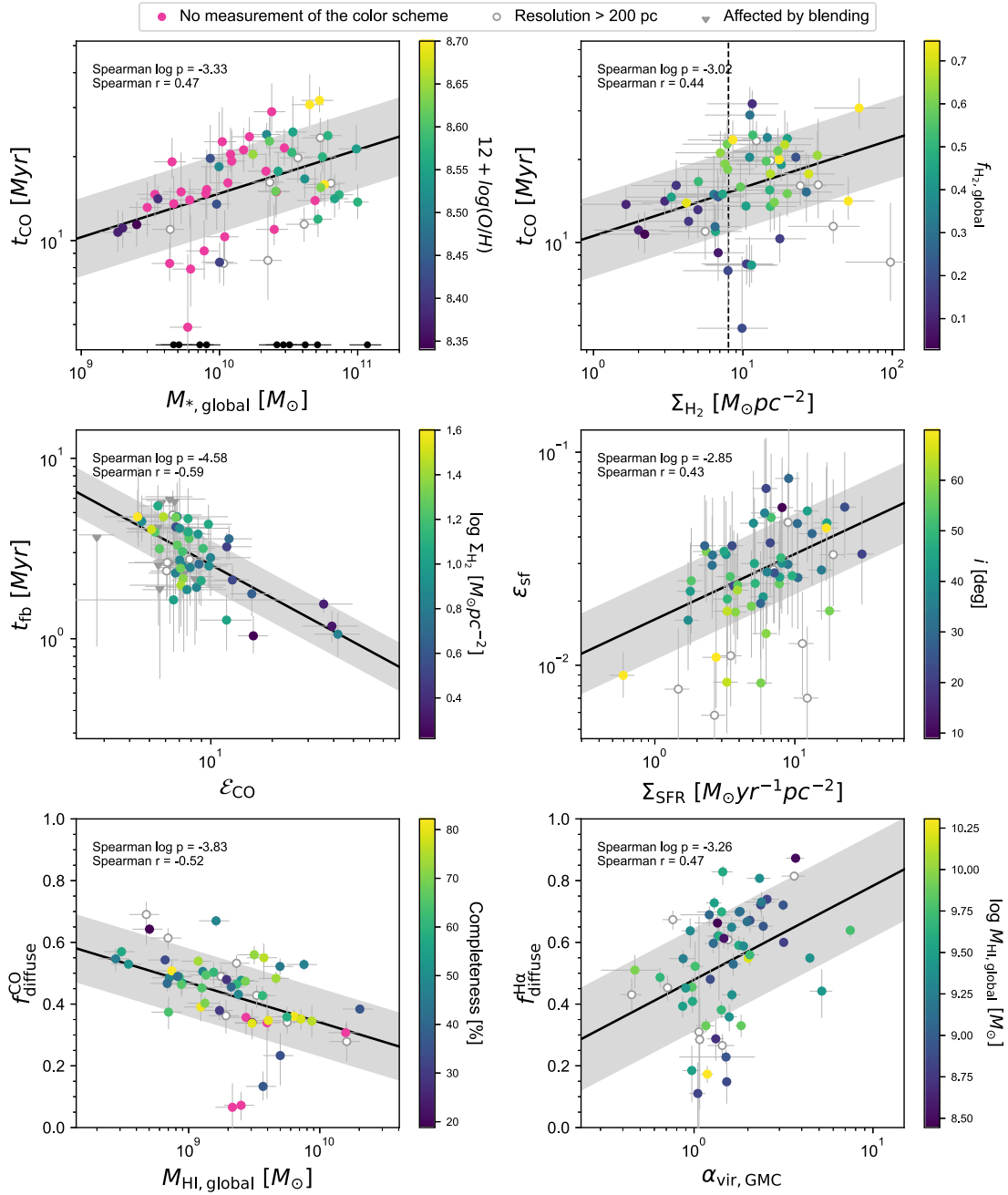
Figure 6. Examples of six statistically significant correlations between our measurements and galaxy or average GMC properties. In the upper panel, the measured cloud lifetime (t_{CO}) is shown as a function of stellar mass ($M_{*,\,global}$; left) and molecular gas surface density (Σ_{H_2}; right), where points are colour coded by metallicity ($12 + \log(O/H)$) and molecular gas fraction ($f_{H_2,global}$), respectively. The critical density identified by Chevance et al. (2020b) is also shown for comparison (dashed line). In the middle left-hand panel, the measured feedback time-scale (t_{fb}) is shown as a function of the surface density contrast between CO emission peaks and the galactic average ($\mathcal{E}_{CO}$), colour coded by the molecular gas surface density (Σ_{H_2}). The middle right-hand panel shows the integrated star formation efficiency (ϵ_{sf}) as a function of SFR surface density (Σ_{SFR}), where the points are colour coded by inclination (i). The lower left-hand panel shows the diffuse CO emission fraction ($f_{diffuse}^{CO}$) as a function of the global atomic gas mass ($M_{HI,global}$), where the points are colour coded by completeness of the CO observation (Leroy et al. 2021b). In the lower right-hand panel, the diffuse H α emission fraction ($f_{diffuse}^{H\alpha}$) is shown as a function of average virial parameter of GMCs ($\alpha_{vir,GMC}$), colour coded by the global atomic gas mass ($M_{HI,global}$). Galaxies without measurements corresponding to each colour bar scheme are denoted in magenta. Grey circles are the galaxies with resolution worse than 200 pc. Grey triangles indicate upper limits for galaxies suffering from blending of sources (see Section A). These grey points are excluded in our correlation analysis. For individual data points, 1σ uncertainties are shown. In each panel, the best-fitting linear regression (solid line), 1σ scatter of the data around the fit (shaded area), and the Spearman p-values and correlation coefficients are indicated. We also show the distribution of $M_{*,\,global}$ for the 10 galaxies excluded from our sample due to their limited number of emission peaks (black circles; see Section 2 and Section A).

Other strong correlations with the cloud lifetime and properties related to the stellar mass and/or molecular gas mass of the galaxy (SFR and $M_{\rm tot,\,global}$) are likely to be driven by the correlations explained above. Several studies have also reported such connections between global properties of the galaxy and the ensemble average properties of clouds (Hughes et al. 2013; Colombo et al. 2014; Hirota et al. 2018; Sun et al. 2018, 2020b, a; Schruba et al. 2019). In the upper left-hand panel of Fig. 6, we also include the distribution of $M_{*,\,global}$ for ten galaxies that are excluded from our sample due their small number of emission peaks (see Section 2 and Section A). They are randomly distributed in $M_{*,\,global}$, indicating that selectively including CO-bright galaxies does not bias this result.

The cloud lifetime also positively correlates with the molecular gas fraction ($f_{\rm H_2,global}$), as well as with molecular gas surface densities measured with and without diffuse emission ($\Sigma_{\rm H_2}$ and $\Sigma_{\rm H_2}^{\rm compact}$, respectively). The relation with molecular gas surface density might seem to contradict theoretical expectations (e.g. Kim et al. 2018), because denser clouds are expected to collapse faster, form stars and disperse more quickly than lower-density clouds. As proposed by Chevance et al. (2020b), the observed strong correlation might be related to the transition from an atomic gas-dominated to a molecular gas-dominated environment, as shown by the coloured points in the upper right-hand panel of Fig. 6. Chevance et al. (2020b) have found that at a critical density threshold of 8 $\rm M_\odot\,pc^{-2}$ (similar to the gas phase transition threshold), the cloud lifetime shows a better agreement with the galactic dynamical time-scale above this threshold and with the internal dynamical time-scale. This value is similar to the molecular gas surface density at which the gas phase transition occurs $\sim 10\,\rm M_\odot pc^{-2}$, at near solar-metallicity (e.g. Wong & Blitz 2002; Bigiel et al. 2008; Leroy et al. 2008; Schruba et al. 2011). In the upper right-hand panel of Fig. 6, this transition density is shown as a dashed line for comparison. In an atomic gas-dominated environment ($f_{\rm H_2} < 0.5$), CO is only emitted by the central region of the clouds, tracing the densest regions. However, in a molecular gas-dominated environment ($f_{\rm H_2} > 0.5$), we detect more CO emission coming from an extended envelope of the molecular clouds (e.g. Shetty, Clark & Klessen 2014). This may increase the measured cloud lifetimes, as the assembly phase of the envelope is additionally taken into account, compared to when only the densest phase is included. In addition, in a low-surface density environment, the clouds will spend a longer time in the CO-dark phase, as a higher density threshold is required to make CO visible, resulting in a measured cloud lifetime shorter than the actual molecular cloud assembly time (Bolatto et al. 2013). Similarly to the dependence on galaxy mass discussed above, observational biases due to CO sensitivity level also play a role, making us miss a higher fraction of low-mass clouds in atomic gas-dominated environments.

For the feedback time-scale, during which CO and Hα overlap, we find the strongest correlation with $\mathcal{E}_{\rm CO}$, which is the surface density contrast in the CO map between the emission peaks and the galactic average. The feedback time-scale becomes shorter with increasing $\mathcal{E}_{\rm CO}$. In the middle left-hand panel of Fig. 6, points are colour coded by $\Sigma_{\rm H_2}$ and suggest that when $\mathcal{E}_{\rm CO}$ is higher (i.e. sharper CO emission peaks), feedback-driven dispersal of the clouds makes the CO emission become undetected faster. This can be understood physically as the CO emission will become invisible faster after the onset of star formation when the surrounding medium is sparse, indicated by the low molecular gas surface density, allowing a faster dispersal of molecular clouds.

Similarly to the dependencies we have identified for $t_{\rm CO}$, we find that $t_{\rm fb}$ also correlates with $M_{\rm H_2}^{\rm compact}$, $M_{\rm H_2}$, $M_{\rm H_2,global}$, SFR, and $f_{\rm H_2,global}$. We suspect these correlations arise at least partially because $t_{\rm fb}$ and $t_{\rm CO}$ strongly correlate with each other (with a Spearman correlation coefficient of 0.72). Interestingly, unlike $t_{\rm CO}$, we find a less significant correlation with stellar mass, which does not satisfy our significance cut with $p = 0.03$. This can be explained by the fact that the feedback time captures the phase when clouds are star forming, implying that the density is high enough, which typically corresponds to a CO-bright phase. Therefore, we miss less of the CO-dark phase that is proportionally more important in the low-mass galaxies.

The mean separation length between independent regions (λ), which is linked to the scale at which molecular gas and young stars start to become spatially decorrelated, shows a strong positive correlation with the mixing scale traced by metallicity measurements of H II regions in PHANGS–MUSE galaxies from Kreckel et al. (2020) and Williams et al. (2022). This trend indicates that for galaxies with broader and more efficient mixing in the ISM, molecular gas and young stars are separated by a larger distance. This might be physically understood, because a broader mixing length, most likely driven by stellar feedback, will push the gas further away from its original position. This would imply that the dispersal of the molecular cloud after star formation is kinetically driven, rather than by the photodissociation of the CO molecules. However, we note that this correlation could be at least partially driven by the resolution as it becomes weaker (with Spearman correlation coefficient from 0.78 to 0.66 with $p = 0.02$) when the two galaxies with the highest resolution (NGC 0628 and NGC 5068) are excluded.

We find a strong correlation between our measurements of integrated star formation efficiency ($\epsilon_{\rm sf}$) and SFR surface density ($\Sigma_{\rm SFR}$), as shown in the middle right-hand panel of Fig. 6. This correlation might seem like it can be simply understood as that a higher integrated star formation efficiency per star formation event, at least, partially would be driven by a higher SFR. However, we cannot rule out the possibility that this relation arises due a strong correlation between $t_{\rm CO}$ and $\Sigma_{\rm H_2}^{\rm compact}$ explained above, making $\epsilon_{\rm sf}$ to be mostly dependent on $\Sigma_{\rm SFR}$ by construction (see equation 2). Moreover, potentially not enough extinction correction for highly inclined galaxies, shown as coloured points in Fig. 6, can also contribute to this trend.

For the diffuse CO emission fraction ($f_{\rm diffuse}^{\rm CO}$), which is measured within our method during the diffuse emission filtering process of Hygate et al. (2019), we find the strongest anticorrelation with the H I mass ($M_{\rm H\,I,\,global}$). Another correlation with $M_{\rm tot,\,gas}$ is driven by this strong correlation with $M_{\rm H\,I,\,global}$. We find that as $M_{\rm H\,I,\,global}$ decreases, the diffuse molecular component becomes more important. We conjecture that this can be due to an observational bias, as the completeness of the CO maps (indicated as coloured data points in Fig. 6) is low for low-mass galaxies due to our limited sensitivity, suggesting that we are missing a larger fraction of small, faint clouds in such galaxies. However, contrary to our expectation, $f_{\rm diffuse}^{\rm CO}$ and completeness of CO emission maps from Leroy et al. (2021b) do not reveal a strong trend with each other (see Table 4).

Lastly, the diffuse Hα emission fraction ($f_{\rm diffuse}^{\rm H\alpha}$) shows a strong correlation with the average virial parameter of GMCs ($\alpha_{\rm vir,\,GMC}$). We suspect this can be due to a more pervasive medium of GMCs (higher $\alpha_{\rm vir,\,GMC}$) allowing more ionizing photons to leak out from star-forming regions, compared to more bound clouds. Furthermore, as indicated by the coloured points in Fig. 6, galaxies with higher $f_{\rm diffuse}^{\rm H\alpha}$ tend to have lower atomic gas mass ($M_{\rm H\,I,\,global}$), which is in line with observations showing deeper penetration of ionizing photons into the surrounding ISM in lower mass (and lower metallicity) galaxies (Cormier et al. 2015; Chevance et al. 2016).
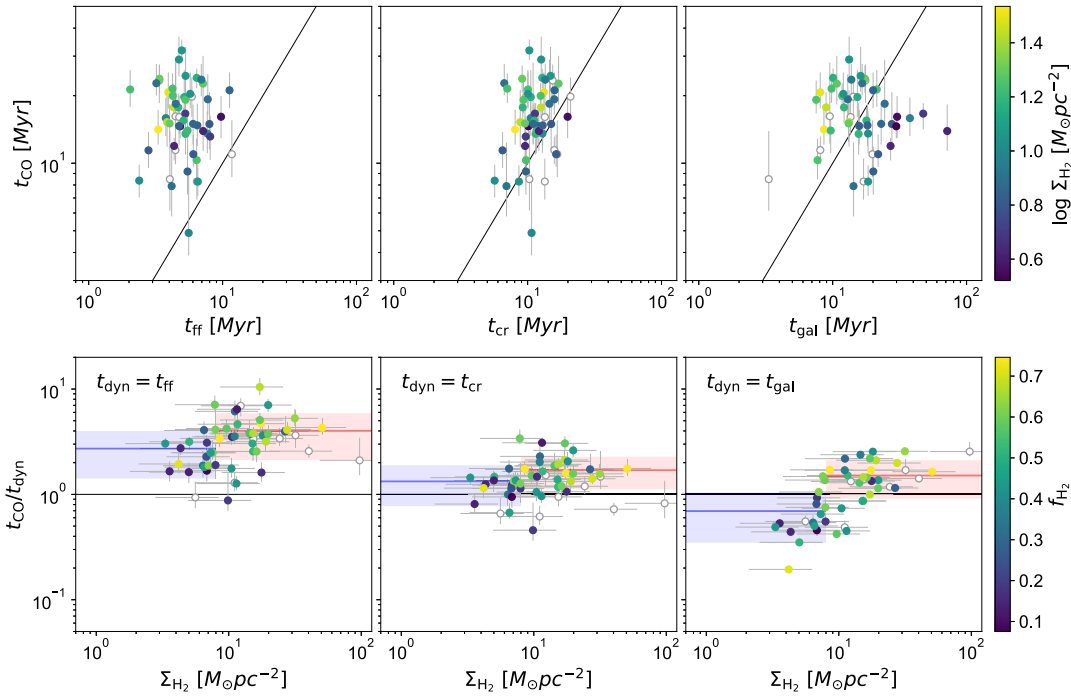
Figure 7. Comparison of our measured cloud lifetime (t_{CO}) with analytical predictions, which are, from left to right, the free-fall time (t_{ff}), the crossing time of GMCs (t_{cr}), and the galactic time-scale, considering the effect of large-scale dynamics (t_{gal}). In the upper panels, the one-to-one relation is shown as a solid line and the data points are colour coded by surface molecular gas density (Σ_{H_2}). The lower panels show the ratios of t_{CO} and analytical predictions (t_{dyn}), where t_{dyn} is the free fall time (left), the crossing time (middle) or the galactic dynamical time-scale (right), as a function of Σ_{H_2}, where the points are colour coded by molecular gas fraction (f_{H_2}). In all panels, galaxies where our analysis can only be run at resolution larger than 200 pc are shown as grey circles. The black horizontal line shows where $t_{CO} = t_{dyn}$. The blue and red lines, respectively, indicate the mean of the time-scale ratios for galaxies below and above Σ_{H_2} of $8 M_{\odot}$ pc^{-2} (from Chevance et al. 2020b) with the shaded regions representing the 16th–84th percentile. This density threshold is from Chevance et al. (2020b), below which t_{CO} shows better agreement with internal dynamical times (t_{ff} and t_{cr}) compared to the t_{gal}, and the other way around at densities higher than this threshold.

5.2 Comparison with characteristic time-scales

In order to understand the dynamical mechanisms that govern cloud lifetimes, we compare our measurements of t_{CO} with analytical predictions, which are related to local cloud dynamics (GMC free-fall time and GMC crossing time; t_{ff} and t_{cr}, respectively), or large-scale dynamics of the ISM (t_{gal}; Jeffreson & Kruijssen 2018). We adopt the CO-luminosity-weighted harmonic average of t_{ff} from the cloud catalogue established for the PHANGS–ALMA galaxies by Hughes (in preparation), which uses the CPROPS algorithm (Rosolowsky et al. 2021) to determine the physical properties of GMCs. Here, t_{cr} is defined as r_{GMC}/σ_{vel}, where r_{GMC} is the radius of GMC and σ_{vel} is the cloud velocity dispersion (σ_{vel}). We first obtain t_{cr} for each GMC in a given galaxy and calculate CO-luminosity-weighted harmonic average of t_{cr}. For t_{gal}, we use the analytic theory presented in Jeffreson & Kruijssen (2018). This theory assumes that cloud lifetimes are environmentally dependent and can be estimated by combining the time-scales of numerous processes governing the cloud evolution: the gravitational collapse of the mid-plane ISM (τ_{ff}), galactic shear (τ_{β}), spiral arm interactions (τ_{Ω_P}), epicyclic perturbations (τ_{κ}), and cloud–cloud collisions (τ_{cc}). As the galactic shear (τ_{β}) is a dynamically dispersive process unlike the other four mechanisms compressing the clouds, the cloud lifetime is expressed as $t_{gal}^{-1} = |\tau_{ff} + \tau_{\Omega_P} + \tau_{\kappa} + \tau_{cc} - \tau_{\beta}|$. We determine these time-scales in five different radial bins for each galaxy (see also Section 5.1), using equations from Jeffreson & Kruijssen (2018), the radial profiles

of velocity dispersion from CO moment 2 maps, and the rotational curves measured by Lang et al. (2020). We then calculate harmonic averages of t_{gal} obtained in five radial bins. Five galaxies, for which the rotation curve is not available, are omitted from this comparison.

In the upper panel of Fig. 7, we show our measurements of t_{CO} as functions of the analytically predicted time-scales. In the lower panel, the ratios of t_{CO} over these predicted time-scales are shown as a function of Σ_{H_2}. For comparison, we also calculate the mean and 1σ range of these ratios only considering galaxies with molecular gas surface density below and above the atomic-to-molecular transition density described in the previous subsection ($8 M_{\odot}$ pc^{-2}; Chevance et al. 2020b). We find that on average, $t_{CO} = (2.7 \pm 1.3) t_{ff}$ and $t_{CO} = (4.0 \pm 1.9) t_{ff}$, respectively, below and above the transition density with error bars representing 16–84 per cent range. Measured cloud lifetimes t_{CO} are almost always longer than t_{ff}, independently of the molecular gas surface density. The crossing time t_{cr} shows a better agreement with t_{CO} compared to t_{ff}, especially in low molecular gas surface density environments ($\Sigma_{H_2} \leq 8 M_{\odot}$ pc^{-2}), with an average of $t_{CO} = (1.3 \pm 0.6) t_{cr}$. At higher densities, t_{CO} increasingly deviates from t_{cr}, with an average of $t_{CO} = (1.7 \pm 0.6) t_{cr}$.

Finally, the right-hand panels of Fig. 7 show that, in low molecular gas surface density environments, our measurements of t_{CO} are significantly lower than t_{gal}, with an average of $t_{CO} = (0.7 \pm 0.3) t_{gal}$. By contrast, in higher-density ($\geq 8 M_{\odot}$ pc^{-2}; molecular gas dominated) environments, where the majority of the molecular gas has high CO emissivity, t_{CO} becomes even longer than t_{gal} for most of the

galaxies, with an average of $t_{\rm CO} = (1.5 \pm 0.6)\,t_{\rm gal}$. This difference in two density regimes can be explained by the fact that $t_{\rm gal}$ takes into account all the cold gas, including the phase that is not strongly CO-emitting, while our measurements of $t_{\rm CO}$ are based on CO-bright clouds. Therefore, $t_{\rm gal}$ is typically longer than $t_{\rm CO}$, especially in low molecular gas surface density environments. Moreover, this indicates that in low-surface density environments (atomic gas-dominated), the assembly of CO-bright molecular clouds seems to be less coupled to galactic dynamics, but rather occurs on internal cloud-dynamical time-scales such as the crossing time. Following the analytic theory by Jeffreson & Kruijssen (2018), we can also quantify which galactic-dynamical mechanisms are relevant for setting the analytical cloud lifetime. The relevance is deemed significant when the time-scales of a given dynamical process is smaller than $2 \times \tau_{\rm min}$, where $\tau_{\rm min}$ is the smallest time-scale among the five processes. The minimum time-scale has the greatest influence on setting the $t_{\rm gal}$, and is $\tau_{\rm ff}$ in most cases whereas shear is also found to be relevant in some environments with $\tau_\beta = (3.7 \pm 2.3)\,\tau_{\rm min}$, on average. This shows that the predicted lifetime of these molecular clouds results from a competition between the gravitational collapse of the mid-plane ISM and galactic shear, which causes clouds to be pulled apart by differential rotation. At high density where $t_{\rm CO}$ shows a good agreement with $t_{\rm gal}$, this implies that the assembly of molecular clouds and their evolution may be significantly influenced by galactic dynamics. Meidt et al. (2015) have reached a similar conclusion using GMCs in M51, where GMC evolution appears to be regulated by shear.

6 CONCLUSION

We present a systematic determination of evolutionary sequences of GMCs from the molecular gas phase to exposed young stellar regions across an unprecedented sample of 54 molecular gas-rich main sequence galaxies from the PHANGS–ALMA survey (Leroy et al. 2021b). We have applied the statistical method developed by Kruijssen & Longmore (2014) and Kruijssen et al. (2018) to CO and Hα emission maps at cloud-scale resolution ($\sim$100 pc) and measured the cloud lifetime ($t_{\rm CO}$), the feedback time-scale (duration for which CO and Hα are spatially overlapping; $t_{\rm fb}$), as well as the average separation length between independent star-forming regions evolving from molecular clouds to exposed young stellar regions (λ). We also derive other physical quantities such as the feedback velocity ($v_{\rm fb}$), the integrated star formation efficiency ($\epsilon_{\rm sf}$), and the diffuse emission fraction for both CO and Hα maps ($f_{\rm diffuse}^{\rm CO}$ and $f_{\rm diffuse}^{\rm H\alpha}$). By capitalizing on a statistically representative sample of galaxies from PHANGS, we have correlated our measurements with global galaxy and average cloud properties. This allows us to quantitatively link galactic-scale environmental properties to the small-scale evolutionary cycle of molecular clouds, star formation and feedback. The metrics explored here include properties related to galaxy mass, surface density of molecular gas and SFR, morphology, metallicity, velocity dispersion, pressure, and galactic dynamics. Our main conclusions are as follows:

(i) Across our sample of galaxies, we find that molecular clouds assemble and survive for a time-scale of 16.4 ± 5.5 Myr on average, demonstrating that GMCs are transient objects that disperse after a few dynamical times via feedback from young massive stars. The feedback time-scale is 3.2 ± 1.1 Myr on average (excluding galaxies for which only an upper limit could be constrained) and constitutes 10–30 per cent of the cloud lifetime. Our measurements of these time-scales are in good agreement with those obtained using other methods (cloud classification based on their stellar content, e.g.

Kawamura et al. 2009; Corbelli et al. 2017; determination of gas-free stellar cluster ages, e.g. Grasha et al. 2019). Our results further confirm the conclusion of previous works that there is a decorrelation between gas and young stars on the cloud scale (Schruba et al. 2010; Kreckel et al. 2018; Schinnerer et al. 2019; Pan et al. 2022), which can be explained by assuming that galaxies are composed of regions, undergoing evolution from gas to stars, that are separated by $100-400$ pc on average.

(ii) We find that the star formation in these regions is inefficient, with an integrated cloud-scale star formation efficiency ($\epsilon_{\rm sf}$) ranging from 0.8 to 7.5 per cent. We measure feedback velocities ($v_{\rm fb}$) of 10–30 km s^{-1}. Overall, these results are consistent with those from our previous measurements, conducted on a significantly smaller number of galaxies (Kruijssen et al. 2019b; Chevance et al. 2020b; Kim et al. 2021a; Chevance et al. 2022). We also determine the fraction of diffuse emission in each CO and Hα map based on its morphology. We find average fractions of 45 ± 10 per cent in CO and 53 ± 19 per cent in Hα.

(iii) We find several statistically significant correlations between our measurements and global galaxy (or average cloud) properties (Table 5). In brief, $t_{\rm CO}$ shows positive correlations with quantities related to galaxy mass, as well as with the molecular gas surface density. These correlations can be explained by the existence of a CO-dark phase, during which the molecular clouds are beginning to assemble. Indeed, we miss more of this phase at low-mass (low-metallicity) and less dense environments as these environments require higher gas column density in order to shield CO molecules from being dissociated, compared to high-mass and high-density environment. Moreover, in high-surface density environments, we also capture the extended region of the GMCs, unlike in low-surface density (atomic gas-dominated) environments where CO is only tracing the densest centres of the GMCs. This results in longer cloud lifetimes in galaxies with a higher molecular gas surface density.

(iv) The feedback time-scale $t_{\rm fb}$ also shows correlations with quantities related to galaxy mass, most likely because $t_{\rm CO}$ and $t_{\rm fb}$ are correlated. However, $t_{\rm fb}$ does show an interesting relation with $\mathcal{E}_{\rm CO}$, which is the surface density contrast measured on a CO map between emission peaks and the galactic average. We find that $t_{\rm fb}$ is shorter with increasing $\mathcal{E}_{\rm CO}$ (i.e. towards sharper emission peaks). This can be physically understood as the result of feedback, where CO emission becomes undetected faster after the onset of massive star formation when the surrounding medium is more sparse.

(v) The star formation efficiency $\epsilon_{\rm sf}$ shows a strong correlation with $\Sigma_{\rm SFR}$, which can at least partly be understood as a higher SFR leading to a higher integrated star formation efficiency per star formation event. However, other factors can also contribute to this trend such as, the tight correlation between $t_{\rm CO}$ and $\Sigma_{\rm H_2}$, as well as the dependence of extinction correction on inclination.

(vi) We find a strong negative correlation with the diffuse gas fraction ($f_{\rm diffuse}^{\rm CO}$) and the global atomic gas mass ($M_{\rm H\,I, global}$). We attribute this correlation to the low completeness of CO observations in low-mass galaxies.

(vii) Diffuse Hα emission fraction strongly correlates with average virial parameter of GMCs ($\alpha_{\rm vir, GMC}$), which seems to indicate that a more pervasive medium of less bound GMCs allows more ionizing photons to escape the star-forming region and to penetrate deeper into the surrounding gas.

(viii) We find that, at all the density regimes probed here, $t_{\rm CO}$ is longer than $t_{\rm ff}$ (from Rosolowsky et al. 2021; Hughes et al. in preparation) by a factor of 3.5 ± 1.8. By contrast, we find a good agreement with crossing time (from Rosolowsky et al. 2021; Hughes

et al. in preparation) with $t_{CO} = (1.5 \pm 0.6)\,t_{cr}$. The agreement becomes better when only the galaxies with low molecular gas surface density ($\Sigma_{H_2} < 8M_\odot\,pc^{-2}$) are considered, with $t_{CO} = (1.3 \pm 0.6)\,t_{cr}$. At higher surface densities, the agreement becomes slightly worse with $t_{CO} = (1.7 \pm 0.6)\,t_{cr}$. Lastly, in the low-density regime ($< 8\,M_\odot\,pc^{-2}$), t_{CO} is shorter than the time-scale expected for galactic-dynamical processes to act, with $(0.7 \pm 0.3)\,t_{gal}$, implying that t_{gal} overpredicts the cloud lifetime traced by CO emission. However, in higher surface density environments, $t_{CO} = (1.5 \pm 0.6)\,t_{gal}$, t_{CO} even becomes longer than t_{gal}. The difference in low-surface density environments is likely due to the fact that GMCs spend a large fraction of their lifetime being CO-dark, and this phase is by construction excluded from t_{CO}, which measures the CO visibility lifetime. By contrast, the Jeffreson & Kruijssen (2018) model does not make any distinction regarding on the CO emissivity of the different gas phases, and t_{gal} includes both the CO-dark and CO-bright phases. This results in an increase of t_{CO}/t_{gal} with the molecular gas surface density (also see Chevance et al. 2020b).

We have quantified the evolutionary lifecycle of GMC formation, evolution, and dispersal across an unprecedented sample of 54 nearby disc galaxies. We have demonstrated that this lifecycle depends on the large-scale galactic environment. In this work, we have determined the evolution from cold gas to exposed young stellar regions using CO and Hα maps. In the future, we plan to further extend and refine this evolutionary timeline, for a subset of our galaxy sample, by including other observations at different wavelengths: ionized emission lines from MUSE, mid-infrared from the *James Webb Space Telescope*, and H I from the VLA and Meerkat. This will allow us to determine the time-scales of all the successive phases of the gas that participate in star formation.

DATA AVAILABILITY

The data underlying this article will be shared on reasonable request to the corresponding author.

REFERENCES

Anand G. S. et al., 2021, MNRAS, 501, 3621
Barnes A. T., Longmore S. N., Dale J. E., Krumholz M. R., Kruijssen J. M. D., Bigiel F., 2020, MNRAS, 498, 4906
Barnes A. T. et al., 2021, MNRAS, 508, 5362
Barnes A. T. et al., 2022, A&A, 662, L6
Belfiore F. et al., 2022, A&A, 659, A26
Benincasa S. M. et al., 2020, MNRAS, 497, 3993
Bigiel F., Leroy A., Walter F., Brinks E., de Blok W. J. G., Madore B., Thornley M. D., 2008, AJ, 136, 2846
Blitz L., Fukui Y., Kawamura A., Leroy A., Mizuno N., Rosolowsky E., 2007, in Reipurth B., Jewitt D., Keil K., eds, Protostars and Planets V. Univ. Arizona Press, Tucson, AZ, p. 81
Bolatto A. D., Wolfire M., Leroy A. K., 2013, ARA&A, 51, 207
Chevance M. et al., 2016, A&A, 590, A36
Chevance M. et al., 2020a, Space Sci. Rev., 216, 50
Chevance M. et al., 2020b, MNRAS, 493, 2872
Chevance M. et al., 2022, MNRAS, 509, 272
Clark P. C., Glover S. C. O., Klessen R. S., Bonnell I. A., 2012, MNRAS, 424, 2599
Colombo D. et al., 2014, ApJ, 784, 4
Corbelli E. et al., 2017, A&A, 601, A146
Cormier D. et al., 2015, A&A, 578, A53
Da Silva R. L., Fumagalli M., Krumholz M., 2012, ApJ, 745, 145

3026   *J. Kim et al.*

Da Silva R. L., Fumagalli M., Krumholz M. R., 2014, MNRAS, 444, 3275
Den Brok J. S. et al., 2021, MNRAS, 504, 3221
Dobbs C. L., Pringle J. E., 2013, MNRAS, 432, 653
Dobbs C. L., Pringle J. E., Duarte-Cabral A., 2015, MNRAS, 446, 3608
Elmegreen B. G., 2000, ApJ, 530, 277
Emsellem E. et al., 2022, A&A, 659, A191
Engargiola G., Plambeck R. L., Rosolowsky E., Blitz L., 2003, ApJS, 149, 343
Fitzpatrick E. L., 1999, PASP, 111, 63
Fukui Y. et al., 2008, ApJS, 178, 56
Grasha K. et al., 2018, MNRAS, 481, 1016
Grasha K. et al., 2019, MNRAS, 483, 4707
Grudić M. Y., Kruijssen J. M. D., Faucher-Giguère C.-A., Hopkins P. F., Ma X., Quataert E., Boylan-Kolchin M., 2021, MNRAS, 506, 3239
Haffner L. M. et al., 2009, Rev. Mod. Phys., 81, 969
Hartmann L., 2001, AJ, 121, 1030
Hartmann L., Ballesteros-Paredes J., Heitsch F., 2012, MNRAS, 420, 1457
Haydon D. T., Fujimoto Y., Chevance M., Kruijssen J. M. D., Krumholz M. R., Longmore S. N., 2020a, MNRAS, 497, 5076
Haydon D. T., Kruijssen J. M. D., Chevance M., Hygate A. P. S., Krumholz M. R., Schruba A., Longmore S. N., 2020b, MNRAS, 498, 235
Herrera C. N. et al., 2020, A&A, 634, A121
Heyer M., Dame T. M., 2015, ARA&A, 53, 583
Hirota A. et al., 2018, PASJ, 70, 73
Hollyhead K., Bastian N., Adamo A., Silva-Villa E., Dale J., Ryon J. E., Gazak Z., 2015, MNRAS, 449, 1106
Holm S., 1979, Scand. J. Stat., 6, 65
Hughes A. et al., 2013, ApJ, 779, 46
Hygate A. P. S., 2020, PhD thesis, Ruperto-Carola-University of Heidelberg
Hygate A. P. S., Kruijssen J. M. D., Chevance M., Schruba A., Haydon D. T., Longmore S. N., 2019, MNRAS, 488, 2800
Jeffreson S. M. R., Kruijssen J. M. D., 2018, MNRAS, 476, 3688
Jeffreson S. M. R., Kruijssen J. M. D., Keller B. W., Chevance M., Glover S. C. O., 2020, MNRAS, 498, 385
Jeffreson S. M. R., Keller B. W., Winter A. J., Chevance M., Kruijssen J. M. D., Krumholz M. R., Fujimoto Y., 2021, MNRAS, 505, 1678
Kawamura A. et al., 2009, ApJS, 184, 1
Kennicutt Robert C. J., 1998, ApJ, 498, 541
Kennicutt Robert C. J. et al., 2003, PASP, 115, 928
Kim J.-G., Kim W.-T., Ostriker E. C., 2018, ApJ, 859, 68
Kim J. et al., 2021a, MNRAS, 504, 487
Kim J.-G., Ostriker E. C., Filippova N., 2021b, ApJ, 911, 128
Kreckel K., Blanc G. A., Schinnerer E., Groves B., Adamo A., Hughes A., Meidt S., 2016, ApJ, 827, 103
Kreckel K. et al., 2018, ApJ, 863, L21
Kreckel K. et al., 2019, ApJ, 887, 80
Kreckel K. et al., 2020, MNRAS, 499, 193
Kruijssen J. M. D., Longmore S. N., 2014, MNRAS, 439, 3239
Kruijssen J. M. D., Schruba A., Hygate A. P. S., Hu C.-Y., Haydon D. T., Longmore S. N., 2018, MNRAS, 479, 1866
Kruijssen J. M. D., Pfeffer J. L., Crain R. A., Bastian N., 2019a, MNRAS, 486, 3134
Kruijssen J. M. D. et al., 2019b, Nature, 569, 519
Krumholz M. R., 2014, Phys. Rep., 539, 49
Krumholz M. R., Fumagalli M., da Silva R. L., Rendahl T., Parra J., 2015, MNRAS, 452, 1447
Lancaster L., Ostriker E. C., Kim J.-G., Kim C.-G., 2021, ApJ, 922, L3
Lang P. et al., 2020, ApJ, 897, 122
Lee J. C. et al., 2022, ApJS, 258, 10
Leitherer C. et al., 1999, ApJS, 123, 3
Leroy A. K., Walter F., Brinks E., Bigiel F., de Blok W. J. G., Madore B., Thornley M. D., 2008, AJ, 136, 2782
Leroy A. K. et al., 2013, AJ, 146, 19
Leroy A. K. et al., 2019, ApJS, 244, 24
Leroy A. K. et al., 2021a, ApJS, 255, 19
Leroy A. K. et al., 2021b, ApJS, 257, 43
Leroy A. K. et al., 2022, ApJ, 927, 149
McLeod A. F., Dale J. E., Evans C. J., Ginsburg A., Kruijssen J. M. D., Pellegrini E. W., Ramsay S. K., Testi L., 2019, MNRAS, 486, 5263
McLeod A. F. et al., 2020, ApJ, 891, 25
Meidt S. E. et al., 2013, ApJ, 779, 45
Meidt S. E. et al., 2015, ApJ, 806, 72
Meidt S. E. et al., 2018, ApJ, 854, 100
Meidt S. E. et al., 2020, ApJ, 892, 73
Miura R. E. et al., 2012, ApJ, 761, 37
Murray N., Chang P., 2015, ApJ, 804, 44
Murray N., Rahman M., 2010, ApJ, 709, 424
Nazé Y., Chu Y.-H., Points S. D., Danforth C. W., Rosado M., Chen C. H. R., 2001, AJ, 122, 921
Onodera S. et al., 2010, ApJ, 722, L127
Pan H.-A. et al., 2022, ApJ, 927, 9
Patra N. N., 2020, A&A, 638, A66
Pellegrini E. W., Reissl S., Rahner D., Klessen R. S., Glover S. C. O., Pakmor R., Herrera-Camus R., Grand R. J. J., 2020, MNRAS, 498, 3193
Pety J. et al., 2013, ApJ, 779, 43
Pilyugin L. S., Grebel E. K., Zinchenko I. A., Kniazev A. Y., 2014, AJ, 148, 134
Querejeta M. et al., 2021, A&A, 656, A133
Rahman N. et al., 2011, ApJ, 730, 72
Rahner D., Pellegrini E. W., Glover S. C. O., Klessen R. S., 2017, MNRAS, 470, 4453
Roman-Duval J., Heyer M., Brunt C. M., Clark P., Klessen R., Shetty R., 2016, ApJ, 818, 144
Rosolowsky E. et al., 2021, MNRAS, 502, 1218
Sánchez S. F. et al., 2014, A&A, 563, A49
Sánchez S. F. et al., 2019, MNRAS, 484, 3042
Santoro F. et al., 2022, A&A, 658, A188
Schinnerer E. et al., 2019, ApJ, 887, 49
Schlafly E. F., Finkbeiner D. P., 2011, ApJ, 737, 103
Schruba A., Leroy A. K., Walter F., Sandstrom K., Rosolowsky E., 2010, ApJ, 722, 1699
Schruba A. et al., 2011, AJ, 142, 37
Schruba A., Kruijssen J. M. D., Leroy A. K., 2019, ApJ, 883, 2
Scoville N. Z., Hersh K., 1979, ApJ, 229, 578
Scoville N. Z., Thakkar D., Carlstrom J. E., Sargent A. I., 1993, ApJ, 404, L59
Semenov V. A., Kravtsov A. V., Gnedin N. Y., 2021, ApJ, 918, 13
Shetty R., Clark P. C., Klessen R. S., 2014, MNRAS, 442, 2208
Sun J. et al., 2018, ApJ, 860, 172
Sun J. et al., 2020a, ApJ, 892, 148
Sun J. et al., 2020b, ApJ, 901, L8
Sun J. et al., 2022, AJ, 164, 43
Tomičić N. et al., 2021, ApJ, 907, 22
Tress R. G., Smith R. J., Sormani M. C., Glover S. C. O., Klessen R. S., Mac Low M.-M., Clark P. C., 2020, MNRAS, 492, 2973
Tress R. G., Sormani M. C., Smith R. J., Glover S. C. O., Klessen R. S., Mac Low M.-M., Clark P., Duarte-Cabral A., 2021, MNRAS, 505, 5438
Utomo D. et al., 2018, ApJ, 861, L18
Ward J. L., Chevance M., Kruijssen J. M. D., Hygate A. P. S., Schruba A., Longmore S. N., 2020, MNRAS, 497, 2286
Ward J. L., Kruijssen J. M. D., Chevance M., Kim J., Schruba A., Longmore S. N., in press, MNRAS
Ward J. L., Oliveira J. M., van Loon J. T., Sewiło M., 2016, MNRAS, 455, 2345
Whitmore B. C. et al., 2014, ApJ, 795, 156
Williams J. P., de Geus E. J., Blitz L., 1994, ApJ, 428, 693
Williams T. G. et al., 2022, MNRAS, 509, 1303
Wolfire M. G., Hollenbach D., McKee C. F., 2010, ApJ, 716, 1191
Wong T., Blitz L., 2002, ApJ, 569, 157
Yim K., Wong T., Xue R., Rand R. J., Rosolowsky E., van der Hulst J. M., Benjamin R., Murphy E. J., 2014, AJ, 148, 127
Yim K., Wong T., Rand R. J., Schinnerer E., 2020, MNRAS, 494, 4558
Zabel N. et al., 2020, MNRAS, 496, 2155

APPENDIX A: ACCURACY OF OUR RESULTS

In order to validate the accuracy of our measurements, we verify that the requirements listed in section 4.4 of Kruijssen et al. (2018) are fulfilled. Satisfaction of these criteria indicates that the constrained parameters (t_{CO}, t_{fb}, and λ) are measured with an accuracy of at least 30 per cent:

(i) The duration of t_{CO} and $t_{H\alpha}$ should differ by less than one order of magnitude. This is satisfied by $|\log_{10}(t_{H\alpha}/t_{CO})| \leq 0.58$.

(ii) The ratio $\lambda/l_{ap,\,min}$ ranges from 1.06 to 3.63 for the galaxies in our sample. For eight galaxies out of 54 (IC1954, NGC 1087, NGC

1385, NGC 1546, NGC 1672, NGC 4298, NGC 4540, NGC 4548), we measure $\lambda/l_{ap,min} < 1.5$, implying that for these galaxies, only t_{CO} is constrained with sufficient accuracy, while the constrained t_{fb} and λ are upper limits. For the remaining galaxies, we ensure that the mean separation length between independent regions are sufficiently resolved by our observations.

(iii) We ensure that the number of identified peaks in both CO and Hα emission maps is always above 35. Galaxies without enough peaks were initially removed from our galaxy sample as described in Section 2.

(iv) The CO-to-Hα flux ratios measured locally focusing on CO (Hα) peaks should never be below (above) the galactic average. As shown in Fig. 1, this criterion is fulfilled, implying that we filter out the large-scale diffuse emission that is not associated with peaks enclosed in the aperture.

(v) The global star formation history of the analysed region, during the last evolutionary cycle (ranging $9-35$ Myr), should not vary more than 0.2 dex, when averaged over time width of t_{CO} or $t_{H\alpha}$. This is to ensure that we homogeneously sample the evolutionary timelines from gas to star with the identified peaks. Unfortunately, SFR over the last course of cloud lifetime for the galaxies in our sample are not known. However, we expect that the variation of SFR in the last ~ 35 Myr to be minor when time averaged by t_{CO} or $t_{H\alpha}$ as these low redshift galaxies are mostly undergoing a secular evolution, especially when the galactic centres and bars are excluded.

(vi) Each region, independently undergoing evolution from gas to star, should be detectable in both tracers at some point in their life. This implies that sensitivity of the CO and Hα should be matched, allowing the faintest CO peak to evolve into H II regions that is bright enough to be detected in the Hα map. In order to check if this criterion is satisfied, we first calculate the minimum star-forming region mass expected to form from the detected molecular clouds by multiplying the typical 5σ point source sensitivity of the CO map ($\sim 10^5$ M$_\odot$pc^{-2}; Leroy et al. 2021b) by the typical star formation efficiency constrained in our method ($\epsilon_{sf} = 2.8 \pm 1.5$ per cent). We then compare this minimum mass to the mass of the stellar population required to produce ionizing radiation that matches the typical 5σ sensitivity of Hα map on the scale of the typical individual star-forming regions ($\lambda \approx 250$ pc). We use the STARBURST99 model (Leitherer et al. 1999) to obtain the initial mass of the stellar population assuming that stars formation took place instantaneously 5 Myr ago. We find that the typical minimum mass of the stellar population obtained from CO maps (3000 $M_\odot$) matches well with that from Hα maps (4000 $M_\odot$).

Our measurements satisfy almost all of the requirements listed above with an exception of (ii). This implies that while t_{CO} is constrained with high accuracy, we do not have sufficient resolution to precisely constrain the λ and t_{fb}, for 8 galaxies in our sample. Only upper limits can be obtained for these values. Below, we use four more criteria listed in Kruijssen et al. (2018) to further determine the validity of t_{fb}. To do so, we first introduce the filling factor of SFR or gas tracer peaks, which is defined as $\zeta = 2r/\lambda$, where r is the mean radius of the corresponding peaks. This ζ characterizes how densely the peaks are located in a map. The average ζ is calculated by weighting the filling factors of gas and SFR tracer peaks with their associated time-scales:

(i) When peaks are densely distributed potentially overlapping with each other, the density contrast used for identifying peaks ($\delta \log_{10} \mathcal{F}$) should be small enough to identify adjacent peaks. In Fig. A1, we confirm that our adopted $\delta \log_{10} \mathcal{F}$ is small enough, compared to the upper limit prescribed by Kruijssen et al. (2018).

Figure A1. In the top panel, we show the adopted density contrasts ($\delta \log_{10} \mathcal{F}$) used for the peak identification in each Hα (blue) and CO (red) emission map, as a function of the average filling factor ζ. The shaded area is the parameter space where the peak identification is affected by blending of sources (Kruijssen et al. 2018). We confirm that we adopt small enough $\delta \log_{10} \mathcal{F}$ to identify adjacent peaks even in maps with high filling factor. In the bottom panel, we show the ratio of the feedback time-scale (t_{fb}) and the total duration of the evolutionary cycle (τ), as a function of the average filling factor ζ. The shaded area is the parameter space where the contamination by adjacent peaks affects the measurement of the feedback time-scale. As a result, in grey we show six galaxies where only an upper limit of t_{fb} can be determined by not satisfying the condition (viii).

(ii) Spatial overlap of adjacent peaks due to high filling factor can falsely be attributed to a longer duration of the measured feedback time-scale. In this case, only an upper limit on the feedback time-scale can be determined. In order to check whether we sufficiently resolve independent regions, we compare in Fig. A1 the analytical prescription of Kruijssen et al. (2018) with our measurements of t_{fb}/τ, where τ is the total duration of the entire evolutionary cycle ($\tau = t_{CO} + t_{H\alpha} - t_{fb}$). We find that this condition is not fulfilled for six galaxies (NGC 1097, NGC 2090, NGC 3627, NGC 4540, NGC 4548, NGC 4569), two of which overlap with galaxies that do not satisfy condition (ii).

(iii) As shown in the lower panel of Fig. A1, we ensure the conditions $t_{fb} > 0.05\tau$ and $t_{fb} < 0.95\tau$ are verified for all galaxies.

(iv) Similarly to condition (v), the global SFR of the analysed region should not vary more than 0.2 dex during the entire evolutionary lifecycle when averaged over t_{fb}. This is satisfied using the same argument in (v) stated above.

(v) After masking obviously crowed regions such as the galaxy centre, visual inspection does not reveal abundant region blending. In conclusion, we find that most of our measurements are constrained with high accuracy. The only exceptions are λ in 8 galaxies that do not satisfying condition (ii) and t_{fb} in 12 galaxies that do not satisfy both conditions (ii) and (viii). Only upper limits for these values can be constrained for this subset of galaxies.

[1]*Astronomisches Rechen-Institut, Zentrum für Astronomie der Universität Heidelberg, Mönchhofstraße 12-14, D-69120 Heidelberg, Germany*

[2]*Institüt für Theoretische Astrophysik, Zentrum für Astronomie der Universität Heidelberg, Albert-Ueberle-Strasse 2, D-69120 Heidelberg, Germany*

[3]*Department of Astronomy, The Ohio State University, 140 West 18th Ave, Columbus, OH 43210, USA*

[4]*Max-Planck Institut für Extraterrestrische Physik, Giessenbachstraße 1, D-85748 Garching, Germany*

[5]*Argelander-Institut für Astronomie, Universität Bonn, Auf dem Hügel 71, D-53121 Bonn, Germany*

[6]*The Observatories of the Carnegie Institution for Science, 813 Santa Barbara Street, Pasadena, CA 91101, USA*

[7]*Departamento de Astronomía, Universidad de Chile, Casilla 36-D, Santiago, Chile*

[8]*Department of Physics & Astronomy, University of Wyoming, Laramie, WY 82071, USA*

[9]*Department of Physics, University of Connecticut, 196A Auditorium Road, Storrs, CT 06269, USA*

[10]*Research School of Astronomy and Astrophysics, Australian National University, Canberra, ACT 2611, Australia*

[11]*ARC Centre of Excellence for All Sky Astrophysics in 3 Dimensions (ASTRO 3D), Australia*

[12]*International Centre for Radio Astronomy Research, University of Western Australia, 7 Fairway, Crawley, 6009, WA, Australia*

[13]*CNRS, IRAP, 9 Av. du Colonel Roche, BP 44346, F-31028 Toulouse cedex 4, France*

[14]*Université de Toulouse, UPS-OMP, IRAP, F-31028 Toulouse cedex 4, France*

[15]*Universität Heidelberg, Interdisziplinäres Zentrum für Wissenschaftliches Rechnen, Im Neuenheimer Feld 205, D-69120 Heidelberg, Germany*

[16]*School of Mathematics and Physics, University of Queensland, St Lucia 4067, Australia*

[17]*Department of Physics, Tamkang University, No.151, Yingzhuan Road, Tamsui District, New Taipei City 251301, Taiwan*

[18]*IRAM, 300 rue de la Piscine, F-38406 Saint Martin d'Hères, France*

[19]*Sorbonne Université, Observatoire de Paris, Université PSL, CNRS, LERMA, F-75005 Paris, France*

[20]*Observatorio Astronómico Nacional (IGN), C/Alfonso XII 3, Madrid E-28014, Spain*

[21]*4-183 CCIS, University of Alberta, Edmonton, AB T6G 2E1, Canada*

[22]*National Astronomical Observatory of Japan, 2-21-1 Osawa, Mitaka, Tokyo 181-8588, Japan*

[23]*Max Planck Institut für Astronomie, Königstuhl 17, D-69117 Heidelberg, Germany*

[24]*Department of Physics and Astronomy, McMaster University, 1280 Main Street West, Hamilton, ON L8S 4M1, Canada*

[25]*Canadian Institute for Theoretical Astrophysics (CITA), University of Toronto, 60 St George Street, Toronto, ON M5S 3H8, Canada*

[26]*Dipartimento di Fisica e Astronomia, Università di Firenze, Via G. Sansone 1, I-50019 Sesto Fiorentino, Firenze, Italy*

[27]*INAF – Osservatorio Astrofisico di Arcetri, Largo E. Fermi 5, I-50127 Firenze, Italy*

[28]*Observatorio Astronómico Nacional (IGN), C/Alfonso XII 3, Madrid E-28014, Spain*

This paper has been typeset from a TEX/LATEX file prepared by the author.

Chapter 3

On the duration of the embedded phase of star formation

Authors:

Jaeyeon Kim, Mélanie Chevance, J. M. Diederik Kruijssen,
Andreas Schruba, Karin Sandstrom et al.

Jaeyeon Kim is the principal author of this article. The method was developed by Dr. Kruijssen. Jaeyeon Kim, Dr. Chevance, and Dr. Kruijssen had the idea for the paper. Jaeyeon Kim performed calculations and analysis of the observations. Jaeyeon Kim produced all the figures and tables and wrote the manuscript. All authors collaborated with corrections and suggestions to the manuscript, and Jaeyeon Kim performed the last improvements during the review process.

On the duration of the embedded phase of star formation

Jaeyeon Kim [ID],[1]* Mélanie Chevance [ID],[1] J. M. Diederik Kruijssen [ID],[1] Andreas Schruba,[2] Karin Sandstrom,[3] Ashley T. Barnes [ID],[4] Frank Bigiel,[4] Guillermo A. Blanc,[5,6] Yixian Cao,[7] Daniel A. Dale,[8] Christopher M. Faesi,[9] Simon C. O. Glover [ID],[10] Kathryn Grasha [ID],[11] Brent Groves,[12] Cinthya Herrera,[13] Ralf S. Klessen [ID],[10,14] Kathryn Kreckel [ID],[1] Janice C. Lee,[15] Adam K. Leroy,[16] Jérôme Pety,[13,17] Miguel Querejeta,[18] Eva Schinnerer,[19] Jiayi Sun [ID],[16] Antonio Usero,[18] Jacob L. Ward[1] and Thomas G. Williams [ID][19]

Affiliations are listed at the end of the paper

ABSTRACT

Feedback from massive stars plays a key role in molecular cloud evolution. After the onset of star formation, the young stellar population is exposed by photoionization, winds, supernovae, and radiation pressure from massive stars. Recent observations of nearby galaxies have provided the evolutionary timeline between molecular clouds and exposed young stars, but the duration of the embedded phase of massive star formation is still ill-constrained. We measure how long massive stellar populations remain embedded within their natal cloud, by applying a statistical method to six nearby galaxies at $20-100$ pc resolution, using CO, *Spitzer* 24 μm, and Hα emission as tracers of molecular clouds, embedded star formation, and exposed star formation, respectively. We find that the embedded phase (with CO and 24 μm emission) lasts for $2-7$ Myr and constitutes $17-47$ per cent of the cloud lifetime. During approximately the first half of this phase, the region is invisible in Hα, making it heavily obscured. For the second half of this phase, the region also emits in Hα and is partially exposed. Once the cloud has been dispersed by feedback, 24 μm emission no longer traces ongoing star formation, but remains detectable for another $2-9$ Myr through the emission from ambient CO-dark gas, tracing star formation that recently ended. The short duration of massive star formation suggests that pre-supernova feedback (photoionization and winds) is important in disrupting molecular clouds. The measured time-scales do not show significant correlations with environmental properties (e.g. metallicity). Future JWST observations will enable these measurements routinely across the nearby galaxy population.

Key words: stars: formation – ISM: clouds – galaxies: evolution – galaxies: ISM – galaxies: star formation.

1 INTRODUCTION

Massive stars (>8 M$_\odot$) form in the densest regions of molecular clouds. Once formed, these stars emit large quantities of ionizing photons creating H II regions and generate strong winds, which together alter the structure of their birth clouds and the surrounding interstellar medium. After a relatively short lifetime ($4-20$ Myr; Leitherer et al. 2014; Barnes et al. 2020; Chevance et al. 2020a), these massive stars die in supernova explosions injecting energy and momentum into their surroundings. Theoretical studies of giant molecular clouds (GMCs) indicate that these feedback processes are responsible for freeing the young stars from their parental clouds and destroying the GMCs (see e.g. Krumholz 2014; Dale 2015; Chevance et al. 2020b, for recent reviews). However, it is still debated which feedback mechanisms efficiently disrupt the birth clouds and which affect the diffuse interstellar medium on large scales (e.g. Lucas, Bonnell & Dale 2020; Barnes et al. in preparation).

Observationally, several studies have constrained the time-scale for GMC destruction by stellar feedback in the Milky Way and in

nearby galaxies using optical and ultraviolet (UV) star formation tracers, which are sensitive to recent, not heavily obscured star formation. Rapid dispersion of GMCs, within a cloud dynamical time-scale ($\lesssim 10$ Myr), has been suggested based on the age distributions of stars in nearby star-forming regions and young stellar associations (Elmegreen 2000; Hartmann 2001). For GMCs in the Milky Way, M33, and the Large Magellanic Cloud (LMC), somewhat longer feedback time-scales of $10-20$ Myr have been proposed by classifying molecular clouds into different types based on the (non-)existence of their star formation activity (Engargiola et al. 2003; Blitz et al. 2007; Kawamura et al. 2009; Miura et al. 2012; Corbelli et al. 2017). Such methods have limitations because individual GMCs and star-forming regions need to be resolved. In addition, most of these studies only constrain the duration of the cloud dispersal after the young stars have become partially exposed. The exact role of each different feedback mechanism remains ambiguous, because the total duration of the embedded phase of star formation, including a heavily obscured phase, has not been quantified.

Studies of star-forming regions in the Milky Way and some nearby galaxies show that the embedded phase of massive star formation lasts for $2-5$ Myr, where the duration of the heavily obscured phase is found to be $\sim 0.1-2$ Myr (Lada & Lada 2003; Whitmore et al.

2014; Corbelli et al. 2017). During the earliest stage of star formation, young massive stars are still embedded in their natal gas. As a result, Hα emission is heavily or partially obscured due to the extinction provided by the dust in dense gas surrounding the young stars. Despite this, on-going star formation is detectable using mid-infrared, hydrogen infrared recombination lines, radio recombination lines, and free–free radio continuum emission (Lockman 1989; Kennicutt 1998a; Calzetti et al. 2005; Kennicutt et al. 2007; Prescott et al. 2007; Murphy et al. 2011; Vutisalchavakul & Evans 2013; Querejeta et al. 2019). In particular, the 24 μm emission in the mid-infrared observed by the Multiband Imaging Photometer (MIPS) aboard the *Spitzer* Space Telescope provides an unbiased tracer of embedded massive star formation (e.g. see Kennicutt & Evans 2012 for review), as long as the star-forming region has a fully sampled initial mass function (Vutisalchavakul & Evans 2013). 24 μm emission originates from stochastically heated small dust grains that do not require ionizing photons to be excited but do empirically correlate with tracers of massive star formation and so can be used as a tracer of the presence of large amounts of dust-reprocessed photospheric light from massive stars. Therefore, the 24 μm emission is assumed to turn on only once massive stars are present. However, the radiation field from older stars (i.e. late-type B stars with an age of $\lesssim$100 Myr) can make a non-negligible contribution to the dust heating and thus the mid-infrared dust emission (Draine & Li 2007; Verley et al. 2009; Leroy et al. 2012). The exact contribution at 24 μm wavelength is found to vary strongly between galaxies (e.g. 85 per cent in M31 by Viaene et al. 2017, 20 per cent in M33 by Williams et al. 2019, and up to around > 60 per cent within the Galactic centre of the Milky Way, see Koepferl et al. 2015).

Following the theoretical model of star formation by Schmidt (1959), it is now observationally well-known that on galactic scales there is a tight correlation between the molecular gas surface density and the star formation rate (SFR) surface density (the 'star formation relation'; Silk 1997; Kennicutt 1998b; Bigiel et al. 2008; Leroy et al. 2013). However, this relation is also observed to break down on scales smaller than $\sim$1 kpc (e.g. Onodera et al. 2010; Schruba et al. 2010; Ford et al. 2013; Leroy et al. 2013; Kreckel et al. 2018; Williams, Gear & Smith 2018; Kruijssen et al. 2019; Schinnerer et al. 2019). This breakdown is caused by the small-scale de-correlation between GMCs and young stellar regions on sub-kpc scales and can be explained by assuming that individual regions in a galaxy follow independent lifecycles, during which clouds assemble, form stars, and get disrupted by feedback (Schruba et al. 2010; Feldmann, Gnedin & Kravtsov 2011; Kruijssen & Longmore 2014).

Kruijssen & Longmore (2014) and Kruijssen et al. (2018) developed a formalism that translates the observed de-correlation quantitatively into the evolutionary timeline of GMCs from cloud formation to subsequent star formation, and finally cloud dispersal. In brief, this method uses the spatial variation of the gas-to-SFR flux ratio observed at different spatial scales ranging from cloud ($\sim$100 pc) to galactic ($\sim$1 kpc) scales for apertures placed on either gas peaks or SFR tracer peaks. These measurements are then used to determine the duration of each phase of the evolutionary cycle: the cloud lifetime, the time-scale a SFR tracer is visible, and the phase during which both molecular gas and SFR tracers overlap, which represents the duration of massive star formation as well as the time-scale for molecular gas to be removed or dissociated by feedback. This method does not rely on high angular resolution as much as previous methods, using stellar ages or relative fractions of GMCs with and without internal star formation activity, since it only requires the mean separation length between regions undergoing independent evolution (100–200 pc; Chevance et al. 2020c) to be resolved instead

of resolving individual star-forming regions (10–50 pc; Kawamura et al. 2009).

This method has been used to characterize the evolutionary timelines between molecular gas and exposed young stellar populations using CO and Hα observations. The first applications of this method to a number of galaxies covering a large range of galactic environments (Kruijssen et al. 2019; Chevance et al. 2020a,c; Hygate 2020; Ward et al. 2020a; Zabel et al. 2020) have shown that GMCs live for 10–30 Myr. CO and Hα emission are found to be coincident for 1–5 Myr, during which time feedback from the young stellar population disperses the molecular gas of their birth clouds. Considering that supernova explosions are expected 4–20 Myr after massive stars are formed (Leitherer et al. 2014; Chevance et al. 2020a), the short duration of overlapping CO and Hα emission suggests that pre-supernova feedback, such as photoionization and stellar winds, is important for disrupting star-forming molecular clouds (also see Barnes et al. 2020 Chevance et al. 2020a). Ward et al. (2020b) have also used this method and extended the evolutionary timeline of star-forming regions by incorporating H I emission to trace atomic gas. The measured atomic gas cloud lifetime in the LMC is $\sim$50 Myr and almost no overlap with the exposed star-forming phase is detected.

In this paper, we go a step further in the characterization of the GMC evolutionary lifecycle and use CO, 24 μm, and Hα emission as tracers for molecular gas, embedded star formation, and exposed star formation, respectively, for six nearby galaxies (IC 342, LMC, M31, M33, M51, and NGC 300). Previous applications of the statistical method to the same galaxies have focussed on characterizing the GMC lifecycle using CO emission as a tracer of the molecular gas and Hα emission as a tracer of the young massive stars (NGC 300: Kruijssen et al. 2019; M51: Chevance et al. 2020c; M33: Hygate 2020; and the LMC: Ward et al. 2020a). We derive novel measurements of the GMC lifetimes in IC 342 and M31 in this paper (see Appendix B); these are based on CO and Hα observations presented in Schruba et al. (2021a), Schruba et al. (2021b). Employing *Spitzer* 24 μm observations allows us to probe the earliest phase of star formation where the stars are still heavily obscured, and quantify how long it takes young star-forming regions to emerge from their natal cloud (at which point the H II regions created by their ionizing radiation become visible).

The structure of this paper is as follows. In Section 2 and Appendix A, we describe the observational data used in our analysis. In Section 3, we summarize the statistical method used here and describe the associated input parameters for the galaxies in our sample. This is complemented by Appendix B, where we present in more detail the application of this method to IC 342 and M31. In Section 4, we then present the derived duration of the embedded massive star-forming phase, which can be separated into a heavily obscured phase of star formation and a partially exposed phase of star formation based on the existence of Hα emission. The total duration of the 24 μm emitting phase is also presented. In addition, we explore how the durations of these phases vary with environmental properties, across the small galaxy sample for which these measurements are possible. We discuss the robustness of our results and compare them with the literature in Section 5. Last, we present our conclusions in Section 6.

2 OBSERVATIONAL DATA

We apply our analysis to six nearby galaxies: IC 342, the LMC, M31, M33, M51, and NGC 300. The size of our sample is mostly limited by the angular resolution of the *Spitzer* MIPS observations at 24 μm

(∼6.4 arcsec, Rieke et al. 2004; corresponding to 2−110 pc for the galaxies in our sample, including M51 for which we use a map at higher angular resolution, see Section 2.1) and the fact that we need to resolve at least the separation length between star-forming regions undergoing independent evolutionary lifecycles (∼100−200 pc) to apply our analysis (see Section 5.1.1 and Kruijssen et al. 2018). Here, we provide a summary of the observational data used to trace the molecular gas (emission from low-*J* CO transitions), embedded massive stars (24 μm emission), and exposed young stellar regions (H α emission). Composite three-colour images of the CO, 24 μm, and H α maps are presented in Fig. 1, whereas the individual CO and 24 μm maps are shown in Appendix A. The physical and observational properties of the galaxies in our sample are listed in Table 1.

2.1 Descriptions of multiwavelength data sets

IC 342. We adopt a distance of 3.45 Mpc (Wu et al. 2014), an inclination of 31.0°, and a position angle of 42.0° (Meidt, Rand & Merrifield 2009). The adopted metallicity at the galactic centre is $12 + \log(O/H)_0 = 8.83 \pm 0.04$, with a radial gradient of -0.0500 ± 0.0085 dex kpc^{-1}, as measured by Pilyugin et al. (2014) using the strong-line 'counterpart' method by Pilyugin, Grebel & Mattsson (2012). We use a combination of NOEMA and IRAM 30-m observations of the ^{12}CO ($J = 1-0$) transition (denoted as CO(1–0) in the following) from Schruba et al. (2021a) to trace molecular gas in IC 342, covering out to 7.7 kpc in galactic radius. The final data cube has a circular beam size of 3.6 arcsec, a spectral resolution of 5 km s^{-1}, and a sensitivity of 135 mK per 5 km s^{-1} velocity channel. Integrating over 10 km s^{-1}, this translates to a 5σ point source sensitivity of $5\sigma(M_{H_2}) \approx 6.1 \times 10^4$ M$_\odot$ when the CO(1–0)-to-H$_2$ conversion factor (α_{CO}) listed in Table 2 is assumed. In order to trace embedded star formation, we retrieved *Spitzer* MIPS 24 μm image from the Local Volume Legacy (LVL) Survey (Dale et al. 2009). In addition to the procedure described in Dale et al. (2009), we mask foreground stars with a G-band magnitude ≤22 mag using the Gaia DR2 catalogue (Gaia Collaboration 2018), as well as background galaxies via visual inspection of extended and non-circular sources. We then subtract background emission by fitting a plane determined at 2−2.5 R_{25} from the galactic centre where R_{25} is the optical radius of the galaxy, obtained from the Lyon Extragalactic Database (Paturel et al. 2003a,b; Makarov et al. 2014). H α emission has been observed with the Mosaic Imager on the Mayall 4-m telescope. We utilize calibrated narrow-band H α and R-band images kindly provided by Kimberly Herrmann (private communication). We post-process these images as described in Schruba et al. (2021a). In brief, we subtract continuum emission from the H α image, mask Milky Way stars using the Gaia DR2 catalogue, subtract a sky background by fitting a 1st order polynomial plane at galactic radii >10 kpc, and correct for Galactic extinction adopting $A(H\alpha) = 1.3$ mag which is derived from E($B-V$) = 0.494 mag (Schlafly & Finkbeiner 2011) and an extinction curve with $R_V = 3.1$ (Cardelli, Clayton & Mathis 1989).[1]

---

[1] As explained in the discussion of each galaxy, we do not adopt the same literature for the reddening (E($B − V$)) or the extinction law when correcting for Galactic extinction. This is to follow what has been done previously for each galaxy, in our first applications of the statistical method using CO and H α emission only (Kruijssen et al. 2019; Chevance et al. 2020c; Hygate 2020; Ward et al. 2020a). Nevertheless, similarly to the CO(1–0)-to-H$_2$ and SFR conversion factor (see Section 3.2), we note that our choice of correction factor does not affect our measurements of time-scales and region separation length, but only the derived total SFR and the integrated star formation efficiency.

For all the H α maps used here, we do not attempt to correct for the internal extinction so that it traces exposed star-forming regions. The resulting H α map has an angular resolution of 0.85 arcsec. Due to limited coverage of the CO survey and blending of bright sources at the galaxy centre, we restrict our analysis to regions where CO observations have been made within galactic radii 1.0−7.7 kpc, as shown in Fig. 1.

LMC. We adopt a distance of 50 kpc (Pietrzyński et al. 2019), an inclination of 22.0°, and a position angle of 168.0° (Kim et al. 1998). The adopted metallicity at the centre of the LMC is $12 + \log(O/H)_0 = 8.35 \pm 0.03$, with a radial gradient of 0.0105 ± 0.0105 dex kpc^{-1}, as measured by Toribio San Cipriano et al. (2017) using a direct measurement of electron temperature (T_e) from spectra of H II regions (direct T_e-based method). We employ the CO(1–0) data presented in the third data release of the Magellanic Mopra Assessment (MAGMA; Wong et al. 2011, 2017) to trace molecular gas. MAGMA is a CO mapping survey of the LMC and SMC using the Mopra 22-m Telescope at the Australia Telescope National Facility. For the LMC, the observations were conducted as a follow-up study of the NANTEN survey (Fukui et al. 2008) by targeting a subset of previously identified molecular clouds (∼160 out of 272 clouds), with an improved resolution in order to resolve the GMCs (∼11 pc). In Fig. 1, white dotted lines show the coverage of the MAGMA survey and solid white circles indicate regions where molecular gas has been detected by the NANTEN survey, but not further targeted with the MAGMA survey. We exclude these white circled regions, where we know GMCs exist, from our analysis.[2] However, we still include other regions not observed by the MAGMA survey, which might have diffuse and faint CO emission. We note that the inclusion of these sightlines, not covered by the MAGMA survey, should have a negligible impact on our results because diffuse and faint emission is eventually removed in our analysis through a filtering process (see Section 3). Moreover, the MAGMA survey covers most (∼80 per cent) of the total CO emission from the LMC observed by the NANTEN survey (Wong et al. 2011). The observed CO emission from the MAGMA survey also shows good agreement with the molecular gas map produced using dust continuum emission modelling (Jameson et al. 2016), indicating that we cover most of the emission from GMCs. The resulting angular resolution of the MAGMA CO data is 45 arcsec, and the sensitivity is 0.3 K per 0.526 km s^{-1} velocity channel. Integrating over 10 km s^{-1}, this translates to a 5σ point source sensitivity of $5\sigma(M_{H_2}) \approx 2.2 \times 10^3$ M$_\odot$ (assuming the α_{CO} from Table 2). The *Spitzer* MIPS 24 μm image is from the SAGE project (Meixner et al. 2006), covering 7° × 7° of the galaxy. The continuum subtracted H α map is from the Southern H-Alpha Sky Survey Atlas (Gaustad et al. 2001) and has a resolution of 48 arcsec. We correct for Galactic extinction using $A(H\alpha) = 0.16$ mag, which is derived from E($B-V$) = 0.06 mag (Staveley-Smith et al. 2003) and an extinction curve with $R_V = 3.1$ (Cardelli et al. 1989). For the analysis here, we include emission from 0−3 kpc in galactic radius, where the outer boundary is indicated in Fig. 1.

M31. We adopt a distance of 0.78 Mpc (Dalcanton et al. 2012), an inclination of 37.7°, and a position angle of 77.7° (Corbelli et al. 2010). The adopted metallicity at the galactic centre is $12 + \log(O/H)_0 = 8.8 \pm 0.1$, with a radial gradient of

---

[2] Using the cloud catalogue from the NANTEN survey (Fukui et al. 2008), Ward et al. (2020a) have modelled the CO emission from the GMCs that were not observed by MAGMA and have shown that excluding these regions from our analysis has a negligible effect on our measurements.
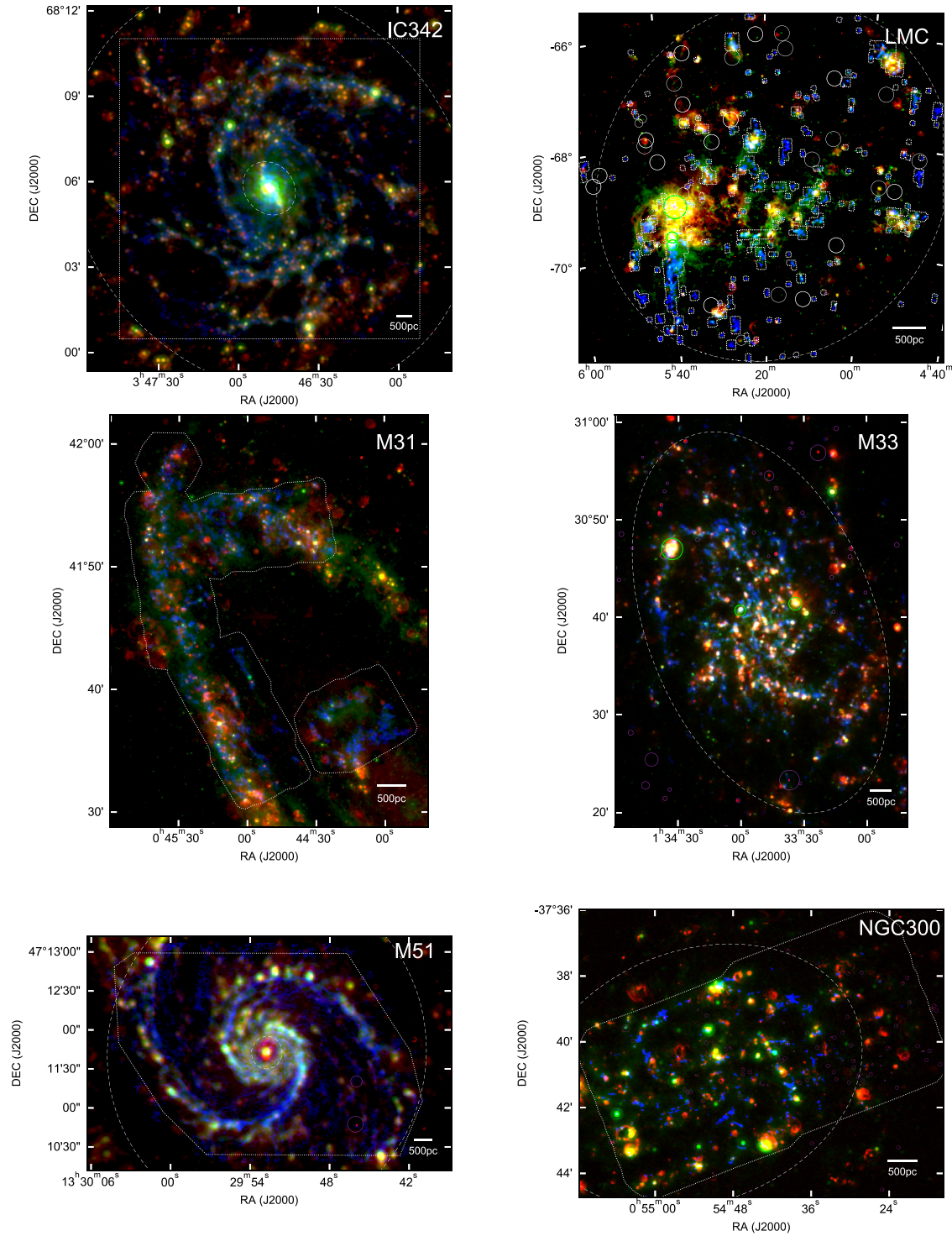
Figure 1. Composite three-colour images of the six galaxies in our sample. The CO(1-0) emission (CO(2-1) for M33) is presented in blue, *Spitzer* MIPS 24 μm in green, and H α in red. Galaxies are sorted by alphabetical order. The range of galactic radii included in the analysis is indicated by the white dashed ellipses. The inner ellipses of IC 342 and M51 show galaxy centres excluded from our analysis. The white dotted line shows the area where CO emission was observed in each galaxy (excluding the high noise edges of the map) and is not shown for M33 because it is outside the field of view. The massive star-forming regions of 30 Doradus in the LMC and NGC 604 in M33, as well as bright 24 μm peaks are masked (green circles; see Section 2.3). In the LMC, regions that were not targeted by the MAGMA survey but are known to host gas clouds are masked (white solid circles). Foreground stars that were not removed in the image reduction process and image artefacts are also masked (purple circles). A physical scale of 500 pc is shown in each image.

Table 1. Physical and observational properties of our galaxy sample.

Galaxy	Stellar mass[a]	Metallicity[b,c]	Distance	Inclination	Position angle	CO observations	CO resolution	24 μm resolution	Spatial resolution[d]
	$(\log_{10} M_\odot)$	$(Z/Z_\odot)$	(Mpc)	(deg)	(deg)		(arcsec)	(arcsec)	(pc)
IC 342	10.2 ± 0.1	0.90 ± 0.20	3.45	31.0	42.0	NOEMA + IRAM 30-m	3.6	6.4	107
LMC	9.3 ± 0.1	0.48 ± 0.03	0.05	22.0	168.0	ATNF	45	6.4	11
M31 (NGC 224)	11.0 ± 0.1	0.76 ± 0.20	0.78	77.7	37.7	CARMA + IRAM 30-m	5.5	6.4	24
M33 (NGC 598)	9.4 ± 0.1	0.50 ± 0.06	0.84	55.0	201.1	IRAM 30-m	12	6.4	49
M51 (NGC 5194)	10.7 ± 0.1	1.37 ± 0.20	8.6	21.0	173.0	PdBI + IRAM 30-m	1.1	2.4	100
NGC 300	9.3 ± 0.1	0.48 ± 0.06	2.0	42.0	111.0	ALMA	2.1	6.4	62

[a]Adopted from Skibba et al. (2012) for the LMC and Sick et al. (2015) for M31, while others are from Leroy et al. (2019).
[b]CO luminosity weighted metallicity over the considered field of view.
[c]Obtained using $Z/Z_\odot = (O/H)/(O/H)_\odot$, with the solar oxygen abundance $12 + \log(O/H)_\odot = 8.69$ (Asplund et al. 2009).
[d]Coarsest spatial resolution of the CO and 24 μm maps.

Table 2. Input parameters of the analysis using 24 μm as SFR tracers for each galaxy. Other parameters not mentioned here are the same as in our previous analysis using Hα as an SFR tracer.

Quantity	IC 342	LMC	M31	M33	M51	NGC 300	Description
$l_{ap,\,min}$ (pc)	116	25	52	65	90	60	Minimum aperture size to convolve the input maps to
$l_{ap,\,max}$ (pc)	3000	2000	3000	2500	3000	2560	Maximum aperture size to convolve the input maps to
N_{ap}	15	15	15	15	15	15	Number of aperture sizes used to create array of logarithmically spaced aperture size in the range ($l_{ap,\,min}$, $l_{ap,\,max}$)
$N_{pix,min}$	20	10	20	20	10	100	Minimum number of pixels for a valid peak
$\Delta\log_{10}\mathcal{F}_{CO}$	2.0	2.5	1.3	2.2	2.5	2.0	Logarithmic range below flux maximum covered by flux contour levels for molecular gas peak identification
$\delta\log_{10}\mathcal{F}_{CO}$	0.05	0.15	0.02	0.10	0.05	0.10	Logarithmic interval between flux contour levels for molecular gas peak identification
$\Delta\log_{10}\mathcal{F}_{24\,\mu m}$	3.8	2.8	2.3	3.0	4.0	2.0	Logarithmic range below flux maximum covered by flux contour levels for SFR tracer peak identification
$\delta\log_{10}\mathcal{F}_{24\,\mu m}$	0.05	0.05	0.05	0.10	0.05	0.10	Logarithmic interval between flux contour levels for SFR tracer peak identification
t_{ref} (Myr)	20.0	11.1	14.0	14.5	30.5	10.8	Reference time-scale spanned by molecular gas tracer
$t_{ref,\,errmin}$ (Myr)	2.3	1.7	1.9	1.5	4.8	1.7	Downwards uncertainty on reference time-scale
$t_{ref,\,errmax}$ (Myr)	2.0	1.6	2.1	1.6	9.2	2.1	Upwards uncertainty on reference time-scale
SFR ($M_\odot yr^{-1}$)	0.97	0.12	0.041	0.18	1.63	0.063	Total SFR in the analysed area
$\sigma(SFR)$ ($M_\odot yr^{-1}$)	0.19	0.03	0.008	0.04	0.32	0.013	Uncertainty of the total SFR
$\log_{10}\alpha_{CO}$	0.65	0.83	0.69	0.81	0.59	0.82	Logarithm of CO(1–0)-to-H_2 conversion factor
$\sigma_{rel}(\alpha_{CO})$	0.5	0.5	0.5	0.5	0.5	0.5	Relative uncertainty of α_{CO}
n_λ	13	7	10	10	16	8	Characteristic width for the Gaussian filter used to remove diffuse emission in Fourier space

$-0.022 \pm 0.014\,\text{dex kpc}^{-1}$, as measured by Zurita & Bresolin (2012) using the strong-line calibration from Pilyugin (2001). To trace molecular gas, we use CO(1–0) data first appeared in Caldú-Primo & Schruba (2016), with full details presented in Schruba et al. (2021b). These data are obtained by combining CARMA interferometry data and IRAM 30-m data, the latter from Nieten et al. (2006). The CARMA observations cover 87 kpc² of M31's star-forming disc at galactic radii of 6−13 kpc. They have an angular resolution of 5.5 arcsec, a spectral resolution of 2.5 km s⁻¹, and a sensitivity of 175 mK per 2.5 km s⁻¹ velocity channel. Integrating over 10 km s⁻¹, this translates to a 5σ point source sensitivity of $5\sigma(M_{H_2}) \approx 7.3 \times 10^3\,M_\odot$ (assuming the α_{CO} from Table 2). We utilize the velocity masked moment-zero map, which is designed to be flux-complete (see Schruba et al. 2021b for details). We employ

the *Spitzer* MIPS 24 μm map presented in Gordon et al. (2006). This map is already background subtracted, and we refer the reader to the original paper for more information on the data reduction procedure. The Hα emission map is discussed in Schruba et al. (2021b) and has been created from calibrated narrow-band Hα and R-band images from the Local Group Galaxies Survey (Massey et al. 2006). The observations were carried out by the Mosaic Imager on the Mayall 4-m telescope. The calibrated data were post-processed as described in Schruba et al. (2021b), which include Hα continuum subtraction, masking of Milky Way stars using the Gaia DR2 catalogue (Gaia Collaboration 2018), a sky background subtraction by fitting a plane at galactic radii >20 kpc, and a correction for the contamination by [N II] by assuming that both [N II] lines contribute 35 per cent of the total Hα emission, following Azimlu, Marciniak & Barmby (2011).

The Galactic extinction is corrected by adopting a factor $A(H\alpha) = 0.14$ mag, which is derived from $E(B-V) = 0.05$ mag (Schlafly & Finkbeiner 2011) and an extinction curve with $R_V = 3.1$ (Cardelli et al. 1989). The resulting $H\alpha$ map has an angular resolutions of 1.5 arcsec. We perform our analysis on the field of view spanned by the CO observations.

M33. We adopt a distance of 0.84 Mpc (Gieren et al. 2013), an inclination of $55.08°$, and a position angle of $201.1°$ (Koch et al. 2018). The adopted metallicity at the galactic centre is $12 + \log(O/H)_0 = 8.48 \pm 0.04$, with a radial gradient of -0.042 ± 0.010 dex kpc^{-1}, as measured by Bresolin (2011) using a direct T_e-based method. We use the $^{12}CO(J = 2 - 1)$ transition (denoted as CO(2–1) in the following) data presented in Gratier et al. (2010) and Druard et al. (2014) to trace molecular gas. The observations were carried out using the HEterodyne Receiver Array (Schuster et al. 2004) on the IRAM 30-m telescope covering the galaxy out to radii of 7 kpc. The resulting angular resolution is 12 arcsec and the average noise level is 20 mK per 2.6 km s^{-1} velocity channel. Integrating over 10 km s^{-1}, this noise level translates to a 5σ point source sensitivity of $5\sigma(M_{H_2}) \approx 6.2 \times 10^3$ M$_\odot$ (assuming the α_{CO} from Table 2). We retrieve *Spitzer* MIPS 24 μm image from the LVL Survey (Dale et al. 2009). We then apply the same post-processing procedures as described above for IC 342. The narrow-band $H\alpha$ data are from Greenawalt (1998). The observations were carried out using the Burrell-Schmidt 0.6-m telescope at the Kitt Peak National Observatory (KPNO). Detailed information about the image reduction process can be found in Hoopes & Walterbos (2000). The Galactic extinction is corrected by using $A(H\alpha) = 0.1$ mag, obtained from $E(B-V) = 0.0413$ mag (Schlegel, Finkbeiner & Davis 1998) and an extinction curve with $R_V = 3.1$ (Fitzpatrick & Massa 2007). The resolution of the $H\alpha$ emission map is 2.0 arcsec. We restrict our analysis to galactocentric radii ≤ 5 kpc, as outlined in Fig. 1.

M51. We adopt a distance of 8.6 Mpc (Jacobs et al. 2009), an inclination of $21.0°$, and a position angle of $173.0°$ (Colombo et al. 2014). The adopted metallicity at the galactic centre is $12 + \log(O/H)_0 = 8.88 \pm 0.053$, with a radial gradient of -0.0223 ± 0.0037 dex kpc^{-1}, as measured by Pilyugin et al. (2014) using the strong-line 'counterpart' method (Pilyugin et al. 2012). We use the CO(1–0) data of the inner 10×6 kpc^2 of the M51 presented in Pety et al. (2013) as part of the PdBI Arcsecond Whirlpool Survey (PAWS; Schinnerer et al. 2013). The surveyed region is visible in Fig. 1. The PdBI observations were carried out using A, B, C, and D configurations. The IRAM 30-m telescope was used to recover emission at low spatial frequencies. The final data have an angular resolution of 1.1 arcsec and a sensitivity of 0.39 K per 5 km s^{-1} velocity channel. Integrating over 10 km s^{-1}, this noise level translates to a 5σ point source sensitivity of $5\sigma(M_{H_2}) \approx 8.9 \times 10^4$ M$_\odot$ (assuming the α_{CO} from Table 2). The integrated intensity map was created by applying a mask to the data cube as described in Pety et al. (2013). Due to the limited resolution of *Spitzer* MIPS 24 μm imaging (6.4 arcsec; Rieke et al. 2004), we can in principle only apply our method to galaxies closer than ~5 Mpc. However, using the higher resolution (2.4 arcsec) 24 μm map created by Dumas et al. (2011), we are able to expand the application of our method to M51, located at 8.6 Mpc. This map was created by applying the HiRes deconvolution algorithm (Backus et al. 2005) to the 5th *Spitzer* Infrared Nearby Galaxies Survey (SINGS; Kennicutt et al. 2003) data delivery (see Dumas et al. 2011 for more details). However, we note that the artefacts introduced by the deconvolution algorithm could potentially bias our analysis, especially for time-scale-related quantities, by modifying the distribution of the 24 μm flux around bright peaks, limiting the

interpretation of our results for this galaxy. The $H\alpha$ emission map is also from SINGS (Kennicutt et al. 2003). The observations were carried out using the KPNO 2.1-m telescope with the CFIM imager. The map is corrected for Galactic extinction adopting a correction factor $A(H\alpha) = 0.08$ mag, obtained from $E(B - V) = 0.03$ mag (Schlafly & Finkbeiner 2011) and an extinction curve with $R_V = 3.1$ (Fitzpatrick 1999). We also correct for the contamination by [N II] lines by scaling the map by a factor of 0.7. The resolution of the $H\alpha$ emission map is 1.83 arcsec. Because we lack CO observations of the outer galaxy and sources at the galaxy centre are affected by crowding and contamination from active galactic nucleus, we restrict our analysis to the field of view of the CO observations, and within galactic radii of $0.51-5.35$ kpc, as indicated in Fig. 1.

NGC 300. We adopt a distance of 2.0 Mpc (Dalcanton et al. 2009), an inclination of $42.0°$, and a position angle of $111.0°$ (Westmeier, Braun & Koribalski 2011). We adopt a metallicity of $12 + \log(O/H)_0 = 8.46 \pm 0.05$ at the galactic centre and a radial gradient of -0.056 ± 0.015 dex kpc^{-1}, as measured by Toribio San Cipriano et al. (2016) using a direct T_e-based method. We employ ALMA observations of the CO(1–0) transition, from ALMA programmes 2013.1.00351.S and 2015.1.00258.S (PI A. Schruba), to be presented in Schruba et al. (in preparation) and first used in Kruijssen et al. (2019). The observations were performed using the 12-m main array, as well as the 7-m array and total power antennas of the ALMA Compact Array, covering galactic radii out to 4.8 kpc. The resulting data have angular resolution of 2.1 arcsec (~20 pc) and sensitivity of 0.1 K per 2 km s^{-1} channel. Integrating over 10 km s^{-1}, this noise level translates to a 5σ point source sensitivity of $5\sigma(M_{H_2}) \approx 4.3 \times 10^3$ M$_\odot$ (assuming the α_{CO} from Table 2). We retrieve *Spitzer* MIPS 24 μm image from the LVL Survey (Dale et al. 2009) and apply the same post-processing procedures as described above for IC 342. We use the $H\alpha$ image presented in Faesi et al. (2014). This map is created from narrow-band $H\alpha$ data and nearby continuum available in the ESO data archive, and we use here the version kindly shared by Chris Faesi (private communication). The observations were carried out with the Wide Field Imager on the MPG/ESO 2.2-m telescope at *La Silla observatory*. Correction for Galactic extinction is applied using $A(H\alpha) = 0.027$ mag, obtained from $E(B - V) = 0.01$ mag (Schlafly & Finkbeiner 2011) and an extinction curve with $R_V = 3.1$ (Fitzpatrick 1999). We remove contamination of [N II] lines by assuming an intensity ratio $I(N II)/I(H\alpha) = 0.2$. The resolution of the map is 1.35 arcsec. In our analysis, we consider emission from the field of view of the CO observations, and within $0-3$ kpc in galactic radius (beyond which the molecular gas surface density drops precipitously), and the outer boundary is visible in Fig. 1.

2.2 Homogenization of maps to common pixel grid

In order to apply our method, the gas and SFR tracer maps for a given galaxy need to share the same pixel grid. Therefore, for each galaxy, we regrid the map with a smaller pixel size to match the pixel grid of the map with larger pixel size. When the map that is being regridded has a better spatial resolution than the reference map, we first convolve the map with a Gaussian kernel to the resolution of the reference map before regridding to avoid introducing artefacts.[3]

---

[3]When convolving the 24 μm map, we have also tested using a more exact kernel from Aniano et al. (2011) and found that the use of a Gaussian kernel has a negligible impact on our results.

2.3 Construction of masks

We use the small-scale variation of the gas-to-SFR flux ratios to constrain the evolutionary timeline of the molecular clouds (see Section 3). By definition, our measurements are flux-weighted averages (see Kruijssen et al. 2018), which implies that very bright peaks dominating a significant fraction of the total flux can bias our results. Therefore, we mask star-forming regions in some galaxies that are clear outliers in the luminosity function of SFR tracer peaks. Specifically, we first sort the peak fluxes (identified using CLUMPFIND; see Section 3) in descending order. We then look for a gap in the distribution by calculating the ratio of the flux between the nth brightest and the next brightest peak in line, starting from the brightest peak. A gap is defined to exist when the nth peak is more than twice as bright as the $(n + 1)^{\text{th}}$ peak. Whenever a gap is found, we mask all the peaks that are brighter than the $(n + 1)^{\text{th}}$ brightest peak. As a result, we mask three star-forming regions each in the LMC and in M33 before applying our analysis (green circles in Fig. 1). These regions include 30 Doradus in the LMC and NGC 604 in M33, which alone contribute more than 30 per cent of the 24 μm emission of each galaxy. Note that we would be masking the same peaks unless we go down to a brightness difference of 50 per cent (rather than 100 per cent) when defining a gap in the luminosity function. In this case, we would be masking one to four more peaks each in IC 342, M31, and NGC 300. The impact of masking such bright regions on the resulting derived parameters is generally small when averaging over the entire galaxy, but becomes significant if a smaller fraction of the galaxy is considered (see Ward et al. 2020a for the effect of 30 Doradus on the LMC and Chevance et al. 2020c for the effect of the 'headlight cloud' on the spiral galaxy NGC 628, also see Herrera et al. 2020). We also check for bright regions that satisfy this condition in the CO emission maps, but found none. Finally, we also mask artefacts in the maps (purple circles in Fig. 1).

3 METHOD

We employ a statistical method (formalized in the HEISENBERG code) to constrain the evolutionary timeline of GMCs. This timeline can be decomposed into the cloud lifetime, the duration of the embedded phase of star formation (which continues until dispersal of molecular clouds), and the star formation tracer lifetime. The characteristic separation length between star-forming regions undergoing independent evolution is also constrained in our analysis. Here, we provide a summary of the methodology and the main input parameters. We refer the reader to Kruijssen & Longmore (2014) for a detailed explanation of the method, to Kruijssen et al. (2018) for the presentation and validation of the HEISENBERG code, as well as the full list of input parameters, and to Chevance et al. (2020c) for a general application of the method to nine nearby star-forming galaxies. The accuracy of the method has been demonstrated in Kruijssen et al. (2018) using simulated galaxies, and has since been confirmed through extensive observational and numerical testing (Kruijssen et al. 2019; Haydon et al. 2020a; Ward et al. 2020b).

3.1 Description of the analysis method

Galaxies are composed of numerous GMCs and star-forming regions. The fundamental concept of our method is that such regions are independently undergoing their evolution, from molecular clouds to the formation of stars. These evolutionary phases are observed using gas (e.g. CO) and SFR tracers (e.g. Hα or 24 μm). We define the duration of each phase based on the visibility time-scale of the

tracers used. The time-scale during which a gas emission tracer and an SFR tracer co-exist corresponds to the duration of massive star formation plus the time it takes to disrupt its natal molecular gas by stellar feedback (i.e. the feedback time-scale, t_{fb}). In the following, the cloud lifetime will be denoted as t_{CO}, the star formation tracer lifetime as $t_{\text{H}\alpha}$ or $t_{24\,\mu\text{m}}$, and the feedback time-scale as $t_{\text{fb, H}\alpha}$, or $t_{\text{fb, 24}\,\mu\text{m}}$ depending on the SFR tracer used.

During the initial phase of cloud evolution, a given independent region is only visible in the molecular gas tracer. As the cloud collapses and starts forming stars, the region becomes visible both in the gas and SFR tracers. Eventually, the remaining molecular gas is dispersed by stellar feedback and the region is only visible in the SFR tracers. Locally, the gas-to-SFR flux ratio therefore decreases with time during the evolution of a cloud. Observationally, when focussing on a non-star-forming GMC, a higher gas-to-SFR flux ratio is measured compared to the large-scale (∼1 kpc) average gas-to-SFR flux ratio. By contrast, when focussing on a young star-forming region, where most of the molecular gas has been dispersed, a lower gas-to SFR flux ratio is measured. The deviations of the small-scale gas-to-SFR flux ratio compared to the large-scale average, as a function of spatial scale, can be directly related to the duration of the different phases of the GMC lifecycle (Kruijssen & Longmore 2014; Kruijssen et al. 2018).

In practice, we first identify peaks in the gas tracer and SFR tracer emission maps. We then convolve both maps into a range of N_{ap} spatial resolutions spanning from $l_{\text{ap, min}}$ to $l_{\text{ap, max}}$ (see Table 2). The minimum aperture size ($l_{\text{ap, min}}$) is set to a value that is close to the size of the major axis of the deprojected beam of the coarsest resolution between the two maps, whereas the maximum aperture size ($l_{\text{ap, max}}$) covers most of the galaxy. For each convolved map, apertures with the size of the corresponding resolution are placed on the identified gas and SFR tracer peaks. We then measure the gas and SFR tracer flux enclosed in these apertures to obtain the gas-to-SFR flux ratios as a function of aperture size. By fitting an analytical model describing the gas-to-SFR flux ratio as a function of the aperture size and the underlying evolutionary time-scales, we obtain a direct measurement of these time-scales. This can be understood with an idealized example. For a tracer that is longer lived, more peaks are typically identified, covering a larger fraction of the galaxy when small apertures are centred on them, compared to the shorter-lived tracer. The measured flux ratio is therefore closer to the galactic average value for a longer-lived tracer than a shorter-lived one.

We fit the analytical model derived by Kruijssen et al. (2018) to the measured flux ratios in order to constrain the relative duration of the different phases of the molecular cloud and star-forming region lifecycle, as well as the typical separation length between independent regions (λ). The absolute duration of the different phases is then obtained by scaling the relative duration of time-scales with a reference time-scale (t_{ref}). In our previous analyses using CO and Hα observations (Kruijssen et al. 2019; Chevance et al. 2020c, a; Hygate 2020; Ward et al. 2020a), we used the duration of the isolated Hα emitting phase ($t_{\text{ref}} = t_{\text{H}\alpha} - t_{\text{fb, H}\alpha}$), calibrated by Haydon et al. (2020b), Haydon et al. (2020a) using the stellar population synthesis model SLUG2 (da Silva, Fumagalli & Krumholz 2012, 2014; Krumholz et al. 2015), as the reference time-scale. Here, in order to obtain absolute values when applying our analysis to CO and 24 μm maps, we first apply the method to CO and Hα observations. This is to obtain the cloud lifetime (t_{CO}) and its upward and downward uncertainties ($t_{\text{CO, errmin}}$ and $t_{\text{CO, errmax}}$; see Table 3), which are adopted as the reference time-scale (t_{ref}) and its uncertainties ($t_{\text{ref, errmin}}$, and $t_{\text{ref, errmax}}$) in the analysis with CO

Table 3. Physical quantities constrained using the method described in Section 3, describing the evolution of molecular clouds to exposed or embedded stellar populations traced by Hα and 24 μm, respectively. Following the notation throughout this paper, t_{CO} is the cloud lifetime, $t_{fb, H\alpha}$ and $t_{fb, 24\mu m}$ are the duration of the partially exposed and embedded star-forming phase, respectively, and $t_{H\alpha}$ and $t_{24\mu m}$ are the duration of Hα and 24 μm emitting phase, respectively. The region separation length (λ) measured with different SFR tracers, feedback velocity (v_{fb}), and star-formation efficiency (ϵ_{sf}) are also listed.

| Galaxy | CO versus Hα | | | | CO versus 24 μm | | | | |
	t_{CO} (Myr)	$t_{fb, H\alpha}$ (Myr)	$t_{H\alpha}$ (Myr)	λ (pc)	$t_{fb, 24\mu m}$ (Myr)	$t_{24\mu m}$ (Myr)	λ (pc)	v_{fb} (km s^{-1}]	ϵ_{sf} (per cent)
IC 342	$20.0^{+2.0}_{-2.3}$	$2.2^{+0.4}_{-0.5}$	$6.4^{+0.5}_{-0.6}$	120^{+10}_{-10}	$5.2^{+1.5}_{-2.3}$	$7.9^{+1.8}_{-2.2}$	190^{+59}_{-62}	$14.3^{+4.0}_{-1.8}$	$1.9^{+1.4}_{-0.8}$
LMC	$11.1^{+1.6}_{-1.7}$	$1.2^{+0.2}_{-0.2}$	$5.8^{+0.4}_{-0.4}$	71^{+13}_{-8}	$5.0^{+1.6}_{-2.0}$	$13.6^{+3.7}_{-4.8}$	73^{+38}_{-26}	$10.0^{+2.1}_{-1.7}$	$6.8^{+4.9}_{-3.0}$
M31	$14.0^{+2.1}_{-1.9}$	$1.1^{+0.3}_{-0.2}$	$5.5^{+0.4}_{-0.3}$	181^{+28}_{-19}	$2.4^{+1.4}_{-0.8}$	$4.2^{+1.5}_{-0.7}$	128^{+97}_{-23}	$29.5^{+6.9}_{-5.3}$	$0.7^{+0.2}_{-0.2}$
M33	$14.5^{+1.6}_{-1.5}$	$3.3^{+0.6}_{-0.5}$	$7.9^{+0.7}_{-0.6}$	155^{+30}_{-24}	$6.8^{+2.1}_{-2.0}$	$11.9^{+2.9}_{-2.1}$	119^{+60}_{-35}	$10.3^{+1.5}_{-1.3}$	$3.5^{+2.5}_{-1.5}$
M51	$30.7^{+8.7}_{-4.9}$	$4.7^{+2.0}_{-1.1}$	$8.9^{+2.0}_{-1.2}$	140^{+25}_{-17}	$<4.0^a$	$3.6^{+1.2}_{-0.9}$	$<136^a$	$7.9^{+2.0}_{-2.1}$	$3.3^{+2.9}_{-1.4}$
NGC 300	$10.8^{+2.2}_{-1.6}$	$1.5^{+0.2}_{-0.2}$	$6.1^{+0.2}_{-0.2}$	104^{+22}_{-18}	$4.9^{+1.2}_{-1.9}$	$7.9^{+1.5}_{-2.1}$	178^{+125}_{-75}	$9.4^{+0.8}_{-0.7}$	$3.3^{+2.6}_{-1.4}$

^{a} Only a 1σ upper limit can be derived for not satisfying (ii) and (viii) in Section 5.1.1.

and 24 μm observations. The fitted model is thus described by three independent and non-degenerate quantities ($t_{24\mu m}$, $t_{fb, 24\mu m}$, and λ). The best-fitting values are then obtained by minimizing the reduced-χ^2 over these three quantities. The uncertainties of each parameter are propagated consistently throughout the analysis.

The presence of diffuse emission can bias our measurements by adding a large-scale component that is not associated with the identified peaks. This large-scale emission potentially includes diffuse emission originating from sources related to the recent massive star formation, such as low mass molecular clouds, low luminosity H II regions, and ionizing photons that have escaped from H II regions (e.g. Wood et al. 2010; Belfiore et al. in preparation). It may also originate from other mechanisms not related to recent massive star formation, for example, diffuse molecular gas, infrared emission powered by stars of intermediate age, and diffuse ionized gas created by shocks (Martin 1997; Leroy et al. 2012). We remove such diffuse emission in both gas and SFR tracer emission maps iteratively, using the method presented in Hygate et al. (2019), which makes the derived time-scales sensitive to only the massive/luminous molecular clouds and young stellar populations. This method filters emission on spatial scales larger than n_λ times the typical distance between regions λ (as measured from the HEISENBERG code) using a Gaussian high-pass filter in Fourier space. For each galaxy, we adopt the smallest possible value for n_λ, while ensuring the flux loss from the compact emission to be less than 10 per cent (also following Chevance et al. 2020c; Hygate 2020; see Table 2). We do not adopt a fixed filtering scale because we want to maximize the removal of diffuse emission, while minimizing the impact of the filtering on the compact regions. The influence of n_λ on the derived time-scales is fully described in Hygate et al. (2019) and Hygate (2020). In summary, the choice of n_λ does not significantly change the best-fitting model parameters, as long as the adopted n_λ is smaller than 30 and the flux loss from the compact emission is less than 10 per cent. After the diffuse emission is filtered out, a noise mask with a threshold at twice the standard deviation noise level of the emission map is applied. We repeat this process until the convergence condition is reached, which is when the change of the measured value of λ is less than 5 per cent over three consecutive iterations.

3.2 Input parameters

Unless otherwise noted here, we adopt the same parameters as for previous analyses using Hα as an SFR tracer (see Appendix B for

IC 342 and M31, Ward et al. 2020a for the LMC, Hygate 2020 for M33, Chevance et al. 2020c for M51, and Kruijssen et al. 2019 for NGC 300). The parameters not mentioned here include distance, inclination, position angle (see Table 1), as well as parameters related to the fitting process and error propagation, for which default values are adopted as listed in Kruijssen et al. (2018). We use CLUMPFIND (Williams, de Geus & Blitz 1994) to identify gas and SFR tracer peaks in each map. This algorithm finds peaks by drawing closed contours for a set of flux levels, within a given flux range ($\Delta\log_{10}\mathcal{F}$) below the maximum flux level, with an interval of $\delta\log_{10}\mathcal{F}$ between flux levels. The adopted values for our sample are summarized in Table 2. Moreover, to avoid identifying point sources that are likely to be foreground stars that were not masked during the image reduction process or externally illuminated starless dust clumps (see Section 5.3), we only accept peaks that contain more than $N_{pix, min}$ pixels. The area of $N_{pix, min}$ pixels equals 0.2−3.5 times the coarsest beam size. We note that our choices of $\Delta\log_{10}\mathcal{F}$, $\delta\log_{10}\mathcal{F}$, $N_{pix, min}$, $l_{ap, max}$, and N_{ap} don't affect our measurements significantly as long as peaks that are obviously visible in the emission maps have been identified (Kruijssen et al. 2018). As explained above, t_{CO} and its uncertainties determined from our analysis with CO and Hα are used to define the reference time-scales (t_{ref}). However, since we additionally mask some of the bright star-forming regions for the reasons explained in Section 2.3, we re-run the same analysis using Hα as an SFR tracer with updated masks. Our measurements using Hα as an SFR tracer are listed in Table 3, and are in very good agreement with (or identical to) the previously published results. For the analysis with CO and 24 μm, t_{ref} ($= t_{CO}$) includes the feedback phase. The CO(1–0) -to-H$_2$ conversion factor (α_{CO}; including the contribution from heavy elements) is adopted from Bolatto, Wolfire & Leroy (2013), expressed as

$$\alpha_{CO} = \left[2.9 \, M_\odot \, (K \, km \, s^{-1} \, pc^2)^{-1}\right] \times \exp\left(\frac{0.4 \, Z_\odot}{Z}\right). \quad (1)$$

We adopt the metallicity-dependent part, but not the surface density dependence from Bolatto et al. (2013). For simplicity, we adopt a constant α_{CO} value for each galaxy and a conservative uncertainty of 50 per cent. In addition, for M33, which is the only galaxy with CO(2–1) data, we adopt a fixed ratio of CO(2–1) /CO(1–0) = 0.8 (Gratier et al. 2010). Finally, we derive the total SFR for the analysed area by combining 24 μm and Hα emission maps and using the conversion factor from Calzetti et al. (2007), expressed as

$$SFR(M_\odot \, yr^{-1}) = 5.3 \times 10^{-42} \left[L(H\alpha) + 0.031 L(24 \, \mu m)\right], \quad (2)$$
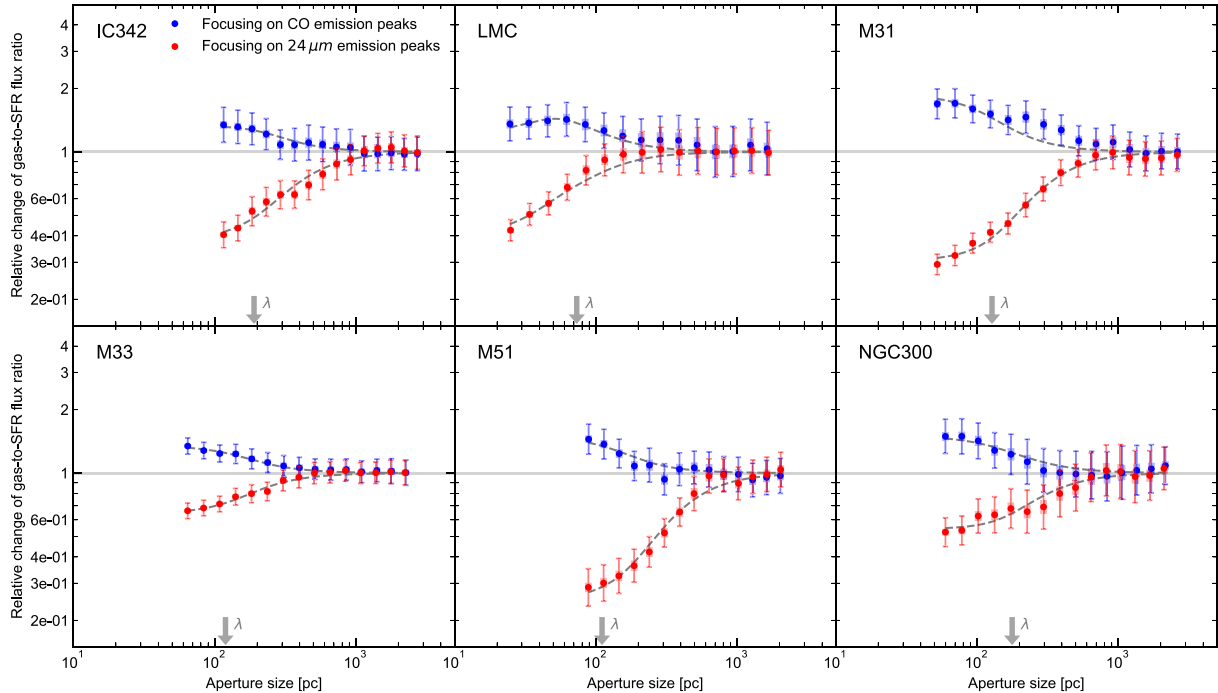
Figure 2. Relative change of the gas-to-SFR (CO-to-24 μm) flux ratio compared to the galactic average as a function of the size of apertures placed on CO (blue) and 24 μm (red) emission peaks. The error bars indicate 1σ uncertainty on each individual data point whereas the shaded area is an effective 1σ uncertainty taking into account the covariance between data points. The galactic average is shown as the solid horizontal line and the dashed line indicates our best-fitting model. The constrained region separation length (λ) is indicated in each panel with the downward arrow and other constrained best-fitting parameters ($t_{fb, 24\,\mu m}$, and $t_{24\,\mu m}$) are listed in Table 3.

where the luminosities have units of erg s^{-1} and $L(24\,\mu m)$ is expressed as $\nu L(\nu)$. We assume a typical uncertainty of 20 per cent for the derived SFR. These conversion factors are only used to derive additional physical quantities such as the molecular gas surface density and the integrated star formation efficiency. We note that the exact values of these conversion factors, unless they vary spatially, do not affect our measurements of primary quantities, which are the durations of the successive phases of cloud evolution and star formation, nor do they affect the region separation length between independent regions.

4 RESULTS

4.1 The molecular cloud lifecycle

Here, we present our results from the application of our method to the maps of CO and 24 μm emission presented in Section 2, as tracers of the molecular gas and the SFR for six nearby galaxies. Fig. 2 shows the gas-to-SFR flux ratios measured around gas and SFR tracer peaks, as a function of aperture size, together with our best-fitting model for each galaxy. Going towards smaller aperture sizes (from ∼1 kpc to ∼50 pc), the measured flux ratios for both branches increasingly deviate from the galactic average, illustrating the spatial de-correlation between the gas and SFR tracer emission peaks. Table 3 summarizes the constrained best-fitting values from applying our analysis to the H α and CO maps, as well as to the 24 μm and CO maps. The first experiment allows us to measure t_{CO}, which is then used as the reference time-scale for the second experiment

(see Section 3). Table 3 also lists other physical quantities which can be derived from our measurements, such as the feedback outflow velocity (v_{fb}; see Section 4.1.5) and the integrated cloud-scale star formation efficiency (ϵ_{sf}; see Section 4.1.4). In Fig. 3, we show an illustration of the evolutionary timelines of molecular clouds and star-forming regions in our galaxy sample. GMCs initially emit only in CO, then in 24 μm after the onset of star formation and finally in H α when the star-forming regions become (partially) exposed.

4.1.1 Feedback time-scale

The use of 24 μm emission enables us to take the heavily obscured phase of star formation into account, which cannot be done with the analysis of only CO and H α emission. The duration of the embedded phase of massive star formation (i.e. feedback time-scale; $t_{fb, 24\,\mu m}$), which continues until disruption of molecular clouds, is measured to be $2-7$ Myr in our sample of galaxies. Our measurements suggest that molecular clouds spend $17 - 47$ per cent of their lifetime with massive stars embedded. For almost all of the galaxies in our sample (except M51), the measured $t_{fb, 24\,\mu m}$ is $1-4$ Myr longer than the one obtained using H α emission ($t_{fb, H\alpha}$; see Table 3). This is expected, as 24 μm is already detected during the heavily obscured phase of star formation, making it visible for a longer duration than H α, which is only detectable when massive stars have formed and surrounding gas and dust have been partially cleared out. By contrast, in the particular case of M51, we find $t_{fb, 24\,\mu m}$ to be shorter than (or comparable within 1σ uncertainty to) the feedback time-scale obtained using H α. We suspect that such a potentially unphysical measurement could be due
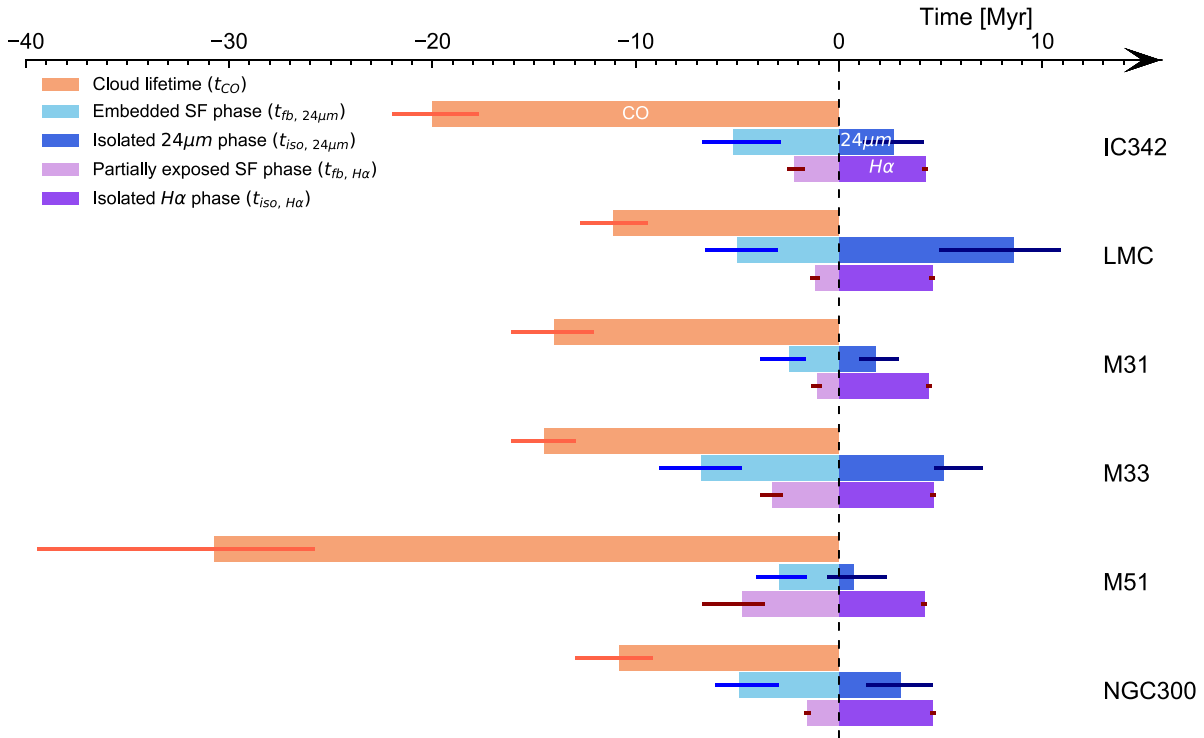
Figure 3. Timeline describing the evolution from molecular clouds to the embedded star-forming phase and then finally to exposed young stellar regions. The time during which CO is visible (=t_{CO}) is indicated in orange, the time during which 24 μm and Hα are visible without CO are shown respectively in dark blue and dark purple. The time-scales for the feedback phase, during which both CO and SFR tracer emissions are observed co-spatially are shown in light blue (for 24 μm) and light purple (for Hα). The corresponding 1σ error bars are also indicated. We note that for M51 the feedback time-scale constrained using 24 μm ($t_{\mathrm{fb, 24\,\mu m}}$) could have been biased by deconvolution artefacts (see Section 4.1.1).

to artefacts in the 24 μm map of M51 introduced by the deconvolution algorithm used to create the high resolution map (Dumas et al. 2011). These artefacts are clearly visible as dark rings around bright peaks in the spiral arms of the galaxy (see Fig. 1 and Appendix A), and may (or may not) make the inferred time-scales less accurate as discussed in Section 2.1.

The measured durations between the onset of embedded star formation and molecular cloud disruption (2−7 Myr), are comparable to the time it takes for the first supernova to explode. This is about 4 Myr for a fully populated stellar initial mass function (Leitherer et al. 2014) and can be up to 20 Myr when the initial mass function is stochastically sampled for the typical stellar region masses considered here (with almost no dependence on metallicity; Chevance et al. 2020a). The measured short feedback time-scales indicate that pre-supernova feedback such as photoionization and stellar winds are mostly responsible for the dispersal of molecular clouds. Our measurements of the feedback time-scale show a good agreement with the typical age of star clusters when they stop being associated with their natal GMCs both in the Milky Way and nearby galaxies (2−7 Myr; Lada & Lada 2003; Whitmore et al. 2014; Hollyhead et al. 2015; Corbelli et al. 2017; Grasha et al. 2018, 2019). This is further discussed in Section 5.2. Radiation magnetohydrodynamic simulations of GMCs by Kim, Ostriker & Filippova (2020) suggest a similar duration of the star formation and feedback time-scales (4−8 Myr). The measured duration for embedded star formation is somewhat shorter than the age spread

of star clusters in the LMC (7−12 Myr) measured by Efremov & Elmegreen (1998), on the scale of the mean radius of SFR tracer peaks (∼10−50 pc). This is expected as the actual size of a star-forming region is necessarily smaller than the size of a SFR tracer peak, which is limited by the spatial resolution of our maps. The agreement gets better if we only consider the age spreads measured among young stellar clusters (1−4 Myr; from star clusters with ages of 1−10 Myr).

4.1.2 Duration of the 24 μm emitting phase

Across all galaxies in our sample, we find that the 24 μm emission phase lasts for 4−14 Myr. For M33, we note that our measurement of $t_{24\,\mu m}$ is in very good agreement with the one from Corbelli et al. (2017), where 24 μm emission is found to last for ∼10 Myr after the onset of massive star formation by applying a cloud classification method to M33. The ratio between duration of visibility for 24 μm and Hα emissions ($t_{24\,\mu m}/t_{H\alpha}$) ranges from 0.4 to 2.3.

The 24 μm emission does not originate only from embedded young massive stars, but also from late-type B stars and the interstellar radiation field, which make a non-negligible contribution to the dust heating (Draine & Li 2007; Verley et al. 2009). The contribution of the sources not related to recent local massive star formation to the 24 μm emission is more homogeneously spread in the galaxy compared to the more clustered young stellar population (e.g. Dale et al. 2007; Leroy et al. 2012) and results in an additional diffuse

component of the 24 µm emission on large scales. We separate this diffuse emission from the compact emission of young stellar regions by applying the filtering process described in Section 3. The fact that in most galaxies the end of the 24 µm emission phase is before or similar to the end of the H α emission phase (see Fig. 3) shows that this procedure effectively removed contamination from stellar populations not related to recent massive star formation. In Section 5.3, we discuss in more detail the effects of starless dust clumps illuminated by external radiation, and late-type B stars still preferentially located near their birth sites, which might not be removed by our filtering process.

We note that, while the duration of the isolated H α emitting phase ($t_{\mathrm{iso,H\alpha}} = t_{\mathrm{H\alpha}} - t_{\mathrm{fb,H\alpha}}$) is almost constant in all the galaxies in our sample by construction (Haydon et al. 2020b), the duration of isolated 24 µm emission ($t_{\mathrm{iso,24\,\mu m}} = t_{24\,\mu m} - t_{\mathrm{fb,24\,\mu m}}$) appears to vary across the sample ranging from ~ 2 Myr (excluding M51) to the end of the H α emitting phase ($8.6^{+2.3}_{-3.7}$ Myr). This isolated phase originates from stochastic heating of small dust grains in the CO dark clouds. We find this phase to be shorter for star-forming regions in more metal-rich galaxies (see Figs 3 and 4). This is discussed in more detail in Section 4.3.

4.1.3 Region separation length

As visible in Fig. 2, gas and SFR tracer peaks are spatially decor-related on small spatial scales, revealing that galaxies are made of regions that are independently undergoing evolution from molecular gas to stars. The spatial scale at which the gas-to-SFR ratio diverges from the galactic average (Fig. 2) is linked to the typical distance λ between independent regions. We find that λ ranges from 70 to 190 pc for the galaxies in our sample when considering the 24 µm and CO emission maps. For M51, we do not sufficiently resolve the region separation length and are only able to obtain an upper limit of λ (see Section 5.1.1). For the other galaxies, we find that λ derived using 24 µm maps and H α maps agree to within the formal uncertainties.

While the physical mechanisms that set the region separation length remain debated, a similarity between the region separation length and the gas disc scale height has been reported by Kruijssen et al. (2019) in NGC 300, suggesting that the depressurization of H II regions along the direction perpendicular to the galactic disc might be responsible for this characteristic length. Furthermore, the measured values of λ are comparable to the thickness of the vertical distribution of star-forming regions undergoing the earliest stages of evolution (150−200 pc) observed using *Spitzer* IRAC 8 µm maps of edge-on spiral galaxies (NGC 891 and IC 5052; Elmegreen & Elmegreen 2020), to the thickness of the molecular disc measured with CO emission (Scoville et al. 1993; Yim et al. 2014; Heyer & Dame 2015; Patra 2020; Yim et al. 2020), and also to the amplitude of the oscillation seen in the Radcliffe Wave recently discovered in the vicinity of the Sun (Alves et al. 2020). Finally, the region separation length roughly coincides with the spatial wavelength of velocity corrugations in NGC 4321 (Henshaw et al. 2020), indicating that it matches the scale on which the molecular interstellar medium is reorganized by cloud-scale matter flows. Further investigation is needed to verify quantitatively whether the correlation observed by Kruijssen et al. (2019) holds more generally in nearby galaxies.

4.1.4 Star-formation efficiency

The SFR surface density (Σ_{SFR}) corresponds to the mass of newly formed stars inferred for a given SFR tracer, divided by that SFR

tracer's emission time-scale. Similarly, the rate of molecular gas formation can be expressed as $\Sigma_{\mathrm{gas}}/t_{\mathrm{CO}}$, where Σ_{gas} is the surface density of molecular gas and the t_{CO} is the time-scale over which molecular gas assembles and form stars. By dividing these two rates, the time-averaged star formation efficiency per star-forming event (ϵ_{sf}) can be computed as:

$$\epsilon_{\mathrm{sf}} = \frac{t_{\mathrm{CO}}\Sigma_{\mathrm{SFR}}}{\Sigma_{\mathrm{gas}}}. \tag{3}$$

When calculating Σ_{gas}, we only consider the compact CO emission, after the filtering of diffuse emission (see Section 3), which is also consistent with the flux we use to determine t_{CO}. By doing this, we selectively include the CO emission that participates in the massive star formation process while excluding emission that is likely to originate from diffuse molecular gas and small clouds. The filtering process removes 10 per cent to 50 per cent of the CO emission from the unfiltered maps. However, Σ_{SFR} is calculated using the total SFR, obtained by combining H α and 24 µm emission to account for the effect of internal extinction (see Section 2). We note that our assumption implies that we attribute all of the diffuse emission in SFR tracer maps to recent massive star formation (e.g. leakage of ionizing photons from H II regions). This ignores the fact that diffuse emission may also originate from mechanisms that are not related to recent massive star formation, such as diffuse ionized gas created by shocks and evolved post-asymptotic giant branch stars, as well as infrared emission powered by older stellar populations, which are known to have a relatively minor contribution to the dust heating (Nersesian et al. 2020). Under these conditions, we measure a low star formation efficiency per star-forming event in our sample of galaxies with $\epsilon_{\mathrm{sf}} = 0.7 - 6.8$ per cent. This is consistent with previous measurements in these galaxies using H α as a tracer of recent star formation and other wavelengths such as *GALEX* FUV and *WISE* 22 µm (Leroy et al. 2012, 2019) to estimate the global SFR (Chevance et al. 2020c; Hygate 2020; Ward et al. 2020a).We note that for NGC 300, we find ϵ_{sf} to be slightly higher (but compatible within 1σ uncertainty) than that measured in Kruijssen et al. (2019). The difference is because Kruijssen et al. (2019) only considered H α emission when calculating the global SFR.

We also compare our measurements for ϵ_{sf} to the fraction of gas converted into stars per gravitational free-fall time, which is expressed as $\epsilon_{\mathrm{ff}} = t_{\mathrm{ff}}\Sigma_{\mathrm{SFR}}/\Sigma_{\mathrm{gas}}$ and measured by Leroy et al. 2017, Utomo et al. 2018 and Schruba, Kruijssen & Leroy (2019) for most of the galaxies in our sample. We find that our measurements for the LMC, M31, M33, and NGC 300 are somewhat (≤ 4.0 per cent) higher than the star formation efficiency per free-fall time (ϵ_{ff}) measured by Schruba et al. (2019), which are 2.5 per cent, 0.7 per cent, 1.5 per cent, and 1.2 per cent, respectively. Because the cloud lifetime in these galaxies is similar to the free-fall time-scale (Schruba et al. 2019), this difference is mostly due to the fact that we measure gas surface density from the diffuse emission filtered CO map, in order to calculate the fraction of compact clouds turning into stars. For M51, the difference becomes more significant ($\epsilon_{\mathrm{ff}} = 0.3 - 0.36$ per cent; Leroy et al. 2017; Utomo et al. 2018) and is because cloud lifetime is almost five times the free-fall time-scale.

4.1.5 Feedback velocity

As a result of the energetic feedback from young massive stars, CO emission becomes rapidly undetectable after the onset of star formation. This is most likely due to a phase and density change of the neighbouring medium through kinetic dispersal, ionization, and photodissociation. We combine the time-scale over which molecular

498   *J. Kim et al.*
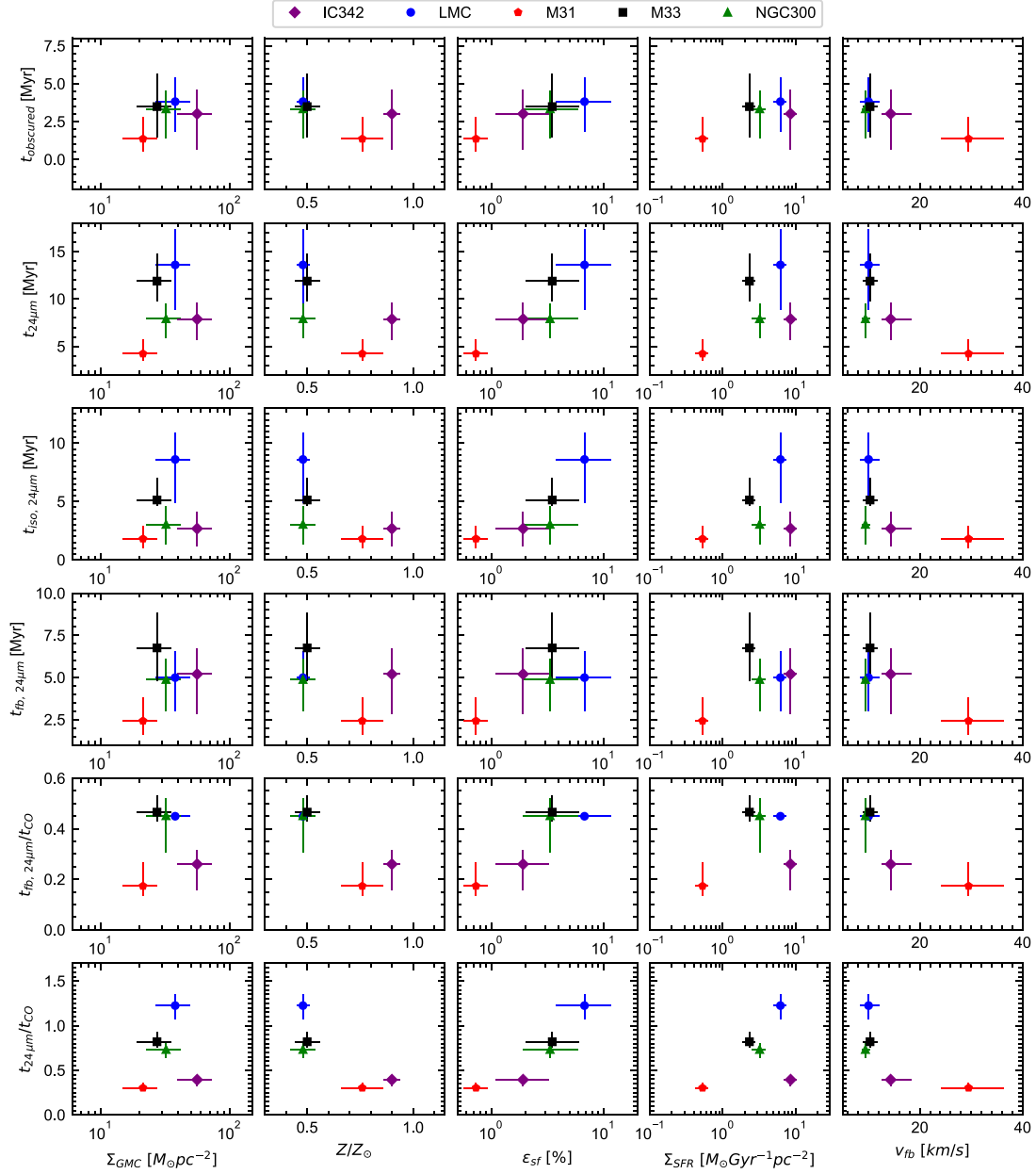
Figure 4. In the top four rows, our measurements of the duration of the heavily obscured phase ($t_{obscured} = t_{fb, 24\,\mu m} - t_{fb, H\alpha}$), the 24 µm emitting phase ($t_{24\,\mu m}$), the isolated 24 µm emitting phase ($t_{iso, 24\,\mu m} = t_{24\,\mu m} - t_{fb, 24\,\mu m}$), and the feedback phase ($t_{fb, 24\,\mu m}$) are shown as a function of galactic (or cloud-scale) properties, i.e. the mass-weighted mean molecular gas surface density of GMCs (Σ_{GMC}) measured in Schruba et al. (2019) and Schruba et al. (2021a), metallicity ($Z/Z_\odot$), star formation efficiency (ϵ_{sf}), SFR surface density (Σ_{SFR}), and the feedback velocity (v_{fb}). The bottom two rows show the ratios of the feedback time-scale and the 24 µm emitting phase to the cloud lifetime ($t_{fb, 24\,\mu m}/t_{CO}$, and $t_{24\,\mu m}/t_{CO}$), as a function of the same galactic properties.

clouds are disrupted by feedback, t_{fb}, with the characteristic size of the clouds detected in CO, r_{CO}, to define the feedback velocity as $v_{fb} = r_{CO}/t_{fb}$. The size of the cloud is measured in our method by fitting a Gaussian profile to the surface density contrast between the peak and the background, and ranges between 10 and 40 pc for the sample of our galaxies. The velocity represents the speed of the kinetic removal of molecular gas or the phase transition

front, depending on the nature of the dispersal mechanism. We use here $t_{fb, H\alpha}$ to define v_{fb}, assuming that disruption of the molecular gas starts with the young stellar population becoming partially exposed, whereas the 24 µm is emitted even during the heavily obscured phase where the expansion of the H II region has not yet begun and during which gas accretion on to the cloud potentially continues.

The derived v_{fb} ranges between 9 and 30 km s^{-1}, which is comparable to the measurements of expansion velocities of nearby H II regions. For example, the expansion velocities of five H II regions in NGC 300 are measured to be in the range of $5-30$ km s^{-1} (McLeod et al. 2020). Similar values are also found for H II regions in the LMC (Nazé et al. 2001, 2002; McLeod et al. 2019) and the Milky Way (Murray & Rahman 2010; Barnes et al. 2020). Numerical simulations of star-forming regions (e.g. Kim, Kim & Ostriker 2018) also support this range of values.

4.2 Heavily obscured phase of star formation

In order to probe the earliest phase of star formation, which is only associated with 24 μm emission and not with H α because of strong attenuation provided by the surrounding gas, we measure the duration of the heavily obscured phase of star formation as the difference between the feedback time-scale for 24 μm emission (i.e. the total duration of the embedded phase of star formation) and the one for H α emission (i.e. the duration of the partially exposed phase of star formation): $t_{\mathrm{obscured}} = t_{\mathrm{fb, 24\,\mu m}} - t_{\mathrm{fb, H\alpha}}$. We omit M51 here because the insufficient resolution of the 24 μm map only allows for the determination of an upper limit on $t_{\mathrm{fb, 24\,\mu m}}$ (see Section 5.1.1) and the presence of deconvolution artefacts (see Section 2.1) could have biased our measurements, especially for time-scale-related quantities. However, we retain M51 in our sample at large, to show our (unsuccessful) attempt in applying the method to a 24 μm emission map that has been created using the HiRes deconvolution algorithm (Backus et al. 2005). Across the rest of our galaxy sample, we find $t_{\mathrm{obscured}} = 3.0 \pm 0.9$ Myr, with a full range of $1.4-3.8$ Myr (see Fig. 4). The measured duration is comparable to age estimates of heavily obscured star clusters in the Milky Way ($0.5-3$ Myr; see Lada & Lada 2003, and references therein). A similar duration of the highly embedded star-forming phase has recently been reported by Elmegreen & Elmegreen (2019), Elmegreen & Elmegreen (2020), where such a phase is suggested to last for $1-2$ Myr based on the mass measurement of star-forming cores in nearby spiral galaxies using 8 μm emission. The measurement of 2.4 Myr for the heavily obscured phase using a cloud classification method by Corbelli et al. (2017) also supports the values we obtain here (see more in Section 5.2).

4.3 Relation with environmental properties

We now explore potential environmental dependences of the durations of the successive phases of cloud evolution and star formation. In Fig. 4, our measurements of the durations of the heavily obscured phase (t_{obscured}), the total 24 μm emission phase ($t_{24\,\mu m}$), the isolated 24 μm emission phase ($t_{\mathrm{iso,24\,\mu m}} = t_{24\,\mu m} - t_{\mathrm{fb, 24\,\mu m}}$), and the feedback phase ($t_{\mathrm{fb, 24\,\mu m}}$) are shown in the top four rows as a function of local cloud-scale and galactic properties such as the mass-weighted mean molecular gas surface density of GMCs (Σ_{GMC}; measured by Schruba et al. 2021a for IC342 and Schruba et al. 2019 for the other galaxies), metallicity (relative to solar metallicity), integrated star formation efficiency per star formation event (ϵ_{sf}), SFR surface density (Σ_{SFR}), and the feedback velocity (v_{fb}).[4]

In order to look for correlations with these environmental properties, we use LINMIX (Kelly 2007), a Bayesian method accounting

---

[4]The measurement of Σ_{GMC} for IC 342 is calculated excluding the five most massive clouds (with mass $>2 \times 10^7\,\mathrm{M_\odot}$), which contribute 13 per cent of the total mass contained in molecular clouds. Including these clouds would not change our conclusion.

for measurement errors in linear regression. We do not find any statistically significant trend, which is defined to exist when the correlation coefficient is positive or negative with 95 per cent probability. While this is not shown in Fig. 4, we also found no statistically significant correlation with the galaxy-averaged molecular gas surface density (Σ_{gas}). However, we note that $t_{24\,\mu m}$ and $t_{\mathrm{iso,24\,\mu m}}$ appear to be somewhat shorter towards increasing metallicity and decreasing star formation efficiency. While it is difficult to distinguish what is driving this trend, as metallicity and star formation efficiency are correlated in our sample of galaxies, we suspect that metallicity could be the primary driver of this trend. Indeed, winds from massive stars become more energetic with increasing metallicity (Maeder 1992), resulting in a faster dispersal of the surrounding gas and decay of $t_{24\,\mu m}$ emission. We note that one might expect to see longer (isolated) 24 μm emitting time-scale for metal-rich galaxies since the dust-to-gas ratio correlates with metallicity (Rémy-Ruyer et al. 2014). This is not what we find here, which can be explained by our use of relative changes of gas-to-SFR tracer flux ratio compared to the galactic average, instead of using absolute flux ratios, when constraining the timeline of GMC evolution.

The relative fractions of $t_{\mathrm{fb, 24\,\mu m}}$ and $t_{24\,\mu m}$ compared to t_{CO} are plotted against galactic properties in the bottom two rows of Fig. 4. We again see an anticorrelation of these durations with metallicity and a correlation with star formation efficiency, while no statistically significant trend is found with respect to galactic properties using the same regression analysis (Kelly 2007). Our results (bottom row) show that clouds in the LMC, M33, and NGC 300 spend a larger fraction of their lifetime with embedded massive star formation ($\sim$40 per cent) compared to clouds in IC 342 and M31 ($\sim$20 per cent), with an average of 36 per cent across our sample of galaxies.

5 DISCUSSION

5.1 Robustness of the results

5.1.1 Satisfaction of guidelines in Kruijssen et al. (2018)

We verify here that our analysis satisfies the requirements listed in section 4.4 of Kruijssen et al. (2018). Satisfaction of these criteria indicates that the constrained parameters $t_{24\,\mu m}$, $t_{\mathrm{fb, 24\,\mu m}}$, and λ are measured with an accuracy of at least 30 per cent. For the analysis using H α as an SFR tracer, we only check the accuracy for IC 342 and M31, because the measurements for other galaxies have already been validated by previous studies (see Kruijssen et al. 2019; Chevance et al. 2020c; Hygate 2020; Ward et al. 2020a).

(i) The duration of gas and stellar phases should always differ less than one order of magnitude. This condition is satisfied by $|\log_{10}(t_{\mathrm{H\alpha}}/t_{\mathrm{CO}})| \leq 0.5$ for IC 342 and M31, and $|\log_{10}(t_{24\,\mu m}/t_{\mathrm{CO}})| \leq 0.92$ for all the galaxies in our sample, where the difference between $t_{24\,\mu m}$ and t_{CO} is the largest in M51 while those for other galaxies are $|\log_{10}(t_{24\,\mu m}/t_{\mathrm{CO}})| \leq 0.52$.

(ii) For almost all of the galaxies (except M51), we measure $\lambda \geq 1.6 l_{\mathrm{ap, min}}$, which ensures that the region separation length is sufficiently resolved by our observations. For M51, we measure $\lambda = 1.2 l_{\mathrm{ap, min}}$, implying that $t_{24\,\mu m}$ can be constrained with sufficient accuracy, but only upper limits can be derived for λ and $t_{\mathrm{fb, 24\,\mu m}}$.

(iii) The number of identified emission peaks is always above 35, both in the CO and the 24 μm emission maps, as well as in the H α maps of IC 342 and M31.

(iv) The measured gas-to-SFR flux ratios focussing on gas (SFR tracer) peaks should never be below (above) the galactic average.

This condition may not always be true in the presence of a diffuse emission reservoir. As visible in Fig. 2, this criterion is satisfied after we filter out the large-scale diffuse emission in both tracer maps.

(v) In order to perform accurate measurements, we require the global star formation history to not vary more than 0.2 dex during the duration of the whole evolutionary cycle (ranging from ∼15 to 35 Myr for our sample) when averaged over time intervals of width $t_{24\,\mu m}$ or t_{CO}. Using multiwavelength data of the LMC and synthetic stellar population models, Harris & Zaritsky (2009) studied the star formation history in the LMC and found a roughly consistent SFR during the duration of the whole evolutionary cycle. The criterion is also satisfied in M33 and NGC 300 as shown by Kang et al. (2012), Kang et al. (2016) using chemical evolution models to reconstruct the star formation rate history. Using data from the PHAT survey, the recent star formation history of M31 is confirmed to be quiescent without significant variations (Lewis et al. 2015; Williams et al. 2017). By performing spectral energy distribution (SED) fitting to the multiwavelength data of M51, the SFR in M51 is also measured to be roughly constant for the last 100 Myr (Eufrasio et al. 2017). The star formation history of IC 342 is not known. However, we do not expect it to experience significant variations in the global star formation rate during the last ∼30 Myr when averaged over $t_{24\,\mu m} = 8$ Myr. In addition, we mask the starburst nucleus of this galaxy, which experienced a major burst of star formation ∼60 Myr ago (Böker, van der Marel & Vacca 1999).

(vi) Each independent region should be detectable at given sensitivity in both tracers at some point in their life. In order to check if this condition is satisfied in our sample of galaxies, we first calculate the minimum star-forming region mass expected to form from the detected molecular clouds by multiplying the star formation efficiency obtained in our method (see Table 3) by the 5σ point-source sensitivity limit of the CO map. We then compare this mass to the mass of the stellar population required to provide an ionizing radiation luminosity that matches the 5σ sensitivities of 24 μm and H α maps on the scale of individual star-forming regions (λ). We use the Starburst99 model (Leitherer et al. 1999) to calculate the initial mass of the stellar population assuming stars formed instantaneously 5 Myr ago (similarly to the H α emitting time-scale). Since Starburst99 only provides models for the H α luminosity as a function of the age of the stellar population at different metallicities, we use the relation from Kennicutt & Evans (2012, and references therein), $\log SFR = \log(L_{H\alpha}) - 41.27 = \log(\nu L_{24\,\mu m}) - 42.69$, to obtain a similar estimation of the 24 μm luminosity. We find that the minimum mass of the stellar population obtained from CO maps agrees well with that obtained from 24 μm and H α maps (ranging from 100 to 5000 $M_\odot$ for the galaxies in our sample), suggesting that the sensitivity of the gas and SFR tracer maps are well-matched and the faintest CO peak is likely to evolve into the faintest H II region. In principle, clouds can disperse dynamically before forming massive stars and then reassemble. In this case, the time spent before GMC dispersal would be added by our method to the measured lifetimes of clouds that do form massive stars. However, Kruijssen et al. (2019) and Chevance et al. (2020c) show that this is unlikely to happen because the clouds are found to live only for about one dynamical time-scale, not leaving enough time for clouds to disperse and recollapse before forming massive stars.

Most of our measurements of $t_{24\,\mu m}$ and λ for all the galaxies in our sample as well as the t_{CO} and λ for IC 342 and M31 with H α as an SFR tracer are validated by satisfying the conditions listed above. The only exception is for M51, where we neither have sufficient resolution to accurately constrain the region separation length nor

the feedback time-scale. Only upper limits can be obtained for these values. In order to determine whether our measurements are reliable for $t_{fb,\,24\,\mu m}$ for all the galaxies in our sample and $t_{fb,\,H\alpha}$ for IC 342 and M31, we use four additional criteria listed in Kruijssen et al. (2018). To do so, we first introduce the filling factor of SFR tracer or gas peaks as $\zeta = 2r/\lambda$, where r is the mean radius of the corresponding peaks. This parameter characterizes how densely the peaks are distributed in a map.

i) If peaks are densely distributed and potentially overlapping with each other, the density contrast used for peak identification ($\delta\log_{10}\mathcal{F}$) should be small enough to identify adjacent peaks. We compare in Fig. 5 our values for $\delta\log_{10}\mathcal{F}$ with the upper limit prescribed by Kruijssen et al. (2018) and show that our choice enables the appropriate detection of neighbouring peaks, even in densely populated environments.

ii) For an accurate measurement of the feedback time-scale, contamination by neighbouring peaks should be small enough. Indeed, spatial overlap of neighbouring peaks due to low resolution or blending can be falsely attributed to a temporal overlap, therefore artificially increasing the duration of the measured feedback time-scale. In this case, only an upper limit on the feedback time-scale can be determined. In Fig. 5, we compare the analytical prescription of Kruijssen et al. (2018) with our measurements of t_{fb}/τ and average ζ, where τ is the total duration of the whole evolutionary cycle ($\tau = t_{CO} + t_{24\,\mu m} - t_{fb,\,24\,\mu m}$). The average ζ is obtained by weighting the filling factors for gas and SFR tracer peaks by their corresponding time-scales. We find that this condition is not satisfied for $t_{fb,\,24\,\mu m}$ in M51. Only upper limits on this quantity can be determined (see Table 3).

iii) Fig. 5 shows that the conditions $t_{fb} > 0.05\tau$ and $t_{fb} < 0.95\tau$ are verified for all galaxies.

iv) Similarly to condition (v), the SFR should not vary more than 0.2 dex during the entire timeline when averaged over the width of feedback time-scale. This condition is also satisfied using the same reasoning, as stated in (v) above.

v) After masking obvious blended regions such as galactic centres, visual inspection of the maps does not reveal abundant blending (Fig. 1).

Overall, we find that our measurements are reliable except for λ and $t_{fb,\,24\,\mu m}$ in M51. These two measurements should formally be considered as upper limits as they do not satisfy conditions (ii) and (viii). However, we note that the deconvolution artefacts present in the 24 μm map of M51 may (or may not) bias the feedback time-scale and therefore the value we obtain as the upper limit should be considered uncertain.

5.1.2 Effect of spatial resolution and inclination on the measured quantities

In order to test the potential effect of spatial resolution on our measurements, we have degraded the resolution of the CO and 24 μm emission maps of NGC 300 to the coarsest resolution among our galaxy sample (107 pc, see Table 1) and repeated the analysis described in Section 3. We choose NGC 300 for this test as it does not require bright star-forming regions to be masked like in the LMC and M33, making the application of the method more straightforward. We find that time-scales ($t_{24\,\mu m} = 8.4^{+3.8}_{-2.1}$ Myr; $t_{fb,\,24\,\mu m} = 4.8^{+1.5}_{-2.6}$ Myr) and the mean separation length ($\lambda = 217^{+145}_{-112}$ pc) measured at a different spatial resolution are consistent within 1σ uncertainties with the results of Table 3, confirming previous resolution tests on
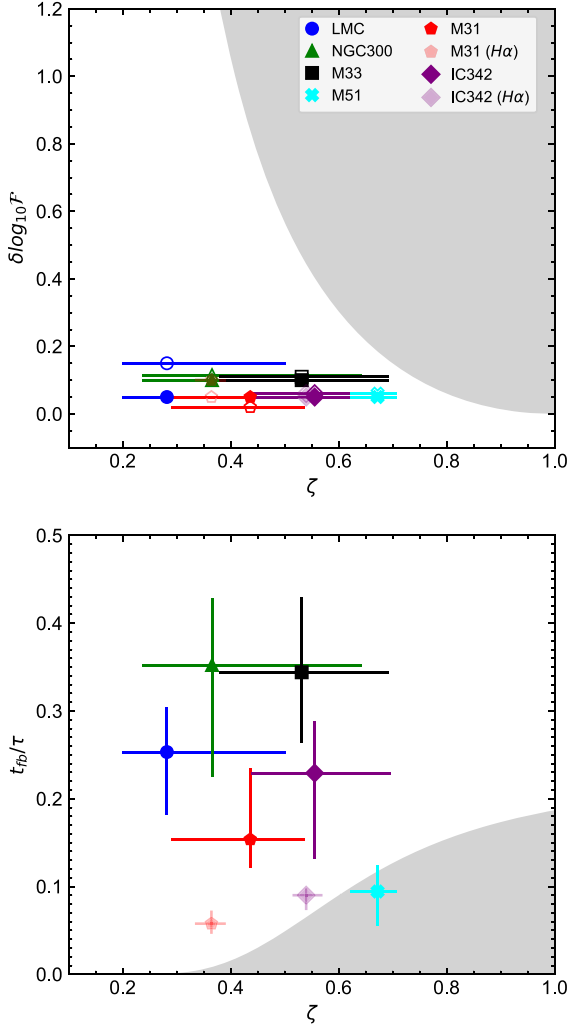
Figure 5. Effects of blending on the feedback time-scale measurements. The top panel shows the adopted density contrasts ($\delta \log_{10} \mathcal{F}$) used for peak identification in each 24 µm (filled symbols) and CO (open symbols) emission map, as a function of the average filling factor ζ. The transparent markers for IC 342 and M31 indicate the adopted $\delta \log_{10} \mathcal{F}$ and measured ζ for the analysis with Hα as SFR tracer. The shaded area indicates the region of the parameter space where peak identification is affected by blending (Kruijssen et al. 2018). Our results are well outside of the shaded area, confirming that we adopt small enough $\delta \log_{10} \mathcal{F}$ to identify adjacent peaks even in maps with high-filling factor. The bottom panel shows the ratio between the feedback time-scale ($t_{\rm fb}$) and the total duration of the whole evolutionary cycle (τ) as a function of the average filling factor. The grey shaded area indicates the region of the parameter space where the contamination by neighbouring peaks affects the measurement of the feedback time. As a result, only an upper limit can be determined for $t_{\rm fb, 24\,\mu m}$ in M51, whereas accurate measurements can be made for all other galaxies.

simulated galaxies (Kruijssen et al. 2018) and on NGC 300 (Kruijssen et al. 2019) using Hα as a SFR tracer.

We have also examined the possible effect of inclination on our measurements by repeating the analysis on CO and 24 µm emission maps of NGC 300, which have been artificially inclined further to match the highest inclination angle among our galaxy sample

(M31; $i = 77.7°$). We find that measured time-scales ($t_{24\,\mu m} = 10.4^{+2.7}_{-2.0}$ Myr, $t_{\rm fb, 24\,\mu m} = 3.9^{+1.0}_{-0.9}$ Myr) and the mean separation length ($\lambda = 192^{+130}_{-60}$ pc) agree within 1σ uncertainties with those of NGC 300 from Table 3. This is already expected from a similar test performed by Kruijssen et al. (2018) using simulated galaxies, where our method has been shown to provide reliable measurements even for a highly inclined galaxy as long as independent star-forming regions are sufficiently resolved ($\lambda \geq 1.5 l_{\rm ap, min}$; see (ii) in Section 5.1.1).

5.2 Comparison with other works

The duration of the embedded star-forming phase has been measured in M33 by Corbelli et al. (2017), using IRAM CO data and the mid-infrared source catalog created by Sharma et al. (2011). In their work, GMCs and star-forming regions are classified into different evolutionary stages based on the presence of CO emission and SFR tracers such as 24 µm and Hα or UV emission. The clouds are defined to be in an inactive stage when no sign of star formation is detected, an embedded star-forming phase when CO emission is observed in association with 24 µm but without associated Hα or FUV emission. The region is defined to be at an exposed star-forming phase when Hα or FUV emission becomes visible.

The age estimates of the exposed star-forming regions (referred to as C-type in Corbelli et al. 2017) from SED fitting are available in Sharma et al. (2011), and are obtained using photometric data at various wavelengths simultaneously, such as UV, Hα, and 24 µm. The age of the C-type phase corresponds to the time it takes for the cloud to evolve from the end of the heavily obscured phase of star formation (observed with 24 µm but without Hα) to the end of the exposed young stellar region phase (both 24 µm and Hα are observed). This duration therefore corresponds to $t_{24\,\mu m} - t_{\rm obscured}$ in our analysis. Corbelli et al. (2017) find that the C-type phase in M33 lasts for 8 Myr (without quoted uncertainty), which is in excellent agreement with our measurement of $8.4^{+3.6}_{-3.0}$ Myr. For the duration of the heavily obscured phase of star formation (CO and 24 µm emission without Hα; referred to as B-type), Corbelli et al. (2017) find 2.4 Myr, which is similar to the duration we measure, not only for M33 ($3.5^{+1.2}_{-1.9}$ Myr), but for most of the galaxies in our sample (1.4 − 3.8 Myr; see Section 4.2). Lastly, as for the duration of the inactive phase (referred to as A-type), we measure $t_{\rm CO} - t_{\rm fb, 24\,\mu m} = 7.7^{+1.4}_{-1.7}$ Myr, which is somewhat longer than the measurement of 4 Myr from Corbelli et al. (2017). However, given the uncertainties in age estimates using SED fitting (on the order of 0.1 dex) and the absence of any uncertainties on their estimates, the evolutionary timeline of molecular clouds of M33 from Corbelli et al. (2017) and our analysis are in good agreement.

The time it takes for the star-forming regions to become exposed has also been measured using wavelengths other than 24 µm as a tracer for the embedded star formation. Calzetti et al. (2015) have measured ages of young massive star clusters in the dwarf starburst galaxy NGC 5253 by applying SED modelling techniques on UV-optical-near-infrared *Hubble Space Telescope* photometry. While the star clusters have ages spanning from 1 to 15 Myr, the age estimate of one very heavily attenuated cluster with a clear near-infrared excess indicates that the duration of the heavily obscured phase of star formation is longer than (or similar to) 1 Myr for this particular star-forming region. Whitmore et al. (2014) used free–free radio continuum emission to detect heavily obscured star-forming regions, and charaterized the evolutionary timeline from quiescent molecular clouds to exposed star-forming phase using age estimates from SED fitting of young stellar regions in the overlap region of the merging

Antennae galaxies. The duration of the heavily obscured phase (referred to as Stage 2 in Whitmore et al. 2014) and the feedback time-scale (including the embedded phase; referred to as Stage 3 in Whitmore et al. 2014) are measured to be 0.1−1 and 1−3 Myr, somewhat shorter than the duration we measure with 24 μm, which are 1−4 and 2−7 Myr, respectively. We note that this difference could be because (i) the measurements are for galaxies undergoing a merger, unlike our sample; (ii) a different tracer is used to trace embedded star formation; and (iii) age estimates in highly extincted regions have considerable uncertainties (Hollyhead et al. 2015).

In conclusion, despite differences in methods, wavelengths, and galaxies used when constraining the evolutionary cycle of star-forming regions, our results are in good agreement with the measured time-scales for the heavily obscured phase and feedback phase found in previous literature. The key step made in the present paper is to generalize these results to a sample of five galaxies (except M51), analysed homogeneously with a single analysis framework that is agnostic about which entities constitute a GMC or star-forming region.

5.3 Effects of infrared emission not associated with local recent massive star formation

24 μm emission is widely used as a tracer for embedded star formation, as it captures emission of massive stars that has been reprocessed by dust grains (see e.g. Calzetti et al. 2007; Kennicutt & Evans 2012; Vutisalchavakul & Evans 2013). However, one of the known issues with using 24 μm emission to trace recent star formation is that the interstellar radiation field, late-type B stars (age of ∼100 Myr), and dust clumps heated by external radiation such as nearby star-forming regions also contribute to the emission at this wavelength (Calzetti et al. 2007; Murphy et al. 2011; Kennicutt & Evans 2012; Leroy et al. 2012).

The difference in spatial distributions associated with each process generating 24 μm emission allows us to separate the emission for recent star formation events from other sources. The 24 μm emission originating from the interstellar radiation field has an extended morphology, because it originates from small dust grains in the diffuse interstellar medium (Draine & Li 2007; Draine et al. 2007; Verley et al. 2009; Rahman et al. 2011; Leroy et al. 2012). Such diffuse emission, constituting on average of 55 per cent of the 24 μm emission, is therefore expected to be removed during our filtering process.

On the other hand, the effect of 24 μm emission associated with late-type B stars and starless dust clumps might not be filtered out because they are more inhomogeneously distributed, similarly to the emission from young star-forming regions. To estimate the effect of late-type B stars and externally illuminated dust clumps on our measurements, we make use of the far-infrared source catalogue of the LMC provided by Seale et al. (2014). In this catalogue, young stellar objects and dust clumps (that may or may not have deeply embedded forming stars) are identified, as well as sources not related to recent star formation such as asymptotic giant branch stars, planetary nebulae, and supernova remnants using literature catalogues (Seale et al. 2014 and references therein). In order to test whether the inclusion of 24 μm emission from older stars and dust clumps could bias our results, we mask these sources and repeat our analysis of the LMC. When masking dust clumps, we mask all the probable candidates in Seale et al. (2014) as it is difficult to distinguish whether these clumps harbour deeply embedded stars or are heated by external radiation. We find that the older stars and dust clumps have a negligible effect on our results. In practice, older stars

and dust clumps are not usually identified as SFR tracer peaks in our analysis due to their low brightness and small size, which does not satisfy the requirement of a minimum number of pixels to be identified as a peak in our method.

In conclusion, once the diffuse emission has been filtered, the 24 μm maps mostly contain emission from young stars. Any potential bias due to the interstellar radiation field, late-type B stars, and dust clumps is negligible and our measurements of $t_{24\,\mu m}$ provide an accurate characterization of the duration of (partially) embedded massive stars.

6 CONCLUSION

We present a characterization of the evolutionary timeline from molecular clouds to young stellar regions in six nearby galaxies by applying the statistical method developed by Kruijssen & Longmore (2014) and Kruijssen et al. (2018) to CO and 24 μm emission maps at cloud-scale (20−100 pc) resolution. With this method, we measure the duration of the 24 μm emission phase ($t_{24\,\mu m}$), the duration of the feedback phase ($t_{\rm fb, 24\,\mu m}$) during which massive star formation continues embedded in molecular clouds, the duration of the heavily obscured star formation phase with no associated H α emission ($t_{\rm obscured}$), and the average distance between independent star-forming regions evolving from clouds to massive star formation (λ). We also derive other physical quantities such as the feedback velocity ($v_{\rm fb}$) and the integrated star formation efficiency per star formation event ($\epsilon_{\rm sf}$) from our measurements.

Across our sample of galaxies, we find that molecular clouds are quickly disrupted within 2−7 Myr after the onset of embedded massive star formation (traced by 24 μm emission) by stellar feedback, supporting the fact that GMCs are dispersed within a cloud dynamical time-scale, as suggested by Elmegreen (2000) and Hartmann (2001). The measured feedback time-scale, which includes the duration of the massive star-forming phase, constitutes 17−47 per cent of the cloud lifetime of 10−30 Myr. The feedback time-scales are generally shorter than the time it takes for the first supernova to explode (4−20 Myr), when stochasticity of the initial mass function is taken into account (Chevance et al. 2020a), suggesting that early feedback mechanisms such as photoionization and stellar winds are mainly responsible for the dispersal of molecular clouds. Previous works have found similar duration of this phase using age estimates of star clusters in the Milky Way and some nearby galaxies (Lada & Lada 2003; Whitmore et al. 2014; Corbelli et al. 2017). After the molecular gas is dispersed, the 24 μm emission decays within 2−9 Myr. Our results further support the conclusion of earlier work that galaxies are composed of independent star-forming regions separated by ∼100−200 pc (Kruijssen et al. 2019; Chevance et al. 2020c), which may correspond to the vertical gas disc scale height (see Kruijssen et al. 2019). These regions are undergoing an inefficient star-forming process with integrated cloud-scale star formation efficiencies ($\epsilon_{\rm sf}$) of 0.7−6.8 per cent. The measured star formation efficiencies are consistent with previous measurements in these galaxies using other tracers to estimate the global SFR. We obtain feedback velocities ($v_{\rm fb}$) of 8−30 km s^{-1}, which is consistent with the observed expansion velocities of nearby H II regions (e.g. Murray & Rahman 2010; McLeod et al. 2019, 2020; Barnes et al. 2020).

By combining our measurements with those using H α as a tracer for exposed star-forming regions, we also measure the duration of the heavily obscured phase (detected with CO and 24 μm but without H α emission). Our results show that this period lasts for 3.0 ± 0.9 Myr (with a full range of 1.4−3.8 Myr across our sample of galaxies). We

do not detect any significant correlation of the duration of this heavily obscured phase with galactic properties. This measured duration is in good agreement with values suggested by previous works using different wavelengths, methods, and galaxies.

Furthermore, we study the correlation of our measurements with galactic (or cloud-scale) properties, such as mass-weighted mean surface density of GMCs, metallicity, star formation efficiency, SFR surface density, and the feedback velocity. While we do not find statistically significant trends, the durations of the total and isolated 24 μm emission phases ($t_{24\,\mu m}$ and $t_{iso,24\,\mu m}$) may weakly decrease with increasing metallicity. We conjecture that this dependence results from winds of massive stars being stronger and more energetic at higher metallicities, which leads to a more effective dispersal of the clouds. No such trends with metallicity are observed for the feedback time-scale and the duration of the heavily obscured phase.

In order to gain a better understanding of the mechanisms driving the early feedback process, a systematic measurement of the embedded phase in a large number of galaxies in various environments is essential. Due to the limited resolution of *Spitzer* 24 μm observations (6.4 arcsec), we have been able to perform this analysis for only six nearby galaxies and accurately constrain the duration of the embedded phase in five of them. In the future, the MIRI imager aboard the *James Webb Space Telescope*, with a field of view of $1' \times 2'$, will reach an angular resolution of 0.7 arcsec. This will enable the application of the same method to galaxies located out to 25 Mpc, covering a much wider range of galaxy properties and morphologies, allowing us to explore how the feedback processes govern the evolution of molecular clouds during the early stages of star formation, as a function of the galactic environment.

ACKNOWLEDGEMENTS

DATA AVAILABILITY

The data underlying this article will be shared on reasonable request to the corresponding author.

REFERENCES

Alves J. et al., 2020, Nature, 578, 237
Aniano G., Draine B. T., Gordon K. D., Sandstrom K., 2011, PASP, 123, 1218
Asplund M., Grevesse N., Sauval A. J., Scott P., 2009, ARA&A, 47, 481
Azimlu M., Marciniak R., Barmby P., 2011, AJ, 142, 139
Backus C., Velusamy T., Thompson J., Arballo J., 2005, Astronomical Data Analysis Software and Systems XIV, 347, Hires: Super-resolution for the Spitzer Space Telescope. p. 61
Barnes A. T., Longmore S. N., Dale J. E., Krumholz M. R., Kruijssen J. M. D., Bigiel F., 2020, MNRAS, 498, 4906
Bigiel F., Leroy A., Walter F., Brinks E., de Blok W. J. G., Madore B., Thornley M. D., 2008, AJ, 136, 2846
Blitz L., Fukui Y., Kawamura A., Leroy A., Mizuno N., Rosolowsky E., 2007, in Reipurth B., Jewitt D., Keil K., eds, Protostars and Planets V. p. 81
Böker T., van der Marel R. P., Vacca W. D., 1999, AJ, 118, 831
Bolatto A. D., Wolfire M., Leroy A. K., 2013, ARA&A, 51, 207
Bresolin F., 2011, ApJ, 730, 129
Caldú-Primo A., Schruba A., 2016, AJ, 151, 34
Calzetti D. et al., 2005, ApJ, 633, 871
Calzetti D. et al., 2007, ApJ, 666, 870
Calzetti D. et al., 2015, ApJ, 811, 75
Cardelli J. A., Clayton G. C., Mathis J. S., 1989, ApJ, 345, 245
Chevance M. et al., 2020a, preprint (arXiv:2010.13788)
Chevance M. et al., 2020b, Space Sci. Rev., 216, 50
Chevance M. et al., 2020c, MNRAS, 493, 2872
Colombo D. et al., 2014, ApJ, 784, 4
Corbelli E. et al., 2017, A&A, 601, A146
Corbelli E., Lorenzoni S., Walterbos R., Braun R., Thilker D., 2010, A&A, 511, A89
da Silva R. L., Fumagalli M., Krumholz M., 2012, ApJ, 745, 145
da Silva R. L., Fumagalli M., Krumholz M. R., 2014, MNRAS, 444, 3275
Dalcanton J. J. et al., 2009, ApJS, 183, 67
Dalcanton J. J. et al., 2012, ApJS, 200, 18

Dale D. A. et al., 2007, ApJ, 655, 863
Dale D. A. et al., 2009, ApJ, 703, 517
Dale J. E., 2015, New A Rev., 68, 1
Draine B. T. et al., 2007, ApJ, 663, 866
Draine B. T., Li A., 2007, ApJ, 657, 810
Druard C. et al., 2014, A&A, 567, A118
Dumas G., Schinnerer E., Tabatabaei F. S., Beck R., Velusamy T., Murphy E., 2011, AJ, 141, 41
Efremov Y. N., Elmegreen B. G., 1998, MNRAS, 299, 588
Elmegreen B. G., 2000, ApJ, 530, 277
Elmegreen B. G., Elmegreen D. M., 2019, ApJS, 245, 14
Elmegreen B. G., Elmegreen D. M., 2020, ApJ, 895, 71
Engargiola G., Plambeck R. L., Rosolowsky E., Blitz L., 2003, ApJS, 149, 343
Eufrasio R. T. et al., 2017, ApJ, 851, 10
Faesi C. M., Lada C. J., Forbrich J., Menten K. M., Bouy H., 2014, ApJ, 789, 81
Feldmann R., Gnedin N. Y., Kravtsov A. V., 2011, ApJ, 732, 115
Fitzpatrick E. L., 1999, PASP, 111, 63
Fitzpatrick E. L., Massa D., 2007, ApJ, 663, 320
Ford G. P. et al., 2013, ApJ, 769, 55
Fukui Y. et al., 2008, ApJS, 178, 56
Gaia Collaboration, 2018, A&A, 616, A1
Gaustad J. E., McCullough P. R., Rosing W., Van Buren D., 2001, PASP, 113, 1326
Gieren W. et al., 2013, ApJ, 773, 69
Gordon K. D. et al., 2006, ApJ, 638, L87
Grasha K. et al., 2018, MNRAS, 481, 1016
Grasha K. et al., 2019, MNRAS, 483, 4707
Gratier P. et al., 2010, A&A, 522, A3
Greenawalt B. E., 1998, PhD thesis, New Mexico State University
Harris J., Zaritsky D., 2009, AJ, 138, 1243
Hartmann L., 2001, AJ, 121, 1030
Haydon D. T., Fujimoto Y., Chevance M., Kruijssen J. M. D., Krumholz M. R., Longmore S. N., 2020a, MNRAS, 497, 5076
Haydon D. T., Kruijssen J. M. D., Chevance M., Hygate A. P. S., Krumholz M. R., Schruba A., Longmore S. N., 2020b, MNRAS, 498, 235
Henshaw J. D. et al., 2020, Nat. Astron., 4, 1064
Herrera C. N. et al., 2020, A&A, 634, A121
Heyer M., Dame T. M., 2015, ARA&A, 53, 583
Hollyhead K., Bastian N., Adamo A., Silva-Villa E., Dale J., Ryon J. E., Gazak Z., 2015, MNRAS, 449, 1106
Hoopes C. G., Walterbos R. A. M., 2000, ApJ, 541, 597
Hygate A. P. S., 2020, PhD thesis, Ruperto-Carola-University of Heidelberg
Hygate A. P. S., Kruijssen J. M. D., Chevance M., Schruba A., Haydon D. T., Longmore S. N., 2019, MNRAS, 488, 2800
Jacobs B. A., Rizzi L., Tully R. B., Shaya E. J., Makarov D. I., Makarova L., 2009, AJ, 138, 332
Jameson K. E. et al., 2016, ApJ, 825, 12
Kang X., Chang R., Yin J., Hou J., Zhang F., Zhang Y., Han Z., 2012, MNRAS, 426, 1455
Kang X., Zhang F., Chang R., Wang L., Cheng L., 2016, A&A, 585, A20
Kawamura A. et al., 2009, ApJS, 184, 1
Kelly B. C., 2007, ApJ, 665, 1489
Kennicutt Robert C. J. et al., 2003, PASP, 115, 928
Kennicutt Robert C. J. et al., 2007, ApJ, 671, 333
Kennicutt Robert C. J., 1998a, ARA&A, 36, 189
Kennicutt Robert C. J., 1998b, ApJ, 498, 541
Kennicutt R. C., Evans N. J., 2012, ARA&A, 50, 531
Kim S., Staveley-Smith L., Dopita M. A., Freeman K. C., Sault R. J., Kesteven M. J., McConnell D., 1998, ApJ, 503, 674
Kim J.-G., Kim W.-T., Ostriker E. C., 2018, ApJ, 859, 68
Kim J.-G., Ostriker E. C., Filippova N., 2020, preprint (arXiv:2011.07772)
Koch E. W. et al., 2018, MNRAS, 479, 2505
Koepferl C. M., Robitaille T. P., Morales E. F. E., Johnston K. G., 2015, ApJ, 799, 53
Kreckel K. et al., 2018, ApJ, 863, L21
Kruijssen J. M. D. et al., 2019, Nature, 569, 519

Kruijssen J. M. D., Longmore S. N., 2014, MNRAS, 439, 3239
Kruijssen J. M. D., Schruba A., Hygate A. e. P. S., Hu C.-Y., Haydon D. T., Longmore S. N., 2018, MNRAS, 479, 1866
Krumholz M. R., 2014, Phys. Rep., 539, 49
Krumholz M. R., Fumagalli M., da Silva R. L., Rendahl T., Parra J., 2015, MNRAS, 452, 1447
Lada C. J., Lada E. A., 2003, ARA&A, 41, 57
Leitherer C. et al., 1999, ApJS, 123, 3
Leitherer C., Ekström S., Meynet G., Schaerer D., Agienko K. B., Levesque E. M., 2014, ApJS, 212, 14
Leroy A. K. et al., 2012, AJ, 144, 3
Leroy A. K. et al., 2013, AJ, 146, 19
Leroy A. K. et al., 2017, ApJ, 846, 71
Leroy A. K. et al., 2019, ApJS, 244, 24
Lewis A. R. et al., 2015, ApJ, 805, 183
Lockman F. J., 1989, ApJS, 71, 469
Lucas W. E., Bonnell I. A., Dale J. E., 2020, MNRAS, 493, 4700
Maeder A., 1992, A&A, 264, 105
Makarov D., Prugniel P., Terekhova N., Courtois H., Vauglin I., 2014, A&A, 570, A13
Martin C. L., 1997, ApJ, 491, 561
Massey P., Olsen K. A. G., Hodge P. W., Strong S. B., Jacoby G. H., Schlingman W., Smith R. C., 2006, AJ, 131, 2478
McLeod A. F. et al., 2020, ApJ, 891, 25
McLeod A. F., Dale J. E., Evans C. J., Ginsburg A., Kruijssen J. M. D., Pellegrini E. W., Ramsay S. K., Testi L., 2019, MNRAS, 486, 5263
Meidt S. E., Rand R. J., Merrifield M. R., 2009, ApJ, 702, 277
Meixner M. et al., 2006, AJ, 132, 2268
Miura R. E. et al., 2012, ApJ, 761, 37
Murphy E. J., Chary R. R., Dickinson M., Pope A., Frayer D. T., Lin L., 2011, ApJ, 732, 126
Murray N., Rahman M., 2010, ApJ, 709, 424
Nazé Y., Chu Y.-H., Points S. D., Danforth C. W., Rosado M., Chen C. H. R., 2001, AJ, 122, 921
Nazé Y., Chu Y.-H., Guerrero M. A., Oey M. S., Gruendl R. A., Smith R. C., 2002, AJ, 124, 3325
Nersesian A. et al., 2020, A&A, 643, A90
Nieten C., Neininger N., Guélin M., Ungerechts H., Lucas R., Berkhuijsen E. M., Beck R., Wielebinski R., 2006, A&A, 453, 459
Onodera S. et al., 2010, ApJ, 722, L127
Patra N. N., 2020, A&A, 638, A66
Paturel G., Theureau G., Bottinelli L., Gouguenheim L., Coudreau-Durand N., Hallet N., Petit C., 2003a, A&A, 412, 57
Paturel G., Theureau G., Bottinelli L., Gouguenheim L., Coudreau-Durand N., Hallet N., Petit C., 2003b, A&A, 412, 57
Pety J. et al., 2013, ApJ, 779, 43
Pietrzyński G. et al., 2019, Nature, 567, 200
Pilyugin L. S., 2001, A&A, 369, 594
Pilyugin L. S., Grebel E. K., Mattsson L., 2012, MNRAS, 424, 2316
Pilyugin L. S., Grebel E. K., Zinchenko I. A., Kniazev A. Y., 2014, AJ, 148, 134
Prescott M. K. M. et al., 2007, ApJ, 668, 182
Querejeta M. et al., 2019, A&A, 625, A19
Rahman N. et al., 2011, ApJ, 730, 72
Rémy-Ruyer A. et al., 2014, A&A, 563, A31
Rieke G. H. et al., 2004, ApJS, 154, 25
Schinnerer E. et al., 2013, ApJ, 779, 42
Schinnerer E. et al., 2019, ApJ, 887, 49
Schlafly E. F., Finkbeiner D. P., 2011, ApJ, 737, 103
Schlegel D. J., Finkbeiner D. P., Davis M., 1998, ApJ, 500, 525
Schmidt M., 1959, ApJ, 129, 243
Schruba A. et al., 2021a, ApJ, to be submitted
Schruba A., Leroy A. K., Walter F., Sandstrom K., Rosolowsky E., 2010, ApJ, 722, 1699
Schruba A., Kruijssen J. M. D., Leroy A. K., 2019, ApJ, 883, 2
Schruba A., Leroy A. K., Bolatto A. D., Dalcanton J. J., Sandstrom K. M., Scoville N., Walter F., Weisz D. R., 2021b, ApJ, to be submitted
Schuster K. F. et al., 2004, A&A, 423, 1171

Scoville N. Z., Thakkar D., Carlstrom J. E., Sargent A. I., 1993, ApJ, 404, L59

Seale J. P. et al., 2014, AJ, 148, 124

Sharma S., Corbelli E., Giovanardi C., Hunt L. K., Palla F., 2011, A&A, 534, A96

Sick J., Courteau S., Cuillandre J.-C., Dalcanton J., de Jong R., McDonald M., Simard D., Tully R. B., 2015, in Cappellari M., Courteau S., eds, Vol. 311, Galaxy Masses as Constraints of Formation Models, p. 82

Silk J., 1997, ApJ, 481, 703

Skibba R. A. et al., 2012, ApJ, 761, 42

Staveley-Smith L., Kim S., Calabretta M. R., Haynes R. F., Kesteven M. J., 2003, MNRAS, 339, 87

Toribio San Cipriano L., García-Rojas J., Esteban C., Bresolin F., Peimbert M., 2016, MNRAS, 458, 1866

Toribio San Cipriano L., Domínguez-Guzmán G., Esteban C., García-Rojas J., Mesa-Delgado A., Bresolin F., Rodríguez M., Simón-Díaz S., 2017, MNRAS, 467, 3759

Utomo D. et al., 2018, ApJ, 861, L18

Verley S., Corbelli E., Giovanardi C., Hunt L. K., 2009, A&A, 493, 453

Viaene S. et al., 2017, A&A, 599, A64

Vutisalchavakul N., Evans Neal J. I., 2013, ApJ, 765, 129

Ward J. L., Chevance M., Kruijssen J. M. D., Kim J. J., Hygate A. P. S., Schruba A., Longmore S. N., 2020a, MNRAS, to be submitted

Ward J. L., Chevance M., Kruijssen J. M. D., Hygate A. P. S., Schruba A., Longmore S. N., 2020b, MNRAS, 497, 2286

Westmeier T., Braun R., Koribalski B. S., 2011, MNRAS, 410, 2217

Whitmore B. C. et al., 2014, ApJ, 795, 156

Williams B. F. et al., 2017, ApJ, 846, 145

Williams T. G., Gear W. K., Smith M. W. L., 2018, MNRAS, 479, 297

Williams T. G., Baes M., De Looze I., Relaño M., Smith M. W. L., Verstocken S., Viaene S., 2019, MNRAS, 487, 2753

Williams J. P., de Geus E. J., Blitz L., 1994, ApJ, 428, 693

Wong T. et al., 2011, ApJS, 197, 16

Wong T. et al., 2017, ApJ, 850, 139

Wood K., Hill A. S., Joung M. R., Mac Low M.-M., Benjamin R. A., Haffner L. M., Reynolds R. J., Madsen G. J., 2010, ApJ, 721, 1397

Wu P.-F., Tully R. B., Rizzi L., Dolphin A. E., Jacobs B. A., Karachentsev I. D., 2014, AJ, 148, 7

Yim K., Wong T., Xue R., Rand R. J., Rosolowsky E., van der Hulst J. M., Benjamin R., Murphy E. J., 2014, AJ, 148, 127

Yim K., Wong T., Rand R. J., Schinnerer E., 2020, MNRAS, 494, 4558

Zabel N. et al., 2020, MNRAS, 496, 2155

Zurita A., Bresolin F., 2012, MNRAS, 427, 1463

APPENDIX A: INDIVIDUAL IMAGES OF EMISSION MAPS USED IN OUR ANALYSIS

In Figs A1 and A2, we present the CO and 24 µm emission maps used in our analysis to trace molecular gas and young stellar regions, respectively.
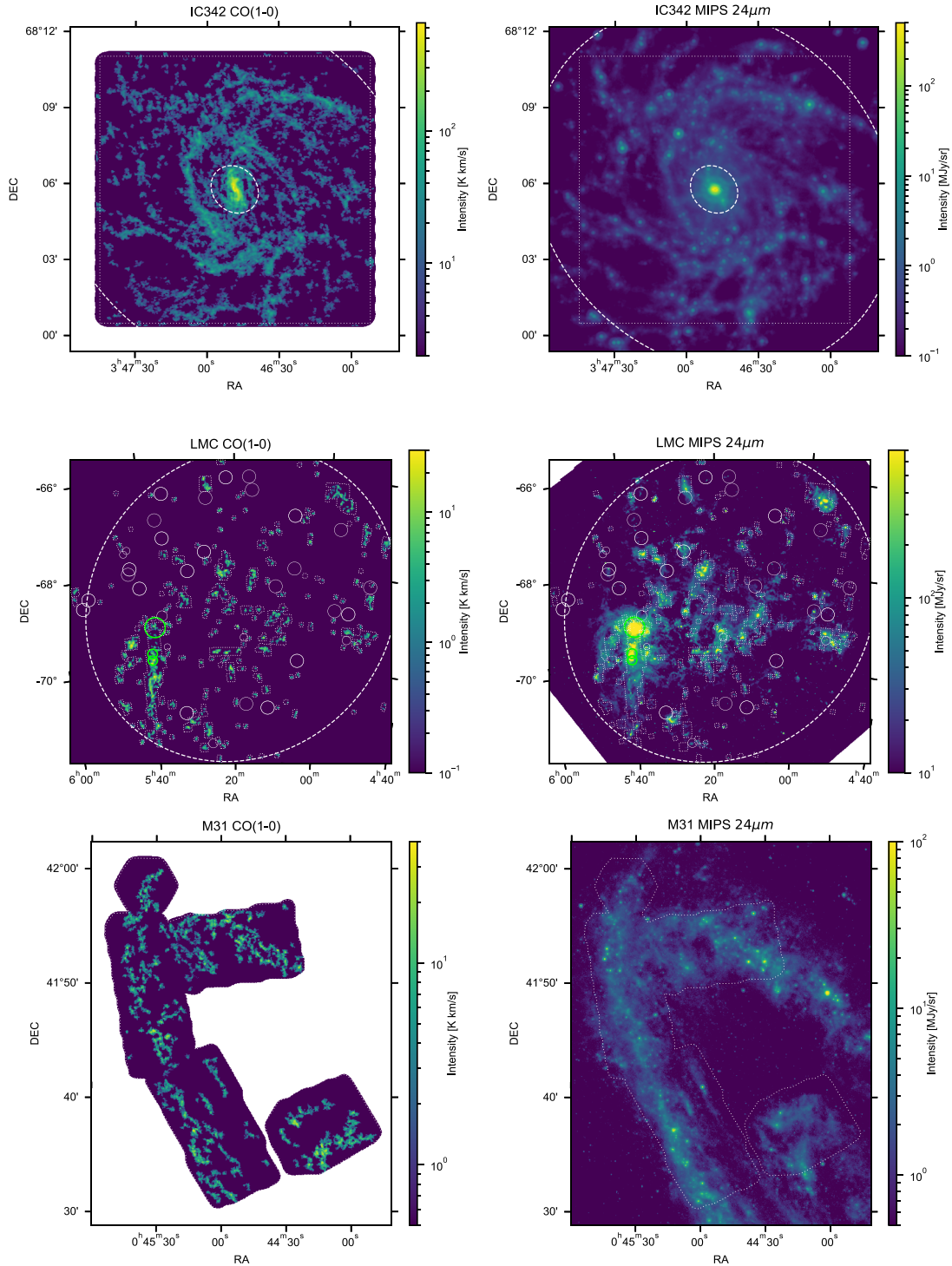
Figure A1. Maps of CO(1–0) emission (left-hand panels) and 24 μm emission (right-hand panels) for the IC 342, LMC, and M31. The ranges of galactic radii included in our analysis are indicated by white dashed ellipses. The white dotted line shows the coverage of the CO observations. In the LMC, regions where molecular gas exists but was not targeted by the MAGMA survey are masked (white solid circles). The masked bright star-forming regions are shown by green circles. We also mask foreground stars, background galaxies, and map artefacts (purple circles).
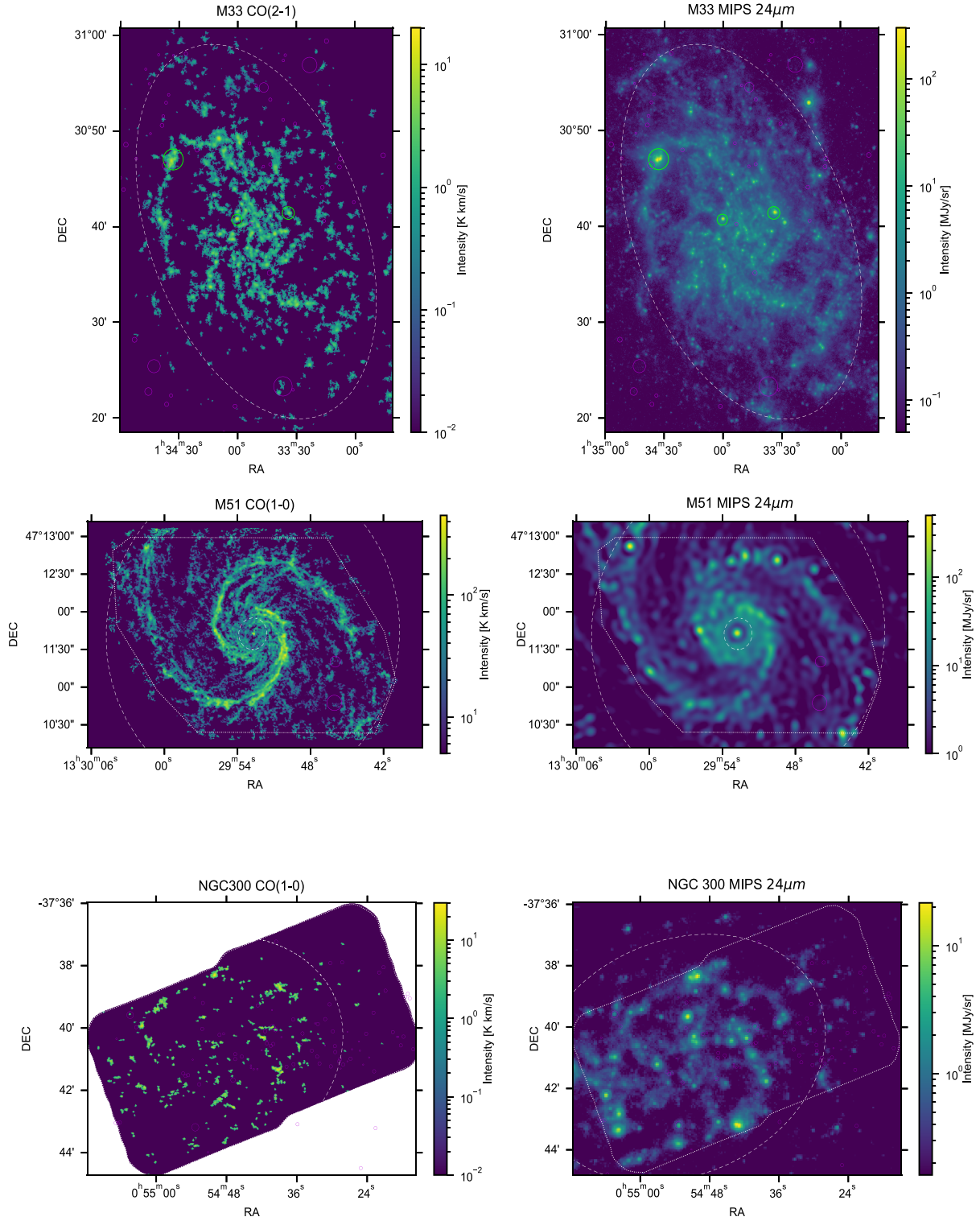
Figure A2. Same as Fig. A1, but here for M33, M51, and NGC 300. Integrated intensity maps of CO(1–0) are shown for M51 and NGC 300, while CO(2–1) is shown for M33.

508   *J. Kim et al.*

APPENDIX B: MOLECULAR CLOUD LIFETIMES IN IC 342 AND M31

In order to derive absolute durations of the different phases of cloud evolution and star formation (see Section 3), we have used the cloud lifetime (t_{CO}) as the reference time-scale in our analysis (see Table 2). For four out of six galaxies in our sample, the cloud lifetime has been constrained in previous works using $H\alpha$ as a tracer for exposed star-forming regions. Here, we describe the characterization of the cloud lifecycle of IC 342 and M31, by applying the same method as described in Section 3 using CO and $H\alpha$ emission maps to trace molecular gas and young stellar regions, respectively.

Fig. B1 shows the $H\alpha$ emission maps of IC 342 and M31 used to trace young massive star-forming regions. A summary of the observational data is presented in Section 2.1. Table B1 lists the adopted main input parameters specific to the analysis using CO
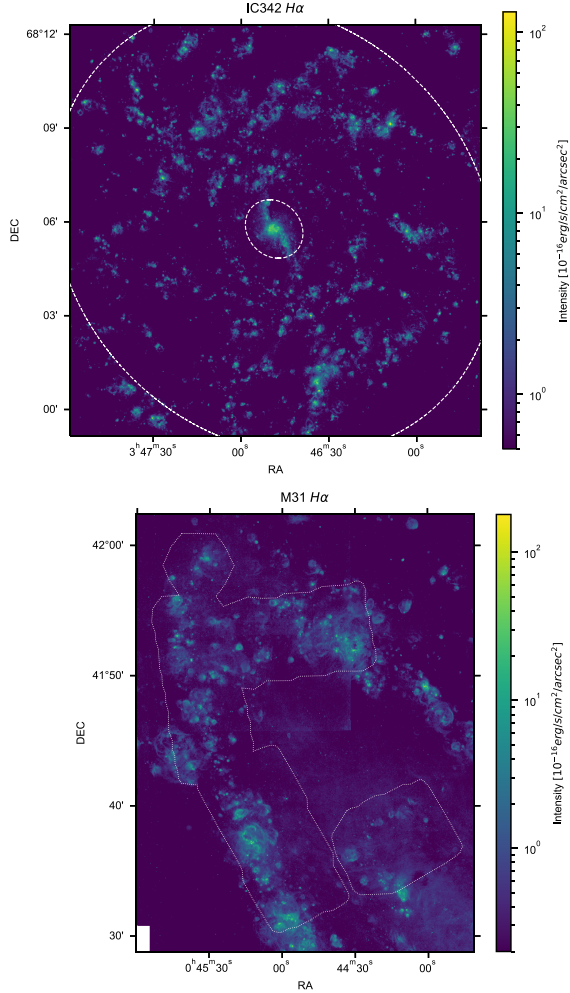
Table B1. Main input parameters of the analysis using $H\alpha$ as an SFR tracer for IC 342 and M31. For other input parameters, we use the default values listed in table 2 of Kruijssen et al. (2018).

Quantity	IC 342	M31
$l_{ap, min}$ (pc)	65	45
$l_{ap, max}$ (pc)	3000	4000
N_{ap}	15	15
$N_{pix, min}$	10	20
$\Delta\log_{10}\mathcal{F}_{CO}$	1.1	1.2
$\delta\log_{10}\mathcal{F}_{CO}$	0.05	0.05
$\Delta\log_{10}\mathcal{F}_{H\alpha}$	2.8	2.0
$\delta\log_{10}\mathcal{F}_{H\alpha}$	0.05	0.1
t_{ref} (Myr)	4.25	4.42
$t_{ref, errmin}$ (Myr)	0.15	0.18
$t_{ref, errmax}$ (Myr)	0.15	0.19
n_λ	12	10

and $H\alpha$ as molecular gas and SFR tracers, respectively. Other input parameters are listed in Tables 1 and 2. We set the minimum aperture size ($l_{ap, min}$) to match the CO map resolution as it is coarser compared to the $H\alpha$ map resolution. The reference time-scales (t_{ref}) for the exposed young stellar phase (duration of the isolated $H\alpha$ emission phase) are adopted from Haydon et al. (2020b). The duration does not include the feedback time-scale, so the total duration of the $H\alpha$ emission phase ($t_{H\alpha}$) equals $t_{ref} + t_{fb, H\alpha}$.

In Fig. B2, we show the measured deviations of the enclosed gas-to-SFR flux ratios in apertures centred on CO and $H\alpha$ peaks, compared to the galactic average, together with our best-fitting model. Table 3 lists the constrained quantities for the best-fitting model. We have verified the accuracy of these measurements in Section 5.1. As seen in our results using 24 μm as an SFR tracer, we find a spatial de-correlation between gas and SFR tracer emission peaks. We measure cloud lifetimes of $20.0^{+2.0}_{-2.3}$ Myr for IC 342 and $14.0^{+2.1}_{-1.9}$ Myr for M31. The measured cloud lifetimes are within the range of our previous measurements of other galaxies where GMCs are found to live for $10-30$ Myr (Kruijssen et al. 2019; Chevance et al. 2020c; Hygate 2020; Ward et al. 2020a; Zabel et al. 2020). We suspect that the difference between the two cloud lifetimes are related to the different environments in which the molecular clouds are located, as recently suggested by Chevance et al. (2020c). In this case, the cloud evolution in IC 342, which has a high molecular gas surface density (9.55 $M_\odot$ pc^{-2}), is likely to be governed by galactic dynamical processes, whereas internal dynamics such as free-fall and crossing times are the determinant factor for cloud evolution in low molecular gas surface density environments such as M31 ($\sim$1 $M_\odot$ pc^{-2}). The duration over which CO and $H\alpha$ emission overlap is short ($2.2^{+0.4}_{-0.5}$ Myr in IC 342 and $1.1^{+0.3}_{-0.2}$ Myr in M31), as seen in previous measurements of other galaxies (Chevance et al. 2020a). These short feedback time-scales indicate that molecular clouds are destroyed shortly after the star-forming region becomes exposed, making them visible in $H\alpha$. Finally, we find that independent star-forming regions are separated by 120^{+10}_{-10} pc in IC 342 and 181^{+28}_{-19} pc in M31, comparable to our measurements with 24 μm as an SFR tracer, as well as our previous findings with $H\alpha$ for different galaxies.

Figure B1. Same as Fig. A2, for $H\alpha$ emission maps of IC 342 and M31.
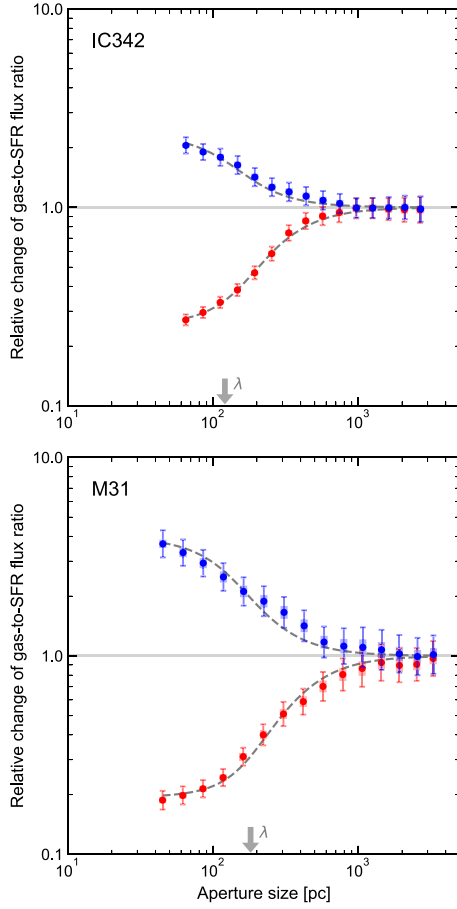
Figure B2. Relative change of the gas-to-SFR (CO-to-Hα) flux ratio compared to the galactic average as a function of size of apertures placed on CO (blue) and Hα (red) emission peaks. The error bars indicate 1σ uncertainty on each individual data point whereas the shaded area is an effective 1σ uncertainty taking into account the covariance between data points. Our best-fitting model is shown as dashed line and the solid horizontal line indicates the galactic average. The measured region separation length (λ) is indicated in each panel and other constrained best-fitting parameters (t_{CO} and $t_{fb,H\alpha}$) are listed in Table 3.

[1]*Astronomisches Rechen-Institut, Zentrum für Astronomie der Universität Heidelberg, Mönchhofstraße 12-14, D-69120 Heidelberg, Germany*
[2]*Max-Planck Institut für Extraterrestrische Physik, Giessenbachstraße 1, D-85748 Garching, Germany*
[3]*Center for Astrophysics and Space Sciences, Department of Physics, University of California, San Diego, 9500 Gilman Drive, La Jolla, CA 92093, USA*
[4]*Argelander-Institut für Astronomie, Universität Bonn, Auf dem Hügel 71, D-53121 Bonn, Germany*
[5]*The Observatories of the Carnegie Institution for Science, 813 Santa Barbara Street, Pasadena, CA 91101, USA*
[6]*Departamento de Astronomía, Universidad de Chile, Casilla 36-D, Santiago, Chile*
[7]*Aix Marseille Univ, CNRS, CNES, LAM (Laboratoire d'Astrophysique de Marseille), Marseille, France*
[8]*Department of Physics & Astronomy, University of Wyoming, Laramie, WY 8207, USA*
[9]*Department of Astronomy, University of Massachusetts - Amherst, 710 N. Pleasant St., Amherst, MA 01003, USA*
[10]*Institut für Theoretische Astrophysik, Zentrum für Astronomie der Universität Heidelberg, Albert-Ueberle-Strasse 2, D-69120 Heidelberg, Germany*
[11]*Research School of Astronomy and Astrophysics, Australian National University, Canberra, ACT 2611, Australia*
[12]*International Centre for Radio Astronomy Research, University of Western Australia, 7 Fairway, Crawley, WA 6009, Australia*
[13]*IRAM, 300 rue de la Piscine, F-38406 Saint Martin d'Hères, France*
[14]*Universität Heidelberg, Interdisziplinäres Zentrum für Wissenschaftliches Rechnen, Im Neuenheimer Feld 205, D-69120 Heidelberg, Germany*
[15]*Caltech/IPAC MC 314-6 (Keith Spalding Building) 1200 E California Blvd Pasadena, CA 91125, USA*
[16]*Department of Astronomy, The Ohio State University, 140 West 18th Ave, Columbus, OH 43210, USA*
[17]*Sorbonne Université, Observatoire de Paris, Université PSL, CNRS, LERMA, F-75005 Paris, France*
[18]*Observatorio Astronómico Nacional (IGN), C/Alfonso XII 3, Madrid E-28014, Spain*
[19]*Max Planck Institut für Astronomie, Königstuhl 17, D-69117 Heidelberg, Germany*

This paper has been typeset from a TEX/LATEX file prepared by the author.

Chapter 4

PHANGS-JWST First Results: Duration of the early phase of massive star formation in NGC628

Authors:

Jaeyeon Kim, Mélanie Chevance,
J. M. Diederik Kruijssen et al.

https://doi.org/10.3847/2041-8213/aca90a

CrossMark

PHANGS–JWST First Results: Duration of the Early Phase of Massive Star Formation in NGC 628

Jaeyeon Kim[1] , Mélanie Chevance[1,2] , J. M. Diederik Kruijssen[2] , Ashley. T. Barnes[3] , Frank Bigiel[3] ,
Guillermo A. Blanc[4,5] , Médéric Boquien[6] , Yixian Cao[7] , Enrico Congiu[5] , Daniel A. Dale[8] , Oleg V. Egorov[9] ,
Christopher M. Faesi[10] , Simon C. O. Glover[1] , Kathryn Grasha[11,12] , Brent Groves[13] , Hamid Hassani[14] ,
Annie Hughes[15] , Ralf S. Klessen[1,16] , Kathryn Kreckel[9] , Kirsten L. Larson[17] , Janice C. Lee[18,19] , Adam K. Leroy[20,21] ,
Daizhong Liu[7] , Steven N. Longmore[2,22] , Sharon E. Meidt[23] , Hsi-An Pan[24] , Jérôme Pety[25,26] , Miguel Querejeta[27] ,
Erik Rosolowsky[14] , Toshiki Saito[28] , Karin Sandstrom[29] , Eva Schinnerer[30] , Rowan J. Smith[31] , Antonio Usero[27] ,
Elizabeth J. Watkins[9] , and Thomas G. Williams[30,32]
[1] Zentrum für Astronomie der Universität Heidelberg, Institut für Theoretische Astrophysik, Albert-Ueberle-Str. 2, D-69120 Heidelberg, Germany
kim@uni-heidelberg.de
[2] Cosmic Origins Of Life (COOL) Research DAO[33]
[3] Argelander-Institut für Astronomie, Universität Bonn, Auf dem Hügel 71, D-53121, Bonn, Germany
[4] The Observatories of the Carnegie Institution for Science, 813 Santa Barbara St., Pasadena, CA, USA
[5] Departamento de Astronomía, Universidad de Chile, Camino del Observatorio 1515, Las Condes, Santiago, Chile
[6] Centro de Astronomía (CITEVA), Universidad de Antofagasta, Avenida Angamos 601, Antofagasta, Chile
[7] Max-Planck-Institut für Extraterrestrische Physik (MPE), Giessenbachstr. 1, D-85748 Garching, Germany
[8] Department of Physics and Astronomy, University of Wyoming, Laramie, WY 82071, USA
[9] Astronomisches Rechen-Institut, Zentrum für Astronomie der Universität Heidelberg, Mönchhofstraße 12-14, D-69120 Heidelberg, Germany
[10] University of Connecticut, Department of Physics, 196A Auditorium Road, Unit 3046, Storrs, CT 06269, USA
[11] Research School of Astronomy and Astrophysics, Australian National University, Canberra, ACT 2611, Australia
[12] ARC Centre of Excellence for All Sky Astrophysics in 3 Dimensions (ASTRO 3D), Australia
[13] International Centre for Radio Astronomy Research, University of Western Australia, 7 Fairway, Crawley, 6009 WA, Australia
[14] Department of Physics, University of Alberta, Edmonton, AB T6G 2E1, Canada
[15] IRAP, Université de Toulouse, CNRS, CNES, UPS, (Toulouse), France
[16] Universität Heidelberg, Interdisziplinäres Zentrum für Wissenschaftliches Rechnen, Im Neuenheimer Feld 205, D-69120 Heidelberg, Germany
[17] AURA for the European Space Agency (ESA), Space Telescope Science Institute, 3700 San Martin Drive, Baltimore, MD 21218, USA
[18] Gemini Observatory/NSF's NOIRLab, 950 N. Cherry Avenue, Tucson, AZ, USA
[19] Steward Observatory, University of Arizona, 933 N Cherry Avenue, Tucson, AZ 85721, USA
[20] Department of Astronomy, The Ohio State University, 140 West 18th Avenue, Columbus, OH 43210, USA
[21] Center for Cosmology and Astroparticle Physics, 191 West Woodruff Avenue, Columbus, OH 43210, USA
[22] Astrophysics Research Institute, Liverpool John Moores University, IC2, Liverpool Science Park, 146 Brownlow Hill, Liverpool L3 5RF, UK
[23] Sterrenkundig Observatorium, Universiteit Gent, Krijgslaan 281 S9, B-9000 Gent, Belgium
[24] Department of Physics, Tamkang University, No.151, Yingzhuan Road, Tamsui District, New Taipei City 251301, Taiwan
[25] IRAM, 300 rue de la Piscine, F-38400 Saint Martin d'Hères, France
[26] LERMA, Observatoire de Paris, PSL Research University, CNRS, Sorbonne Universités, F-75014 Paris, France
[27] Observatorio Astronómico Nacional (IGN), C/Alfonso XII, 3, E-28014 Madrid, Spain
[28] National Astronomical Observatory of Japan, 2-21-1 Osawa, Mitaka, Tokyo, 181-8588, Japan
[29] Center for Astrophysics and Space Sciences, Department of Physics, University of California, San Diego 9500 Gilman Drive, La Jolla, CA 92093, USA
[30] Max-Planck-Institut für Astronomie, Königstuhl 17, D-69117, Heidelberg, Germany
[31] Jodrell Bank Centre for Astrophysics, Department of Physics and Astronomy, University of Manchester, Oxford Road, Manchester M13 9PL, UK
[32] Sub-department of Astrophysics, Department of Physics, University of Oxford, Keble Road, Oxford OX1 3RH, UK

Abstract

The earliest stages of star formation, when young stars are still deeply embedded in their natal clouds, represent a critical phase in the matter cycle between gas clouds and young stellar regions. Until now, the high-resolution infrared observations required for characterizing this heavily obscured phase (during which massive stars have formed, but optical emission is not detected) could only be obtained for a handful of the most nearby galaxies. One of the main hurdles has been the limited angular resolution of the Spitzer Space Telescope. With the revolutionary capabilities of the James Webb Space Telescope (JWST), it is now possible to investigate the matter cycle during the earliest phases of star formation as a function of the galactic environment. In this Letter, we demonstrate this by measuring the duration of the embedded phase of star formation and the implied time over which molecular clouds remain inert in the galaxy NGC 628 at a distance of 9.8 Mpc, demonstrating that the cosmic volume where this measurement can be made has increased by a factor of >100 compared to Spitzer. We show that young massive stars remain embedded for $5.1^{+2.7}_{-1.4}$ Myr ($2.3^{+2.7}_{-1.4}$ Myr of which being heavily obscured), representing $\sim$20% of the total cloud lifetime. These values are in broad agreement with previous measurements in five nearby ($D < 3.5$

---

[33] coolresearch.io

1

Mpc) galaxies and constitute a proof of concept for the systematic characterization of the early phase of star formation across the nearby galaxy population with the PHANGS–JWST survey.

Unified Astronomy Thesaurus concepts: Star formation (1569); Galaxies (573); Giant molecular clouds (653); Interstellar medium (847)

1. Introduction

Over the last two decades, a growing number of multi-wavelength, cloud-scale observations have revealed a spatial offset between cold molecular gas and H II regions in galaxies (Engargiola et al. 2003; Blitz et al. 2007; Kawamura et al. 2009; Onodera et al. 2010; Schruba et al. 2010; Miura et al. 2012; Meidt et al. 2015; Corbelli et al. 2017; Kruijssen et al. 2019b; Schinnerer et al. 2019; Barnes et al. 2020; Pan et al. 2022). The statistical characterization of this offset has enabled a quantitative description of the evolutionary life cycle of giant molecular clouds (GMCs), during which gas is turning into stars (Kruijssen et al. 2019b; Chevance et al. 2020a, 2020b, 2022a, 2022b; Zabel et al. 2020; Kim et al. 2021, 2022; Lu et al. 2022; Ward et al. 2022). These studies have illustrated that GMCs are transient objects that survive for 1–3 dynamical timescales (10–30 Myr, with typical associated uncertainties of ∼25%) and are dispersed quickly by feedback from newly formed stars, after a long phase during which GMCs appear inert and devoid of massive stars (70%–90% of the cloud lifetime), before the star formation is detected through Hα emission. In these studies, GMCs have masses over 10^4–$10^5 M_\odot$ and the lifetimes of these objects represent the time they spend being bright in CO emission, until the molecular gas has been dispersed by the resulting H II region.

However, the earliest phases of star formation are heavily embedded and invisible in Hα due to the extinction from the surrounding dense gas and dust. Therefore, the duration of these phases and the time that clouds spend being truly inert are still poorly constrained, and so is the time needed for the feedback from these heavily embedded stars to blow out enough of the natal cloud to enable the detection of Hα emission. This limits our understanding of the physical mechanisms playing a role in the first stages of star formation. Measuring these characteristic timescales is crucial to establish which mechanisms are responsible for dispersing the molecular clouds (e.g., Lopez et al. 2014) and for distinguishing whether star formation is delayed by the decay of initial turbulence (e.g., Gnedin et al. 2016; Padoan et al. 2017) or suppressed by galactic-scale dynamics, such as the shear associated with spiral arms and differential rotation preventing collapse of the clouds (e.g., Meidt et al. 2018).

High-resolution infrared observations (∼1 pc scale) of star-forming regions in the Milky Way have revealed that molecular clouds spend 30%–40% of their lifetime with embedded stars (Lada & Lada 2003; Battersby et al. 2017). Massive protoclusters (∼$10^4 M_\odot$) in our Galaxy are actively forming stars and appear to have a very short starless phase (<0.5 Myr; Ginsburg et al. 2012). In nearby galaxies, the timescales between successive stages of the gas-to-stars evolutionary cycle can be estimated by combining ages of star clusters with distances between these clusters and their neighboring GMCs. These results suggest that the embedded star-forming phase lasts for 2–5 Myr, of which the initial 0–2 Myr are heavily obscured, i.e., ongoing star formation is detected in mid-infrared or in radio continuum but invisible in Hα and ultraviolet emission (Whitmore et al. 2014; Calzetti

et al. 2015; Corbelli et al. 2017; Grasha et al. 2018; Turner et al. 2022).

Kruijssen & Longmore (2014) and Kruijssen et al. (2018) have introduced a statistically rigorous method that translates the observed spatial decorrelation between cold gas and star formation rate (SFR) tracers into their underlying timescales. In Kim et al. (2021), this method has been applied to six nearby star-forming galaxies using CO, Spitzer 24 μm, and Hα emission maps, tracing molecular clouds, embedded star formation, and exposed star formation, respectively. This provided systematic constraints on the duration of the embedded phase of star formation for five of these six galaxies, which was shown to last for 2–7 Myr, constituting 20%–50% of the cloud lifetime. The first half of this phase is heavily obscured and only detected in CO and 24 μm, while being invisible in Hα emission. Until now, the number of galaxies where we could constrain these timescales was restricted to these five galaxies, with distances of $D < 3.5$ Mpc. This small sample was due to the limited resolution of the Spitzer 24 μm observations (6″) and the requirement that the observations need to resolve each galaxy into its distinctive units of star formation (e.g., GMCs and H II regions, typically separated by ∼100 pc). The results of deconvolution algorithms (Backus et al. 2005) applied to more distant galaxies (M51 at 8.6 Mpc; Dumas et al. 2011) did not lead to a sufficient data quality to successfully perform this measurement.

The Mid-Infrared Instrument (MIRI) on board the James Webb Space Telescope (JWST) has opened a new era of infrared astronomy with unprecedented spatial resolution and sensitivity in the mid-infrared. In particular, observations at 21 μm tracing embedded young stellar populations reach a resolution of 0″.67, allowing the cloud-to-star life cycle to be characterized, with the above method, out to considerably larger distances of up to 25 Mpc. The PHANGS[34] collaboration is carrying out the PHANGS–JWST survey (Lee et al. 2022b this Issue; Program ID 02107) to map the star-forming disk of 19 galaxies in a wide range of wavelengths, from 2 to 21 μm. This translates into a physical scale of 20–60 pc in the 21 μm band for the galaxies in this sample (at distances between 5 and 20 Mpc). So far, four of these galaxies have been observed (IC 5332, NGC 628, NGC 1365, NGC 7496) with MIRI JWST. In this Letter, we extend our previous analysis by Kim et al. (2021) by characterizing the duration of the early phase of star formation in one of these initial galaxies, NGC 628, which is the most nearby (yet 3 times further away than the most distant galaxy analyzed in Kim et al. 2021), and for which the duration of the CO- and Hα-bright phases have already been obtained in our previous works (Chevance et al. 2020a; Kim et al. 2022). Following previous works using Spitzer 24 μm as a tracer for embedded massive stars (Calzetti et al. 2015; Corbelli et al. 2017; Kim et al. 2021), we define the duration of "embedded star formation" probed at 21 μm with JWST as the total phase during which CO and 21 μm are found to be overlapping,

---

[34] The Physics at High Angular resolution in Nearby GalaxieS project: http://phangs.org.

whereas the "heavily obscured phase" refers to the phase where both CO and 21 μm are detected *without* associated Hα emission.

2. Observations

In order to trace embedded star formation, we use the 21 μm emission map observed with MIRI on board JWST as a part of PHANGS–JWST survey. This data was obtained from the Mikulski Archive for Space Telescopes (MAST) at the Space Telescope Science Institute.[35] This mid-infrared wavelength has been widely used as a tracer of embedded star formation, because a substantial fraction of the emission, especially that with compact morphology, originates from dust excitation by radiation from surrounding massive stars and empirically exhibits a correlation with tracers of massive star formation (Kennicutt & Evans 2012; Galliano et al. 2018; Hassani et al. 2022; Leroy et al. 2022; Thilker et al. 2023). In particular, using four initial targets, Hassani et al. (2022) have found that 90% of compact 21 μm sources are associated with H II regions detected in extinction corrected Hα maps from MUSE. Furthermore, Hassani et al. (2022) have shown that background galaxies and evolved stars identified in the 21 μm map are faint, only constituting $\sim$3% of the total 21 μm emission flux and therefore they are unlikely to affect our measurements, because the quantities constrained with our methodology are flux weighted (see Section 3). The JWST map has a physical resolution of $\sim$30 pc at the distance of NGC 628 (9.84 Mpc; Anand et al. 2021a, 2021b) and a 1σ surface brightness sensitivity of $\sim$0.3 MJy sr^{-1} at the native resolution of 0$\farcs$67. Details on the data reduction can be found in Lee et al. (2022b).

In Figure 1, we show a comparison between the Spitzer MIPS map at 24 μm and the JWST MIRI map at 21 μm of NGC 628. The increase in resolution by a factor of almost 10 allows us to resolve individual regions in the galaxy. A composite three-color image of the CO, 21 μm, and Hα emission maps is also provided, where the spatial small-scale decorrelation of these tracers is illustrated by the color variations. The Hα emission map is from PHANGS-Hα (Preliminary version; A. Razza et al. 2022, in preparation) observed using the Wide Field Imager instrument at the MPG-ESO 2.2 m telescope at the La Silla Observatory.

We use the ^{12}CO($J = 2$–1) transition (CO hereafter) from PHANGS–ALMA as a tracer of molecular gas. A detailed description of the full sample and data reduction can be found in Leroy et al. (2021b, 2021a). The observations were carried out with the 12 m array, as well as with the 7 m and total power antennas of the Atacama Large Millimeter/submillimeter Array (ALMA). We use the moment-0 map at the native resolution reduced with an inclusive signal masking scheme with high completeness (the "broad" mask; see Leroy et al. 2021a) The resulting CO map has a resolution of 1$\farcs$12 ($\sim$50 pc) and a 5σ molecular gas mass sensitivity of $5 \times 10^4 M_\odot$ (Leroy et al. 2021b). After the removal of diffuse emission (see Section 3), the faintest identified CO emission peak has a mass of $10^5 M_\odot$.

In order to perform the next steps of the analysis (see Section 3), we first convolve and then reproject the 21 μm emission map to match the resolution and the pixel grid of the CO map. During the convolution, we use a kernel that translates the JWST MIRI point-spread function to a Gaussian, matched to the beam of the CO map and generated using the method of Aniano et al. (2011). Our statistical method (described in Section 3) makes use of the relative spatial distribution of the molecular clouds and young stellar regions to derive their associated timescales and therefore the astrometric precision of the CO and 21 μm map must be sufficient to detect offsets. Extensive experiments of the method with simulated data show that an acceptable astrometric precision is 1/3 of the beam (Kruijssen et al. 2018; Hygate et al. 2019), which corresponds here to $\sim$0$\farcs$4. Lee et al. (2022b) have shown that MIRI images, aligned using asymptotic giant branch stars and PHANGS-HST data (Lee et al. 2022a), have astrometric uncertainties of $\pm$0$\farcs$1, comfortably satisfying the required precision. The astrometric precision of the Hα map is also measured to be within the acceptable precision with 0$\farcs$1–0$\farcs$2 by matching stellar sources to the Gaia DR2 catalog (Gaia Collaboration et al. 2018) or SINGS and Wide Field Imager data (Chevance et al. 2020a; A. Razza et al. 2022, in preparation).

Following our previous analysis (e.g., Kim et al. 2021, 2022), we further mask very bright regions that can potentially bias our measurements of timescales (yellow circles in Figure 1). These bright peaks represent outliers in the luminosity function of the peaks identified using CLUMPFIND (Williams et al. 1994) and also seen in Hassani et al. (2022). The galactic center (white circle) is also excluded from our analysis, because crowding of sources makes it difficult to identify star-forming regions and molecular clouds in this environment.

3. Method

We now briefly describe our analysis method (the "uncertainty principle for star formation," formalized in the HEISENBERG[36] code) and the main input parameters used. We refer readers to Kruijssen et al. (2018) for a full description and rigorous validation of the code using simulated galaxies and Kruijssen & Longmore (2014) for an introduction of the method. This method has been applied to $\sim$60 observed galaxies (Kruijssen et al. 2019a; Chevance et al. 2020a, 2022a; Haydon et al. 2020; Ward et al. 2020, 2022; Zabel et al. 2020; Kim et al. 2021, 2022; Lu et al. 2022), including NGC 628, using CO and Hα as tracers of molecular gas and SFR. Unless stated otherwise, here we adopt the same input parameters for this galaxy as in Chevance et al. (2020a) and Kim et al. (2022), describing the main properties of the galaxy and the CO and Hα observations.

Our method exploits the relative spatial distributions of tracers of successive phases of the evolution from GMCs to young stellar regions. Contrary to the observed tight correlation on approximately kiloparsec scales between molecular gas and SFR tracers (e.g., CO and Hα) that defines the well known "star formation relation" (e.g., Kennicutt 1998; Bigiel et al. 2008), small-scale ($\sim$100 pc) observations resolving galaxies into independent star-forming regions and clouds reveal spatial offsets between them, increasing the observed scatter of the star formation relation. This small-scale decorrelation can be naturally explained by galaxies being composed of "independent" regions, each undergoing independent evolution from

---
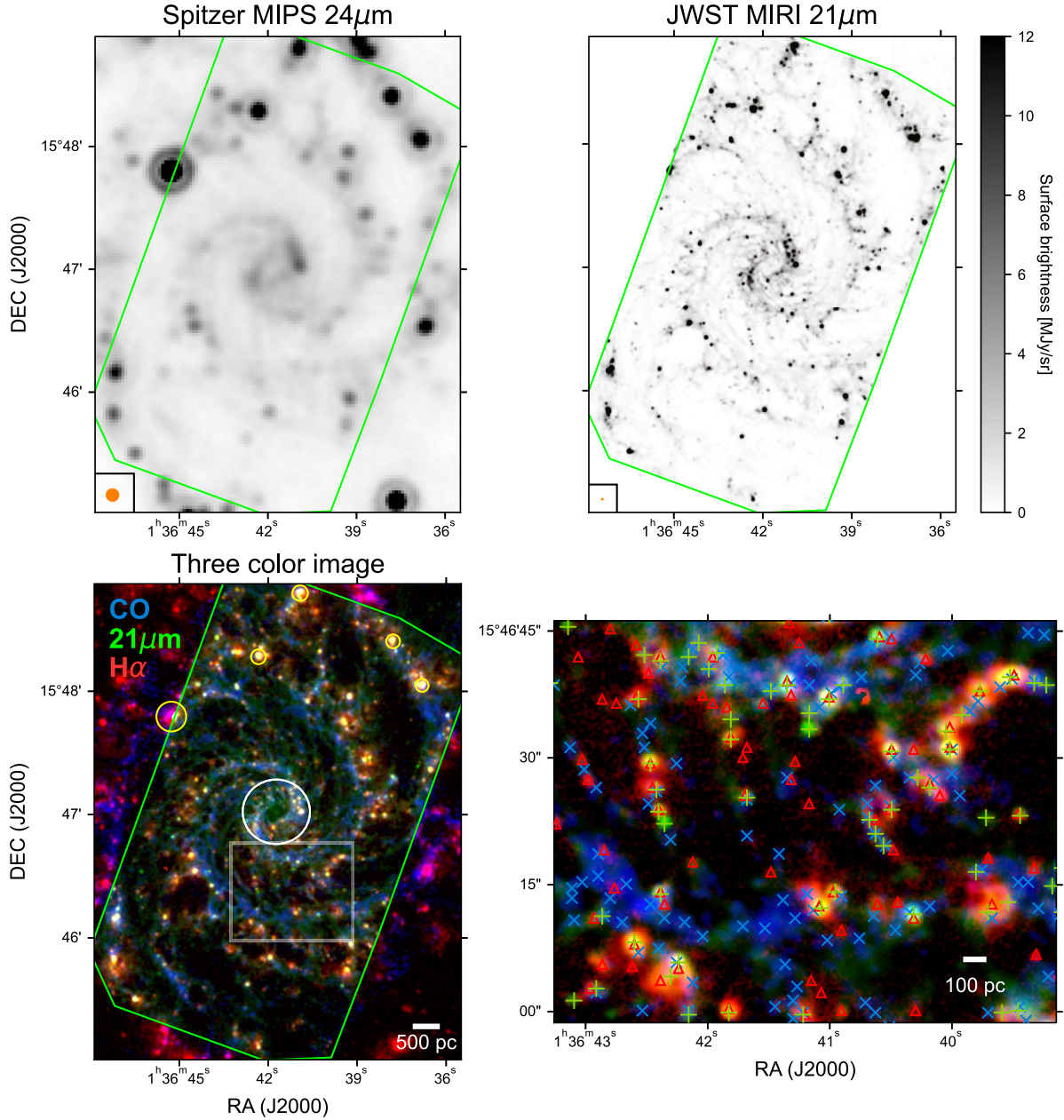
Figure 1. Top: comparison between the Spitzer 24 μm map (left) and the JWST 21 μm map (middle), which has 10 times better resolution (0″67) compared to Spitzer (6″). Orange circles show the beam in each panel. Bottom: composite three-color images obtained by combining CO (blue), 21 μm (green), and Hα (red). The bottom right panel shows the zoomed-in image of the white rectangular region marked in the bottom left panel, with symbols indicating the distribution of emission peaks using the same color scheme. Emission peaks of CO (indicated with ×), 21 μm (+), and Hα (△) show spatial offsets, indicating that these represent distinctive stages of star formation. The JWST field of view is outlined in green. The crowded galactic center (white circle), as well as extremely bright star-forming regions (yellow circles) are excluded from our analysis (see text).

molecular cloud assembly to star formation and feedback, which disperses the natal clouds and leaves young stellar regions without associated molecular gas (Onodera et al. 2010; Schruba et al. 2010; Kruijssen & Longmore 2014). Our methodology assumes that the spatial distribution of such regions is locally isotropic on the scale of the mean separation length between regions (a few 100 pc), which is the largest scale that our measurements are sensitive to. This means that

our measurements are not affected by galactic-morphological features, such as gaseous spiral arms that produce linear features on kiloparsec scales (Kruijssen et al. 2018).

To translate the observed decorrelation of cold gas and star formation tracers into the underlying evolutionary timescales associated with each tracer (Kruijssen et al. 2018), we first identify peaks in the CO and 21 μm maps using CLUMPFIND (Williams et al. 1994). This algorithm uses contours on the map

Table 1
Derived Characteristic Properties of the Evolutionary Cycle Traced by the CO and Hα Emission Maps, as well as the CO and 21 μm Emission Maps

Hα as an SFR Tracer	
t_{CO}	$23.9^{+2.5}_{-2.8}$ Myr
$t_{\mathrm{fb,H\alpha}}$	$2.7^{+0.5}_{-0.6}$ Myr
$\lambda_{\mathrm{H\alpha}}$	96^{+13}_{-11} pc
21 μm as an SFR Tracer	
$t_{21\ \mu\mathrm{m}}$	$8.8^{+3.6}_{-1.4}$ Myr
$t_{\mathrm{fb,21\ \mu m}}$	$5.1^{+2.7}_{-1.4}$ Myr
$\lambda_{21\ \mu\mathrm{m}}$	90^{+51}_{-17} pc
Duration of Heavily Obscured Phase	
t_{obsc}	$2.3^{+2.7}_{-1.4}$ Myr

for a set of flux levels separated by a step size $\delta \log_{10} \mathcal{F}$, with a full range $\Delta \log_{10} \mathcal{F}$ starting from the maximum flux level. For the 21 μm emission map, we adopt $\delta \log_{10} \mathcal{F} = 0.05$ and $\Delta \log_{10} \mathcal{F} = 2.0$, where the choice of this full range is well justified given the distribution of 21 μm peaks in Hassani et al. (2022, after excluding bright outliers). For the CO emission map, we adopt $\delta \log_{10} \mathcal{F} = 0.05$ and $\Delta \log_{10} \mathcal{F} = 1.1$, similar to our previous analysis (Chevance et al. 2020a; Kim et al. 2022). On each identified peak, we then center apertures with a range of sizes from the cloud scale ($l_{\mathrm{ap,min}} = 50$ pc, similar to 1 beam size) to the galactic scale ($l_{\mathrm{ap,max}} = 1.5$ kpc). For each aperture size, we measure the deviation of the gas-to-SFR tracer flux ratio around all peaks compared to the galactic average value.

We then fit an analytical function (see Section 3.2.11 of Kruijssen et al. 2018) to the measured flux ratios as a function of aperture size, which depends on the relative duration of emission of each tracer, the relative duration for which they overlap, and the typical separation length between independent regions (λ). The absolute values of the timescales are obtained by multiplying the best-fitting relative timescale by a known reference timescale (t_{ref}). Here, we use the cloud lifetime (t_{CO}) derived in our previous analysis (Chevance et al. 2020a; Kim et al. 2022) as t_{ref}. Since we mask four regions that are extremely bright in 21 μm (see Section 2 and Figure 1), we repeat our previous analysis of NGC 628 using narrowband Hα as an SFR tracer (Chevance et al. 2020a; Kim et al. 2022) to see how the masking impacts the measurements. The results are consistent within the uncertainties, and our new measurements for the masked map are shown in Table 1 (discussed below). Masking additional bright regions only results in negligible differences in our measurements of the timescales obtained with Hα emission (again within uncertainties).

Having obtained the lifetime of the CO-bright emission, we can derive the absolute lifetimes of the 21 μm emission. The fitted model is described by three independent quantities: the timescale over which CO and the SFR tracer are found to be overlapping ($t_{\mathrm{fb,21\ \mu m}}$), the 21 μm emitting timescale ($t_{21\ \mu\mathrm{m}}$), and the typical separation between independent regions ($\lambda_{21\ \mu\mathrm{m}}$). The overlapping timescale represents the time over which embedded massive star formation takes place, as well as the time it takes for stellar feedback to disperse the surrounding gas. The fit to the observations returns a three-dimensional probability distribution function (PDF) of the free parameters, which is then marginalized to obtain the one-dimensional PDF of each parameter. The uncertainties quoted here are defined as

the 32nd percentile of the part of the PDF below the best-fitting value, and the 68th percentile of the part of the PDF above the best-fitting value (Kruijssen et al. 2018).

As part of the analysis process, we filter out potential diffuse emission in both CO and 21 μm maps using the method presented in Hygate et al. (2019). This is necessary as the presence of diffuse emission can bias our measurements by adding a reservoir of large-scale emission that is not associated with the identified peaks within the aperture, and therefore does not participate in the cycling that is being characterized here. Similarly to our previous analysis of NGC 628 (Chevance et al. 2020a; Kim et al. 2022), we iteratively remove emission on scales larger than 15 $\lambda_{21\ \mu\mathrm{m}}$ using a Gaussian high-pass filter in Fourier space. The threshold of 15 $\lambda_{21\ \mu\mathrm{m}}$ was chosen to ensure that the flux loss from the compact region is about 10%, following the prescription by Hygate et al. (2019), Kruijssen et al. (2019b), Chevance et al. (2020a), and Kim et al. (2021, 2022). However, we note that using a higher or lower multiples of $\lambda_{21\ \mu\mathrm{m}}$ (from 10 to 20) do not significantly impact our measurements (within 1σ uncertainties).

In the CO map, filtering extended structures (that constitute ∼60% of the emission) results in lowering the signal-to-noise ratio of small, faint clouds, allowing us to focus on molecular clouds that are likely to form massive stars. Before filtering, the faintest identified CO emission peak has a mass of $10^4 M_\odot$, whereas after filtering the faintest identified CO emission peak has a mass of $10^5 M_\odot$, which is likely to give birth to massive stars when assuming a standard initial mass function. In the 21 μm map, this removes large-scale emission (constituting ∼50% of the total emission) originating from the interstellar radiation field, which is not related to recent massive star formation but has a nonnegligible contribution to the dust heating (Draine & Li 2007; Verley et al. 2009). Thilker et al. (2023) report a fraction of mid-infrared emission arising from filamentary structures (∼30%) that is qualitatively similar to the ∼50% obtained here. The fraction of large-scale emission removed is also broadly consistent with the contribution of the interstellar radiation field to Spitzer 24 μm wavelength measured in the Milky Way and in Local Group galaxies (20%–85%; Koepferl et al. 2015; Viaene et al. 2017; Williams et al. 2019). Leroy et al. (2012, 2022) also measure 40%–60% of the mid-infrared emission to originate from molecular gas heated by the interstellar radiation field.

4. Results

Table 1 lists results from the application of our method to the CO and 21 μm maps, tracing molecular gas and embedded star formation, respectively. In Figure 2 (left) and Appendix B, we present the measured variation of gas-to-SFR tracer flux ratio compared to the galactic average, as a function of aperture size. Toward small scales, the flux ratios increasingly diverge from the galactic average, illustrating the spatial decorrelation between CO and 21 μm emission on cloud scales. The right panel of Figure 2 shows the constrained timeline after combining our results for both SFR tracers. At first, clouds are only detected in CO emission for a duration of $t_{\mathrm{CO}} - t_{\mathrm{fb,21\ \mu m}} = 18.8^{+2.7}_{-3.6}$ Myr. Then, after the onset of the heavily obscured phase of star formation, 21 μm emission is detected together with CO emission (but without associated Hα) for $t_{\mathrm{obsc}} = 2.3^{+2.7}_{-1.4}$ Myr. Feedback from these newly formed stars progressively disperses the surrounding gas, revealing young stars emerging from their natal GMC in Hα
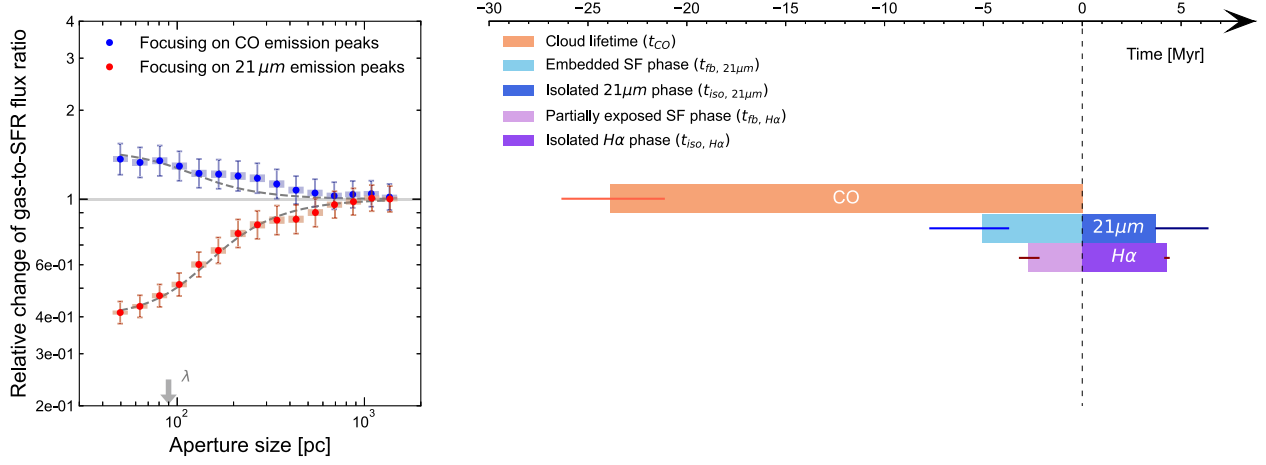
Figure 2. The left panel shows the measured deviation of gas-to-SFR tracer (CO-to-21 μm) flux ratios compared to the galactic average as a function of the size of apertures centered on CO and 21 μm emission peaks. The data underlying this figure can be found in Appendix B. The error bars show the 1σ uncertainty of each measurement whereas the shaded region within the error bar indicates the effective 1σ error, considering the covariance between data points. Our best-fitting model (dashed line), as well as the galactic average (horizontal line) are also shown. The constrained λ is indicated with a downward arrow and other best-fitting parameters ($t_{21\,\mu m}$ and $t_{fb,21\,\mu m}$) are listed in Table 1. The right panel illustrates the evolutionary sequence from inert molecular clouds to embedded star formation, partially exposed star formation, and finally to fully revealed young stellar regions. The duration of the CO emitting phase (t_{CO}) is shown in orange while the time during which 21 μm and Hα emission are detected without associated CO emission are shown in dark blue and dark purple, respectively. The feedback timescale, which is the time for which both CO and an SFR tracer are found coincident, is shown in light blue (for 21 μm) and light purple (for Hα). The error bars indicate the 1σ uncertainty for each measurement.

emission for $t_{fb,H\alpha} = 2.7^{+0.5}_{-0.6}$ Myr. Finally, the molecular gas is completely dispersed, leaving only the young stellar regions to be detected through both SFR tracers for about $t_{21\,\mu m} - t_{fb,21\,\mu m}$ or $t_{H\alpha} - t_{fb,H\alpha}$ of ∼4 Myr on average. In Appendix A, we verify that the measured timescales are reliable with an accuracy of 30% or better. This implies that these measurements achieve a similar level of confidence to those for the more nearby galaxies presented in Kim et al. (2021), despite having been made for a galaxy at a much greater distance.

4.1. Duration of the Embedded ($t_{fb,21\,\mu m}$) and Heavily Obscured (t_{obsc}) Phases of Star Formation

Because star formation can only continue until molecular clouds have been dispersed, we define the duration of the embedded phase of star formation as the time during which CO and 21 μm emission are found to be overlapping (i.e., the feedback timescale, $t_{fb,21\,\mu m}$). We measure $t_{fb,21\,\mu m} = 5.1^{+2.7}_{-1.4}$ Myr in NGC 628, which represents ∼20% of the cloud lifetime (t_{CO}). These two values fall into the range of those constrained in five nearby galaxies (2–7 Myr, 20%–50%) by Kim et al. (2022).

The feedback timescale measured with 21 μm (5.1$^{+2.7}_{-1.4}$ Myr) is longer than the one obtained using Hα (2.7$^{+0.5}_{-0.6}$ Myr) as an SFR tracer. This difference can be explained by the fact that the earliest stages of star formation are invisible in Hα emission due to the extinction from the surrounding dense gas and dust, while 21 μm is detected as it originates from the reemission of absorbed stellar light by small dust grains (e.g., Kennicutt et al. 2007; Galliano et al. 2018). We find that this heavily obscured phase of star formation ($t_{obsc} = t_{fb,21\,\mu m} - t_{fb,H\alpha}$) lasts for 2.3$^{+2.7}_{-1.4}$ Myr,[37] showing a good agreement with the range of

values constrained in five nearby galaxies (1–4 Myr) by Kim et al. (2021).

The short durations of $t_{fb,21\,\mu m}$ and t_{obsc} support our previous claim that presupernova feedback likely drives the dispersal of molecular clouds, as supernovae take longer to detonate (4–20 Myr; Chevance et al. 2020a, 2022a, also see Barnes et al. 2022; Della Bruna et al. 2022). Similar values of $t_{fb,21\,\mu m}$ and t_{obsc} have been measured using ages of stellar clusters and their association with neighboring GMCs (Whitmore et al. 2014; Grasha et al. 2018, 2019), as well as using H II region morphologies (Hannon et al. 2019, 2022). We note that the "heavily obscured phase" is also referred to as "embedded" in other works in this Issue, which report qualitatively similar durations of this phase (Rodriguez et al. 2022; Whitmore et al. 2023).

4.2. Duration of the Total 21 μm Emitting Phase

In NGC 628, we measure the total duration of the 21 μm emitting phase ($t_{21\,\mu m}$) to be 8.8$^{+3.6}_{-1.4}$ Myr, which falls into the range of our previous measurements of this timescale in nearby galaxies (4–14 Myr; Kim et al. 2021). After the star formation is terminated by the dispersal of molecular clouds, the emission at 21 μm can still be detected for ∼4 Myr, due to the remaining dust in the H II region, which is heated by the high-mass stars that have not yet ended their lives. As shown in Figure 2, the end of this isolated 21 μm emitting phase (after CO has disappeared) corresponds broadly to the end of the Hα emitting phase, indicating that our diffuse emission-filtered 21 μm map effectively traces emission related to recent massive star formation. Furthermore, as shown in Figure 2, almost 80% of the total 21 μm emitting timescale coincides with the Hα emitting timescale, showing a good agreement with Hassani et al. (2022) who find that 90% of the 21 μm emission peaks in four initial PHANGS–JWST galaxies are associated with Hα emission. Our result also agrees with those of Linden et al. (2022), who find that

---

[37] The uncertainties on t_{obsc} are obtained using formal error propagation and therefore are similar to those on $t_{fb,21\,\mu m}$, which shows larger errors than $t_{fb,H\alpha}$. These uncertainties on t_{obsc} should be considered as an upper limit, because no covariance between $t_{fb,H\alpha}$ and $t_{fb,21\,\mu m}$ is assumed, which is unlikely to be true.

80% of young massive star cluster candidates identified with JWST near-infrared emission also have an optical counterpart. This also explains why 21 μm and Hα emission show a tighter correlation than 21 μm and CO emission (Leroy et al. 2022).

### 4.3. Characteristic Distance between Independent Regions

Figure 2 shows that GMCs and young stellar regions are spatially decorrelated on small scales, illustrating that galaxies are composed of independent regions in different phases of their evolution from gas to stars. Our method measures the characteristic distance between these regions, which we denote as $\lambda_{21\,\mu m}$ and $\lambda_{H\alpha}$ depending on which SFR tracer is being used. We find $\lambda_{21\,\mu m} = 90^{+51}_{-17}$ pc, showing a very good agreement with $\lambda_{H\alpha} = 96^{+13}_{-11}$ pc. This $\lambda_{21\,\mu m}$ falls into the range of values found in five nearby galaxies using Spitzer MIPS 24 μm as an SFR tracer (70–200 pc Kim et al. 2022), as well as that found in a larger sample of 54 galaxies using Hα as an SFR tracer (100–400 pc; Chevance et al. 2020a; Kim et al. 2022).

5. Conclusion

Using novel observations of NGC 628 at a wavelength of 21 μm from MIRI on JWST, together with CO from ALMA and narrowband Hα emission maps at matched resolution, we have characterized the evolutionary cycle of GMCs from their inert phase, to the onset of embedded massive star formation, the partially exposed star-forming phase, and finally to H II regions free of cold molecular gas. This is the first time that the start and the duration of the embedded phase of star formation can be characterized at a distance greater than 3.5 Mpc, unlocking the necessary statistics and dynamic range for characterizing the environmental dependence of the physical processes driving the earliest phases of massive star formation.

We find that the time during which GMCs in NGC 628 are truly free from massive star formation ($= t_{CO} - t_{fb,21\,\mu m}$) is $18.8^{+2.7}_{-3.6}$ Myr. The duration of the embedded phase of star formation ($t_{fb,21\,\mu m}$) is $5.1^{+2.7}_{-1.4}$ Myr, representing $\sim$20% of the cloud lifetime. The Hα emission is heavily obscured during almost the entire first half of this phase, resulting in t_{obsc} of $2.3^{+2.7}_{-1.4}$ Myr. Then, the star-forming region partially reveals itself from its natal GMC, causing the CO emission to be detected in association with 21 μm and Hα emission for a duration of $t_{fb,H\alpha} = 2.7^{+0.5}_{-0.6}$ Myr. Finally, the molecular cloud is completely dispersed by stellar feedback, and only SFR tracers are detected for another $\sim$5 Myr without associated CO emission.

In Figure 3, the distribution of our PHANGS–JWST target galaxies as well as the five galaxies from Kim et al. (2022) are shown in the plane spanned by the galaxy stellar mass ($M_{*,global}$) and the galaxy-wide SFR (SFR$_{global}$). As a proof of concept, we have measured the timescales of the embedded and heavily obscured phases of star formation in one of the JWST target galaxies, NGC 628. No trend is found between the duration of the embedded phase (here denoted by $t_{fb,MIR}$ because the figure combines measurements from Spitzer at 24 μm and from JWST at 21 μm) and the galaxy properties (e.g., mass, SFR, offset from the main sequence), but NGC 628 represents an important extension of the parameter space shown here. Our results highlight the power of JWST by demonstrating that the quality of the data enables the embedded phase of star formation to be systematically characterized for a
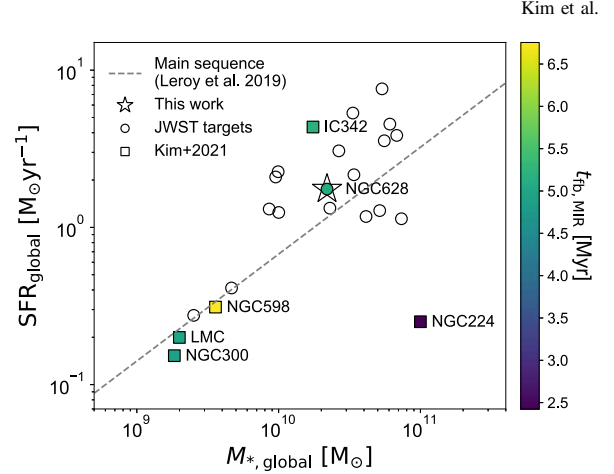
Figure 3. Galaxy-wide SFR (SFR$_{global}$) as a function of stellar mass ($M_{*,global}$) for the PHANGS–JWST targets (circles), as well as nearby galaxies from (squares; Kim et al. 2021). For NGC 628 (this work) and nearby galaxies, the data points are colored by the duration of the embedded phase of star formation, derived using mid-infrared as an SFR tracer ($t_{fb,MIR}$), which is JWST 21 μm for NGC 0628 and Spitzer 24 μm for other galaxies. The dashed line shows the star-forming main sequence of local galaxies (Leroy et al. 2019).

galaxy located at 9.8 Mpc. With the arrival of JWST, the volume where such measurements can be done has increased by a factor of >100 (with $D < 25$ Mpc), compared to what was possible with Spitzer (with $D < 3.5$ Mpc). Our measurements are in good agreement with those from our previous work in the small sample of five nearby galaxies (at $D < 3.5$ Mpc; Kim et al. 2021) for which such measurements were possible previously, and our results also achieve a comparable uncertainty of 30%.

In the near future, a systematic determination of these timescales will become possible with the PHANGS–JWST survey, significantly increasing the total number of galaxies where this measurement can be performed to 24, where 19 of them come from PHANGS–JWST and have distances up to 20 Mpc. This will for the first time cover a wide range of parameters (e.g., galaxy masses, morphological types, and interstellar medium properties) across a statistically representative sample. Specifically, with the addition of the full PHANGS–JWST galaxy sample, the ranges of GMC properties where we can characterize this early phase of star formation become much wider. For example, the range of average internal pressure of GMCs in our previous galaxy sample (Kim et al. 2021) was 10^4–10^5 K cm^{-3} and will be expanded up to 10^7 K cm^{-3}. Similarly, the average molecular gas surface density was 10^1–10^2 $M_\odot$ pc^{-2} and now can be probed up to 10^3 $M_\odot$ pc^{-2} (Rosolowsky et al. 2021; A. Hughes et al. 2022, in preparation). This will allow us to characterize how the processes regulating the early stages of massive star formation depend on the galactic environment.

Kim et al.

Appendix A
Accuracy of Our Measurements

Kruijssen et al. (2018, Section 4.4) have outlined a set of criteria that our measurements have to satisfy in order to be considered reliable with an accuracy of 30% or better. Here, we verify that these requirements are fulfilled, demonstrating that the constrained $t_{21\,\mu m}$, $t_{fb,21\,\mu m}$, and $\lambda_{21\,\mu m}$ are accurate. We refer to our previous papers (Chevance et al. 2020a, 2022a; Kim et al. 2022) for a validation of our measurements using Hα as an SFR tracer.

1. The emitting timescale of molecular gas and SFR tracer should not differ by one order of magnitude. This is satisfied by $|\log_{10}(t_{21\,\mu m}/t_{CO})| = 0.35$.

2. Individual regions within a galaxy should be sufficiently resolved and this is ensured by $\lambda_{21\,\mu m}/l_{ap,min} = 1.9$.

3. We confirm that the number of identified peaks in each CO and 21 μm map is more than 35 peaks and is $\sim$400 on average.

4. The CO-to-21 μm flux ratio measured locally when focusing on CO (respectively, 21 μm) peaks should not fall below (respectively, above) the galactic average. This is visibly satisfied in Figure 2 and confirms that any diffuse, large-scale emission has been appropriately filtered in both maps.

5. In order to ensure that the identified peaks represent a temporal manifestation of regions undergoing independent evolution from gas to stars, the galaxy-wide SFR during the last GMC cycle ($\tau = t_{CO} + t_{21\,\mu m} - t_{fb,21\mu m} = 27.5$ Myr) should not vary by more than 0.2 dex, when averaged over a bin size of t_{CO} or $t_{21\,\mu m}$. This is confirmed by the star formation history derived using MUSE data and spectral fitting by I. Pessa et al. (2022, in preparation), where the SFR is found to not vary significantly during the most recent $\sim$30 Myr, when time averaged by $t_{21\,\mu m} \approx 10$ Myr.

6. Individual regions should be observable in both molecular gas and the SFR tracer at some point in their evolution. This implies that the CO and 21 μm maps should be sensitive to similar regions. In order to confirm this, we first compute the minimum mass of the young stellar population that is expected to form within the observed clouds, by multiplying the 5σ sensitivity of the CO map ($5 \times 10^4\,M_\odot$) by the integrated star formation efficiency ($5.5^{+4.0}_{-2.3}$%), measured for clouds in NGC 628 (Kim et al. 2022). Then, this value is compared to the mass of a hypothetical young stellar population that emits photons at the 5σ sensitivity of the 21 μm map on the scale of star-forming regions ($\lambda_{21\,\mu m}$). We use the STARBURST99 model (Leitherer et al. 1999) to estimate Hα luminosity, which is converted to 21 μm using the conversion factor from Leroy et al. (2022) to estimate the mass, assuming instantaneous star forma- tion, 5 Myr ago. As a result, we find a reasonable agreement of the expected minimum mass of the stellar population between that obtained from CO map ($\sim$2500 $M_\odot$) and that from 21 μm map ($\sim$1500 $M_\odot$).

Kim et al.
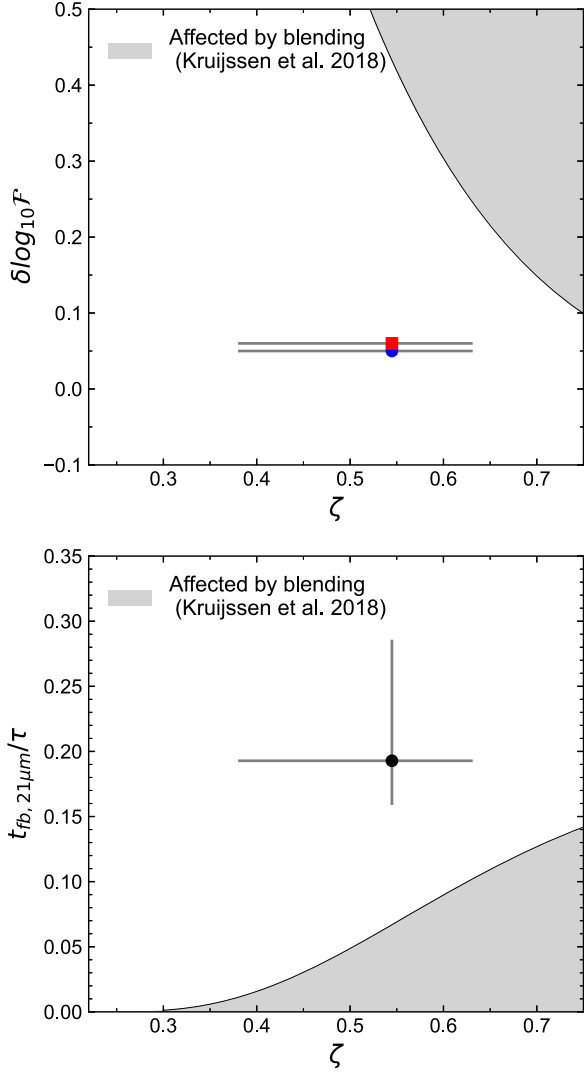
Figure 4. The top panel shows the flux contrast ($\delta \log_{10} \mathcal{F}$) used to identify peaks on CO (blue) 21 μm (red) map as a function of the average filling factor ζ. The bottom panel shows the ratio of the feedback timescale ($t_{\mathrm{fb},21\ \mu\mathrm{m}}$) and the total duration of the GMC life cycle (τ) as a function of ζ. In both panels, the shaded region shows the parameter space where crowding of sources can lead to an overestimation of the feedback timescale. Our data points are well outside of this region, confirming that we sufficiently resolve star-forming regions and our measurement of $t_{\mathrm{fb},21\ \mu\mathrm{m}}$ is reliable.

However, we note that the resolution and sensitivity of the ALMA map may quickly become the limiting factor to these measurements using JWST observations.

7. When peaks are crowded and potentially overlapping with each other, the flux contrast used for peak identification ($\delta \log_{10} \mathcal{F}$) should be small enough to pick out adjacent peaks, and avoid overestimating the feedback timescale. Kruijssen et al. (2018) have prescribed an upper limit of this value as a function of the average filling factor of gas and SFR tracer peaks (ζ). This ζ is defined as $2r/\lambda$, where r is the mean radius of the peaks of a given tracer. The total ζ is obtained by averaging the filling factor for the gas and SFR tracer peaks, weighted by their associated emission timescales. In Figure 4, we show that our selection of $\delta \log_{10} \mathcal{F}$ for both CO and 21 μm is below the upper limit determined by Kruijssen et al. (2018).

8. Even when the previous condition is met, peaks can be overlapping with neighboring peaks due to high filling factors, and this can falsely cause a longer feedback timescale to be measured. In this case, the measured feedback timescale would only be an upper limit. In Figure 4, we compare our measurements of $t_{\mathrm{fb},21\ \mu\mathrm{m}}/\tau$ and ζ to the analytic prescription by Kruijssen et al. (2018), in which the shaded area represents the parameter space where crowding of peaks are affecting our measurements of the feedback timescale. Our measurements are well outside of this shaded region, indicating that peaks are sufficiently resolved.

9. We confirm that the conditions $t_{\mathrm{fb}} > 0.05\,\tau$ and $t_{\mathrm{fb}} < 0.95\,\tau$ are satisfied by $t_{\mathrm{fb}} \approx 0.2\,\tau$, as shown in the lower panel of Figure 4.

10. With a similar reasoning as for condition 5, we do not expect the galaxy-wide SFR to vary more than 0.2 dex during the last course of τ, when time averaged over the feedback timescale.

11. After masking the crowded galactic center, we confirm that visual inspection does not reveal regions with abundant blending.

Appendix B
Data Used in Figure 2

The left panel of Figure 2 shows the measured deviation of CO-to-21 μm flux ratio relative to the galactic average, as a function of the size of apertures centered on CO and 21 μm emission peaks. The measured flux ratios increasingly diverge from the galactic average value toward smaller scales, illustrating that molecular gas and young stellar regions are spatially decorrelated. Table 2 lists the measured flux ratios as a function of the aperture size used to make the left panel of Figure 2.

Table 2
Data Used in Figure 2

Aperture Size (pc)	Centered on CO Peaks	σ_{min}	σ_{max}	σ_{min}^{shade}	σ_{max}^{shade}	Centered on 21 μm Peaks	σ_{min}	σ_{max}	σ_{min}^{shade}	σ_{max}^{shade}
50	1.37	0.16	0.18	0.03	0.03	0.41	0.03	0.04	0.01	0.01
63	1.33	0.15	0.17	0.03	0.03	0.43	0.04	0.04	0.01	0.01
81	1.35	0.15	0.17	0.04	0.04	0.47	0.04	0.04	0.01	0.01
103	1.29	0.14	0.16	0.04	0.04	0.51	0.04	0.05	0.01	0.01
131	1.22	0.13	0.14	0.03	0.03	0.60	0.06	0.06	0.01	0.01
166	1.22	0.13	0.15	0.03	0.04	0.67	0.06	0.07	0.02	0.02
211	1.20	0.13	0.15	0.04	0.04	0.77	0.08	0.09	0.02	0.02
268	1.18	0.13	0.15	0.03	0.04	0.82	0.08	0.09	0.02	0.02
340	1.13	0.12	0.14	0.03	0.03	0.85	0.09	0.10	0.02	0.02
431	1.07	0.11	0.12	0.03	0.03	0.86	0.09	0.10	0.02	0.02
544	1.05	0.11	0.12	0.03	0.03	0.90	0.09	0.11	0.02	0.02
690	1.03	0.10	0.11	0.02	0.03	0.96	0.09	0.11	0.02	0.02
866	1.04	0.10	0.11	0.02	0.02	0.98	0.10	0.11	0.02	0.02
1088	1.04	0.10	0.11	0.02	0.02	1.01	0.10	0.11	0.02	0.02
1360	1.02	0.10	0.11	0.02	0.02	1.00	0.10	0.11	0.02	0.02

Note. Relative changes of the CO-to-21 μm flux ratio compared to the galactic average as a function of the size of apertures focused on CO and 21 μm emission peaks. The downward and upward 1σ uncertainties of each measurement (σ_{min} and σ_{max}), as well as those accounting for the covariance between data points are listed (σ_{min}^{shade} and σ_{max}^{shade}).

ORCID iDs

Jaeyeon Kim ● https://orcid.org/0000-0002-0432-6847
Mélanie Chevance ● https://orcid.org/0000-0002-5635-5180
J. M. Diederik Kruijssen ● https://orcid.org/0000-0002-8804-0212
Ashley. T. Barnes ● https://orcid.org/0000-0003-0410-4504
Frank Bigiel ● https://orcid.org/0000-0003-0166-9745
Guillermo A. Blanc ● https://orcid.org/0000-0003-4218-3944
Médéric Boquien ● https://orcid.org/0000-0003-0946-6176
Yixian Cao ● https://orcid.org/0000-0001-5301-1326
Enrico Congiu ● https://orcid.org/0000-0002-8549-4083
Daniel A. Dale ● https://orcid.org/0000-0002-5782-9093
Oleg V. Egorov ● https://orcid.org/0000-0002-4755-118X
Christopher M. Faesi ● https://orcid.org/0000-0001-5310-467X
Simon C. O. Glover ● https://orcid.org/0000-0001-6708-1317
Kathryn Grasha ● https://orcid.org/0000-0002-3247-5321
Brent Groves ● https://orcid.org/0000-0002-9768-0246
Hamid Hassani ● https://orcid.org/0000-0002-8806-6308
Annie Hughes ● https://orcid.org/0000-0002-9181-1161
Ralf S. Klessen ● https://orcid.org/0000-0002-0560-3172
Kathryn Kreckel ● https://orcid.org/0000-0001-6551-3091
Kirsten L. Larson ● https://orcid.org/0000-0003-3917-6460
Janice C. Lee ● https://orcid.org/0000-0002-2278-9407
Adam K. Leroy ● https://orcid.org/0000-0002-2545-1700
Daizhong Liu ● https://orcid.org/0000-0001-9773-7479
Steven N. Longmore ● https://orcid.org/0000-0001-6353-0170
Sharon E. Meidt ● https://orcid.org/0000-0002-6118-4048
Hsi-An Pan ● https://orcid.org/0000-0002-1370-6964
Jérôme Pety ● https://orcid.org/0000-0003-3061-6546
Miguel Querejeta ● https://orcid.org/0000-0002-0472-1011
Erik Rosolowsky ● https://orcid.org/0000-0002-5204-2259
Toshiki Saito ● https://orcid.org/0000-0001-9016-2641
Karin Sandstrom ● https://orcid.org/0000-0002-4378-8534
Eva Schinnerer ● https://orcid.org/0000-0002-3933-7677
Rowan J. Smith ● https://orcid.org/0000-0002-0820-1814
Antonio Usero ● https://orcid.org/0000-0003-1242-505X
Elizabeth J. Watkins ● https://orcid.org/0000-0002-7365-5791
Thomas G. Williams ● https://orcid.org/0000-0002-0012-2142

References

Anand, G. S., Lee, J. C., Van Dyk, S. D., et al. 2021a, MNRAS, 501, 3621
Anand, G. S., Rizzi, L., Tully, R. B., et al. 2021b, AJ, 162, 80
Aniano, G., Draine, B. T., Gordon, K. D., & Sandstrom, K. 2011, PASP, 123, 1218
Astropy Collaboration, Robitaille, T. P., Tollerud, E. J., et al. 2013, A&A, 558, A33
Backus, C., Velusamy, T., Thompson, T., & Arballo, J. 2005, in ASP Conf. Ser. 347, Hires: Super-resolution for the Spitzer Space Telescope, ed. P. Shopbell, M. Britton, & R. Ebert (San Francisco, CA: ASP), 61
Barnes, A. T., Chandar, R., Kreckel, K., et al. 2022, A&A, 662, L6
Barnes, A. T., Longmore, S. N., Dale, J. E., et al. 2020, MNRAS, 498, 4906
Battersby, C., Bally, J., & Svoboda, B. 2017, ApJ, 835, 263
Bigiel, F., Leroy, A., Walter, F., et al. 2008, AJ, 136, 2846
Blitz, L., Fukui, Y., Kawamura, A., et al. 2007, in Protostars and Planets V, ed. B. Reipurth, D. Jewitt, & K. Keil (Tucson, AZ: Univ. Arizona Press), 81
Calzetti, D., Johnson, K. E., Adamo, A., et al. 2015, ApJ, 811, 75
Chevance, M., Kruijssen, J. M. D., Hygate, A. P. S., et al. 2020a, MNRAS, 493, 2872
Chevance, M., Kruijssen, J. M. D., Krumholz, M. R., et al. 2022a, MNRAS, 509, 272
Chevance, M., Kruijssen, J. M. D., Vazquez-Semadeni, E., et al. 2020b, SSRv, 216, 50
Chevance, M., Krumholz, M. R., McLeod, A. F., et al. 2022b, arXiv:2203.09570
Corbelli, E., Braine, J., Bandiera, R., et al. 2017, A&A, 601, A146
Della Bruna, L., Adamo, A., McLeod, A. F., et al. 2022, A&A, 666, A29
Draine, B. T., & Li, A. 2007, ApJ, 657, 810
Dumas, G., Schinnerer, E., Tabatabaei, F. S., et al. 2011, AJ, 141, 41
Engargiola, G., Plambeck, R. L., Rosolowsky, E., & Blitz, L. 2003, ApJS, 149, 343
Gaia Collaboration, Brown, A. G. A., Vallenari, A., et al. 2018, A&A, 616, A1
Galliano, F., Galametz, M., & Jones, A. P. 2018, ARA&A, 56, 673
Ginsburg, A., Bressert, E., Bally, J., & Battersby, C. 2012, ApJL, 758, L29
Gnedin, N. Y., et al. 2016, Saas-Fee Advanced Course, 43, 85
Grasha, K., Calzetti, D., Adamo, A., et al. 2019, MNRAS, 483, 4707
Grasha, K., Calzetti, D., Bittle, L., et al. 2018, MNRAS, 481, 1016
Hannon, S., Lee, J. C., Whitmore, B. C., et al. 2019, MNRAS, 490, 4648
Hannon, S., Lee, J. C., Whitmore, B. C., et al. 2022, MNRAS, 512, 1294

Harris, C. R., Millman, K. J., van der Walt, S. J., et al. 2020, Natur, 585, 357
Hassani, H., Rosolowsky, E., Leroy, A. K., et al. 2022, ApJL, in press, arXiv:2212.01526
Haydon, D. T., Kruijssen, J. M. D., Chevance, M., et al. 2020, MNRAS, 498, 235
Hygate, A. P. S., Kruijssen, J. M. D., Chevance, M., et al. 2019, MNRAS, 488, 2800
Kawamura, A., Mizuno, Y., Minamidani, T., et al. 2009, ApJS, 184, 1
Kennicutt, R. C., Jr. 1998, ApJ, 498, 541
Kennicutt, R. C., Jr., Calzetti, D., Walter, F., et al. 2007, ApJ, 671, 333
Kennicutt, R. C., & Evans, N. J. 2012, ARA&A, 50, 531
Kim, J., Chevance, M., Kruijssen, J. M. D., et al. 2021, MNRAS, 504, 487
Kim, J., Chevance, M., Kruijssen, J. M. D., et al. 2022, MNRAS, 516, 3006
Kim, J., Chevance, M., Kruijssen, J. M. D., et al. 2023, ApJL, 944, L20
Koepferl, C. M., Robitaille, T. P., Morales, E. F. E., & Johnston, K. G. 2015, ApJ, 799, 53
Kruijssen, J. M. D., & Longmore, S. N. 2014, MNRAS, 439, 3239
Kruijssen, J. M. D., Pfeffer, J. L., Crain, R. A., & Bastian, N. 2019a, MNRAS, 486, 3134
Kruijssen, J. M. D., Schruba, A., Chevance, M., et al. 2019b, Natur, 569, 519
Kruijssen, J. M. D., Schruba, A., Hygate, A. P. S., et al. 2018, MNRAS, 479, 1866
Lada, C. J., & Lada, E. A. 2003, ARA&A, 41, 57
Lee, J. C., Whitmore, B. C., Thilker, D. A., et al. 2022a, ApJS, 258, 10
Lee, J., Sandstrom, K. M., Leroy, A. K., et al. 2022b, ApJL, in press, arXiv:2212.02667
Leitherer, C., Schaerer, D., Goldader, J. D., et al. 1999, ApJS, 123, 3
Leroy, A. K., Bigiel, F., de Blok, W. J. G., et al. 2012, AJ, 144, 3
Leroy, A. K., Hughes, A., Liu, D., et al. 2021a, ApJS, 255, 19
Leroy, A. K., Sandstrom, K. M., Lang, D., et al. 2019, ApJS, 244, 24
Leroy, A. K., Schinnerer, E., Hughes, A., et al. 2021b, ApJS, 257, 43
Leroy, A., et al. 2022, ApJL, submitted
Linden, S. T., Evans, A. S., Armus, L., et al. 2022, arXiv:2210.05763
Lopez, L. A., Krumholz, M. R., Bolatto, A. D., et al. 2014, ApJ, 795, 121
Lu, A., Boyce, H., Haggard, D., et al. 2022, MNRAS, 514, 5035
Meidt, S. E., Hughes, A., Dobbs, C. L., et al. 2015, ApJ, 806, 72
Meidt, S. E., Leroy, A. K., Rosolowsky, E., et al. 2018, ApJ, 854, 100
Miura, R. E., Kohno, K., Tosaki, T., et al. 2012, ApJ, 761, 37
Onodera, S., Kuno, N., Tosaki, T., et al. 2010, ApJL, 722, L127
Padoan, P., Haugbølle, T., Nordlund, Å., & Frimann, S. 2017, ApJ, 840, 48
Pan, H.-A., Schinnerer, E., Hughes, A., et al. 2022, ApJ, 927, 9
Rodriguez, J., Lee, J., Whitmore, B., et al. 2022, ApJL, in press, arXiv:2211.13426
Rosolowsky, E., Hughes, A., Leroy, A. K., et al. 2021, MNRAS, 502, 1218
Schinnerer, E., Hughes, A., Leroy, A., et al. 2019, ApJ, 887, 49
Schruba, A., Leroy, A. K., Walter, F., Sandstrom, K., & Rosolowsky, E. 2010, ApJ, 722, 1699
Thilker, D., Lee, J. C., Deger, S., et al. 2023, ApJL, 944, L13
Turner, J. A., Dale, D. A., Lilly, J., et al. 2022, MNRAS, 516, 4612
Verley, S., Corbelli, E., Giovanardi, C., & Hunt, L. K. 2009, A&A, 493, 453
Viaene, S., Baes, M., Tamm, A., et al. 2017, A&A, 599, A64
Virtanen, P., Gommers, R., Oliphant, T. E., et al. 2020, NatMe, 17, 261
Ward, J. L., Chevance, M., Kruijssen, J. M. D., et al. 2020, MNRAS, 497, 2286
Ward, J. L., Kruijssen, J. M. D., Chevance, M., Kim, J., & Longmore, S. N. 2022, MNRAS, 516, 402
Whitmore, B. C., Brogan, C., Chandar, R., et al. 2014, ApJ, 795, 156
Whitmore, B., Chandar, R., Rodriguez, J., et al. 2023, ApJL, 944, L14
Williams, J. P., de Geus, E. J., & Blitz, L. 1994, ApJ, 428, 693
Williams, T. G., Baes, M., De?Looze, I., et al. 2019, MNRAS, 487, 2753
Zabel, N., Davis, T. A., Sarzi, M., et al. 2020, MNRAS, 496, 2155

Chapter 5

Conclusions

The aim of this thesis is to improve our current understanding of the processes regulating the cycle of matter between molecular gas and young stars and how they differ in various environments. My work has been focused on tackling these major questions in star formation by systematically determining the characteristic timescales of the successive phases of star formation.

In the first section of this chapter, we provide a brief overview of the main results presented in this thesis (Section 5.1). In the second section, we discuss the findings of our research and present possible future directions (Section 5.2).

5.1   Summary

Following the introduction in Chapter 1, this section summarises the key points and conclusions of each chapter, while readers are referred to the original articles for technical details.

Chapter 2

Observations at GMC scales (~ 100 pc) have shown distinct distributions of molecular gas and young stellar regions, tracing different phases of star formation (Kawamura et al., 2009; Corbelli et al., 2017; Kruijssen et al., 2019; Schinnerer et al., 2019; Chevance et al., 2020a; Pan et al., 2022). We have characterised the relative spatial distributions of GMCs and Hii regions by applying the robust statistical method developed by Kruijssen and Longmore (2014) and Kruijssen et al. (2018) to cloud-scale CO and narrowband Hα observations from the PHANGS survey, tracing molecular clouds and exposed young stellar regions respectively.

By doing so, we have established systematic measurements of the evolutionary sequence of GMCs from an inert molecular gas phase to Hii regions, across 54 main-sequence galaxies, which is the largest and most statistically complete sample to-date. Specifically, we have provided constraints on the cloud lifetime, the feedback time-scale (i.e., the duration over which CO and Hα emission overlap), and characteristic separation length between star-

forming regions, independently undergoing their evolution from gas to stars. Furthermore, we derive other physical quantities such as the star formation efficiency per cloud lifetime, feedback velocity, and diffuse emission fraction.

Across these galaxies, GMC lifetime is measured to be about $1-3$ times the GMC turbulence crossing timescale ($5-30$ Myr), with an average of 16 ± 6 Myr. We have found that CO and Hα emission overlap for $1-5$ Myr, with an average of 3.2 ± 1.1 Myr. This overlapping time-scale represents the time it takes for emerging massive stars (visible in Hα) to disrupt the surrounding molecular gas (either by kinetic dispersal or by the photodissociation of CO molecules). The short time-scale indicates that cloud dispersal is primarily driven by pre-supernova feedback, such as photoionisation and stellar winds. Supernovae then explode in a pre-processed environment and have an effect on kpc-scales. This fast transition from gas to stars on GMC-scale spatially offsets GMCs and young stellar regions, which are found to be separated by $100-400$ pc on average. We have demonstrated that measured star formation efficiencies in these clouds are low ($1-8\%$), illustrating that rapid stellar feedback strongly restricts the conversion of gas to stars by limiting their lifetime. The feedback velocity is measured to be $10-30 \mathrm{kms}^{-1}$. Finally, the average diffuse emission fraction in each CO and Hα map is 45 ± 10 and 53 ± 19 per cent, respectively. In general, these findings align with those obtained in our earlier works, which were based on a much smaller sample of galaxies (Kruijssen et al., 2019; Chevance et al., 2020a; Kim et al., 2021a).

With this large sample, covering a wide range of galaxy environmental properties, we were able to quantify links between the small-scale GMC evolution and the large-scale host galaxy properties. Namely, GMC lifetimes are measured to be shorter in lower mass and lower molecular gas surface density galaxies. These trends are in part due to the presence of significant molecular gas not detected in CO in such environments (e.g. Bolatto et al., 2013; Madden et al., 2020). In addition, more massive galaxies, which tend to have a higher molecular gas surface density, have a higher mid-plane pressure (Sun et al., 2020b), providing an external pressure that allows clouds to survive for a longer time. Our results also indicate that the feedback time-scale decreases as the CO emission becomes sharper (a larger density contrast between to CO emission peak and the galactic average), which can be explained as an effect of feedback where the CO emission becomes undetectable more quickly after the onset of massive star formation when surrounding interstellar medium is sparser. Finally, we have identified a strong correlation between the fraction of diffuse Hα emission and the average virial parameter of GMCs. This can be physically understood as a more pervasive medium of GMCs allows more ionising photons to escape from the star-forming region and reach further into the surrounding gas.

Chapter 3

The earliest star-forming phases are heavily-obscured and thus Hα emission is attenuated by gas and dust within the cloud. After the formation of massive stars, the young stellar region progressively reveals itself through various stellar feedback processes (photoionisation, winds, supernovae, and radiation pressure). In order to understand physical mechanisms responsible for this in more detail, characterisation of the earliest stages is crucial. As

shown in Chapter 2, the evolutionary timeline between molecular clouds and exposed young stars has been constrained in numerous nearby galaxies, but the duration of the embedded massive star-forming phase, including the phase missed in Hα emission, remains elusive.

In Chapter 3, for five nearby galaxies (with distances less than 3.5 Mpc), we have refined the GMC evolutionary sequence, previously defined using CO and Hα, by measuring the duration of the (heavily) obscured star formation with *Spitzer* 24 μm, using the methodology from Kruijssen and Longmore (2014) and Kruijssen et al. (2018). We find that molecular clouds undergo a rapid dispersion within 2 to 7 Myr after the onset of massive star formation (indicated by 24μm emission). The feedback time-scale includes the duration of the massive star-forming phase and makes up 20−50% of the overall cloud lifetime (10−30 Myr). This is in good agreement with previous works using different methods (Lada and Lada, 2003; Whitmore et al., 2014; Calzetti et al., 2015; Corbelli et al., 2017). The first half of this embedded phase, 1−4 Myr, is heavily obscured and therefore is invisible in Hα emission. Once the feedback processes have dispersed the cloud, the 24μm emission no longer indicates ongoing massive star formation. However, the 24μm emission from ambient gas remains detectable for an additional 2−9 Myr, possibly origination from dust excited by interstellar radiation field or radiation from relatively low-mass stars.

Chapter 4

Prior to the launch of JWST, such measurements of the embedded phase (as shown in Chapter 3) could only be conducted for a small number of the closest galaxies, due to the limited angular resolution and sensitivity of *Spitzer*. Using initial data from PHANGS–JWST (Lee et al., 2022b), in Chapter 4, we have further demonstrated that the (heavily) obscured phase can be reliably characterised in NGC628, located at $D = 9.8$ Mpc. For the first time, we were able to constrain the beginning and duration of the embedded phase of star formation at a distance greater than 3.5 Mpc, paving the way to achieve the statistics and dynamic range required to understand the relationship between the physical processes driving massive star formation and their environment.

We have shown that the interval during which GMCs in NGC628 are devoid of young massive stars is $18^{+2.7}_{-3.6}$ Myr. The embedded phase of star formation lasts for $5.1^{+2.7}_{-1.4}$ Myr and constitutes 20% of the total GMC lifetime. During almost the initial half of this phase, star-forming regions are heavily obscured ($2.3^{+2.7}_{-1.4}$ Myr), thus undetected in Hα emission. Subsequently, the star-forming region becomes partially exposed, enabling the detection of Hα emission along with CO and 21 μm emission for $2.7^{+0.5}_{-0.6}$ Myr. Finally, the molecular clouds are completely dispersed by the stellar feedback, leaving behind only SFR tracers to be detected for an additional ∼5 Myr, without accompanying CO emission.

5.2 Discussion and future directions

The interstellar medium is shaped by galaxies and is reshaped rapidly by feedback from stars formed within. There are still improvements in various directions that can be made to foster our understanding of star formation, feedback, and ultimately galaxy evolution.

One of the greatest questions yet to be resolved in the field is the identification of the physical mechanisms responsible for the *full* cycle of star formation, that is, starting from the assembly of atomic gas (Hɪ) into giant molecular clouds (GMCs), followed by (heavily) embedded star formation, and culminating in feedback-created Hɪɪ regions and termination of further star formation. As presented in this thesis, the evolutionary timeline between molecular clouds and exposed young stellar regions has recently been measured in various galaxies, showing that GMCs are rapidly dispersed by stellar feedback exposing the young stellar population. Despite these new insights, the question of how atomic gas, dust, and molecular gas interact and how feedback and star formation proceed in various environments remain unanswered. The main limitation in *expanding* and *refining* this GMC timeline to include the multi-phase and complete picture of star formation has been the lack of cloud-scale Hɪ and embedded star formation observations. This severely limited the range of environments in which these processes could be characterised and therefore hindered our capacity to fully understand and describe them.

These limitations can now be overcome with the Near Infrared Camera (NIRCam) Instrument and the Mid-Infrared Instrument (MIRI) aboard JWST, opening a new era in infrared astronomy. In particular, ongoing large programme on JWST, targeting star-forming discs of 19 galaxies with distances of $D = 5-20\,$Mpc at $2-21\,\mu$m wavelength (PHANGS-JWST; Lee et al., 2022b), as well as ancillary data (ALMA, AstroSat, HST, MUSE) can all be used to trace distinct parts of the multi-phase baryon cycle. By capitalising on this data, an important step forward is to (1) obtain environmental dependences of the neutral gas cloud lifetime, (2) describe the heavily obscured phase of star formation (3) probe the destruction and growth of dust grains during this early phase, and (4) put realistic constraints on interstellar medium conditions that allow globular cluster formations by extending my analysis to extremely high density environments.

This will answer critical questions like: What characterises the complete picture of star formation, starting from diffuse atomic gas to fully revealed young stellar regions? How do these processes depend on environments?

5.2.1   Environmental dependence of neutral cloud lifetime

As shown in Chapter 2, we have found that the GMC lifetime is longer for galaxies with higher mass (higher metallicity) and higher molecular gas surface density (molecular gas-dominated). These trends can be explained by two physical arguments, 1) a large fraction of GMCs in a low-mass (low-metallicity) and low-molecular gas surface density (atomic gas-dominated) environments is not detected in CO emission (CO-dark molecular gas), resulting in apparently short-lived GMCs and/or 2) high-mass galaxies, which have higher molecular gas surface density, have higher mid-plane pressure, creating conditions for longer-lived GMCs.

To distinguish how much this trend is affected by the presence of CO-dark molecular gas, high-resolution tracers of the neutral gas, which are independent of their ability to emit CO, are crucially needed. This is possible with the polycyclic aromatic hydrocarbon emission at 7.7 and 11.3 μm observed with MIRI JWST for 19 galaxies, reaching physical scales of $10-20\,$pc. Using the first four targets, Sandstrom et al. (2022) have recently demonstrated

that this polycyclic aromatic hydrocarbon emission, arising from excitation of small dust grains, effectively traces both the cold and warm neutral media. These two components can be separated using their morphology. Firstly, the necessary step is to constrain the neutral gas cloud lifetime, not affected by the potential presence of CO-dark molecular gas, and traces the assembly of GMCs from the relatively diffuse H I by applying the statistical method (Kruijssen and Longmore, 2014; Kruijssen et al., 2018) to this polycyclic aromatic hydrocarbon emission. Furthermore, these neutral cloud lifetimes can be directly compared to the time-scales of galactic dynamical processes (e.g. shear, epicyclic motion) influencing cloud lifetime (e.g. Meidt et al., 2015; Jeffreson et al., 2020; Sun et al., 2022), using rotational curve measurements (Lang et al., 2020), allowing the identification of physical mechanisms regulating the matter cycle between gas and stars. Furthermore, in low-mass and/or low-molecular gas surface density envrionment, observations of the nearest galaxies (mostly dwarfs and the Milky Way) suggest that atomic hydrogen is more vulnerable to stellar feedback compared to molecular gas, where atomic gas shows unique distributions of bubbles or shells of colder gas and dust, which have been carved out by expanding pockets of hot gas (Kim et al., 1999; Walter et al., 2007; Dawson et al., 2013; Lim et al., 2020). Expansion of the environmental axis with PHANGS-JWST, will provide important insights into the interaction between gas and stellar feedback (Watkins et al., 2022).

The polycyclic aromatic hydrocarbon emission maps can be separated into cold and warm neutral media components using their morphology. Again using the same methodology, measuring how fast the transition from H I to molecular gas phase takes place will have important implications on the cooling rate and fragmentation scale of the interstellar medium (Jappsen et al., 2005). Similarly to environmental dependences found in Chapter 2, the important next step will be to identify environmental dependences of these time-scales and complete the multi-phase timeline of cloud-scale star formation, from H I to the fully revealed H II regions, using 19 PHANGS-JWST galaxies.

Lastly, direct measurements of atomic gas will also shed light on obtaining these time-scales. For the Local Group, Very Large Array and Australian Square Kilometre Array Pathfinder started to capture the H I distributions and kinematics, offering our current best views on the physical state, substructure, and its link to the stellar feedback. Soon the Next Generation Very Large Array and Square Kilometer Array will carry this view to other galaxies.

5.2.2   Characterization of the heavily obscured massive star formation

In Chapter 2, we have demonstrated that GMCs are quickly dispersed by stellar feedback within $1-5\,$Myr, after a long inactive phase before massive star formation is detected in Hα emission. However, the earliest phases of star formation are heavily obscured, and not detected in Hα, due to the extinction from the surrounding dense gas and dust. Measuring the time clouds spend being truly inactive is important to distinguish whether star formation is delayed by the decay of initial turbulence (Padoan et al., 2017) or suppressed by galactic scale dynamics (Meidt et al., 2018).

To start answering this question, in Chapter 3, we have reported that the duration of star formation doubles ($1-4\,$Myr longer) when the heavily obscured phase is taken into

account by using *Spitzer* 24 μm as an SFR tracer, instead of Hα only. Later in Chapter 4, I illustrate that this key time-scale of the heavily obscured phase of star formation can be obtained at similar accuracy as in Chapter 3, using the novel MIRI JWST 21 μm observations of NGC628 ($D = 9.8$ Mpc). This shows that the cosmic volume where such measurements can be performed increases by a factor of $\sim$200 and in distances up to $\sim$ 25 Mpc, in principle.

So far, based on the analysis of six galaxies shown in Chapter 3 and Chapter 4, we have not identified any statistically significant trend between the duration of (heavily) obscured phase and galaxy properties, but this can change by including the rest of 18 more PHANGS-JWST targets, which span wide ranges in parameter space (e.g. galaxy mass, morphology, interstellar medium conditions). For example, only when using nearby galaxies, the range of average internal pressure of GMCs is $10^4 - 10^5$Kcm^{-3}, which will be expanded up to 10^7Kcm^{-3}. The average molecular gas surface density (measured at GMC-scale) only ranged from $10^1 - 10^2 M_\odot$pc^{-2} and now will be investigated further up to $10^3 M_\odot$pc^{-2} (Rosolowsky et al., 2021). A systematic determination of this heavily obscured star formation time-scales with the PHANGS–JWST survey will enable the investigation of environmental dependences of the processes regulating the early stages of star formation. Understanding this phase is important as this is when early feedback mechanisms such as photoionisation, radiation pressure, and stellar winds are at work. Several studies, using physical properties of feedback-driven H$\textsc{ii}$ regions, have shown that the pressure induced by pre-supernovae feedback increases at lower metallicity and lower density environments (Lopez et al., 2014; McLeod et al., 2021; Barnes et al., 2022; Della Bruna et al., 2022). Measurements of the heavily obscured phase will be able to provide additional constraints on the properties of the stellar population driving this feedback, as well as pinpoint the time when the leakage of energy and ionising photons starts to happen, allowing more robust and realistic estimates of the pressure term. Furthermore, ages of optically identified stellar associations from PHANGS–HST (Lee et al., 2022b), as well as the degree of local dust extinction derived from the PHANGS–MUSE data (Emsellem et al., 2022) can be used to achieve a better understanding this phase.

5.2.3   Probing the formation and destruction rate of dust grains

While dust hinders our view of star formation in ultraviolet and optical wavelengths, the evolution of dust size is closely linked to the recent star formation. For example, small dust grains facilitate molecular gas formation by catalytic reactions on their surfaces (Hollenbach and Salpeter, 1971), dust grows from stellar ejecta (supernova, asymptotic giant branch stars), but is also destroyed by strong radiation and shocks from young stars (Galliano et al., 2018). Understanding how dust grains and star-forming regions co-evolve is crucial to determine the local reddening curve, efficiency of cooling, and chemical reaction rates (Wolfire et al., 2022).

Using the statistical model from Kruijssen and Longmore (2014), Figure 5.1 shows results from preliminary analysis of the Large Magellanic Cloud in far-infrared wavelengths ($100-500$ μm) from *Herschel*, tracing warm and cold dust where shorter the wavelength the warmer the dust is. We can already point out interesting findings. Far infrared emission at
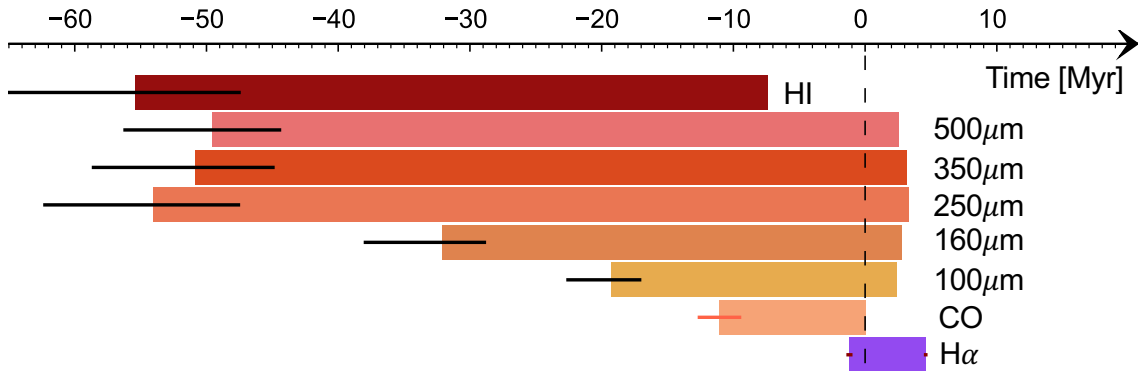
Figure 5.1: *Multi-tracer timeline of star formation in the Large Magellanic Cloud. Far-infrared emission (250−500 μm) tracing cold dust covers the whole duration of Hᵢ and CO emitting timescale. Far-infrared emission at shorter wavelengths (160 and 100 μm bands) traces warm dust and therefore the gas component more directly related to star formation. This far-infrared is emitted for ∼ 4 Myr, after the CO emission has disappeared (vertical dashed line), suggesting that dust takes longer to be destroyed by stellar feedback than CO molecules.*

500, 350, and 250 μm, tracing cold dust overdensities covers the whole duration of Hᵢ and CO emitting timescale, without huge dependence on the wavelength. This is in agreement with our expectations where cold dust is tracing both the atomic as well as molecular gas (Sandstrom et al., 2022). As the wavelength becomes shorter tracing warmer dust (160 and 100 μm), the emission no longer fully correlates with Hᵢ but does still fully cover the molecular cloud lifetime, tracing gas component that is more directly related to star formation. The overlapping timescale between far-infrared at all wavelengths and Hα is longer than that measured between CO and Hα. This illustrates that dust takes 4 Myr longer to be destroyed by stellar feedback compared to the CO molecules (Kim et al. in prep.).

Similar to this preliminary work, the high-resolution JWST maps of strong polycyclic aromatic hydrocarbon emission at 3.3, 7.7, and 11.3μm can be used as tracers for dust. In particular, the flux ratio 3.3 μm/11 μm can be used as a powerful diagnostic tool to trace sizes of the PAHs (Lai et al., 2020; Draine et al., 2021). By separating small and large dust grains using 3.3 μm/11 μm colors, the lifetime of each dust grain with different sizes can be obtained. This can be further used to determine how long these dust grains survive after the onset of massive star formation. It will be possible to study the evolution of dust grains and determine whether the supernovae explosions act as an important source for dust growth or whether radiation and shocks from Hᵢᵢ regions are more powerful in destroying the grains.

5.2.4 Linking local constraints of time-scales to the origin of globular clusters

Globular clusters are thought to form from GMCs residing in high-pressure and high-density discs, which are prevalent in the high-redshift universe (Kruijssen, 2015). One of the things that prominently makes globular clusters different from normal young stellar clusters is the existence of multiple stellar populations. Almost all the globular clusters in the Milky Way host multiple stellar populations that are distinctively separated in their Hertzsprung–Russell diagram as well as in their light element abundances (Bastian and Lardo, 2018). The most well-known light element variation phenomenon is the observed anticorelation between Na and O abundances, while almost no variation in heavy elements is observed (Carretta et al., 2009).

In order to explain this light element variation, most models invoke a self-enrichment scenario where multiple bursts of star formation take place within a gas that has been polluted by ejecta from a previous generation(s) of stars. This requires proto-globular clusters to survive the multiple episodes of star formation. Depending on the enrichment sources, the required characteristic time-scales for the chemical enrichment differ. It can be $< 5\,\mathrm{Myr}$ for models using massive stars as the polluting source (fast rotating massive stars, Decressin et al., 2007; Krause et al., 2013; massive interacting binaries, de Mink et al., 2009; Bastian et al., 2013; supermassive stars, Denissenkov and Hartwick, 2014; Gieles et al., 2018) or much longer ($\sim 10 - 100\,\mathrm{Myr}$) for models adopting asymptotic giant branch stars as the source of enrichment (D'Antona and Caloi, 2004; D'Ercole et al., 2010; D'Antona et al., 2016; Kim and Lee, 2018).

It is possible to put realistic constraints on the interstellar medium conditions required to form globular clusters by measuring the evolutionary timeline of proto-globular clusters. The obvious place to start is GMCs in the Antennae galaxies located at $22\,\mathrm{Mpc}$ (Schweizer et al., 2008), which is a starburst system undergoing a galaxy merger, resembling star formation processes in the early universe (Wilson et al., 2000). The GMCs in the Antennae show a much higher molecular gas surface density of $\Sigma_{\mathrm{H_2}} \approx 10^3 - 10^4\,M_\odot\mathrm{pc}^{-2}$, compared to the typical value of normal disk galaxies ($\Sigma_{\mathrm{H_2}} \approx 10^1 - 10^2\,M_\odot\mathrm{pc}^{-2}$; Sun et al., 2022). All the high-resolution observations required to measure time-scales are publicly available: CO, radio continuum at $345\,\mathrm{GHz}$, $100\,\mathrm{GHz}$ from the Atacama Large Millimeter Array, Hα from the Hubble Space Telescope, respectively tracing molecular gas, dust, embedded, and exposed SF. Whitmore et al. (2014) were the first to attempt to constrain the GMC lifetime in this galaxy. However, no measurement has been made with the statistical rigor and precision needed to time-resolve the star formation histories of massive clusters. Expanding and improving this previous attempt will provide key constraints on how long the proto-globular clusters can survive and form chemically enriched stars. By directly comparing this key value to the survival time expected from the models described above, it will be feasible to determine whether these GMCs are likely forming sites for multiple stellar populations and also test the existing models for the globular cluster formation. Furthermore, in the future, publicly available JWST data will allow a wider search for other candidate clouds that are likely to be undergoing globular cluster formation.

In the era of JWST offering a new view of galaxies, a key next step is providing a

complete picture of star processes and their environmental dependence, from the assembly of diffuse H I into compact molecular clouds, followed by the (heavily) obscured star formation, and finally to feedback-created H II regions. From the strong emission of polycyclic aromatic hydrocarbon and small dust grains, we can trace dust, star formation, and interstellar medium conditions. This emission contains a lot of information, such as radiative transfer, dust properties, heating sources, and interstellar medium structure, which can be used to probe the formation and destruction of dust grains in star-forming regions, as well as put realistic constraints on the environments allowing the formation of globular clusters, connecting how the dominant modes of star formation changed from the early to the present-day universe. It is a very exciting time ahead to obtain a detailed evolutionary timeline, incorporating the multi-phase nature of star formation.

Acknowledgements

Over the course of the last four years, I received a lot of support from people around me in developing this thesis. This challenging process would not have been as enjoyable without their presence. I would like to take this opportunity to express my gratitude.

First of all, I would like to express my gratitude to my supervisors, Mélanie Chevance and Diederik Kruijssen, for their guidance and for many discussions and thoughts about the research. I consider it very fortunate that I was able to participate in the research group, which allowed me to gain insights and a mindset to become an independent researcher. I also thank Cornelis Dullemond, Simon Glover, and Eva Schinnerer for being on my thesis committee, as well as Mathias Bartelmann and Björn Malte Schäfer for being on my examination committee.

I am also grateful to my collaborators in PHANGS, who were essential in making the work presented in this thesis possible. In particular, I thank core paper team members, Adam Leroy, Karin Sandstrom, and Andreas Schruba, for sharing their knowledge, answering all my questions, and supporting my growth as a young scientist.

It was my pleasure to be part of a wonderful group that provided a dynamic and encouraging workspace. I thank every member who has been part of the group, in an order of appearance: Alex Hygate, Daniel Haydon, Sarah Jeffreson, Marta Reina-Campos, Jake Ward, Ben Keller, Jindra Gensior, Sebastian Trujillo-Gomez, Maya Petkova, Andrea Romanelli, and Lise Ramambason.

I am immensely grateful to my mother, father, and sister, for their love, support, and constant encouragement, which have helped shape me into the person I am today. Additionally, I extend my heartfelt thanks to my kind-hearted mother-in-law, father-in-law, and sister-in-law for their warm welcome into their family. Finally, I would like to express my love and appreciation to my husband, Yongjae, for being my best friend, and constant companion, helping me navigate through every challenge that has come our way.

Bibliography

Alatalo, Katherine et al. (July 2013). "The ATLAS^{3D} project - XVIII. CARMA CO imaging survey of early-type galaxies". MNRAS 432.3, 1796–1844. arXiv: `1210.5524 [astro-ph.CO]` (cit. on p. 5).

Barnes, A. T. et al. (June 2022). "Linking stellar populations to H II regions across nearby galaxies. I. Constraining pre-supernova feedback from young clusters in NGC 1672". A&A 662, L6, L6. arXiv: `2205.05679 [astro-ph.GA]` (cit. on p. 80).

Barnes, Ashley T. et al. (Sept. 2020). "Which feedback mechanisms dominate in the high-pressure environment of the central molecular zone?" MNRAS 498.4, 4906–4923. arXiv: `2009.03901 [astro-ph.GA]` (cit. on p. 11).

Bastian, N. et al. (Dec. 2013). "Early disc accretion as the origin of abundance anomalies in globular clusters". MNRAS 436.3, 2398–2411. arXiv: `1309.3566 [astro-ph.GA]` (cit. on p. 82).

Bastian, Nate and Carmela Lardo (Sept. 2018). "Multiple Stellar Populations in Globular Clusters". ARA&A 56, 83–136. arXiv: `1712.01286 [astro-ph.SR]` (cit. on p. 82).

Benincasa, Samantha M. et al. (Sept. 2020). "Live fast, die young: GMC lifetimes in the FIRE cosmological simulations of Milky Way mass galaxies". MNRAS 497.3, 3993–3999. arXiv: `1911.05251 [astro-ph.GA]` (cit. on p. 9).

Bertoldi, Frank and Christopher F. McKee (Aug. 1992). "Pressure-confined Clumps in Magnetized Molecular Clouds". ApJ 395, 140 (cit. on p. 5).

Bigiel, F. et al. (Dec. 2008). "The Star Formation Law in Nearby Galaxies on Sub-Kpc Scales". AJ 136.6, 2846–2871. arXiv: `0810.2541 [astro-ph]` (cit. on pp. 1–3).

Black, John H. and Ewine F. van Dishoeck (Nov. 1987). "Fluorescent Excitation of Interstellar H 2". ApJ 322, 412 (cit. on p. 3).

Blitz, L. and P. Thaddeus (Oct. 1980). "Giant molecular complexes and OB associations. I. The Rosette molecular complex." ApJ 241, 676–696 (cit. on p. 4).

Blitz, L. et al. (Jan. 2007). "Giant Molecular Clouds in Local Group Galaxies". *Protostars and Planets V*. Ed. by Bo Reipurth, David Jewitt, and Klaus Keil, 81. arXiv: `astro-ph/0602600 [astro-ph]` (cit. on p. 3).

Blitz, Leo (Jan. 1993). "Giant Molecular Clouds". *Protostars and Planets III*. Ed. by Eugene H. Levy and Jonathan I. Lunine, 125 (cit. on p. 1).

Bolatto, Alberto D., Mark Wolfire, and Adam K. Leroy (Aug. 2013). "The CO-to-H$_2$ Conversion Factor". ARA&A 51.1, 207–268. arXiv: `1301.3498 [astro-ph.GA]` (cit. on pp. 3, 4, 76).

Bolatto, Alberto D. et al. (Sept. 2017). "The EDGE-CALIFA Survey: Interferometric Observations of 126 Galaxies with CARMA". ApJ 846.2, 159, 159. arXiv: `1704.02504 [astro-ph.GA]` (cit. on p. 5).

Bothwell, M. S. et al. (Dec. 2014). "ALLSMOG: an APEX Low-redshift Legacy Survey for MOlecular Gas - I. Molecular gas scaling relations, and the effect of the CO/H_2 conversion factor". MNRAS 445.3, 2599–2620. arXiv: `1409.4764 [astro-ph.GA]` (cit. on p. 4).

Bouché, N. et al. (Dec. 2007). "Dynamical Properties of z ~2 Star-forming Galaxies and a Universal Star Formation Relation". ApJ 671.1, 303–309. arXiv: `0706.2656 [astro-ph]` (cit. on p. 2).

Brunetti, Nathan et al. (Jan. 2021). "Highly turbulent gas on GMC scales in NGC 3256, the nearest luminous infrared galaxy". MNRAS 500.4, 4730–4748. arXiv: `2011.01250 [astro-ph.GA]` (cit. on p. 7).

Burton, W. B. and M. A. Gordon (Feb. 1978). "Carbon monoxide in the Galaxy. III. The overall nature of its distribution in the equatorial plane." A&A 63.1-2, 7–27 (cit. on p. 4).

Burton, W. B. et al. (Nov. 1975). "The overall distribution of carbon monoxide in the plane of the Galaxy." ApJ 202, 30–49 (cit. on p. 4).

Calzetti, D. et al. (Sept. 2007). "The Calibration of Mid-Infrared Star Formation Rate Indicators". ApJ 666.2, 870–895. arXiv: `0705.3377 [astro-ph]` (cit. on p. 6).

Calzetti, D. et al. (Oct. 2015). "The Brightest Young Star Clusters in NGC 5253." ApJ 811.2, 75, 75. arXiv: `1508.04476 [astro-ph.GA]` (cit. on pp. 7, 11, 77).

Carretta, E. et al. (Oct. 2009). "Na-O anticorrelation and HB. VIII. Proton-capture elements and metallicities in 17 globular clusters from UVES spectra". A&A 505.1, 139–155. arXiv: `0909.2941 [astro-ph.GA]` (cit. on p. 82).

Chevance, Mélanie et al. (Apr. 2020a). "The lifecycle of molecular clouds in nearby star-forming disc galaxies". MNRAS 493.2, 2872–2909. arXiv: `1911.03479 [astro-ph.GA]` (cit. on pp. 1, 3, 9, 12, 75, 76).

Chevance, Mélanie et al. (Apr. 2020b). "The Molecular Cloud Lifecycle". Space Sci. Rev. 216.4, 50, 50. arXiv: `2004.06113 [astro-ph.GA]` (cit. on pp. 3, 5).

Chevance, Mélanie et al. (Jan. 2022a). "Pre-supernova feedback mechanisms drive the destruction of molecular clouds in nearby star-forming disc galaxies". MNRAS 509.1, 272–288. arXiv: `2010.13788 [astro-ph.GA]` (cit. on pp. 1, 12).

Chevance, Mélanie et al. (Mar. 2022b). "The Life and Times of Giant Molecular Clouds". *arXiv e-prints*, arXiv:2203.09570, arXiv:2203.09570. arXiv: `2203.09570 [astro-ph.GA]` (cit. on p. 7).

Colombo, Dario et al. (Mar. 2014a). "The PdBI Arcsecond Whirlpool Survey (PAWS): Environmental Dependence of Giant Molecular Cloud Properties in M51". ApJ 784.1, 3, 3. arXiv: `1401.1505 [astro-ph.GA]` (cit. on p. 8).

Colombo, Dario et al. (Mar. 2014b). "The PdBI Arcsecond Whirlpool Survey (PAWS): Multiphase Cold Gas Kinematic of M51". ApJ 784.1, 4, 4. arXiv: `1401.3759 [astro-ph.GA]` (cit. on pp. 5, 7).

Combes, F. et al. (Aug. 2009). "Molecular gas in NUclei of GAlaxies (NUGA). XII. The head-on collision in NGC 1961". A&A 503.1, 73–86. arXiv: `0906.2493 [astro-ph.CO]` (cit. on p. 5).

Corbelli, Edvige et al. (May 2017). "From molecules to young stellar clusters: the star formation cycle across the disk of M 33". A&A 601, A146, A146. arXiv: `1703.09183 [astro-ph.GA]` (cit. on pp. 3, 11, 75, 77).

D'Antona, F. et al. (May 2016). "A single model for the variety of multiple-population formation(s) in globular clusters: a temporal sequence". MNRAS 458.2, 2122–2139. arXiv: `1602.05412 [astro-ph.GA]` (cit. on p. 82).

D'Antona, Francesca and Vittoria Caloi (Aug. 2004). "The Early Evolution of Globular Clusters: The Case of NGC 2808". ApJ 611.2, 871–880. arXiv: `astro-ph/0405016 [astro-ph]` (cit. on p. 82).

D'Ercole, Annibale et al. (Sept. 2010). "Abundance patterns of multiple populations in globular clusters: a chemical evolution model based on yields from AGB ejecta". MNRAS 407.2, 854–869. arXiv: `1005.1892 [astro-ph.GA]` (cit. on p. 82).

Daddi, E. et al. (May 2010). "Different Star Formation Laws for Disks Versus Starbursts at Low and High Redshifts". ApJ 714.1, L118–L122. arXiv: `1003.3889 [astro-ph.CO]` (cit. on p. 2).

Davis, Timothy A. et al. (May 2022). "WISDOM Project - X. The morphology of the molecular ISM in galaxy centres and its dependence on galaxy structure". MNRAS 512.1, 1522–1540. arXiv: `2203.01358 [astro-ph.GA]` (cit. on pp. 5, 8).

Dawson, J. R. et al. (Jan. 2013). "Supergiant Shells and Molecular Cloud Formation in the Large Magellanic Cloud". ApJ 763.1, 56, 56. arXiv: `1211.7119 [astro-ph.GA]` (cit. on p. 79).

de Mink, S. E. et al. (Nov. 2009). "Massive binaries as the source of abundance anomalies in globular clusters". A&A 507.1, L1–L4. arXiv: `0910.1086 [astro-ph.SR]` (cit. on p. 82).

Decressin, T. et al. (Mar. 2007). "Fast rotating massive stars and the origin of the abundance patterns in galactic globular clusters". A&A 464.3, 1029–1044. arXiv: `astro-ph/0611379 [astro-ph]` (cit. on p. 82).

Della Bruna, Lorenza et al. (Oct. 2022). "Stellar feedback in M 83 as observed with MUSE. II. Analysis of the H II region population: Ionisation budget and pre-SN feedback". A&A 666, A29, A29. arXiv: `2206.09741 [astro-ph.GA]` (cit. on p. 80).

den Brok, Mark et al. (Jan. 2020). "The MUSE Atlas of Discs (MAD): Ionized gas kinematic maps and an application to diffuse ionized gas". MNRAS 491.3, 4089–4107. arXiv: `1911.06070 [astro-ph.GA]` (cit. on p. 7).

Denissenkov, P. A. and F. D. A. Hartwick (Jan. 2014). "Supermassive stars as a source of abundance anomalies of proton-capture elements in globular clusters". MNRAS 437.1, L21–L25. arXiv: `1305.5975 [astro-ph.SR]` (cit. on p. 82).

Dib, Sami et al. (May 2007). "The Virial Balance of Clumps and Cores in Molecular Clouds". ApJ 661.1, 262–284. arXiv: `astro-ph/0607362 [astro-ph]` (cit. on p. 5).

Dobbs, C. L. et al. (Jan. 2014). "Formation of Molecular Clouds and Global Conditions for Star Formation". *Protostars and Planets VI*. Ed. by Henrik Beuther et al., 3–26. arXiv: `1312.3223 [astro-ph.GA]` (cit. on pp. 3, 7, 9).

Draine, B. T. et al. (Aug. 2021). "Excitation of Polycyclic Aromatic Hydrocarbon Emission: Dependence on Size Distribution, Ionization, and Starlight Spectrum and Intensity". ApJ 917.1, 3, 3. arXiv: `2011.07046 [astro-ph.GA]` (cit. on p. 81).

Efremov, Yuri N. and Bruce G. Elmegreen (Sept. 1998). "Hierarchical star formation from the time-space distribution of star clusters in the Large Magellanic Cloud". MNRAS 299.2, 588–594. arXiv: `astro-ph/9805259 [astro-ph]` (cit. on p. 10).

Egusa, Fumi et al. (Feb. 2018). "Molecular Gas Properties in M83 from CO PDFs". ApJ 854.2, 90, 90. arXiv: `1801.04025 [astro-ph.GA]` (cit. on p. 8).

Ellison, Sara L. et al. (July 2021). "The EDGE-CALIFA survey: central molecular gas depletion in AGN host galaxies - a smoking gun for quenching?" MNRAS 505.1, L46–L51. arXiv: `2105.02916 [astro-ph.GA]` (cit. on p. 2).

Elmegreen, Bruce G. (Feb. 2000). "Star Formation in a Crossing Time". ApJ 530.1, 277–281. arXiv: `astro-ph/9911172 [astro-ph]` (cit. on p. 10).

Emsellem, Eric et al. (Mar. 2022). "The PHANGS-MUSE survey. Probing the chemo-dynamical evolution of disc galaxies". A&A 659, A191, A191. arXiv: `2110.03708 [astro-ph.GA]` (cit. on pp. 7, 80).

Engargiola, G. et al. (Dec. 2003). "Giant Molecular Clouds in M33. I. BIMA All-Disk Survey". ApJS 149.2, 343–363. arXiv: `astro-ph/0308388 [astro-ph]` (cit. on pp. 3, 10).

Evans Neal J., II, Amanda Heiderman, and Nalin Vutisalchavakul (Feb. 2014). "Star Formation Relations in Nearby Molecular Clouds". ApJ 782.2, 114, 114. arXiv: `1401.3287 [astro-ph.GA]` (cit. on p. 6).

Evans Neal J., II et al. (Apr. 2009). "The Spitzer c2d Legacy Results: Star-Formation Rates and Efficiencies; Evolution and Lifetimes". ApJS 181.2, 321–350. arXiv: `0811.1059 [astro-ph]` (cit. on p. 6).

Evans Neal J., II et al. (Oct. 2021). "Which Molecular Cloud Structures Are Bound?" ApJ 920.2, 126, 126. arXiv: `2107.05750 [astro-ph.GA]` (cit. on pp. 5, 8).

Faesi, Christopher M., Charles J. Lada, and Jan Forbrich (Apr. 2018). "The ALMA View of GMCs in NGC 300: Physical Properties and Scaling Relations at 10 pc Resolution". ApJ 857.1, 19, 19. arXiv: `1801.06238 [astro-ph.GA]` (cit. on p. 5).

Federrath, Christoph and Ralf S. Klessen (Dec. 2012). "The Star Formation Rate of Turbulent Magnetized Clouds: Comparing Theory, Simulations, and Observations". ApJ 761.2, 156, 156. arXiv: `1209.2856 [astro-ph.SR]` (cit. on p. 8).

Freeman, Pamela et al. (June 2017). "The varying mass distribution of molecular clouds across M83". MNRAS 468.2, 1769–1781. arXiv: `1702.07728 [astro-ph.GA]` (cit. on p. 7).

Fukui, Y. et al. (Sept. 2008). "The Second Survey of the Molecular Clouds in the Large Magellanic Cloud by NANTEN. I. Catalog of Molecular Clouds". ApJS 178.1, 56–70. arXiv: `0804.1458 [astro-ph]` (cit. on p. 5).

Galliano, Frédéric, Maud Galametz, and Anthony P. Jones (Sept. 2018). "The Interstellar Dust Properties of Nearby Galaxies". ARA&A 56, 673–713. arXiv: `1711.07434` `[astro-ph.GA]` (cit. on p. 80).

Genzel, R. et al. (Oct. 2010). "A study of the gas-star formation relation over cosmic time". MNRAS 407.4, 2091–2108. arXiv: `1003.5180 [astro-ph.CO]` (cit. on p. 2).

Gieles, Mark et al. (Aug. 2018). "Concurrent formation of supermassive stars and globular clusters: implications for early self-enrichment". MNRAS 478.2, 2461–2479. arXiv: `1804.04682 [astro-ph.GA]` (cit. on p. 82).

Gordon, M. A. and W. B. Burton (Sept. 1976). "Carbon monoxide in the Galaxy. I. The radial distribution of CO, H_2, and nucleons." ApJ 208, 346–353 (cit. on p. 4).

Grasha, K. et al. (Nov. 2018). "Connecting young star clusters to CO molecular gas in NGC 7793 with ALMA-LEGUS". MNRAS 481.1, 1016–1027. arXiv: `1808.02496` `[astro-ph.GA]` (cit. on p. 11).

Grasha, K. et al. (Mar. 2019). "The spatial relation between young star clusters and molecular clouds in M51 with LEGUS". MNRAS 483.4, 4707–4723. arXiv: `1812.06109` `[astro-ph.GA]` (cit. on p. 11).

Gratier, P. et al. (June 2012). "Giant molecular clouds in the Local Group galaxy M 33⋆". A&A 542, A108, A108. arXiv: `1111.4320 [astro-ph.CO]` (cit. on p. 5).

Grisdale, Kearn et al. (Sept. 2018). "Physical properties and scaling relations of molecular clouds: the effect of stellar feedback". MNRAS 479.3, 3167–3180. arXiv: `1801.03104` `[astro-ph.GA]` (cit. on p. 9).

Grudić, Michael Y. et al. (Sept. 2019). "On the nature of variations in the measured star formation efficiency of molecular clouds". MNRAS 488.2, 1501–1518. arXiv: `1809.08348` `[astro-ph.GA]` (cit. on p. 9).

Hao, Cai-Na et al. (Nov. 2011). "Dust-corrected Star Formation Rates of Galaxies. II. Combinations of Ultraviolet and Infrared Tracers". ApJ 741.2, 124, 124. arXiv: `1108.2837 [astro-ph.CO]` (cit. on p. 6).

Hartmann, Lee (Feb. 2001). "On Age Spreads in Star-forming Regions". AJ 121.2, 1030–1039 (cit. on p. 10).

Haydon, Daniel T. et al. (Aug. 2020). "An uncertainty principle for star formation - III. The characteristic emission time-scales of star formation rate tracers". MNRAS 498.1, 235–257. arXiv: `1810.10897 [astro-ph.GA]` (cit. on pp. 6, 12).

Heiderman, Amanda et al. (Nov. 2010). "The Star Formation Rate and Gas Surface Density Relation in the Milky Way: Implications for Extragalactic Studies". ApJ 723.2, 1019–1037. arXiv: `1009.1621 [astro-ph.GA]` (cit. on p. 6).

Heitsch, Fabian, Mordecai-Mark Mac Low, and Ralf S. Klessen (Jan. 2001). "Gravitational Collapse in Turbulent Molecular Clouds. II. Magnetohydrodynamical Turbulence". ApJ 547.1, 280–291. arXiv: `astro-ph/0009227 [astro-ph]` (cit. on p. 8).

Helfer, Tamara T. et al. (Apr. 2003). "The BIMA Survey of Nearby Galaxies (BIMA SONG). II. The CO Data". ApJS 145.2, 259–327. arXiv: `astro-ph/0304294 [astro-ph]` (cit. on p. 4).

Heyer, Mark H., John M. Carpenter, and Ronald L. Snell (Apr. 2001). "The Equilibrium State of Molecular Regions in the Outer Galaxy". ApJ 551.2, 852–866. arXiv: astro-ph/0101133 [astro-ph] (cit. on p. 5).

Heyer, Mark H. et al. (Feb. 2004). "The Molecular Gas Distribution and Schmidt Law in M33". ApJ 602.2, 723–729. arXiv: astro-ph/0311226 [astro-ph] (cit. on p. 2).

Hirota, Akihiko et al. (Aug. 2018). "ALMA ^{12}CO (J = 1-0) imaging of the nearby galaxy M 83: Variations in the efficiency of star formation in giant molecular clouds". PASJ 70.4, 73, 73. arXiv: 1808.01702 [astro-ph.GA] (cit. on p. 7).

Hollenbach, David and E. E. Salpeter (Jan. 1971). "Surface Recombination of Hydrogen Molecules". ApJ 163, 155 (cit. on p. 80).

Hollyhead, K. et al. (May 2015). "Studying the YMC population of M83: how long clusters remain embedded, their interaction with the ISM and implications for GC formation theories". MNRAS 449.1, 1106–1117. arXiv: 1502.03823 [astro-ph.GA] (cit. on p. 11).

Hughes, A. et al. (Aug. 2010). "Physical properties of giant molecular clouds in the Large Magellanic Cloud". MNRAS 406.3, 2065–2086. arXiv: 1004.2094 [astro-ph.CO] (cit. on p. 5).

Hughes, Annie et al. (Dec. 2013). "A Comparative Study of Giant Molecular Clouds in M51, M33, and the Large Magellanic Cloud". ApJ 779.1, 46, 46. arXiv: 1309.3453 [astro-ph.GA] (cit. on p. 8).

Imara, Nia and Christopher M. Faesi (May 2019). "ALMA Observations of Giant Molecular Clouds in the Starburst Dwarf Galaxy Henize 2-10". ApJ 876.2, 141, 141. arXiv: 1812.02180 [astro-ph.GA] (cit. on p. 5).

Jappsen, A. -K. et al. (May 2005). "The stellar mass spectrum from non-isothermal gravo-turbulent fragmentation". A&A 435.2, 611–623. arXiv: astro-ph/0410351 [astro-ph] (cit. on p. 79).

Jeffreson, Sarah M. R. and J. M. Diederik Kruijssen (May 2018). "A general theory for the lifetimes of giant molecular clouds under the influence of galactic dynamics". MNRAS 476.3, 3688–3715. arXiv: 1803.01850 [astro-ph.GA] (cit. on pp. 1, 2, 9).

Jeffreson, Sarah M. R., Vadim A. Semenov, and Mark R. Krumholz (Jan. 2023). "Clouds of Theseus: long-lived molecular clouds are composed of short-lived H2 molecules". *arXiv e-prints*, arXiv:2301.10251, arXiv:2301.10251. arXiv: 2301.10251 [astro-ph.GA] (cit. on p. 8).

Jeffreson, Sarah M. R. et al. (Oct. 2020). "The role of galactic dynamics in shaping the physical properties of giant molecular clouds in Milky Way-like galaxies". MNRAS 498.1, 385–429. arXiv: 2007.00006 [astro-ph.GA] (cit. on pp. 9, 79).

Jeffreson, Sarah M. R. et al. (Aug. 2021). "A scaling relation for the molecular cloud lifetime in Milky Way-like galaxies". MNRAS 505.2, 1678–1698. arXiv: 2105.01073 [astro-ph.GA] (cit. on p. 9).

Kawamura, Akiko et al. (Sept. 2009). "The Second Survey of the Molecular Clouds in the Large Magellanic Cloud by NANTEN. II. Star Formation". ApJS 184.1, 1–17. arXiv: 0908.1168 [astro-ph.CO] (cit. on pp. 3, 11, 75).

Kennicutt Robert C., Jr. (Sept. 1989). "The Star Formation Law in Galactic Disks". ApJ 344, 685 (cit. on p. 2).

— (May 1998). "The Global Schmidt Law in Star-forming Galaxies". ApJ 498.2, 541–552. arXiv: `astro-ph/9712213 [astro-ph]` (cit. on p. 2).

Kennicutt Robert C., Jr. et al. (Aug. 2003). "SINGS: The SIRTF Nearby Galaxies Survey". PASP 115.810, 928–952. arXiv: `astro-ph/0305437 [astro-ph]` (cit. on p. 6).

Kennicutt Robert C., Jr. et al. (Dec. 2007). "Star Formation in NGC 5194 (M51a). II. The Spatially Resolved Star Formation Law". ApJ 671.1, 333–348. arXiv: `0708.0922 [astro-ph]` (cit. on p. 2).

Kennicutt, Robert C. and Neal J. Evans (Sept. 2012). "Star Formation in the Milky Way and Nearby Galaxies". ARA&A 50, 531–608. arXiv: `1204.3552 [astro-ph.GA]` (cit. on pp. 1–3, 6).

Kim, Jaeyeon et al. (June 2021a). "On the duration of the embedded phase of star formation". MNRAS 504.1, 487–509. arXiv: `2012.00019 [astro-ph.GA]` (cit. on p. 76).

Kim, Jenny J. and Young-Wook Lee (Dec. 2018). "Explaining the Multiple Populations in Globular Clusters by Multiple Episodes of Star Formation and Enrichment without Gas Expulsion from Massive Star Feedback". ApJ 869.1, 35, 35. arXiv: `1807.01317 [astro-ph.GA]` (cit. on p. 82).

Kim, Jeong-Gyu, Woong-Tae Kim, and Eve C. Ostriker (May 2018). "Modeling UV Radiation Feedback from Massive Stars. II. Dispersal of Star-forming Giant Molecular Clouds by Photoionization and Radiation Pressure". ApJ 859.1, 68, 68. arXiv: `1804.04664 [astro-ph.GA]` (cit. on p. 9).

Kim, Jeong-Gyu, Eve C. Ostriker, and Nina Filippova (Apr. 2021b). "Star Formation Efficiency and Dispersal of Giant Molecular Clouds with UV Radiation Feedback: Dependence on Gravitational Boundedness and Magnetic Fields". ApJ 911.2, 128, 128. arXiv: `2011.07772 [astro-ph.GA]` (cit. on pp. 5, 8, 9).

Kim, Sungeun et al. (Dec. 1999). "H I Shells in the Large Magellanic Cloud". AJ 118.6, 2797–2823 (cit. on p. 79).

Klessen, Ralf S. and Simon C. O. Glover (Jan. 2016). "Physical Processes in the Interstellar Medium". *Saas-Fee Advanced Course* 43, 85. arXiv: `1412.5182 [astro-ph.GA]` (cit. on p. 7).

Koda, Jin et al. (Aug. 2009). "Dynamically Driven Evolution of the Interstellar Medium in M51". ApJ 700.2, L132–L136. arXiv: `0907.1656 [astro-ph.CO]` (cit. on pp. 3, 10).

Kramer, C. et al. (Jan. 1998). "Clump mass spectra of molecular clouds". A&A 329, 249–264 (cit. on p. 5).

Krause, M. et al. (Apr. 2013). "Superbubble dynamics in globular cluster infancy. II. Consequences for secondary star formation in the context of self-enrichment via fast-rotating massive stars". A&A 552, A121, A121. arXiv: `1302.2494 [astro-ph.GA]` (cit. on p. 82).

Kruijssen, J. M. Diederik (Dec. 2015). "Globular clusters as the relics of regular star formation in 'normal' high-redshift galaxies". MNRAS 454.2, 1658–1686. arXiv: `1509.02163 [astro-ph.GA]` (cit. on p. 82).

Kruijssen, J. M. Diederik and Steven N. Longmore (Apr. 2014). "An uncertainty principle for star formation - I. Why galactic star formation relations break down below a certain spatial scale". MNRAS 439.4, 3239–3252. arXiv: `1401.4459 [astro-ph.GA]` (cit. on pp. 3, 11, 12, 75, 77, 79, 80).

Kruijssen, J. M. Diederik et al. (Sept. 2018). "An uncertainty principle for star formation - II. A new method for characterizing the cloud-scale physics of star formation and feedback across cosmic history". MNRAS 479.2, 1866–1952. arXiv: 1805.00012 [astro-ph.GA] (cit. on pp. 11, 12, 75, 77, 79).

Kruijssen, J. M. Diederik et al. (May 2019). "Fast and inefficient star formation due to short-lived molecular clouds and rapid feedback". Nature 569.7757, 519–522. arXiv: 1905.08801 [astro-ph.GA] (cit. on pp. 3, 12, 75, 76).

Krumholz, Mark R. and Christopher F. McKee (Sept. 2005). "A General Theory of Turbulence-regulated Star Formation, from Spirals to Ultraluminous Infrared Galaxies". ApJ 630.1, 250–268. arXiv: astro-ph/0505177 [astro-ph] (cit. on pp. 2, 6, 8).

Krumholz, Mark R., Christopher F. McKee, and Jason Tumlinson (Dec. 2008). "The Atomic-to-Molecular Transition in Galaxies. I. An Analytic Approximation for Photodissociation Fronts in Finite Clouds". ApJ 689.2, 865–882. arXiv: 0805.2947 [astro-ph] (cit. on p. 3).

— (Mar. 2009). "The Atomic-to-Molecular Transition in Galaxies. II: H I and H_2 Column Densities". ApJ 693.1, 216–235. arXiv: 0811.0004 [astro-ph] (cit. on p. 3).

Kuno, Nario et al. (Feb. 2007). "Nobeyama CO Atlas of Nearby Spiral Galaxies: Distribution of Molecular Gas in Barred and Nonbarred Spiral Galaxies". PASJ 59, 117–166. arXiv: 0705.2678 [astro-ph] (cit. on p. 4).

Kutner, M. L. et al. (July 1977). "The molecular complexes in Orion." ApJ 215, 521–528 (cit. on p. 4).

Lada, C. J. (Oct. 1976). "Detailed observations of the M17 molecular cloud complex." ApJS 32, 603–629 (cit. on p. 4).

Lada, Charles J. and Elizabeth A. Lada (Jan. 2003). "Embedded Clusters in Molecular Clouds". ARA&A 41, 57–115. arXiv: astro-ph/0301540 [astro-ph] (cit. on p. 77).

Lai, Thomas S. -Y. et al. (Dec. 2020). "All the PAHs: An AKARI-Spitzer Cross-archival Spectroscopic Survey of Aromatic Emission in Galaxies". ApJ 905.1, 55, 55. arXiv: 2010.05034 [astro-ph.GA] (cit. on p. 81).

Lancaster, Lachlan et al. (Nov. 2021). "Star Formation Regulation and Self-pollution by Stellar Wind Feedback". ApJ 922.1, L3, L3. arXiv: 2110.05508 [astro-ph.GA] (cit. on p. 9).

Lang, Philipp et al. (July 2020). "PHANGS CO Kinematics: Disk Orientations and Rotation Curves at 150 pc Resolution". ApJ 897.2, 122, 122. arXiv: 2005.11709 [astro-ph.GA] (cit. on p. 79).

Lee, Eve J., Marc-Antoine Miville-Deschênes, and Norman W. Murray (Dec. 2016). "Observational Evidence of Dynamic Star Formation Rate in Milky Way Giant Molecular Clouds". ApJ 833.2, 229, 229. arXiv: 1608.05415 [astro-ph.GA] (cit. on p. 6).

Lee, Janice C. et al. (Jan. 2022a). "The PHANGS-HST Survey: Physics at High Angular Resolution in Nearby Galaxies with the Hubble Space Telescope". ApJS 258.1, 10, 10. arXiv: 2101.02855 [astro-ph.GA] (cit. on p. 7).

Lee, Janice C. et al. (Dec. 2022b). "The PHANGS-JWST Treasury Survey: Star Formation, Feedback, and Dust Physics at High Angular resolution in Nearby GalaxieS". *arXiv*

e-prints, arXiv:2212.02667, arXiv:2212.02667. arXiv: `2212.02667 [astro-ph.GA]` (cit. on pp. 6, 13, 77, 78, 80).

Leroy, A. et al. (June 2005). "The Molecular Interstellar Medium of Dwarf Galaxies on Kiloparsec Scales: A New Survey for CO in Northern, IRAS-detected Dwarf Galaxies". ApJ 625.2, 763–784. arXiv: `astro-ph/0502302 [astro-ph]` (cit. on p. 2).

Leroy, Adam K. et al. (Dec. 2008). "The Star Formation Efficiency in Nearby Galaxies: Measuring Where Gas Forms Stars Effectively". AJ 136.6, 2782–2845. arXiv: `0810.2556 [astro-ph]` (cit. on pp. 1, 2).

Leroy, Adam K. et al. (June 2009). "Heracles: The HERA CO Line Extragalactic Survey". AJ 137.6, 4670–4696. arXiv: `0905.4742 [astro-ph.CO]` (cit. on p. 4).

Leroy, Adam K. et al. (Aug. 2013). "Molecular Gas and Star Formation in nearby Disk Galaxies". AJ 146.2, 19, 19. arXiv: `1301.2328 [astro-ph.CO]` (cit. on p. 2).

Leroy, Adam K. et al. (Dec. 2015). "The Multi-phase Cold Fountain in M82 Revealed by a Wide, Sensitive Map of the Molecular Interstellar Medium". ApJ 814.2, 83, 83. arXiv: `1509.02932 [astro-ph.GA]` (cit. on pp. 5, 8).

Leroy, Adam K. et al. (Nov. 2016). "A Portrait of Cold Gas in Galaxies at 60 pc Resolution and a Simple Method to Test Hypotheses That Link Small-scale ISM Structure to Galaxy-scale Processes". ApJ 831.1, 16, 16. arXiv: `1606.07077 [astro-ph.GA]` (cit. on p. 8).

Leroy, Adam K. et al. (Sept. 2017). "Cloud-scale ISM Structure and Star Formation in M51". ApJ 846.1, 71, 71. arXiv: `1706.08540 [astro-ph.GA]` (cit. on p. 7).

Leroy, Adam K. et al. (Oct. 2019). "A z = 0 Multiwavelength Galaxy Synthesis. I. A WISE and GALEX Atlas of Local Galaxies". ApJS 244.2, 24, 24. arXiv: `1910.13470 [astro-ph.GA]` (cit. on p. 6).

Leroy, Adam K. et al. (Dec. 2021). "PHANGS-ALMA: Arcsecond CO(2-1) Imaging of Nearby Star-forming Galaxies". ApJS 257.2, 43, 43. arXiv: `2104.07739 [astro-ph.GA]` (cit. on pp. 1, 5, 12).

Li, Hui et al. (July 2019). "Disruption of giant molecular clouds and formation of bound star clusters under the influence of momentum stellar feedback". MNRAS 487.1, 364–380. arXiv: `1904.11987 [astro-ph.GA]` (cit. on p. 9).

Lim, Wanggi, James M. De Buizer, and James T. Radomski (Jan. 2020). "Surveying the Giant H II Regions of the Milky Way with SOFIA. II. M17". ApJ 888.2, 98, 98. arXiv: `1912.02855 [astro-ph.GA]` (cit. on p. 79).

Lin, Lihwai et al. (Oct. 2019). "The ALMaQUEST Survey: The Molecular Gas Main Sequence and the Origin of the Star-forming Main Sequence". ApJ 884.2, L33, L33. arXiv: `1909.11243 [astro-ph.GA]` (cit. on p. 5).

Lisenfeld, U. et al. (Oct. 2011). "The AMIGA sample of isolated galaxies. IX. Molecular gas properties". A&A 534, A102, A102. arXiv: `1108.2130 [astro-ph.CO]` (cit. on p. 4).

Lopez, Laura A. et al. (Nov. 2014). "The Role of Stellar Feedback in the Dynamics of H II Regions". ApJ 795.2, 121, 121. arXiv: `1309.5421 [astro-ph.SR]` (cit. on p. 80).

Lu, Anan et al. (Aug. 2022). "WISDOM project - XI. Star formation efficiency in the bulge of the AGN-host Galaxy NGC 3169 with SITELLE and ALMA". MNRAS 514.4, 5035–5055. arXiv: `2206.03316 [astro-ph.GA]` (cit. on p. 12).

Madden, S. C. et al. (Nov. 2020). "Tracing the total molecular gas in galaxies: [CII] and the CO-dark gas". A&A 643, A141, A141. arXiv: 2009.00649 [astro-ph.GA] (cit. on pp. 4, 76).

Mao, S. Alwin, Eve C. Ostriker, and Chang-Goo Kim (July 2020). "Cloud Properties and Correlations with Star Formation in Self-consistent Simulations of the Multiphase ISM". ApJ 898.1, 52, 52. arXiv: 1911.05078 [astro-ph.GA] (cit. on p. 5).

Martin, D. Christopher et al. (Jan. 2005). "The Galaxy Evolution Explorer: A Space Ultraviolet Survey Mission". ApJ 619.1, L1–L6. arXiv: astro-ph/0411302 [astro-ph] (cit. on p. 6).

McKee, Christopher F. and Eve C. Ostriker (Sept. 2007). "Theory of Star Formation". ARA&A 45.1, 565–687. arXiv: 0707.3514 [astro-ph] (cit. on pp. 1, 7).

McLeod, Anna F. et al. (Dec. 2021). "The impact of pre-supernova feedback and its dependence on environment". MNRAS 508.4, 5425–5448. arXiv: 2109.08703 [astro-ph.GA] (cit. on p. 80).

Meidt, Sharon E. et al. (June 2015). "Short GMC Lifetimes: An Observational Estimate with the PdBI Arcsecond Whirlpool Survey (PAWS)". ApJ 806.1, 72, 72. arXiv: 1504.04528 [astro-ph.GA] (cit. on pp. 3, 10, 11, 79).

Meidt, Sharon E. et al. (Feb. 2018). "A Model for the Onset of Self-gravitation and Star Formation in Molecular Gas Governed by Galactic Forces. I. Cloud-scale Gas Motions". ApJ 854.2, 100, 100. arXiv: 1712.06364 [astro-ph.GA] (cit. on pp. 9, 79).

Meidt, Sharon E. et al. (Apr. 2020). "A Model for the Onset of Self-gravitation and Star Formation in Molecular Gas Governed by Galactic Forces. II. The Bottleneck to Collapse Set by Cloud-Environment Decoupling". ApJ 892.2, 73, 73. arXiv: 2001.07459 [astro-ph.GA] (cit. on p. 9).

Messa, M. et al. (Nov. 2020). "Looking for obscured young star clusters in NCG 1313". arXiv e-prints, arXiv:2011.09392, arXiv:2011.09392. arXiv: 2011.09392 [astro-ph.GA] (cit. on p. 11).

Mingozzi, M. et al. (Feb. 2019). "The MAGNUM survey: different gas properties in the outflowing and disc components in nearby active galaxies with MUSE". A&A 622, A146, A146. arXiv: 1811.07935 [astro-ph.GA] (cit. on p. 7).

Miura, R. E. et al. (July 2021). "A giant molecular cloud catalogue in the molecular disc of the elliptical galaxy NGC 5128 (Centaurus A)". MNRAS 504.4, 6198–6215. arXiv: 2104.12442 [astro-ph.GA] (cit. on p. 5).

Miura, Rie E. et al. (Dec. 2012). "Giant Molecular Cloud Evolutions in the Nearby Spiral Galaxy M33". ApJ 761.1, 37, 37. arXiv: 1210.3801 [astro-ph.CO] (cit. on pp. 3, 11).

Miura, Rie E. et al. (Sept. 2018). "ALMA Observations toward the Starburst Dwarf Galaxy NGC 5253. I. Molecular Cloud Properties and Scaling Relations". ApJ 864.2, 120, 120. arXiv: 1808.10089 [astro-ph.GA] (cit. on pp. 5, 7).

Muraoka, Kazuyuki et al. (Dec. 2019). "CO Multi-line Imaging of Nearby Galaxies (COMING). VI. Radial variations in star formation efficiency". PASJ 71, S15, S15. arXiv: 1901.11197 [astro-ph.GA] (cit. on p. 2).

Ochsendorf, Bram B. et al. (June 2017). "What Sets the Massive Star Formation Rates and Efficiencies of Giant Molecular Clouds?" ApJ 841.2, 109, 109. arXiv: 1704.06965 [astro-ph.GA] (cit. on p. 6).

Oka, Tomoharu et al. (Nov. 2001). "Statistical Properties of Molecular Clouds in the Galactic Center". ApJ 562.1, 348–362 (cit. on p. 7).

Onodera, Sachiko et al. (Oct. 2010). "Breakdown of Kennicutt-Schmidt Law at Giant Molecular Cloud Scales in M33". ApJ 722.2, L127–L131. arXiv: 1009.1971 [astro-ph.GA] (cit. on pp. 3, 11).

Padoan, Paolo and Åke Nordlund (Mar. 2011). "The Star Formation Rate of Supersonic Magnetohydrodynamic Turbulence". ApJ 730.1, 40, 40. arXiv: 0907.0248 [astro-ph.GA] (cit. on p. 8).

Padoan, Paolo et al. (May 2017). "Supernova Driving. IV. The Star-formation Rate of Molecular Clouds". ApJ 840.1, 48, 48. arXiv: 1702.07270 [astro-ph.GA] (cit. on p. 79).

Pan, Hsi-An et al. (Jan. 2022). "The Gas-Star Formation Cycle in Nearby Star-forming Galaxies II. Resolved Distributions of CO and Hα Emission for 49 PHANGS Galaxies". *arXiv e-prints*, arXiv:2201.01403, arXiv:2201.01403. arXiv: 2201.01403 [astro-ph.GA] (cit. on pp. 3, 11, 75).

Pereira-Santaella, M. et al. (Mar. 2016). "Sub-kpc star formation law in the local luminous infrared galaxy IC 4687 as seen by ALMA". A&A 587, A44, A44. arXiv: 1601.02427 [astro-ph.GA] (cit. on p. 5).

Pokhrel, Riwaj et al. (May 2021). "The Single-cloud Star Formation Relation". ApJ 912.1, L19, L19. arXiv: 2104.04551 [astro-ph.GA] (cit. on p. 6).

Rahman, Nurur et al. (Feb. 2012). "CARMA Survey Toward Infrared-bright Nearby Galaxies (STING). II. Molecular Gas Star Formation Law and Depletion Time across the Blue Sequence". ApJ 745.2, 183, 183. arXiv: 1110.1630 [astro-ph.CO] (cit. on p. 4).

Rahner, Daniel et al. (Oct. 2017). "Winds and radiation in unison: a new semi-analytic feedback model for cloud dissolution". MNRAS 470.4, 4453–4472. arXiv: 1704.04240 [astro-ph.GA] (cit. on p. 9).

Rickard, L. J. et al. (July 1975). "Detection of extragalactic carbon monoxide at millimeter wavelengths." ApJ 199, L75–L78 (cit. on p. 4).

Rieder, Steven et al. (Feb. 2022). "The formation and early evolution of embedded star clusters in spiral galaxies". MNRAS 509.4, 6155–6168. arXiv: 2111.09720 [astro-ph.GA] (cit. on p. 8).

Roman-Duval, Julia et al. (Nov. 2010). "Physical Properties and Galactic Distribution of Molecular Clouds Identified in the Galactic Ring Survey". ApJ 723.1, 492–507. arXiv: 1010.2798 [astro-ph.GA] (cit. on p. 5).

Rosolowsky, E. (Dec. 2005). "The Mass Spectra of Giant Molecular Clouds in the Local Group". PASP 117.838, 1403–1410. arXiv: astro-ph/0508679 [astro-ph] (cit. on p. 5).

Rosolowsky, Erik et al. (Mar. 2021). "Giant molecular cloud catalogues for PHANGS-ALMA: methods and initial results". MNRAS 502.1, 1218–1245. arXiv: 2101.04697 [astro-ph.GA] (cit. on pp. 1, 5, 8, 9, 80).

Roussel, H. et al. (Nov. 2007). "Warm Molecular Hydrogen in the Spitzer SINGS Galaxy Sample". ApJ 669.2, 959–981. arXiv: 0707.0395 [astro-ph] (cit. on p. 4).

Saintonge, Amélie et al. (July 2011). "COLD GASS, an IRAM legacy survey of molecular gas in massive galaxies - I. Relations between H_2, H I, stellar content and structural properties". MNRAS 415.1, 32–60. arXiv: 1103.1642 [astro-ph.CO] (cit. on p. 4).

Saintonge, Amélie et al. (Dec. 2017). "xCOLD GASS: The Complete IRAM 30 m Legacy Survey of Molecular Gas for Galaxy Evolution Studies". ApJS 233.2, 22, 22. arXiv: 1710.02157 [astro-ph.GA] (cit. on p. 4).

Saintonge, Amélie et al. (Dec. 2018). "JINGLE, a JCMT legacy survey of dust and gas for galaxy evolution studies - I. Survey overview and first results". MNRAS 481.3, 3497–3519. arXiv: 1809.07336 [astro-ph.GA] (cit. on p. 4).

Sanders, D. B., P. M. Solomon, and N. Z. Scoville (Jan. 1984). "Giant molecular clouds in the Galaxy. I - The axisymmetric distribution of H2". ApJ 276, 182–203 (cit. on p. 4).

Sandstrom, Karin M. et al. (Dec. 2022). "PHANGS-JWST First Results: Tracing the Diffuse ISM with JWST Imaging of Polycyclic Aromatic Hydrocarbon Emission in Nearby Galaxies". *arXiv e-prints*, arXiv:2212.11177, arXiv:2212.11177. arXiv: 2212.11177 [astro-ph.GA] (cit. on pp. 78, 81).

Schinnerer, Eva et al. (Dec. 2019). "The Gas-Star Formation Cycle in Nearby Star-forming Galaxies. I. Assessment of Multi-scale Variations". ApJ 887.1, 49, 49. arXiv: 1910.10520 [astro-ph.GA] (cit. on pp. 3, 11, 75).

Schmidt, Maarten (Mar. 1959). "The Rate of Star Formation." ApJ 129, 243 (cit. on p. 2).

Schruba, Andreas, J. M. Diederik Kruijssen, and Adam K. Leroy (Sept. 2019). "How Galactic Environment Affects the Dynamical State of Molecular Clouds and Their Star Formation Efficiency". ApJ 883.1, 2, 2. arXiv: 1908.04306 [astro-ph.GA] (cit. on pp. 5, 7–9).

Schruba, Andreas et al. (Oct. 2010). "The Scale Dependence of the Molecular Gas Depletion Time in M33". ApJ 722.2, 1699–1706. arXiv: 1009.1651 [astro-ph.CO] (cit. on pp. 3, 11).

Schuster, K. F. et al. (Jan. 2007). "A complete ^{12}CO 2-1 map of M 51 with HERA. I. Radial averages of CO, H I, and radio continuum". A&A 461.1, 143–151. arXiv: astro-ph/0609670 [astro-ph] (cit. on p. 2).

Schweizer, François et al. (Oct. 2008). "A New Distance to the Antennae Galaxies (NGC 4038/39) Based on the Type Ia Supernova 2007sr". AJ 136.4, 1482–1489. arXiv: 0807.3955 [astro-ph] (cit. on p. 82).

Scoville, N. Z. and K. Hersh (Apr. 1979). "Collisional growth of giant molecular clouds." ApJ 229, 578–582 (cit. on pp. 3, 10).

Scoville, N. Z. and P. M. Solomon (July 1975). "Molecular clouds in the Galaxy." ApJ 199, L105–L109 (cit. on p. 4).

Scoville, Nick et al. (Feb. 2023). "Cosmic Evolution of Gas and Star Formation". ApJ 943.2, 82, 82 (cit. on p. 10).

Smith, Rowan J. et al. (Feb. 2020). "The Cloud Factory I: Generating resolved filamentary molecular clouds from galactic-scale forces". MNRAS 492.2, 1594–1613. arXiv: 1911.05753 [astro-ph.GA] (cit. on p. 9).

Solomon, P. M. and R. de Zafra (July 1975). "Carbon monoxide in external galaxies." ApJ 199, L79–L83 (cit. on p. 4).

Solomon, P. M. et al. (Nov. 1972). "Molecular Clouds in the Galactic Center Region: Carbon Monoxide Observations at 2.6 Millimeters". ApJ 178, 125–130 (cit. on p. 4).

Solomon, P. M. et al. (Aug. 1987). "Mass, Luminosity, and Line Width Relations of Galactic Molecular Clouds". ApJ 319, 730 (cit. on pp. 1, 5).

Sorai, Kazuo et al. (Dec. 2019). "CO multi-line imaging of nearby galaxies (COMING). IV. Overview of the project". PASJ 71, S14, S14. arXiv: 1910.03863 [astro-ph.GA] (cit. on p. 5).

Stecker, F. W. et al. (Oct. 1975). "Molecular hydrogen in the Galaxy and galactic gamma rays." ApJ 201, 90–97 (cit. on p. 4).

Sternberg, Amiel (Sept. 1988). "The Infrared Response of Molecular Hydrogen Gas to Ultraviolet Radiation: A Scaling Law". ApJ 332, 400 (cit. on p. 3).

Sun, Jiayi et al. (Apr. 2020a). "Dynamical Equilibrium in the Molecular ISM in 28 Nearby Star-forming Galaxies". ApJ 892.2, 148, 148. arXiv: 2002.08964 [astro-ph.GA] (cit. on pp. 7, 8).

Sun, Jiayi et al. (Sept. 2020b). "Molecular Gas Properties on Cloud Scales across the Local Star-forming Galaxy Population". ApJ 901.1, L8, L8. arXiv: 2009.01842 [astro-ph.GA] (cit. on pp. 5, 7, 76).

Sun, Jiayi et al. (Aug. 2022). "Molecular Cloud Populations in the Context of Their Host Galaxy Environments: A Multiwavelength Perspective". AJ 164.2, 43, 43. arXiv: 2206.07055 [astro-ph.GA] (cit. on pp. 1, 2, 5, 7–9, 79, 82).

Toalá, Jesús A., Enrique Vázquez-Semadeni, and Gilberto C. Gómez (Jan. 2012). "The Free-fall Time of Finite Sheets and Filaments". ApJ 744.2, 190, 190. arXiv: 1110.0917 [astro-ph.SR] (cit. on p. 8).

Utomo, Dyas et al. (Nov. 2017). "The EDGE-CALIFA Survey: Variations in the Molecular Gas Depletion Time in Local Galaxies". ApJ 849.1, 26, 26. arXiv: 1704.03481 [astro-ph.GA] (cit. on p. 2).

Utomo, Dyas et al. (July 2018). "Star Formation Efficiency per Free-fall Time in nearby Galaxies". ApJ 861.2, L18, L18. arXiv: 1806.11121 [astro-ph.GA] (cit. on p. 7).

van Dishoeck, E. F. and J. H. Black (Sept. 1986). "Comprehensive Models of Diffuse Interstellar Clouds: Physical Conditions and Molecular Abundances". ApJS 62, 109 (cit. on p. 3).

Verley, S. et al. (Feb. 2010). "Star formation in M 33: the radial and local relations with the gas". A&A 510, A64, A64. arXiv: 0912.2015 [astro-ph.CO] (cit. on p. 2).

Vutisalchavakul, Nalin, II Evans Neal J., and Mark Heyer (Nov. 2016). "Star Formation Relations in the Milky Way". ApJ 831.1, 73, 73. arXiv: 1607.06518 [astro-ph.SR] (cit. on p. 6).

Walter, Fabian et al. (May 2007). "Dust and Atomic Gas in Dwarf Irregular Galaxies of the M81 Group: The SINGS and THINGS View". ApJ 661.1, 102–114. arXiv: astro-ph/0702378 [astro-ph] (cit. on p. 79).

Ward, Jacob L. et al. (July 2020). "Towards a multitracer timeline of star formation in the LMC - I. Deriving the lifetimes of H I clouds". MNRAS 497.2, 2286–2301. arXiv: 2007.03691 [astro-ph.GA] (cit. on p. 12).

Ward, Jacob L. et al. (Sept. 2022). "Towards a multi-tracer timeline of star formation in the LMC – II. The formation and destruction of molecular clouds". *arXiv e-prints*, arXiv:2209.05541, arXiv:2209.05541. arXiv: 2209.05541 [astro-ph.GA] (cit. on pp. 11, 12).

Watkins, Elizabeth J. et al. (Dec. 2022). "PHANGS-JWST First Results: A statistical view on bubble evolution in NGC628". *arXiv e-prints*, arXiv:2212.00811, arXiv:2212.00811. arXiv: 2212.00811 [astro-ph.GA] (cit. on p. 79).

Whitmore, Bradley C. et al. (Nov. 2014). "ALMA Observations of the Antennae Galaxies. I. A New Window on a Prototypical Merger". ApJ 795.2, 156, 156. arXiv: 1410.4473 [astro-ph.GA] (cit. on pp. 11, 77, 82).

Wilson, C. D. et al. (Aug. 2012). "The JCMT Nearby Galaxies Legacy Survey — VIII. CO data and the $L_{CO(3-2)}$-L_{FIR} correlation in the SINGS sample". MNRAS 424.4, 3050–3080. arXiv: 1206.1629 [astro-ph.CO] (cit. on p. 4).

Wilson, Christine D. et al. (Oct. 2000). "High-Resolution Imaging of Molecular Gas and Dust in the Antennae (NGC 4038/39): Super Giant Molecular Complexes". ApJ 542.1, 120–127. arXiv: astro-ph/0005208 [astro-ph] (cit. on p. 82).

Wilson, R. W., K. B. Jefferts, and A. A. Penzias (July 1970). "Carbon Monoxide in the Orion Nebula". ApJ 161, L43 (cit. on p. 4).

Wilson, W. J. et al. (July 1974). "Observations of Galactic Carbon Monoxide Emission at 2.6 Millimeters". ApJ 191, 357–374 (cit. on p. 4).

Wolfire, Mark G., David Hollenbach, and Christopher F. McKee (June 2010). "The Dark Molecular Gas". ApJ 716.2, 1191–1207. arXiv: 1004.5401 [astro-ph.GA] (cit. on pp. 3, 4).

Wolfire, Mark G., Livia Vallini, and Mélanie Chevance (Aug. 2022). "Photodissociation and X-Ray-Dominated Regions". ARA&A 60, 247–318. arXiv: 2202.05867 [astro-ph.GA] (cit. on pp. 4, 80).

Wong, Tony and Leo Blitz (Apr. 2002). "The Relationship between Gas Content and Star Formation in Molecule-rich Spiral Galaxies". ApJ 569.1, 157–183. arXiv: astro-ph/0112204 [astro-ph] (cit. on p. 2).

Wong, Tony et al. (Dec. 2011). "The Magellanic Mopra Assessment (MAGMA). I. The Molecular Cloud Population of the Large Magellanic Cloud". ApJS 197.2, 16, 16. arXiv: 1108.5715 [astro-ph.GA] (cit. on p. 5).

Wright, Edward L. et al. (Dec. 2010). "The Wide-field Infrared Survey Explorer (WISE): Mission Description and Initial On-orbit Performance". AJ 140.6, 1868–1881. arXiv: 1008.0031 [astro-ph.IM] (cit. on p. 6).

Wyder, Ted K. et al. (May 2009). "The Star Formation Law at Low Surface Density". ApJ 696.2, 1834–1853. arXiv: 0903.3015 [astro-ph.CO] (cit. on p. 2).

Young, Judith S. et al. (May 1995). "The FCRAO Extragalactic CO Survey. I. The Data". ApJS 98, 219 (cit. on p. 4).

Zabel, N. et al. (June 2020). "AlFoCS + Fornax3D: resolved star formation in the For-
    nax cluster with ALMA and MUSE". MNRAS 496.2, 2155–2182. arXiv: 2005.13454
    [astro-ph.GA] (cit. on p. 12).